

University of Strathclyde

Department of Pure and Applied Chemistry

Process analytical technologies for particle characterisation and solid form analysis in continuous secondary pharmaceutical manufacturing

Joanna Lothian

A thesis submitted to the Department of Pure and Applied Chemistry, University of Strathclyde, Glasgow, in part fulfilment of the requirements for the degree of Doctor of Philosophy.

2022

This thesis is the result of the author's original research. It has been composed by the author and has not been previously submitted for examination which has led to the award of a degree.

The Copyright of this thesis belongs to the author under the terms of the United Kingdom Copyright Act as qualified by the University of Strathclyde Regulation 3.50. Due acknowledgement must always be made of the use of any material contained in, or derived from, this thesis.

Signed:

A handwritten signature in black ink, appearing to be 'J. J. J.', written in a cursive style.

Date: 31/01/2022

Table of Contents

| | |
|---|-------------|
| ABSTRACT | VI |
| ACKNOWLEDGEMENTS | VII |
| PUBLICATIONS AND CONFERENCE CONTRIBUTIONS | VIII |
| ABBREVIATIONS | IX |
| NOTATION | XI |
| 1. INTRODUCTION AND THEORY | 2 |
| 1.1 REGULATORY BODIES QBD AND DOE..... | 2 |
| 1.2 PHYSIOCHEMICAL PROPERTIES AND DRUG BEHAVIOUR | 6 |
| 1.3 SOLID STATE THEORY..... | 8 |
| 1.3.1 <i>Amorphous and Crystalline forms</i> | 8 |
| 1.3.2 <i>The Amorphous Phase</i> | 17 |
| 1.3.3 <i>Amorphous solid dispersions</i> | 20 |
| 1.4 ANALYSIS OF CHEMICAL AND PHYSICAL PROPERTIES..... | 21 |
| 1.4.1 <i>Particle Characterisation</i> | 21 |
| 1.4.2 <i>Solid State Analysis</i> | 3 |
| 1.5 IN-LINE PARTICLE CHARACTERISATION FOR CONTINUOUS GRANULATION | 7 |
| 1.6 IN-LINE SOLID FORM ANALYSIS OF CONTINUOUS EXTRUSION PROCESSES | 11 |
| 1.7 RESEARCH PROPOSAL..... | 1 |
| 2. INSTRUMENT THEORY | 3 |
| 2.1 TWIN SCREW WET GRANULATION | 3 |
| 2.1.1 <i>Granule Growth</i> | 4 |
| 2.1.2 <i>Wetting and Nucleation</i> | 5 |
| 2.1.3 <i>Components of a twin-screw granulator</i> | 9 |
| 2.2 HOT MELT EXTRUSION..... | 13 |
| 2.2.1 <i>Physical Characterisation</i> | 16 |
| 2.3 SOLID STATE ANALYSIS..... | 20 |
| 2.3.1 <i>X-ray powder diffraction</i> | 20 |
| 2.3.2 <i>DSC</i> | 21 |
| 2.3.3 <i>Fourier transform infrared</i> | 22 |
| 2.3.4 <i>Raman and Terahertz Raman Spectroscopy</i> | 23 |
| 2.4 DATA ANALYSIS..... | 34 |
| 2.4.1 <i>Design of Experiments</i> | 34 |
| 2.4.2 <i>Pre-processing</i> | 37 |

| | | |
|-----------|---|-----------|
| 2.4.3 | Moving average..... | 37 |
| 2.4.4 | Savitzky-Golay 1 st and 2 nd derivatives | 38 |
| 2.4.5 | Standard normal variate | 38 |
| 2.4.6 | Principal component analysis | 39 |
| 2.4.7 | Classical Least Squares..... | 40 |
| 3. | DYNAMIC IMAGE ANALYSIS OF TWIN SCREW GRANULATION | 43 |
| 3.1 | INTRODUCTION | 43 |
| 3.2 | EXPERIMENTAL..... | 45 |
| 3.2.1 | Twin screw granulation set-up..... | 45 |
| 3.2.2 | Screw Configuration..... | 46 |
| 3.2.3 | Materials | 47 |
| 3.2.4 | Methods | 48 |
| 3.3 | RESULTS AND DISCUSSION | 53 |
| 3.3.1 | Off-line analysis of granules | 53 |
| 3.3.2 | On-line monitoring of twin screw granulation..... | 58 |
| 3.3.3 | Design of Experiments: powder feed rate at the centre point 1 kg/h..... | 62 |
| 3.3.4 | Design of Experiments: powder feed rate at the centre point 3 kg/h..... | 83 |
| 3.4 | CONCLUSIONS..... | 87 |
| 3.4.1 | Off-line analysis | 87 |
| 3.4.2 | On-line analysis..... | 88 |
| 4. | DYNAMIC IMAGE ANALYSIS INDUSTRIAL SCALE STUDY OF TWIN SCREW GRANULATION..... | 90 |
| 4.1 | INTRODUCTION | 90 |
| 4.2 | EXPERIMENTAL..... | 91 |
| 4.2.1 | Materials | 91 |
| 4.2.2 | Equipment | 92 |
| 4.2.3 | Methods..... | 93 |
| 4.2.4 | Determination of torque..... | 93 |
| 4.2.5 | Off-line sieve analysis..... | 94 |
| 4.2.6 | Long Run Perturbation studies with Eyecon Image analyses..... | 94 |
| 4.2.7 | Fouling issues and interface development..... | 95 |
| 4.2.8 | Torque studies at powder flow rates of 3 and 6 kg/h with heating element..... | 100 |
| 4.3 | RESULTS AND DISCUSSION | 101 |
| 4.3.1 | Development of the heating element..... | 101 |
| 4.3.2 | Long Run Perturbation studies with Eyecon Image analyses..... | 101 |
| 4.3.3 | Torque studies at a powder flow rate of 1 kg h ⁻¹ | 108 |
| 4.3.4 | Torque studies at powder flow rates of 2 and 5 kg h ⁻¹ | 109 |
| 4.3.5 | Fouling issues and interface development..... | 110 |

| | | |
|-----------|---|------------|
| 4.3.6 | <i>Evaluation of heating element solution at high power feed rates</i> | 112 |
| 4.4 | CONCLUSIONS..... | 116 |
| 5. | TERAHERTZ RAMAN ANALYSIS OF HOT MELT EXTRUSION AMORPHOUS SOLID DISPERSIONS | |
| | 119 | |
| 5.1 | INTRODUCTION | 119 |
| 5.2 | EXPERIMENTAL..... | 122 |
| 5.2.1 | <i>Materials</i> | 122 |
| 5.2.2 | <i>Stearic acid analysis</i> | 125 |
| 5.3 | METHODS..... | 126 |
| 5.3.1 | <i>Off-line analysis of amorphous solid dispersions - comparison of XRPD and Terahertz Raman spectroscopy for characterisation of amorphous content</i> | 126 |
| 5.3.2 | <i>Content uniformity study of amorphous solid dispersions - extrudes and pellets</i> | 128 |
| 5.4 | IN-LINE TERAHERTZ RAMAN ANALYSIS OF HOT MELT EXTRUSION OF PCM-AFF | 131 |
| 5.4.1 | <i>Hot met extruder set up for in-line analysis</i> | 131 |
| 5.4.2 | <i>In-line Terahertz Raman of hot melt extrusion of PCM - AFF</i> | 132 |
| 5.4.3 | <i>Off-line analysis of extrudes of PCM - AFF</i> | 133 |
| 5.4.4 | <i>Off-line analysis of stearic acid with THz Raman</i> | 134 |
| 5.4.5 | <i>In-line analysis of HME Stearic acid with THz Raman</i> | 134 |
| 5.5 | DATA ANALYSIS..... | 134 |
| 5.5.1 | <i>Principal component analysis</i> | 134 |
| 5.6 | RESULTS AND DISCUSSION | 135 |
| 5.6.1 | <i>Off-line analysis of amorphous solid dispersions - comparison of DSC, XRPD and Raman spectroscopy with THz Raman for solid state analysis</i> | 135 |
| 5.6.2 | <i>THz Raman analysis</i> | 159 |
| 5.6.3 | <i>Homogeneity study of amorphous solid dispersions - extrudes and pellets with THz Raman</i> | 162 |
| 5.6.4 | <i>In-line Terahertz Raman of hot melt extrusion of PCM-AFF</i> | 175 |
| 5.6.5 | <i>Terahertz Raman spectroscopy analysis of hot melted stearic Acid</i> | 178 |
| 5.7 | CONCLUSIONS..... | 184 |
| 6. | SOLID STATE ANALYSIS OF SULFAMERAZINE SOLID FORMS WITH TERAHERTZ RAMAN SPECTROSCOPY..... | 188 |
| 6.1 | INTRODUCTION | 188 |
| 6.2 | EXPERIMENTAL..... | 190 |
| 6.2.1 | <i>Materials</i> | 190 |
| 6.2.2 | <i>Methods</i> | 190 |
| 6.2.3 | <i>Data analysis</i> | 195 |
| 6.3 | RESULTS AND DISCUSSION | 195 |

| | | |
|-----------|--|------------|
| 6.3.1 | <i>Method development for production of bulk form II sulfamerazine</i> | 195 |
| 6.3.2 | <i>X-ray powder diffraction of sulfamerazine polymorphs</i> | 199 |
| 6.3.3 | <i>Preparation of form II sulfamerazine by mechanical milling of form I</i> | 206 |
| 6.3.4 | <i>Room temperature milling of Sulfamerazine using a 25mL sample vial</i> | 212 |
| 6.3.5 | <i>FII Sulfamerazine Conformational analysis</i> | 217 |
| 6.3.6 | <i>Preparation of the amorphous form of sulfamerazine via cryo-milling of FI</i> | 220 |
| 6.4 | CONCLUSIONS | 227 |
| 7. | OVERALL CONCLUSIONS AND FUTURE WORK | 230 |
| 7.1 | CONCLUSIONS | 230 |
| 7.1.1 | <i>The assessment of the ability of the Eyecon dynamic image analyser as a process analysis technology for granule characterisation off-line and as an on-line application to Twin Screw Granulation</i> | 231 |
| 7.1.2 | <i>Application of a DoE approach to assess the ability of the Eyecon dynamic image analyser as a process analysis technology for granule size analysis of Twin Screw Granulation Process.</i> | 232 |
| 7.1.3 | <i>To assess low frequency Raman spectroscopy as an alternative to XRPD, DSC and Raman Spectroscopy for physiochemical analysis of amorphous/crystalline content within amorphous solid dispersions</i> | 233 |
| 7.1.4 | <i>To apply low frequency Raman in-line for real time analysis of Hot Melt Extrusion process.</i> | 235 |
| 7.1.5 | <i>To apply low frequency Raman spectroscopy to an industry relevant Hot Melt Extrusion process</i> | 235 |
| 7.1.6 | <i>To study solid state phase transformations of pharmaceuticals using LFRS in real time</i> | 236 |
| 7.2 | FUTURE WORK | 237 |
| 8. | REFERENCES | 240 |
| 9. | APPENDIX | A |
| 9.1 | APPENDIX A | A |
| 9.1.1 | <i>Sample Weights from 1 kg/h Doe Experiment</i> | a |
| 9.1.2 | <i>Calibration of the Screw Feeder</i> | a |
| 9.2 | CALIBRATION OF THE SCREW FEEDER | C |
| 9.2.1 | <i>Twin screw analysis with Raman and Eyecon analysis</i> | c |
| 9.3 | APPENDIX C | I |
| 9.3.1 | <i>Long run experiments screw A and Screw B</i> | i |
| 9.4 | APPENDIX D | J |
| 9.4.1 | <i>Optimum Focal Length for Non-Invasive THz Raman Measurement</i> | j |
| 9.4.2 | <i>Results and Discussion</i> | k |

9.4.3 Conclusions.....m

Abstract

A placebo formulation of granules produced during continuous twin screw granulation were studied *on-line* using a new dynamic image particle size analyser. A DoE approach was carried out in order to evaluate the image analysers ability to study granules produced in a way that represented a continuous manufacturing environment, something not yet reported in the literature. This study proved to be challenging due to fouling issues, however once these were addressed and eliminated, the process analysis technology (PAT) proved to be a useful tool for real time analysis of granules.

A low frequency Raman spectrometer (LFRS), was introduced to in-line and off-line analysis of amorphous solid dispersions (ASD) produced by hot melt extrusion (HME). The study looked at the solubility of Affinisol and paracetamol in polymer matrices directly during HME. Structural phase transitions were observed during HME processes and were successful in determining crystalline and amorphous material in-line and real time. Stability and homogeneity studies of varying concentrations of PCM-AFF ASDs were studied. PCA was used to compare and validate LFRS to XRPD analysis. LFR results were also compared to DSC and Raman Spectroscopy. ASD's with high concentrations of ASD were more unstable showing crystallisation over time. LFRS proved to be a good alternative to DSC and XRPD for solid state analysis. LFR was then applied to resolve a HME industrial issue.

Different solid forms of Sulfamerazine (SMZ) were produced using milling, cryo-milling, bulk material of Form II SMZ was then produced by crystallisation of FI to FII. The different solid states were then analysed using LFR. Classical least squares regression analysis was applied to mixtures of Form I, Form II and the Amorphous form of Sulfamerazine to look at the phase changes with time. LFRS studies determine the presence of unstable amorphous material produced during cryo-milling, something that XRPD was unable to do due to long analysis times and the amorphous SMZ instability.

Acknowledgements

I would like to thank all of those who made this possible, first and foremost my supervisor Dr Alison Nordon for their enthusiastic guidance, unwavering support and encouragement throughout. I would like to express my gratitude and deepest appreciation for the aid and advice they have given me throughout both my under and post graduate studies, valuable advice and for their profound beliefs in my abilities.

I am also deeply thankful to everyone I worked with at GlaxoSmithKline particularly Peter Hamilton, Richard Elkes, Gaik Sui Kee and Duncan Thompson for their guidance through my time there. I feel privileged to have been able to work with such a great team, I learned a wealth of practical information. A big thank you to, and for their time, knowledge,

Many thanks to all of the staff at Strathclyde University both in the Analytical, Chemistry department and those within the centre for continuous manufacturing (CMAC). A special thanks to Magdaline Chong, Pol MacFhionnghaile, Tarik Islam and John Robertson who have been particularly helpful and great to work with or alongside.

I would also like to thank all of staff and academics at the other universities that we were able to train and work with including; Bath, Cambridge, Loughborough, Edinburgh and Heriot Watt universities. A big thank you to the Engineering and Physical Sciences Research Council (EPSRC) for funding this research.

And finally, a huge thanks goes out to my friends and family for the moral and emotional support they have given me over this long process. I could not have done it without you.

Publications and Conference Contributions

Joanna Lothian*, Alison Nordon, Pol Macfhionnghaile, Keddon Powell, Paul Dallin, John Andrews, James Carriere, " Quantitative solid-state analysis of amorphous and crystalline forms of Sulfamerazine using THz Raman spectrometry"; SciX, Minneapolis, Sept 2016

Joanna Lothian*, Alison Nordon, Peter Hamilton, Richard Elkes; "The Monitoring of Secondary Processes Using Process Analytical Technologies"; SciX, Minneapolis, Sept 2016

Abbreviations

- A; Amorphous
- ASD; Amorphous Solid Dispersion
- AFF; Affinisol
- API; Active Pharmaceutical Ingredient
- CLS; Classical Least Squares
- CCSD; Cambridge Structural Database
- cGMPs; Current Good Manufacturing Practice
- DSC; Differential Scanning Calorimetry
- DoE; Design of Experiments
- FDA; Food and Drug Administration
- FTIR; Fourier-transform infrared
- FT-NIR; Fourier-transform Near Infrared
- HME; Hot Melt Extrusion
- HSM; Hot Stage Microscopy
- IR; Infrared
- LFR; Low frequency Raman
- LFRS; Low frequency Raman Spectroscopy
- MIR; Mid-infrared
- MFR; Mid frequency Raman Spectroscopy
- MFRS; Mid frequency Raman Spectroscopy
- MIV; Mid Interval Values
- NMR; Nuclear Magnetic Resonance
- ODF; Oral Dosage Form
- PAT; Process Analytical Technology
- PC; Principal Component
- PCA; Principal Component Analysis
- PCM; Paracetamol
- PLS; Partial Least Squares
- QC; Quality Control

- QbC; Quality by Control
- QbD; Quality by Design
- QbT; Quality-by-Testing
- R&D; Research and Development
- RMSEC; Root Mean Square Error of Calibration
- RS; Raman Spectroscopy
- RSD; Relative Standard Deviation
- SEM; Scanning Electron Microscope
- SD; Solid Dispersion
- STD; Standard Deviation
- SDF; Solid Dosage Form
- SMZ; Sulfamerazine
- SNV; Standard Normal Variate
- SS; Solid State
- TD; Time Domain
- THz; Terahertz
- TGA; Thermogravimetric Analysis
- XRD; X-ray Diffraction
- XRPD; X-ray Powder Diffraction

Notation

- G Gibbs free energy
- ΔG Gibbs free energy difference between two phases
- ΔG^* Critical Gibbs free energy on formation of nucleus
- H Enthalpy
- ΔH Enthalpy difference between two phases
- S Entropy
- ΔS Entropy difference between two phases
- T Temperature
- T_c Crystallisation temperature
- T_d Degradation temperature
- T_m Melting temperature
- T_g Glass transition temperature
- T_{sat} Saturation temperature
- T_{tr} Transition temperature
- U Internal energy
- V Volume
- $\tilde{\nu}$ Raman shift
- λ Wavelength
- λ_{iph} Wavelength of the incident photon
- λ_{sph} Wavelength of the scattered photon

Chapter One
Introduction and Theory

1. Introduction and Theory

This introductory chapter covers regulatory requirements that drive the need for PAT, the move towards continuous manufacturing and the need for in-line analysis in order to monitor physiochemical changes in pharmaceuticals in real time. An overview of the effects of solid form and particle size on the physiochemical properties and their determination of performance, safety, efficacy and manufacture of pharmaceuticals is given. The chapter looks at an overview of solid form, the formation of solid and amorphous dosage forms and will touch on the theory of thermodynamics and kinetics involved in these processes. This is followed by an overview of current technologies available for in-line physical and chemical analysis of these dosage forms and particle characterisation for twin screw secondary manufacturing processes. The available techniques for analysis of solid form is also reviewed. The advantages and disadvantages of these are reviewed and the conclusions presented as a thesis proposal.

1.1 Regulatory bodies QbD and DoE

Traditionally the pharmaceutical industry safeguarded the quality of the final product in a less innovatively engineered batch process, testing batch-based operations, raw materials and end-product characteristics, fixed process conditions, and in-process material.¹ Since the quality attributes of in process material or final product are tested at the end of each batch processing step it is known as Quality-by-Testing (QbT).² The testing limitations to this method have been widely documented and with the Food and Drug Administration's (FDA's) drive towards continuous manufacturing and new technologies available the pharmaceutical industry has taken a more knowledge based

innovatively engineered Quality-by-Design (QbD) approach to pharmaceutical production which has since been evolving to the concept of Quality-by-Control (QbC). The progression of quality assurance is mapped out in Figure 1.1 showing the increase in drug quality with smarter manufacturing and quality control.



Figure 1.1 The progression in quality assurance via QbT, QbD and QbC ²

The drive towards continuous manufacture comes not just from the pharmaceutical companies themselves, regulatory bodies such as the FDA put increased pressure on industries to implement QbD concepts into their manufacturing with the emphasis that quality should be built into the product and the process from which it is developed and manufactured. Quality can be built into pharmaceutical products through comprehensive understanding of the manufacturing process and of the chemical and physical properties of the product being produced. This can be achieved by means of process analytical technologies (PAT). Process analysis technologies are defined as “tools of the systems that utilize, analyse and control real-time measurements of raw and

processed materials during manufacturing to ensure optimal processing conditions are used to produce the final product that consistently conforms to established quality and performance standards”. PAT should therefore be implemented in order to enhance understanding and control of manufacturing processes to support innovation and efficiency in manufacturing development and manufacturing. ^{3,4}

In September 2004, the FDA published a report “Pharmaceutical Current Good Manufacturing Practice (cGMPs) for the 21st century – A risk-based approach” which made a series of recommendations aimed at encouraging the early adoption of new technological advances, facilitating application of modern quality management techniques, encouraging adoption of risk-based approaches, and ensuring regulatory review and inspection polices were consistent, coordinated, and based on state-of-the-art pharmaceutical science. According to the FDA guideline on drug substances it is a regulatory requirement that the solid-state form of a drug be controlled throughout all processing and manufacturing steps. It is also required that the solid-state form of the drug must be known throughout the manufacturing pipeline, as well as during storage and distribution.

In the FDA’s PAT guidance document, it states:

(PAT) is intended to support innovation and efficiency in pharmaceutical development, manufacturing and quality assurance.

And that gains in quality are likely to come from:

- *Reduced production cycle times (C/T) by using on-, in- and/or at line measurements and controls*

- *Preventing rejects, scrap and re-processing*
- *Real-Time-Release (RTR)*
- *Increasing automation to improve operator safety and reduce human errors*
- *Improving energy and material (resource) use and increasing capacity*

Effective PAT would give the means to monitor systems in real time allowing capabilities to be able to build into systems, robust “live” data capture and comprehensive capture of product/process information.

Another drive towards better knowledge and understanding of solid forms comes with the ownership over each chemical entity as patents and the decline in blockbuster drugs. It is well known that the pharmaceutical industry is one of the most research-intensive and innovative sectors of manufacturing. but currently change is slow and it is becoming increasingly harder to come up with new and innovative products. Many existing product patents for what are known as blockbuster drugs are coming to an end, allowing for competitors to come in and steal the market.⁵ Pharmaceutical companies have to deal with the decline in blockbuster sales along with the challenges in finding new chemical entities with high research and development costs. These weak late stage pipelines are putting even more pressures on pharmaceutical companies to access new markets through new innovative and effective drugs along with new ways in which to deliver drugs. Furthermore, increasing costs, regulations and the number of failed drugs means that it is a lengthy, expensive and risky business and roughly only one or two substances developed in the laboratories out of 10,000 ever make it to the market. Real time monitoring capabilities and scientific understanding of CQAs with QbD-PAT-based strategies provide the cornerstone to move towards much better

manufacturing but unfortunately efficient analysis techniques for in-line real time monitoring of pharmaceuticals are limited and many current analysis techniques require lengthy off-line analysis which slows up production, causes waste and disrupts the production line. There are still huge gaps in understanding that can be filled with the correct technologies. To further understand these processes there is a need to know the effects of process parameters on solid forms and the effects of solid form on the physiochemical properties of the product during the lifetime of the drug.

1.2 Physiochemical properties and drug behaviour

It is no secret that many new chemical entities can be challenging due to issues with solubility and/or poor permeability. The ability to choose critical quality attributes (CQAs) such as the solid state and physical characteristics of drugs allows for selection of more desirable properties. New strategies can help with the increase in the number of insoluble drug molecules in the development pipeline. Single and multicomponent solids such as amorphous forms and cocrystals have gained a lot of interest as a way to improve physiochemical properties and clinical performance of APIs without the compromise for their therapeutic benefit. Improvements in physiochemical properties such as density, melting point, colour, stability, hardness, particle size and conductivity can be achieved by altering the physical forms of compounds such as polymorphs, solvates, amorphous, salts, cocrystals and or hydrates. Although diversity is possible to achieve it is still difficult to predict the properties of a specific API and conformer upon crystallisation.⁶ Variation of these properties can affect the solubility, dissolution and the physical/chemical stability, these are very important properties during drug discovery and development. As well as solid form of a drug the physical properties

such as particle size and shape are classed as CQAs in regards to the pharmaceutical production line as they can directly influence the bulk properties and consequently the product performance (dissolution and drug release rate, bioavailability etc.), processability (flow, compaction, blend performance etc), stability and appearance of the end product. There is therefore a need for obtaining real-time data on the particulate properties in order to better control and monitor the size and shape of particles throughout pharmaceutical processes. The different solid-state forms all have differing physical, chemical and mechanical properties which cannot only alter the dissolution rate and transport characteristics of the drug but can lead to changes in bioavailability.⁷ Table 1.1 highlights the effects of different solid forms, on the properties of drugs their process and control.⁸

As mentioned above, the activity, stability, processability and dissolution kinetics of a drug depend on its solid state-structure, and therefore being able to predict the most stable form and to be able to isolate it. Polymorphism and crystallinity changes are one of many challenges faced in the pharmaceutical industry. Polymorphism is usually undesired, but in some cases the metastable polymorphic forms or an amorphous form of a drug may be used advantageously, for example to increase solubility or a poorly soluble compound. More recently the presence of amorphous states in solid dosage forms has attracted a lot of attention due to their specific advantages, and their presence, by accident or design, is known to incorporate distinct properties in the drug product. There are an infinite number of drugs that can be converted to an amorphous form but the metastable nature of these forms means that they tend to recrystallise.

Table 1.1 Property changes resulting from physiochemical properties of pharmaceuticals

Thermokinetic properties

- Dissolution rate
- Nucleation rate
- Morphology
- Crystal growth
- Evaporation rate
- Super saturation

Mechanical Properties

- Hardness,
- Compact ability
- Powder flow, filtration, blend ability and
- Compressibility

Thermodynamic properties

- Melting and sublimation temperatures, and vapour pressure
- Enthalpy, entropy and heat capacity
- Gibbs free energy, chemical potential and solubility
- Metastable zone width (MSZW)

Packing properties

- Molar volume and density
- Conductivity, electrical and thermal
- Refractive index
- Particle morphology
- Hygroscopicity

Spectroscopic properties

- Electronic state transitions
- Vibrational state transitions
- Nuclear spin transition

1.3 Solid State Theory

1.3.1 Amorphous and Crystalline forms

Pharmaceutical solids can take on a diverse range and can be classified in terms of their structure and composition. A structural perspective is based upon the extent to which molecular networks are ordered, these different orders are known as forms and

each differ primarily in H bonding and other intermolecular forces such as Van der Waals and π stretching. A schematic representing API solid form classifications based on structure and composition is shown in Figure 1.2 below.

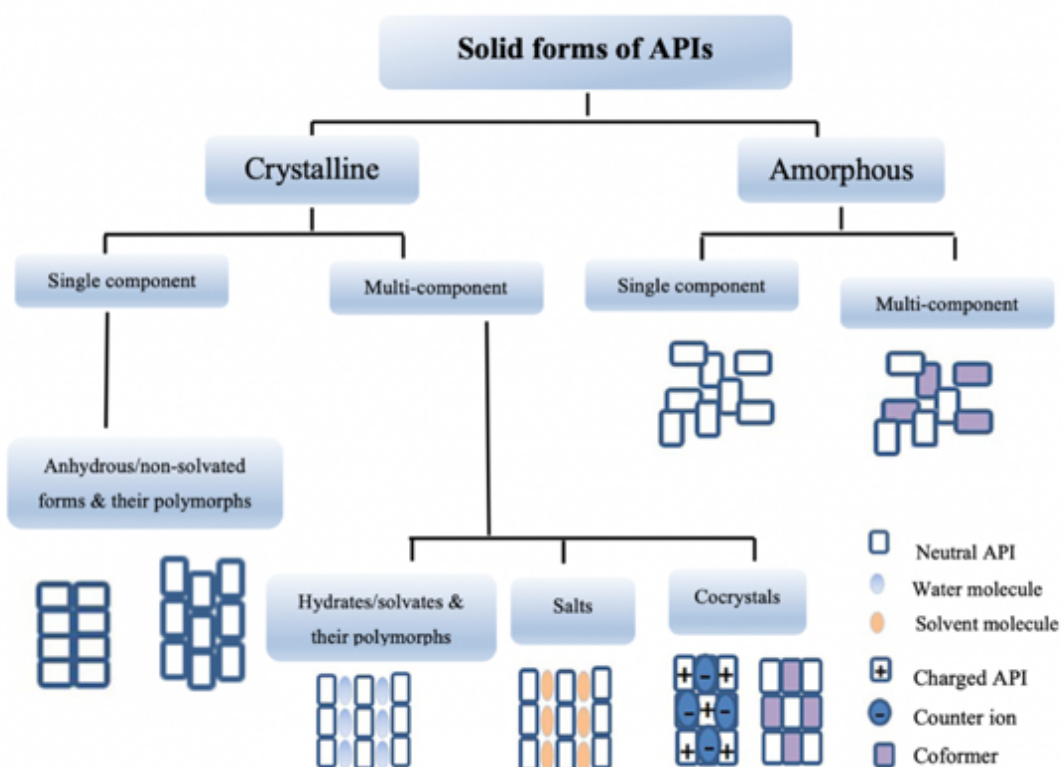


Figure 1.2 Schematic showing the main solid-state forms of pharmaceutical APIs.

9, 10

Most organic and inorganic compounds can exist in one or more crystalline forms. Vippagunta et al ¹¹ defined **crystalline** as: *an ideal crystal solid in which the structural units termed unit cells, are repeated regularly and indefinitely in three dimensions in space.* Each unit cell can be thought of as the simplest repeating pattern in a crystal

and is the smallest unit of volume that contains all of the structural and symmetry information. When a unit cell repeats itself, the network is called a lattice.

Amorphous or disordered solids have local molecular assemblies and lack of long-range translational orientation symmetry. Thus, amorphous and crystalline systems share the same intermolecular forces although the former will exhibit molecular assemblies that lack periodicity. Thus amorphous solids can be thought of as liquids that have been solidified by the removal of thermal energy, a solid that doesn't flow or a solvent in a way that prevents crystallisation.¹²

Polymorphism in crystalline solids is defined as materials with the same chemical composition but with different lattice structures and/or different molecular conformations.¹³ For elements, polymorphism is known as allotropy, for example carbon can present itself as graphite, diamond and more recently graphene.¹⁴ Polymorphism can also be described as *“the ability of a substance to adopt different internal structures and external forms, in response to different conditions of temperature and/or pressure and/or crystallisation”*.¹⁴ The different crystal structures in polymorphs arise when the drug substance crystallises in different crystal packing arrangements and/or different conformations. These give rise to, two main subtypes of polymorphs: 1) conformational and 2) packing polymorphs. **Conformational polymorphism** is when different conformers of the same molecule *“flexible molecules”* occur within different forms.¹⁵ **Packing polymorphism** is when *“rigid”* molecules of the same molecular structure but arrange differently within the three-dimensional space.¹⁶

Pseudo-polymorphism is the term given to **solvates** and **hydrates**. It is a phenomenon that can occur when a molecule of solvent or water are contained within a crystalline structure.¹⁷ Solvates contain molecules of solvent or when that solvent is water it is known as a hydrate. Removing or adding these solvents will change the structure and these become known as polymorphic solvates. Another couple of interesting polymorphs phenomenon, which are outside the scope of this work are concomitant and “*disappearing*” polymorphs.¹⁸ **Concomitant polymorphism** occurs when a compound is formed of several polymorphs.¹⁹ Drugs can also be both crystalline and amorphous with areas of structure and disorder, throughout the solid, or in specific areas such as the surface.

Cocrystals are multicomponent systems typically formed by solution- or solid-phase reactions of APIs in a stoichiometric ratio with cocrystal cofomers, which are often weak acids that tend to be solid under ambient conditions. The resulting cocrystal exhibits different solid-state thermodynamics, leading to changes in physicochemical properties that offer the potential to significantly modify drug pharmacokinetics. **Salts** occur when the drug molecule is protonated by the acid. In a cocrystal the API and conformer remain neutral and engage in hydrogen bonding interactions.^{20,21}

Most drugs exhibit structural polymorphism, formulators in the pharmaceutical industry have the responsibility to formulate a product that is chemically and physically stable whilst being manufacturable and bioavailable.^{22, 23} While it is preferable to develop the most thermodynamically stable form, this form is not always the most bioavailable and other forms such as the amorphous or metastable form is justified as a medical benefit is achieved.²² If we consider a quote by Maria Kuhnert-Brandstätter

²⁴ *“Probably every substance is potentially polymorphic. The only question is whether it is possible to adjust the external conditions in such a way that polymorphism can be realized or not.”* The environmental conditions that APIs are exposed to during manufacture and storage is not the same as the environments that it may be exposed to whilst in the drug product. It is therefore important to study the polymorphic changes that may occur through all of the stages and storage of drug manufacture, transport and storage.

While certain forms of the drug are more desirable, the ability to choose the solid state of the drug allows for selection of more desirable properties and better understanding of drug stability and safety. New polymorphs can help with the increase in the number of insoluble drug molecules in the development pipeline.. Polymorphs may differ in physiochemical properties such as density, melting point, colour, stability, hardness, conductivity, dissolution and physical/chemical stability, very important properties during drug discovery and development. For industry these differences may affect drug manufacture and processing properties, shelf life, texture, flowability and tablet ability and so on. Full polymorphic screening of the targeted API should be done very early in the research and development phase.

Understanding polymorphic transformations is extremely important, both at a fundamental and application (industrial) level. Not only are there ever-increasing regulatory requirements for polymorph screening, as it is fundamental for the drug safety, but knowledge of polymorphs is important in determining the potential uses of a drug. The discovery of new polymorphs can also have a financial drive as patents can be filed for

each polymorph or pseudo-polymorph of a drug, prolonging the rights to that drug for pharmaceutical companies.

Polymorphism was discovered in 1821 by the German chemist Eilhard Mitscherlic,²⁵ but it wasn't until much later (1998) that it was discovered that drugs could transform after production when a second polymorph of the HIV drug ritonavir had taken place of the first during its manufacturing process.²⁶ This second polymorph showed needle like structure, less soluble and more stable than the rod-shaped polymorph originally discovered. Form II took over the production and they could no longer produce form I leading to a pause in production and withdrawal of Ritonavir from the market until they could exclusively make form I again, costing the company a lot of money. Another example of this is the blockbuster drug atorvastatin also known as Lipitor, marketed by Pfizer Inc. An original patent was filed in 1986 and then in 1991 Pfizer filed for a specific patent for atorvastatin calcium and another for the drug's polymorphs (form I, II and IV). Through this strategy they were able to extend the patent of this drug for an additional six years. These strategies are commonly used nowadays to stop more generic pharmaceutical companies from entering the market for these drugs. Still there have been lengthy court battles waged over polymorphic ownership. More recently computational chemistry methods have proved successful in order to predict new potential polymorphs.

From a pharmaceutical perspective, it is important to prepare and select the correct form of drug from the beginning during drug discovery and development. Knowledge of the thermodynamics and kinetics and drug behaviour is important in order to be able to predict and understand the transformations of the potential polymorphs. The most

desirable polymorph to a pharmaceutical company is that which is most stable under ambient conditions as this helps ensure higher levels of purity and stability, this is known as the **thermodynamically stable** form. Of all the polymorphic forms the one with the lowest free energy is the most thermodynamically stable at a specific temperature and pressure of a system. The other forms are metastable and tend to spontaneously transform to the stable form via molecular arrangement. It is, therefore, important to do a full polymorphic screening of a new drug in order to characterise each potential polymorph and their stabilities.

The driving force for these transformations can be determined by the Gibbs free energy (ΔG). The **Gibbs-Helmholtz** equation is an important description of the changes in enthalpy H (J mol^{-1}) and entropy S (J/mol.K) in a system and is given by equations (1.1) and :

$$G = U + pV - TS = H - TS \quad (1.1)$$

$$\Delta G = G_2 - G_1 = \Delta H - T\Delta S \quad (1.2)$$

Where G is defined as the sum of the internal energy (U), and the pressure (p) multiplied by the volume (V). T is the temperature and S the entropy. The change in enthalpy of the system, ΔH , corresponds to the lattice energy difference, while the entropy term is defined as the difference in lattice vibrations and disorder between the two polymorphs.

The free energy in the system at a constant temperature and pressure is given as G . The relative thermodynamic stability of two polymorphs is determined by the difference in their Gibbs free energy ($G_2 - G_1$). Free energy is a measure of thermodynamic potential, enthalpy a measure of internal energy and entropy can be thought of as a measure of the amount of disorder. Therefore, chemicals with the same chemical identity can have different G . Different solid forms have different enthalpy due to different hydrogen bonding between molecules in the solid forms.

In 1897 Ostwald stated *“in the course of transformation of an unstable (or meta-stable) state into a stable one the system does not go directly to the most stable conformation (corresponding to the modification with the lowest free energy) but prefers to reach intermediate stages (corresponding to other possible meta-stable modifications having the closest free energy difference to the initial state.”*²⁷ Put more briefly by Eun Hee Lee¹⁶, when the system leaves any state, the transition occurs to a more stable one. This is not the most stable one but the nearest one under a given condition that the least stable polymorphic form first crystallises. Several attempts have been made to prove this rule however there are some issues as the rule does not seem to fit all systems, as the most stable form can be crystallised directly from solution.

At a given temperature and pressure the polymorph with the lowest free enthalpy are **thermodynamically stable**, other forms are said to be in the **metastable** state. The unstable form will readily convert into the stable form and the metastable form will slowly convert into the stable form. A depiction of the energy levels and stability of polymorphs as they change is shown in Figure 1.3.

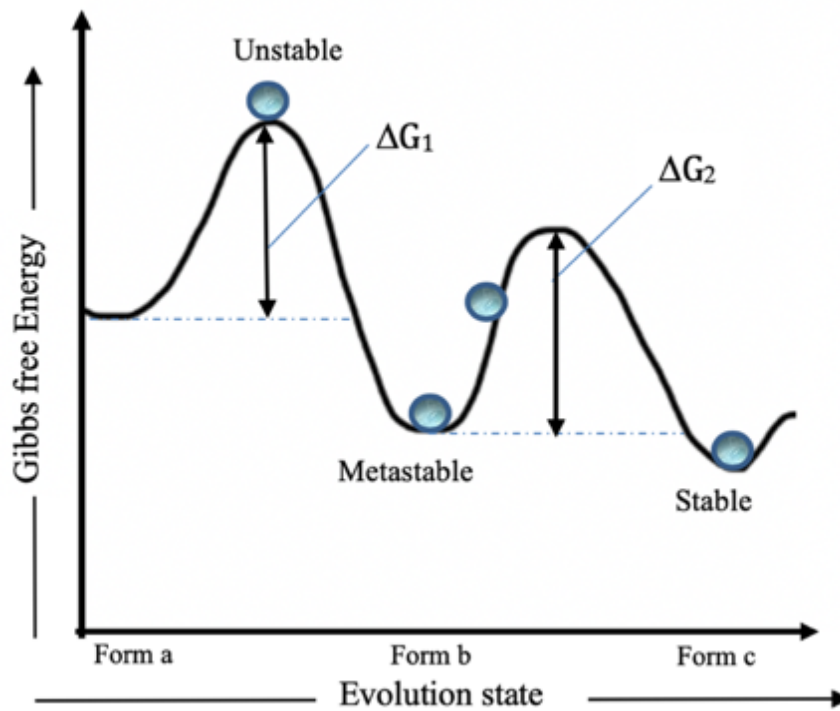


Figure 1.3 Illustration of the definition of stable, metastable, unstable and out of equilibrium showing the change in Gibbs free energy ^{16, 28, 29}

The thermodynamic relationship between two polymorphic forms can be **monotropic** or **enantiotropic**. Figure 1.4 shows the free energy of two polymorphic forms in the liquid state plotted as a function of temperature.

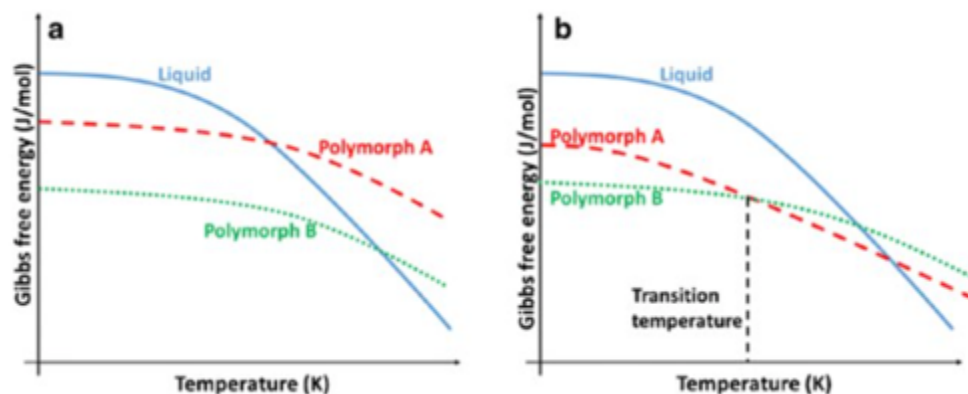


Figure 1.4 The temperature dependence of the free energy (G) for two polymorphic systems of (a) monotropic system, and (b) enantiotropic system³⁰

In a monotropic system one of the polymorphs is stable at all temperatures below the melting point, with all other polymorphic forms being unstable. Above the melting point there might be chance of breakdown. In an enantiotropic system the transition temperature at which free energy between the polymorphs is equal occurs below the melting point. In other words, one polymorph is stable above the transition temperature and the other below.¹⁶

1.3.2 The Amorphous Phase

Polymorphism and crystallinity changes are one of many challenges faced in the pharmaceutical industry, another challenge comes in the analysis of these solid forms, there are a number of factors to consider. The complicated nature of the solid state requires a full suite of analytical tools available to study the system, and the choice of the technique or techniques to use depends on how much information is required about the system and the system itself.³¹ The analysis of amorphous forms presents its own

challenge as these forms are very unstable; despite this it is important to have a clear understanding of how the amorphous active drug is formed and a comprehensive characterisation of its fundamental properties. A good approach to understanding the amorphous state and predicting stability involves: ³²

- *Complete characterisation of the crystalline drug substance*
- *Complete characterisation of the amorphous drug substance*
- *Preparation of stabilised amorphous systems and verification that they do not crystallise*

Currently there is a low number of amorphous pharmaceuticals and excipients listed in the European Pharmacopeia, this may be due to their full potential not being realized owing to their chemical and physical instability and the lack of characterisation tools available to capture them in real time. The current methods, such as X-ray powder diffraction (XRPD) and differential scanning calorimetry (DSC) to analyse materials are mainly off-line.

To gain a better understanding of the thermodynamic properties of crystalline and amorphous forms, consider a single-component system in its most stable crystalline form. Looking at the free-energy temperature diagram illustrated in Figure 1.5, the API is heated until it melts at a specific temperature (T_m), before it gets to T_m , it goes through a glass transition point known as the glass transition temperature (T_g), this can be defined as the temperature at which an amorphous solid undergoes a second order transition. T_g is unique to the amorphous phase and can be thought of as the temperature at which the compound in the amorphous phase turns ‘glassy’. The more polar

the solid or the higher the molecular weight, the greater the value of T_g , while the bulkier the shape of the molecule.

At the glass transition temperature (T_g), the free energy of the polymorphic forms cross. Here the Gibbs free energy is equal for both polymorphs and the polymorphs are in equilibrium. T_g is defined as the temperature beyond which the non-equilibrium glass transforms to the super cooled liquid.

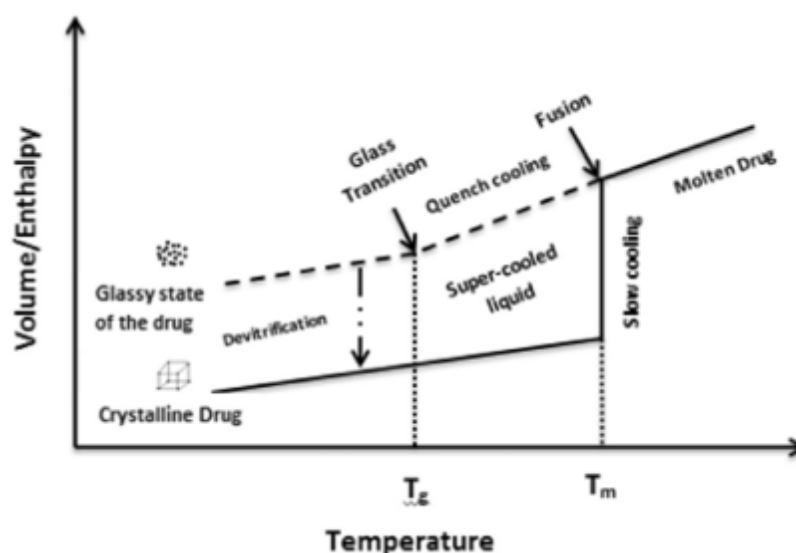


Figure 1.5 Relationship between the T_g and the amorphous, super cooled liquid and the crystal forms of a compound³³

The short-range order of amorphous molecules gives rise to a system with much higher surface free energy, increasing its molecular mobility and resulting in a change of physical properties especially in comparison to that of its crystalline counterpart. Alteration of the API like this has gained a lot of interest in the pharmaceutical industry

due to their higher kinetic solubility, better compressibility and dissolution rates than their crystalline counterparts.^{7, 34, 35}

There are currently a number of traditional methods for the preparation of the amorphous form:

- Mechanical milling³⁶⁻³⁸
- Cryo-milling³⁶
- Preparation from solvent (evaporation)
- Condensation
- Supercooling of melt
- Freeze drying

These are more lab scale productions and are hard to scale up due to their high instability and these amorphous compounds tend to quickly convert back to crystalline making them very hard to characterise and understand with traditional analytical methods.

1.3.3 Amorphous solid dispersions

A common formulation strategy adopted in recent years is the formation of amorphous solid dispersions. ASDs are used to improve the solubility of the active pharmaceutical and to stabilise the amorphous form. ASDs can be defined as molecular mixtures of poorly water-soluble API with hydrophilic carriers.³⁹ The carriers help to modulate the drug release and stabilise the amorphous form. There are currently many different manufacturing methods for ASD production including hot melt extrusion (HME),⁴⁰ Kinetisol®,^{41, 42} spray drying,⁴³ salt formation and the formation of co-crystals to

name a few. ASDs like the amorphous form take advantage of the increase in solubility of the amorphous API resulting from the higher free energy of the amorphous state as previously described in Figure 1.5. Hot melt extrusion uses a polymer as the hydrophilic carrier and is a focus of Chapter 5 of this thesis; HME theory is covered in more detail in the next chapter (Chapter 2).

1.4 Analysis of chemical and physical properties

1.4.1 Particle Characterisation

There have been many papers covering PAT of chemical and physical properties, this section gives an overview of particle characterisation, the chemical analysis technologies that are available and then an overview of publications on three focused studies including in-line analysis of TSG and HME and then solid-state analysis of polymorphs and the amorphous form.

Particles are 3-dimensional objects, and unless they are perfect spheres they cannot be fully described by a single dimension such as radius or diameter. When certain analytical techniques are used, it is usually the 2-d projection of the particle that is observed and there are a number of diameters that can be measured. It is important to note that different techniques will measure the particles in different ways (Feret diameter, surface area etc.) and it follows that they will give different values for particle size depending on the technique. Figure 1.6 shows how particles can be characterised by many different particle sizing techniques. It also follows that in order to be able to compare techniques and to set a standard, all the particles must be spherical. However,

a particle size standard exists for each particle sizing technique, which allows comparison between measurements using different techniques.

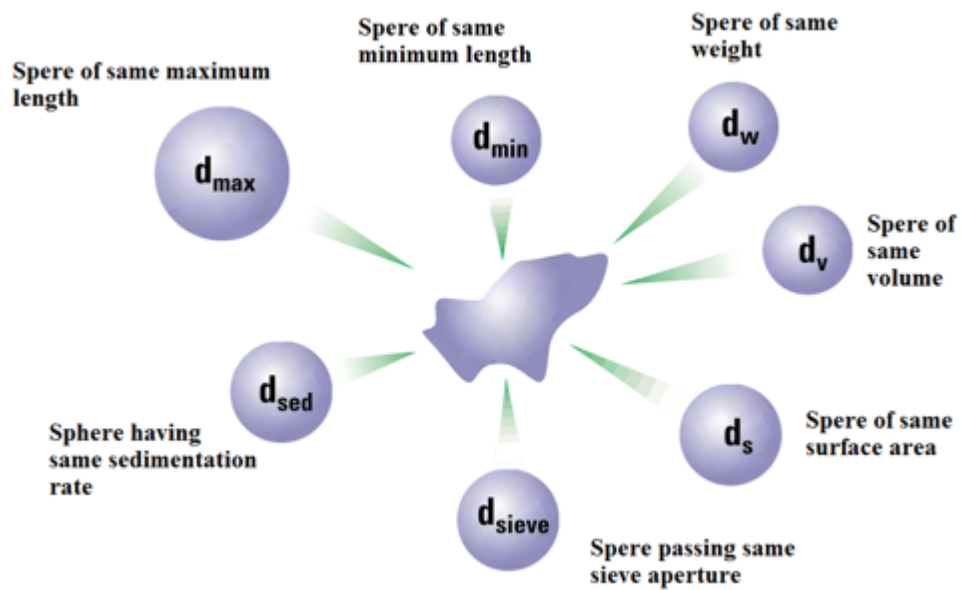


Figure 1.6 Different d values that can be obtained for a single sphere ⁴⁴

Many of the current techniques for the monitoring of particle size assume spherical particles but it is well known that particles come in a variety of shapes and sizes e.g. needles, platelets and that these shapes are often not symmetrical or uniform. Some measurement procedures also require removal of material for separate analysis which may affect the representability of the sample against the bulk material. The most common techniques for monitoring of particle size are listed in Table 1.2.

Table 1.2 Common Particle Sizing Techniques for Particle Size Analysis

| Analysis Technique | Commercial Instruments | On-line | Approximate reported Size Range | Shape | Wet/Dry | Analysis Technique | Some Novel On-Line Lab built examples (from publications) |
|---------------------------|-------------------------------|----------------|--|--------------------|----------------|---------------------------|--|
| Laser Diffraction | Mastersizer | On-line | 0.01µm ~ 3500 µm | With Hydro Insight | Wet & dry | Laser Diffraction | Novel Laser Diffraction Sensor using CMOSPixel Array ⁴⁵ |
| | Insittec Range | On-line | 0.10 µm ~ 2500 µm | No | Wet & dry | | On-line calibration method for droplets. ⁴⁶ |
| | Spraytech | / | 0.10 µm ~ 2000 µm | No | Dry & Spray | | Using a sample line analysis of metal powders in 1 and 25 metre pipe with Mastersizer. ⁴⁷ |
| | Beckman Coulter | / | 0.01 µm ~ 3500 µm | No | Wet | | |
| | Horiba Partica LA | Flow Cell | 0.01 µm ~ 5000 µm | No | Wet & dry | | |
| | HELOS | / | 0.10 µm ~ 8,750 µm | No | Wet & dry | | |
| Light Scattering | Zetasizer | / | 0.30 nm ~ 10 µm | No | Wet | Light Scattering | Emulsification analysis on-line multiple light scatter ⁴⁸ |
| | Unchained Labs | / | 0.30 nm ~ 10 µm | No | Wet | | Novel laser angle scattering ⁴⁹ |
| Dynamic Imaging | Eyecon | On-line | 50.00 µm ~ 5500 µm | No | Dry | Dynamic Imaging | An early report of the use of RGB CCD cameras by Navanen et al. ⁵⁰ |
| | Morphologi- 4ID | / | 0.50 µm ~ 1300 µm | Yes | Wet & dry | | Stereo imaging technique |
| | Quickpic | / | 1.00 µm ~ 34,000 µm | Yes | Wet & dry | | (Flashsizer FS3D) ⁵¹ |
| | PICTOS and Co | On-line | 1.00 µm ~ 10,000 µm | Yes | Wet & dry | | |
| | Hydro Insight | / | 1.00 µm ~ 800 µm | Yes | Wet | | |

A study into the validity of particle size analysis techniques for measurement of the attrition that occurs during drying⁵² looked into the feasibility of using LD and FBRM to monitor particle size. It was found that LD and FBRM could be used to study the attrition that occurs during the drying of needle shaped particles however, for full analysis, image analysis is required. The problem here is that in LD, the algorithm used assumes that the scattered particles are spherical regardless of the actual shape. In addition, FBRM measures the chord length distribution rather than the particle size distribution, which is weighted towards the needle width rather than their length. This means that there are limitations in the information on needle length that can be derived. Another paper by Eric J. Hukkanen⁵³ showed that FBRM gave false results due to laser interaction with the roughness/protrusions on the surface of polymer beads. These studies demonstrate that there are a few problems with the current particle sizing techniques and so there is a need to consider alternatives.

As well as particle size, the shape of constituent particles can also have a significant impact upon the performance or processing of particulate materials and can affect for example, reactivity, solubility and powder flow. Consideration of particle shape is therefore also of high importance especially as most particles are not spherical. Knowledge of the shape along with the particle size can provide even more physical information on the process. The monitoring of particle shape is not possible with the current algorithms used to monitor particle size with techniques such as laser diffraction and FBRM. However, with image analysis a range of metrics can be used.

From 2-dimensional images of the particles the primary measurement information uses the projected area of a particle. From the projected area additional information can be calculated giving a number of size and shape parameters. Many algorithms exist to

condense irregular contour data, into a single value, the particle size, which is expressed by a diameter. The typical size range for image analysis is usually in the range of 1 μm and 30 mm.

Diameters derived from the equivalent circle are calculated either by i) the diameter of a circle of equal projection area (EQPC), this is the diameter of a circle that has the same area as the projection area of the particle, or ii) the diameter of a circle of equal perimeter (PED), this is the diameter of a circle that has the same perimeter as the particle image. The Feret diameter is based on a group of diameters. After considering all possible orientations ($0^\circ \dots 180^\circ$), systems will calculate the Feret maximum (Feret Max) and the Feret minimum (Feret min) diameters. ⁵⁴

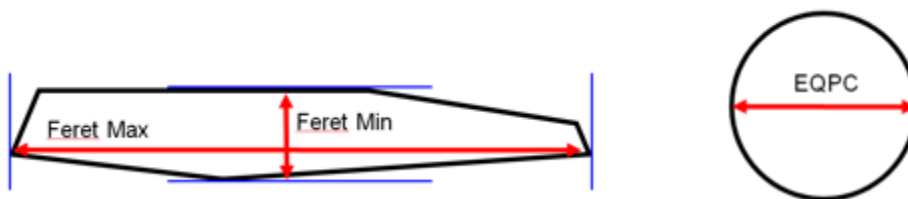


Figure 1.7: Schematic representations of the size descriptions used for image analysis.⁵⁵

With the QICPIC analyser the sample passes through a sample loop and the analysis is done off line for the particle size range 1 μm – 30 mm, this is the widest available range for in-line analysis. Another off-line technique available is Beckman Coulters RapidVUE which can provide aspect ratio, size information and sieve correlations of particles. These off-line techniques are not ideal as sampling and sample work up can be time consuming and may produce results that are not representative of the whole system. On-line image analysers are also commercially available and mostly use

probes which can be situated within the sample. The in-situ particle viewer (ISPV) by Perdux technologies can analyse particles between 1 and 100 μm at temperatures between -20 and 120 $^{\circ}\text{C}$. Similar probe analysers are available for a wider particle size range, such as the particle viewing system (PVM) by Mettler Toledo (2 – 1000 μm) and the process image analyser (PIA) by PharmaVision (0.5 – 2000 μm).

Most of the image analysers use a pulsed light source to capture sharp images and from these the data generated parameters such as: area-equivalent circle, bounding rectangle, chord length, Feret diameters, sphericity, aspect ratio, convexity, fibre length, fibre diameter, elongation, and straightness can be calculated in order to characterize particle size and shape. Although there are many particle image analysers available they still come with their problems. Issues like varying background intensities, overlapping particles and sharpness of the images can affect results.

1.4.2 Solid State Analysis

Several analytical techniques are well documented in the literature and are considered the gold standards for the analysis of solid forms, these techniques include XRPD, TGA, DSC, Raman spectroscopy, electron microscopy and solid-state nuclear magnetic resonance (NMR). Although they have been proven to be successful techniques for analysis they are not without their disadvantages, especially for continuous manufacturing environments. With more modern approaches to analysis and the adoption of more continuous manufacturing processes, industry now favours, real time, non-destructive, in-situ analysis. Figure 1.8 highlights the main solid-state analysis techniques for the study of APIs.

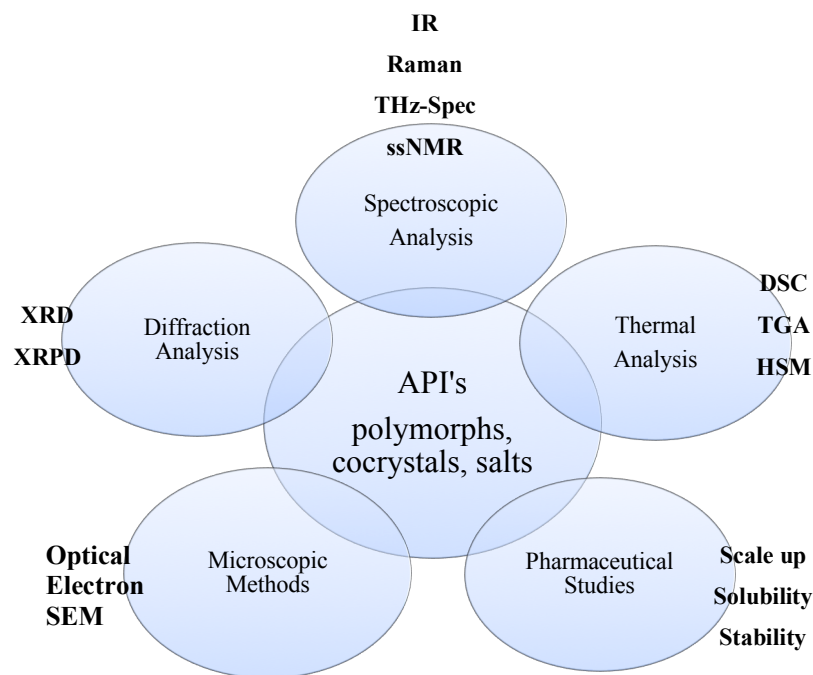


Figure 1.8 Common API analysis techniques categorised into, spectroscopic, thermal, diffraction, microscopic and pharmaceutical analysis

Well established techniques from microscopic, thermal and diffraction analysis have been utilised extensively for solid state analysis on an intermolecular level, while vibrational spectroscopic techniques such as mid-infrared (MIR), near-infrared (NIR) and Raman have shown promise as tools for analysis on a molecular level. Spectroscopic techniques are fast and non-destructive, they also require minimal or no sample preparation. There are a wealth of techniques available for solid form analysis, these like particle characterisation can be selected depending on what you are analysing. The advantages and disadvantages of a number of popular techniques can be found in Table 1.3, the table also lists the information that can be obtained from each technique and whether they have been implemented for in-line analysis of continuous processes or not. .

Table 1.3 Advantages and disadvantages of the most common solid-state analysis techniques.

| Technique | XRPD ⁵⁶ | Thermal Analysis ⁵⁷ 56, 58-60 | Microscopy ^{61,} | Raman ^{7, 60,} 62-65 | FT-IR ^{66, 67} | Solid State NMR ^{20, 68, 69} | THz Spectroscopy 70, 71 72, 73 |
|---------------------------------------|--|--|--|--|---|---|---|
| <i>In-line commercially available</i> | XRD Can be done but tricky. | No | No | Yes | No | Yes | No |
| <i>Research demo published</i> | yes | No | No | Yes | Yes | Yes | Yes |
| <i>Amorphous solids?</i> | No diffraction peaks | Glass transition seen. Often followed by crystallization and melting. 'Fragility' related to width of T _g | No birefringence or irregular pattern/shape | Broadened Spectra | Broadened spectra | Broadened spectra | One smooth peak, no distinct peaks. |
| <i>Information</i> | Amorphous Polymorph Structure | Thermal events – change in mass as a function of temp. Transform kinetics Measures Enthalpy Gives good info on physical properties of polymorphs | Can give information on physical form and potentially polymorphism Birefringence, dispersion colour and crystal habit. | Chemical fingerprint and information Good for polymorphism detection | Polymorph detection – sensitive to molecular structure | Provides information about the structure, orientation and dynamics. Also provides info on components such as contaminants. Useful for determining phase purity, molecular mobility. | Information on solid form |
| <i>Destructive?</i> | No | Yes | No | No | Sample can be retrieved | No | No |
| <i>Advantages</i> | Gold Standard, Well established and accepted | Good for determining stoichiometry of solvates and hydrates, where mass change is attributed to loss of solvent. | Real time crystallisation, visual, can be coupled to spectroscopic devices, visual and good detector of | Quick, real time, inline analysis Gives structural fingerprint. | Simple and easy to use off-line with no sample prep. Can monitor in real time. Fast | Small amount of material. Non-destructive and non-invasive. Little to no sample prep. | High sensitivity Specific analysis Good for mapping |

| | | | | | | | |
|----------------------|--|--|---|---|---|---|--|
| | Great polymorph distinction Quantitative and qualitative | Detect impurities, can be coupled with NIR and Raman to give info on polymorph thermal transformations. Relatively simple and easy to do | polymorph, can pinpoint analysis onto small area | | | Standard curve not needed in order to obtain quantitative data. Large range of sample conditions and types can be examined Can be used on all types of drug formulations e.g. tablets, capsules, suspensions etc. | Access phonon modes |
| <i>Disadvantages</i> | Expensive, Slow, analysis can take up to an hour and sample may have changed. X-ray hazard | Rate at which sample heated can result in overlapping and masking of other thermal events. Generally unsuitable for two phase mixtures Uncertainty of heat of fusion and transition temperatures. | Off-line and static analysis. Need good sample dispersion. | Sensitive to interference e.g. fluorescence & light. | Not good for wet samples, complex mixtures give rise to complex spectra | Only compounds containing carbon can be analysed Bulky equipment and expensive Not good for analysis of amorphous material due to analysis times. Peak assignments can be challenging. | Small areas of analysis only. Can't distinguish between two substances with similar THz spectra |

The overview of techniques given in the table shows that there are a number of options for analysis of solid state. XRPD would be the ideal in-line analysis tool but unfortunately it is very expensive, slow and hard to implement in-line. Raman analysis is the go-to method for in-line analysis but this gives mainly information on the chemical composition, NIR is great for physiochemical analysis but it is specific for carbon containing compounds and not great for amorphous materials due to lengthy analysis times. It could be argued that both physical and chemical analysis can be achieved by the use of multiple techniques. While this is possible, there are higher costs with multiple instruments, each will require the user to be trained, the data might not be easily comparable and it can be difficult to sync each analysis technique to analyse the same process. The ideal analysis tool will be able to give as much information as possible on one platform, this is possible with THz Raman spectroscopy.

1.5 In-line particle characterisation for continuous granulation

The challenges faced with in-line PAT for particle characterisation of critical quality parameters such as size and morphology in TSG are the main focus of this section, other manufacturing processes with relevant PAT have also been studied. The review considers the impact of material feed rate and analysis times, as these are important parameters for industrial manufacturing in a continuous manner.

Several PAT implemented in TSG exclusively focus on particle size distributions and morphology, these are mostly obtained by dynamic image analysis, a popular method for particle characterisation, and a method used in this research. An early report of the use of RGB CCD cameras by Navanen et al.⁵⁰, studied a fluidised bed granulation process.

Topographic images captured on a 6-megapixel CCD camera (SAY-3D -Canon PowerShot S3 IS, Canon Inc) were analysed to determine granules size. Images were captured for feed rates of 2 kg/h. The software algorithms assumed spherical particles based on a circular equivalent, they also struggled with any reflective particles and the image quality was poor.

Fonteyne et al ⁵¹ reported a photometric stereo imaging technique (Flashsizer FS3D) in order to evaluate the PSD, roughness, and shape of granules produced during a (ConsiGma™-25) high sheer granulation process. This technique uses two light sources to produce a greyscale gradient, the gradient fields are subject to a line integration and these are assumed to be particles; volume particle size is then calculated from these images. The study also looked at the feasibility of using Raman and NIR for in-line measurements of anhydrous/monohydrate solid state transformations of theophylline.

A more compact analytical device, the Eyecon was produced in the last decade and since its production there have been many reports of its application to solid dosage form analysis. Treffer et al ⁷⁴ implemented the Eyecon image analyser for analysis of almost spherical pellets produced during a hot melt extrusion process with a flow rate of 1 kg/h. The results from in-line analysis were compared to those obtained off-line using QICPIC, (Sympatec GmbH Germany) which was employed as a reference for particle analysis. Two methods were used before image analysis to separate the pellets. The first used a cooling air system to separate the particles, which failed to capture enough particles, and the second studied two camera positions with a separator and vibrating conveyor. The PSD in the Dv50 was in good agreement with the QICPIC analyser despite there being a

low number of pellets analysed. However, analysis of a low number of particles impacts the reliability of the PSD. Off-line studies with the Eyecon also showed that the system struggled to analyse transparent EVA pellets. The study also reported that the images can provide valuable information on the texture and shape of the particles but this information is not further processed by the software and will require further analysis tools.

A smaller scale study on an 11 mm TSG by Sayin et al. ⁷⁵ also applied the Eyecon for a L/S ratio study on granule size. They agreed that the best indicator of process change due to liquid content could be observed in the D_{10} values. These studies were lab scale and all were performed over very short periods of time, roughly 4 to 5 minutes.

Hagrasy et al. ⁷⁶ used the Eyecon for analysis of granules produced with varying L/S content. The D_{v10} value was found to be more sensitive than the D_{50} and D_{90} values to process shifts for processing times of over 23 minutes at powder feed rates of 4 kg/h. They found that the images were sometimes blurry and out of focus, which was thought to be caused by the reduced distinction between the sizes measured at certain L/S ratios. Despite being in good agreement with off-line sieve analysis it was thought that the size determination may have been skewed due to segregation of samples and sample chute presentation. The sample window was often over filled and that the samples on the chute will present themselves in their preferred orientation effecting the granule size measurement.

A more recent study by Meng et al. ⁷⁷ applied multiple PAT to a lab based 11 mm TSG, this study looked at a QbD approach to develop a number of experiments to study the

effects of granulation on a placebo formulation. Raman, NIR and Eyecon analysed granules presented along a conveyer. The Raman studied the drug content and solid-state transformations, NIR for the physical properties and Eyecon for the size and shape analysis. This idealised lab-based experiment proved successful for monitoring of process changes at maximum screw speeds of 1000 rpm and powder feeds from 20 g/h to 2.5 kg/h for approximately 16 minutes. Again, the D10 value was found to best pick up perturbations from L/S ratio as the Dv90 still showed trends showing dramatic fluctuations. The Eyecon has also been used in TSG, milling and for fluid bed coating processes.⁷⁸

A feedback control method was studied by Madaras^{79, 80} for continuous TSG at a feeding rate of 1 kg/h. Images were captured on a custom made camera (JAI SDK) with particle illumination by a BEL Halogen fibre optic illuminator (90673, BEL, China). The data was analysed by custom made software written in Java, using greyscale filters. This study was described as a continuous study, but each of the experiments were only just over 8 minutes long.

Other non-imaging techniques have also been reported for particle size analysis of TSG and fluid bed granulation, these are based on chord length distribution (CLD) measurements using either spatial filtering velocimetry (SFV)⁸¹ (The Parsum[®] IPP70 SFV probe) or focused beam reflectance measurement (FBRM) (FBRM[®] C35) and another technique that is well established off-line, laser diffraction (LD), which can now be implemented inline using the Insitec[®] range for the Mastersizer.^{82, 83, 84} These techniques are explained extensively in a review by Silva et al.⁸⁵ which looks at a comparison of in and off-line

techniques for particle sizing. Near infrared spectroscopy (NIRS) has also been reported for analysis of the particle size of granules.

1.6 In-line solid form analysis of continuous extrusion processes

As for TSG, PAT can also be implemented with HME processes. NIR spectroscopy is a popular choice for HME analysis but unfortunately it is limited to vibrations from groups such as -CH, -OH, NH and -SH⁸⁶ and chemometric data analysis is also required in order to retrieve the spectral information. Despite these limitations, NIR spectroscopy is sensitive to H bonding and rearrangements in the crystal lattice, which is great for the understanding of molecular interactions.⁸⁷ Saerens et al.⁵⁹ used a PLS model to study the concentration and polymer-drug melt behaviour during HME. NIR successfully detected the change in solid state as well as the amount and strength of the intermolecular interactions. Raman spectroscopy, DSC analysis and FT-IR were applied off-line to provide conformational results. FT-NIR and chemometric modelling has been used in-line to determine API concentration.⁸⁸

Another extremely popular method for analysis in HME is Raman spectroscopy. An extensive review of Raman analysis in pharmaceutical product design was conducted by Paudel et al.⁸⁹ This report highlights the advantages of Raman over other spectroscopic techniques including the fact that Raman does not need a reference light path compared with mid or near IR, meaning it is amenable to fibre optics, allowing for remote sampling.⁹⁰ Saerens et al.⁹¹ applied Raman in-line with PCA for the monitoring of the effects of various process parameters including solid state drug loadings, screw speeds and temperature on the amorphous solid state. Raman can not only provide information on the

solid state but can give information on the drug-polymer interactions during the HME process.^{92, 93}

The advancements in narrow band filters have made THz Raman spectroscopy far more accessible, and so the number of reports of the use of THz Raman spectroscopy for solid state analysis has risen tenfold over the last decade. Its ability for quick, real-time analysis and excellent polymorph detection has made it very appealing across a broad range of disciplines.⁹⁴ The advantages of THz Raman spectroscopy are highlighted in an introductory review paper on THz Raman by Menzes et al.⁹⁵ In this publication they highlight the sensitivity of THz Raman for polymorphic and amorphous form detection. Another advantage from an experimental point of view is that there is little to no sample preparation needed and that measurements can be made with compact diode lasers.

An example of polymorphic characterisation of carbamazepine, an anticonvulsant drug used in the treatment of epilepsy and bipolar disorder, was reported⁹⁶ THz Raman was able to quickly and clearly differentiate the various forms as well as the hydrate structure. The dramatic differences in the spectra were used for identification of solid form and it was also found that the relative strength of the THz Raman region in comparison to the corresponding Raman or fingerprint region was much greater. The study showed that the LFR spectra of large aromatic compounds show intense bands, 10 to 20-fold with complex spectral features. They considered the low frequency region a “*second fingerprint region that is specific for crystalline structure, crystalline disorder, and amorphous states.*” They also state that future development requires a better understanding of the relationship between the crystalline structure and the low frequency spectra. Recent

advances in computational chemistry on lattice dynamics may be the key to understanding this information and to peak assignment.

A paper from Strathclyde by Bordos et al.⁹⁷ has reported the use of THz Raman spectroscopy for in-line analysis of a HME process.

The LFR bands available with THz analyses provides the collective information on the vibrations of both the molecules in crystalline state and those in an amorphous state. These low frequency bands also provide much greater sensitivity for analysis of crystalline and amorphous pharmaceuticals, THz is therefore a good technique for detection of the onset of crystallization within amorphous extrudes.⁹⁸

1.7 Research proposal

The FDA's PAT initiative has motivated the adoption of PAT built into all stages of a pharmaceutical process. The adoption of a QbD approach and the move towards continuous manufacturing has meant that a lot of established analysis techniques that were suitable for batch style manufacturing are now not suitable or are not able to be adapted for real time analysis. While the FDA's PAT initiative is not new, there are still gaps in process understanding that need technologies capable of real time analysis at an industrial level. While some established techniques still serve a purpose, this research focuses on the implementation of two newer analytical techniques for analysis of physical and chemical properties within secondary manufacturing.

The overall aims of this research were:

- To assess the ability of the Eyecon dynamic image analyser as a process analysis technology for granule size analysis of TSG.
- To evaluate using a DoE approach the suitability of the Eyecon dynamic image analyser for the application of real time analysis of granules produced by continuous twin screw granulation.
- To assess low frequency Raman spectroscopy as an alternative to XRPD, DSC and Raman Spectroscopy for physiochemical analysis of amorphous/crystalline content within amorphous solid dispersions.
- To apply low frequency Raman in-line for real time analysis of HME process
To apply low frequency Raman spectroscopy to an industry relevant HME process.
- To study solid state phase transformations of pharmaceuticals using LFRS in real time.

Chapter Two
Instrument Theory

2. Instrument theory

2.1 Twin Screw Wet Granulation

Twin screw wet granulation is very similar to hot melt extrusion as TSG was developed from the modification of a twin-screw hot melt extruder, by removal of the extrusion die at the barrel outlet.⁹⁹ Granulation is a well-known powder processing technique for the manufacturing of oral dosage forms, there are many granulation techniques available but for the purposes of this thesis the focus will be on twin screw wet granulation (TSG). In wet granulation, granules are formed by the addition of a binder, usually water, to primary particles, in the pharmaceutical industry this is usually a mixture of API and tailored blend of excipients. Generally, a granulation solution is added to improve dissolution rates and to agglomerate particles by capillary and viscous forces until more permanent bonds are formed by subsequent drying phases.¹⁰⁰ Figure 2.1 covers some of the main reasons for granulation of these mixtures.

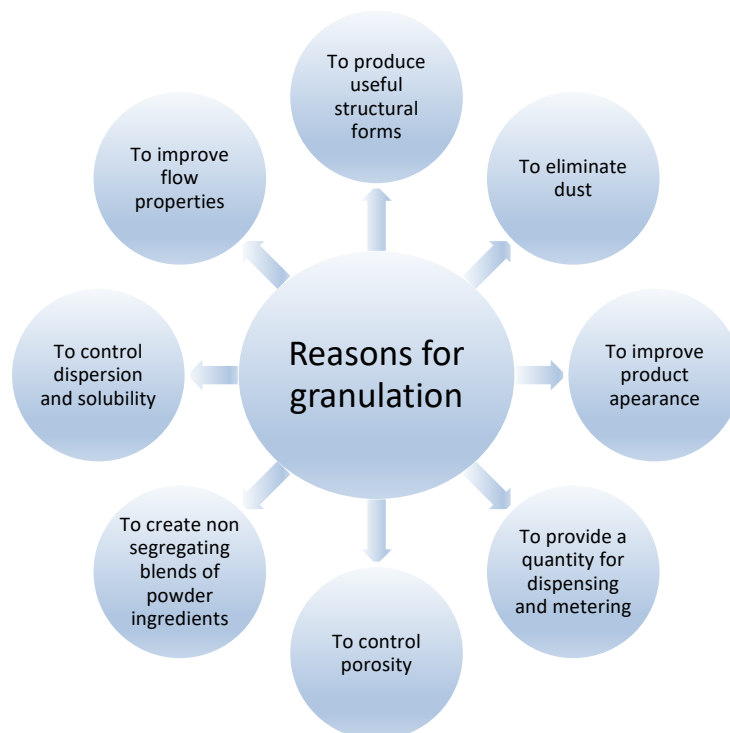


Figure 2.1 Advantages of granulation¹⁰¹

The transformation of powders into agglomerated particles is a step that is usually performed prior to the tableting stage, as stated in Figure 2.1. The formation of granules helps to reduce any aggregation, helps with uniform flow of the material and can help improve compressibility in the tablet dies. Depending on the granule size produced during TSG, the granules can be further processed by the addition of more excipients before tablet compression or for filling hardened gelatine capsules. ³

2.1.1 Granule Growth

Wet granulation can be considered to consist of three main rate processes which can occur simultaneously in all wet granulation units, this is shown in Figure 2.2 below.

1. Wetting and nucleation



2. Consolidation and Coalescence



3. Attrition and breakage



Figure 2.2 The three steps in wet granulation¹⁰²

Nucleation is the binding together of particles to form a small granule and mass by reducing the number and mass of particles in a system while increasing the number of granules. Nucleation is strongly related to the wetting stage as it is promoted from the initial distribution of moisture such as a drop, or from the homogenization of a fluid feed to the bed, as with high shear mixing. As the granules grow they consolidate and coalesce due to forces of compaction caused by agitation by e.g. screws or beds. This stage controls the porosity of the granules and therefore the final properties of the granules such as hardness, strength or dissolution. Granules that are weaker or that contain flaws may then break down into smaller granules by attrition.¹⁰³ Each of the three steps is explained in more detail below.

2.1.2 Wetting and Nucleation

Nucleation is the term used to describe adhesion of two primary particles occurring in the presence of a binder or fluid, this occurs in the wetting stage. Wetting of the powder

and the nuclei size distribution is driven by wetting thermodynamics and kinetics. As the water moves through the solid, it penetrates the powder pores on the surface of the powder forming a nucleus which migrates outwards. The size of the droplets can influence the nucleation mechanism. Schaefer and Mathiesen ¹⁰⁴ propose that there are two different nucleation mechanisms as illustrated in Figure 2.3. There are five granulation states each of these depend on the level of liquid saturation state which vary depending on the powder properties and liquid addition rate.

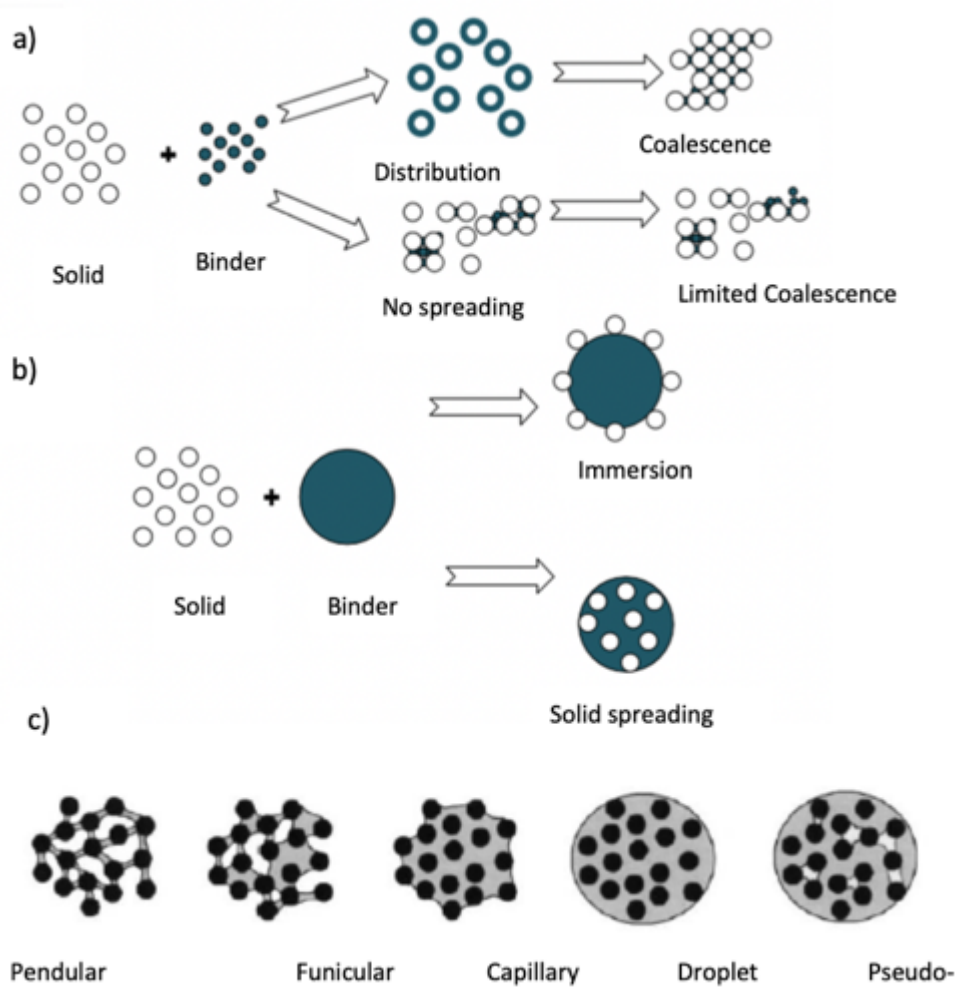


Figure 2.3 Nucleation formation mechanisms a) distribution mechanism when the liquid droplets are smaller than particles and b) immersion mechanism when

liquid droplets are bigger than particles and then c) the liquid bonding between the particles describing the saturation states of wet granules ¹⁰⁵

Liquid bridges hold the particles together in the pendular state, as more liquid is added an increase in saturation occurs and the capillary state occurs with the funicular stage as an intermediate. In the droplet state, there is no air entrapped and the particles are held within a droplet. The pseudo-droplet state, as illustrated, contains air trapped inside and make for a more porous granulate.

The particles are primarily bound together by capillary bridges formed by the attractive forces between the particles and can be affected by the choice in binder. Ideal conditions for wet granulation involve steady growth and the production of a narrow size distribution. The distribution of the wetting/binding agent with the powder has a profound effect on the size distribution of the nuclei. The extent to which the powder is covered and the time it takes for this to happen is an important step in the determination of the physical properties of the granules. If the liquid droplets are relatively small then nucleation is more likely to occur by distribution of the drops onto the surface of the particles, causing the particles to coalesce. This method is more likely to produce more porous granules. If the droplet is much larger in comparison to the particles then the immersion mechanism ((b) in Figure 2.3) is proposed producing particles with more saturated pores. ¹⁰⁶

Granule growth occurs once the liquid has been added to the powder mixture and can continue after the liquid addition. Consolidation occurs as granules collide with other granules and the equipment, causing porosity of the granules to reduce. This is done

by the air being squeezed out of the granules as they rearrange in the system. Porosity is an important granule property as it plays a part in controlling the granule growth mechanisms, as consolidation is required to squeeze binder on to the granule surface during the induction phase. Porosity is directly linked to granule strength, with high porosity granules being weaker than lower porosity ones. Increased porosity of particles can result in better dissolution rates but can also lead to more granule breakage/dust. On the other hand, low porosity granules can slow down the dispersion and dissolution properties of the granules.

Growth by coalescence is when two granules successfully collide to form a larger granule, however if they don't stick they will rebound and growth will not occur. The collision is only successful if certain conditions are met (a) the energy of impact must be absorbed during collision so that the granules rebound ¹⁰¹, and (b) a bond must be formed that is sufficient to hold the newly formed granule together. Coalescence reduces the total number of granules but has no effect on their total mass.

Attrition and breakage is the step where wet or dried granules break due to high impact and/or shear force during wear or compaction in the granulator or during subsequent product handling. ^{4,107} Wet granules can be broken in the granulator or once the granules are finally dried they can fracture or attrit to give fine powders. Granule breakage depends on fracture toughness which depends on the formulation and the number and size depends on the compatibility of the binder with the primary particles. The breakage of wet granules can affect the overall granule size distribution.

The following rate determining processes are key to granulation and determine the final granule properties:

- Granule growth behaviour
- Steady growth
- Induction growth

Different parameters can affect the granule growth behaviour, including:

- Binder content
- Particle size
- Binder surface tension
- Binder viscosity
-




2.1.3 Components of a twin-screw granulator

The granulator consists of two co-rotating screws made up of tightly intermeshing conveying elements. The extrusion mechanism is based on a piston contained within a cylinder in which materials are loaded and pushed through an opening hole. The conveying elements are segmented and can be altered and are a key design parameter in the granulation process. The screw set is tightly enclosed in a metal barrel where they twist together moving and shaping powder into granules. The screw elements are one of the most important parameters as they will decide the available volume for granulation while powder feed rate, water content and feed rate will determine the properties of the final granule produced. The parameters effecting the granules will be discussed further in this section.

2.1.3.1 Twin screw elements

The importance of the screw element combination has been well reported,^{108, 109}. The modular set up of these elements leads to flexibility and endless combinations. The elements are arranged along a metal shaft, and are usually composed of a mixture of conveying, mixing and kneading elements, each of these provide different functions. The functions are summarised in Table 2.1. Forward conveying elements serve as drivers to convey material with forwarding pressure away from the feeder port and onto the kneading and mixing elements. Kneading elements are made out of smaller bilobes which are staggered at different angles, these can be 30°, 60° (forwarding), 90° (neutral) or 30° (reverse).¹¹⁰ The flexibility of the available geometries gives the screws different distributive and dispersive action as well as compounding actions.¹¹¹ The mixing elements are largely used for the distributive mixing of powders; these elements have a large number of teeth on a toothed ring and alternate between the two shafts. Many combinations can be achieved by mixing up these elements including number on each row, width of teeth etc.¹¹²

Table 2.1 Screw elements¹¹²

| Screw Type | Examples | Description |
|-------------------|--|--|
| Conveying element |  | These help to transport and feed materials down the shaft. They can convey forwards (right screws) and backwards (left screws). |
| Kneading element |  | Used to shear and mix, can be staggered at different angles 30°, 60° and 90° to mix forward and 30° negative to mix backwards to exert high stress onto the material. ¹¹⁰ |
| Mixing elements |  | Used for distributive mixing, typically they have large number of teeth which can vary in number per row, width of teeth and pitch direction |

The screw's geometry is designed to blend and uniform the compound in order to reduce the mechanical and thermal stress of the product, which can lead to deterioration of the quality of the product produced. The geometry is also there in order to ensure the best/maximum dispersion and distribution of the materials.

2.1.3.2 Channel fill and screw speed

The screw speed is a critical factor in determining the amount of powder filling the barrel; the barrel fill level has an effect on the torque or power needed to turn the screws, which has an impact on the granule properties. Towards the upper and lower limits of barrel fill level, the granule properties become more dependent on the fill level. The fill level also depends on the feed rate. When the feed rate is high, there is more powder going into the barrel. The more compact the barrel in the granulator, the

more power needed for compaction of the full barrel. It has been found that high feed rates and barrel fill levels result in more dense and stronger granules.^{113, 114} At high screw speeds the powder has a short residence time in the granulator and capacity is greater¹¹³ At lower screw speeds, the barrel fill level increases as does the torque. High screw speeds have a lower barrel fill level and lower mass load and therefore a reduction in torque.

2.1.3.3 Liquid to solid ratio

The liquid to solid ratio is a very important factor when it comes to twin screw granulation. TSG has the advantage over other wet granulation methods in that it does not require high liquid content in order to granulate but can also handle large liquid to solid ratios. The granule distribution of TSG is characteristically bimodal at lower water concentrations, and narrower and more unimodal and at higher L/S concentrations. These unimodal granules however are very large and no good for tableting.^{113, 115} It is thought that the link between high L/S ratio and large granule size is due to the amount of surface wetting caused by the large liquid distribution. This has been the case for a few studies^{102, 115} but it has been found that the shape of the granules can cause the average granule size to decrease with increased L/S ratio.¹¹³ It has been found that there are many factors that can contribute to granule size such as binder addition¹¹⁵ excipients grade e.g. lactose¹¹⁵ and screw configuration¹⁰⁹ to name a few.

2.1.3.4 Formulation

Granules produced for the pharmaceutical industry are generally composed of the desired amount of active pharmaceutical ingredient (API) and excipients. Different types of excipients have different functions and are added in order to improve drug properties

like dissolution, bioavailability which help improve the quality of the drug in the patient. Table 2.2 shows a list of some excipients and their functions.

2.2 Hot Melt Extrusion

Hot melt extrusion (HME) is much like twin screw granulation except the binder solution is replaced with a meltable polymer. In HME, dosage forms are extruded out by forcing a mixture of polymers, thermoplastic binders and API through a die under controlled conditions such as temperature, feed rate and pressure. The desired formulation is fed into the extruder and heated in the barrel above the glass transition temperature (T_g) and sometimes above the melting temperature (T_m) of the polymeric materials in order to achieve a molecular level of mixing of the components.

Table 2.2 Excipients and their function

| Excipients | Function |
|---|---|
| Lactose, sucrose, mannitol, sorbitol, calcium phosphate, calcium carbonate, cellulose | Diluent - Adjust tablet bulk to acceptable mass |
| Starch, cellulose, cross linked, sodium starch glycollate | Disintegrant - Assist tablet disintegration in water |
| PVP, cellulose, starch, sucrose, Pharmacoat | Wet Binder - Bind ingredients together during granulation, emulsifier, thickening and suspending agent. |
| Cellulose, PVP | Dry Binder - Bind ingredients together during compaction |
| Silica, Mg stearate, talc | Glidant - Assist powder/granule flow during tableting |
| Mg stearate, stearic acid, Na lauryl sulphate, polyethylene glycol | Lubricant - Lubricate movement of punches in die |
| Mg stearate, talc, starch, cellulose | Antiadherent - Prevent tablet material sticking to punches, especially markings |

The main two types of extruders are single screw and twin-screw, which each have distinct mechanisms. The research described in this thesis focuses on twin screw extrusion. Twin screw extruders (TSEs) can be co-rotating or counter rotating with intermeshing or non-intermeshing screws. Figure 2.4 shows a schematic of a typical twin-screw hot melt extruder. Materials are fed into the feeder/hopper and are transported down the barrel by the spinning of the screws. The rotation or spinning of the screws mixes and pulls the material down the barrel, heat is applied to this barrel which causes the material to melt. As in TSG, increasing either the feed rate or the screw speed will increase the volume in the barrel, increasing the frictional forces created, resulting in higher heat creation. A combination of this shear and the heat from the heated barrel creates a melting pool for the material in the barrel. There are many combinations of parameters that can affect the final product, screw speed, feed rate, temperature, screw configuration and formulation. It is therefore necessary to implement a QbD approach to determine good methodology for the process.

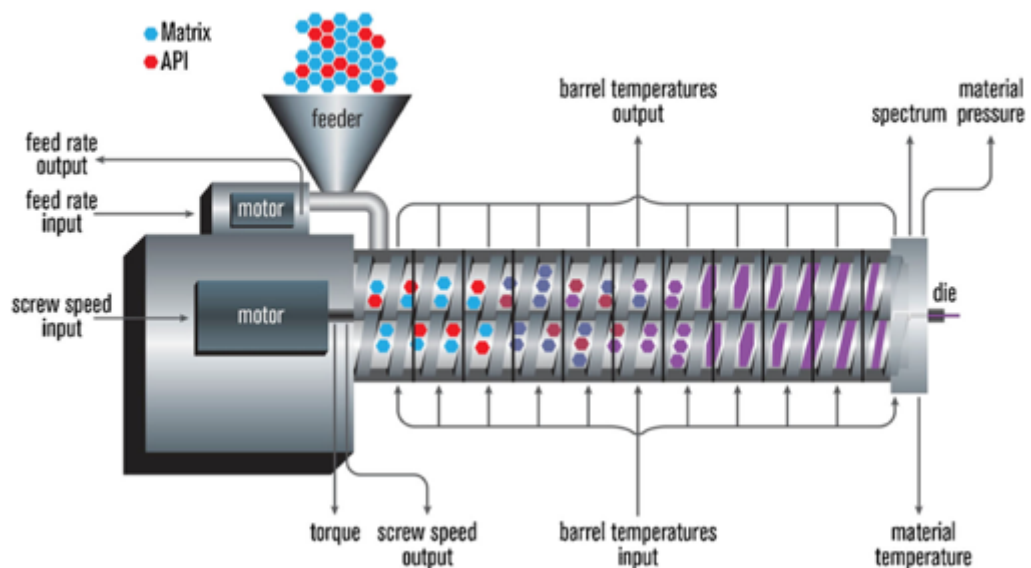


Figure 2.4 Schematic of a twin screw hot melt extruder ¹¹⁶

Processing conditions depend on the chemical stability and the physical properties of the thermal polymer; properties such as melt viscosity, molecular weight, T_g and T_m (in the case of a semi crystalline polymer) should be considered to establish appropriate processing parameters. Polymers are subject to a mechanical shear stress imposed by the rotating screw and thermal stress due to the relatively high processing temperatures and pressures. Under these conditions, polymers may undergo chain scission, depolymerisation or thermal degradation.¹¹⁷ The properties of the API can affect the formulation and their stabilities must be closely monitored during hot melt extrusion due to their exposure to high stress and elevated temperatures. The API may exist in a number of physical states within the polymer; these include crystalline, molecular and amorphous dispersions and eutectics, whereby the drug and polymer are co-dispersed as small crystallites¹¹⁸

Elevated temperatures can cause the solubility of the drug in the polymer to increase. Depending on the processing conditions, some crystalline drugs either melt or become solubilised in the polymer matrix during the process. Recrystallisation and nucleation of drug molecules from the polymer melt is retarded during the cooling and the extrudate due to reduced solute migration and the difficulty of nucleation in a highly viscous polymer medium. Furthermore, polymer viscosity increases with the decrease in temperature.¹¹⁷ During HME, drugs may degrade by hydrolysis, solvolysis and oxidation.

2.2.1 Physical Characterisation

2.2.1.1 Eyecon Image Analyser

The Eyecon Image analyser provides direct image analysis of particle size and shape with a charge-coupled device (CCD) camera. During measurements, the imaging

system captures sharp images using a 1 μ s illumination pulse of light. As illustrated in Figure 2.5, the pulse of light effectively captures the particle as it moves past the analytical window, giving sharp images for analysis. The camera is able to capture 3D information as it is equipped with red, green and blue LED lights, illuminating the sample at different angles, creating a 3D surface map. The colour distribution gives topological information about particle edges for determination of size.

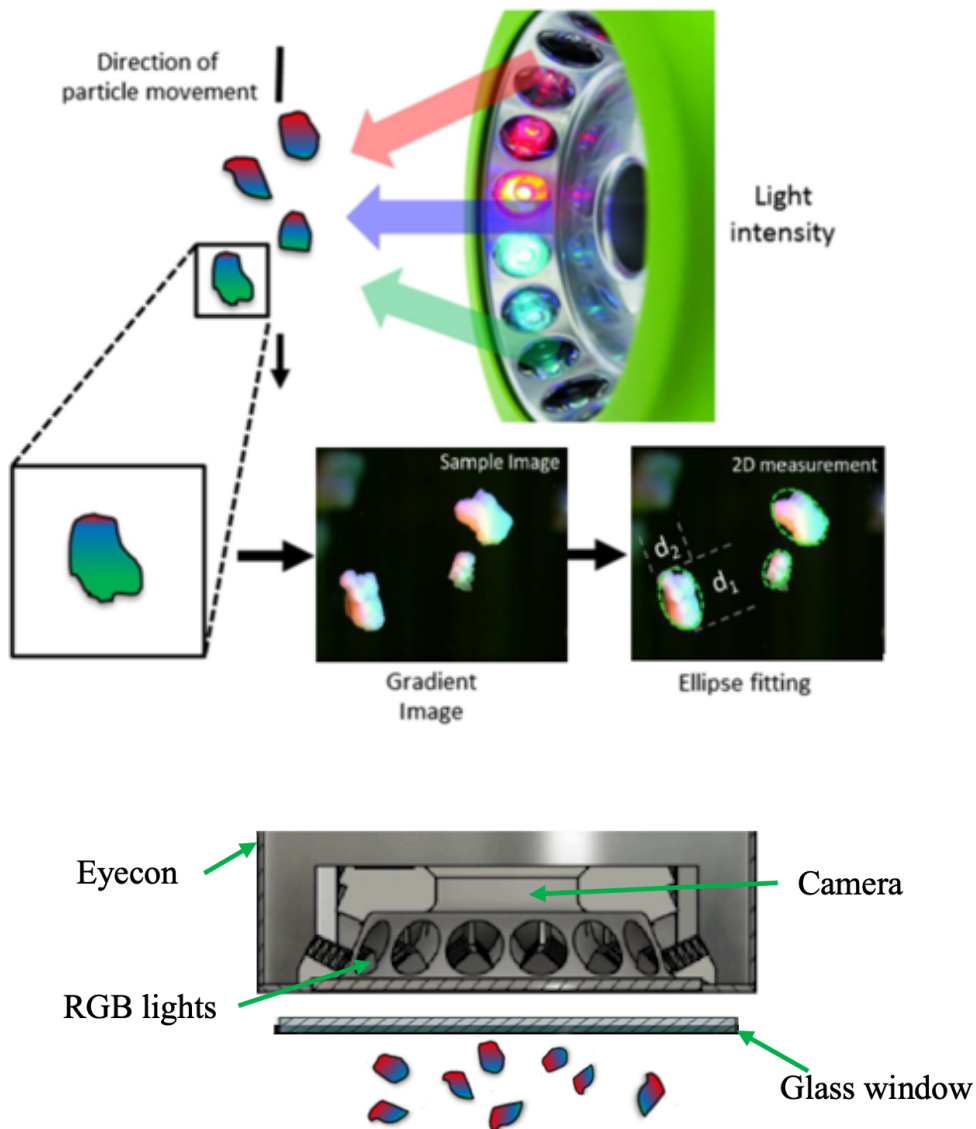


Figure 2.5 Schematic of the Eyecon Image analyser showing how particles are captured using the CCD camera with RGB lighting system, and the diameter measurements d_{min} (d_2) and d_{max} (d_1). (Adapted from reference ⁸⁵)

The Eyecon software uses advanced algorithms to detect the particle edges for each particle. The particles are fitted with an ellipse calculated from the maximum diameter, d_1 , and the minimum diameter, d_2 as show in Figure 2.5, also known as D_{max} and D_{min} . the maximum and minimum diameters. From this the 3D volume of the ellipse surrounding each particle is calculated using equation 2.1.

$$mass\ of\ a\ sphere\ (volume) = \frac{\pi}{6} (D_{min} \times D_{max} \times D_{avg}) \rho \quad (2.1)$$

Where ρ is the density which is assumed to be constant for all particle, assuming this and the and cancelling all other constants the relative mass can be calculated from equation (2.2):

$$relative\ mass = d^3 \quad (2.2)$$

Each particle's diameter is therefore cubed to give its relative mass. These values can be summed to calculate the total relative mass of the sample measured. The values may then be arranged in ascending order and added iteratively until the total reaches 10, 25, 50 or 75 and 90% of the total relative mass of the sample, known as the D10, D25, D50, D75, D90 values. ¹¹⁹

The data can also be represented by cumulative distributions, starting with the smallest fraction, here the quantities for each of the size classes are summed also known as a percentile distributions and number distributions, where each particle is counted for each of the size intervals.

The Eyecon™ can be used for both off and on-line analysis, for off-line analysis the system is said to be in bench top mode. In this mode, the sample is presented in a monolayer on a stainless-steel sample tray to the sample stage. The stage has 25 positions in a pattern that the operator can step through. This pattern is shown in Figure 2.6 along with the Eyecon in benchtop mode.

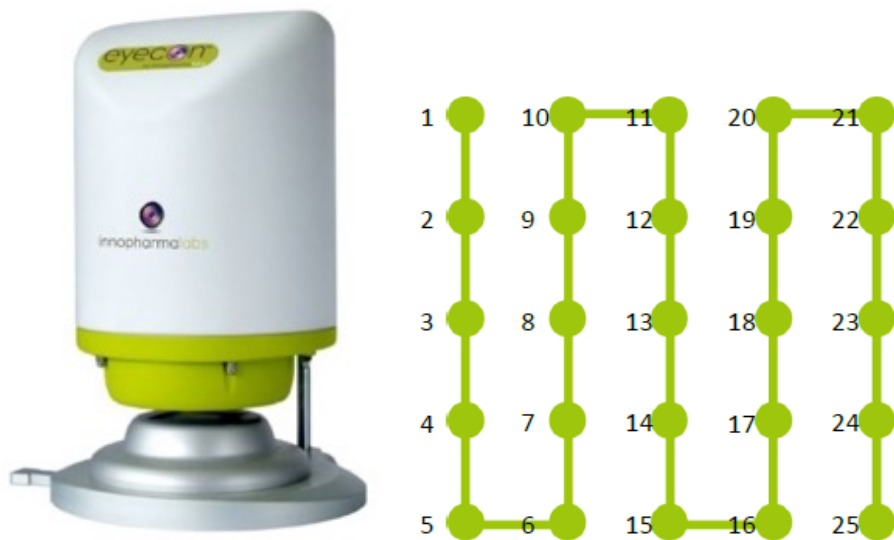


Figure 2.6 The Eyecon set up (left) for off-line analysis showing the sample stage and the stage movement pattern (right) for bench top analysis ¹²⁰

In benchtop mode, the camera autofocuses during each step in the pattern and a traffic light system shows a green light on the software along with a live image of the sample being analysed. When the light goes green the stage is moved to the next consecutive step on the pattern.

The Eyecon has its limitations like all other particle sizing techniques. Some of these are listed below.

- There are limits to the size of particles that can be analysed, 50 – 5500 μm

- The Eyecon struggles to obtain accurate measurements for dark, transparent or very shiny particles.
- The focal length of the system is limited and so material must be analysed close to the camera system.
- The depth of field is small and so samples with a wide range distribution will be difficult to measure.

2.3 Solid state analysis

2.3.1 X-ray powder diffraction

XRPD is a is the go to method for the determination of crystallinity of organic, inorganic and polymeric materials. When X-rays are applied to the samples, atoms are irradiated and generate a series of distinct peaks, giving a characteristic x-ray diffraction pattern which provides a fingerprint of the crystals present in the sample. When properly interpreted, by comparison with standard reference patterns and measurements, this fingerprint allows for identification of the crystalline form. X-rays are a form of electromagnetic radiation of wavelength ranging from 10^{-3} Å to several hundred Å, which will diffract when they hit obstacles.¹²¹ In 1941 Bragg, developed Bragg's law and demonstrated that the obstacles in this case are from the parallel planes of atoms i.e. the repeating pattern of the crystalline material which act as a diffraction grating for the X-rays.¹²² These 3-D crystals need to be present for XRPD patterns to be generated, the absence of these can indicate the presence of amorphous material. i.e. no repeating crystalline pattern.

2.3.2 DSC

DSC is a common method for the analysis of amorphous solid materials as it gives information on the thermodynamic properties. DSC measures the temperatures and heat flows associated with transitions in materials as a function of time and temperature in a controlled atmosphere. The thermograms provide an understanding of the physical changes that a polymorph undergoes during heating. The presence of an endotherm at lower temperatures known as the T_g (glass transition temperature) is a good indicator of the presence of amorphous material. The T_g is a temperature range in which properties of materials transit from solid like (i.e. glassy state) to liquid-like (i.e. supercooled state) upon heating and vice versa.¹²³ Crystalline material presents as exotherms close or on the melting points for each of the polymorphs. The presence of double peaks can indicate the presence of multiple polymorphs. DSC can also give information of transitions between solid phases of materials. It is therefore a widely used analytical method for solid form analysis. DSC is one of the most widely used thermal analytical techniques applied to amorphous solid dispersions. The DSC thermogram shown in Figure 2.7 illustrates the information that can be obtained from the analysis.

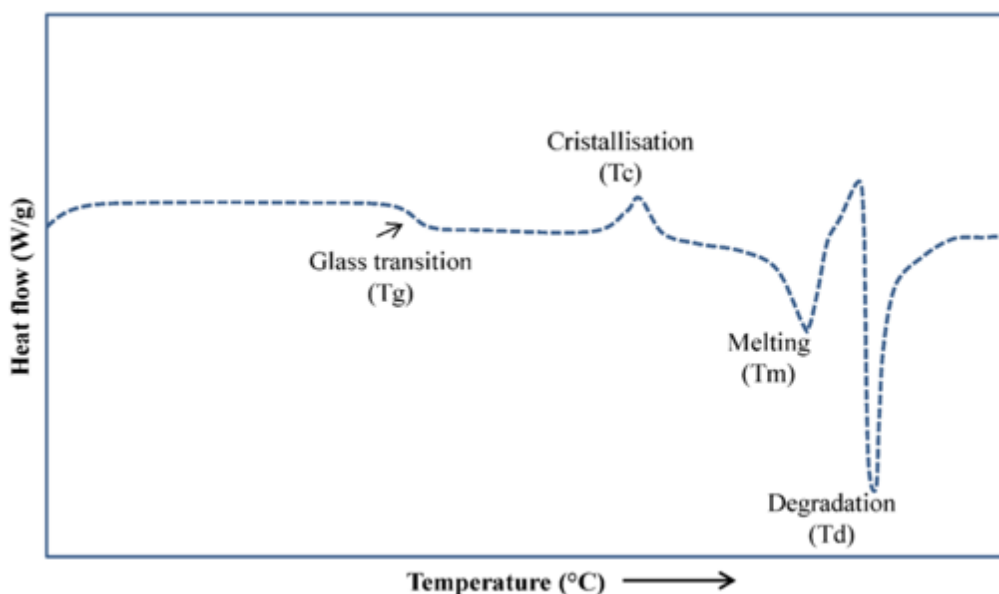


Figure 2.7 Schematic of the thermal transitions represented in semi crystalline material obtained in a DSC thermogram ¹²⁴

T_g represents the glass transition event showing the temperature range over which the properties of a system change from liquid to glass; an important property for amorphous solid dispersions. This transition occurs as the temperature of the system is changed and can give information on the properties of amorphous solid dispersions. Above the T_g , the material is described as a supercooled liquid and said to be in a rubbery state, while below T_g , it is described as a glassy state. T_c is the temperature at which any crystalline material might reorder itself, i.e., a form II to form I transition before it melts at T_m .

2.3.3 Fourier transform infrared

Fourier transform infrared (FTIR) is a spectroscopic technique used to obtain an infrared spectrum of absorption and emission of organic, inorganic and polymeric materials. FT-IR can be used to collect high spectral resolution data over a wide

spectral range typically 400 to 3000 cm^{-1} . Rather than shining a monochromatic light as in Raman analysis, FT-IR uses a broadband light source containing many frequencies of light all at once. The amount of this light absorbed by the sample is measured, the light travels to a Michelson interferometer, which is composed of a fixed and moving mirror, that reflect each wavelength of light.

2.3.4 Raman and Terahertz Raman Spectroscopy

Raman spectroscopy is a spectroscopic technique, theoretically described by Adolf Gustav Stephan Smekal ¹²⁵ in 1923 and then later experimentally confirmed in 1928 by Chandrasekhara Venkata Raman for which he won the Physics Nobel prize in 1930.¹²⁶

Rayleigh scattering (or elastic scattering) is where the frequency of light is unmodified i.e. the scattered photons are of the same energy as the incident photons. Raman scattering (inelastic scattering) occurs when the frequency of light is modified by irradiated molecules undergoing vibrational transitions. Only a small fraction, 1 in $10^6 - 10^9$, of the photons are inelastically scattered so the technique's sensitivity can be quite low. The two possible outcomes with inelastic scattering are Stokes and anti-Stokes. Stokes scattering occurs when a molecule jumps to a higher vibrational state, losing energy to the molecule and anti-Stokes occurs when a molecule jumps to a vibrational state of energy lower than the initial one subsequently gaining energy from the molecule. The difference between the incident and the scattered photons is called the Raman Shift $\tilde{\nu}$. This can be given by the difference in the wavenumber of the incident ($1/\lambda_{\text{iph}}$) and that of the scattered photon ($1/\lambda_{\text{sph}}$)

$$\tilde{\nu} = \frac{1}{\lambda_{iph}} - \frac{1}{\lambda_{sph}} \quad (2.3)$$

where positive values of $\tilde{\nu}$ correspond to Stokes scattering and negative values to anti-Stokes. The Raman spectrum consists of Raman bands, i.e. regions of lower and higher Raman scattering signal. The Raman bands are highly chemically specific and unique to each molecule as they are linked to vibrational modes and/or vibrational processes of the molecule or connected to a combination of these.⁹⁵ The frequency of light scattered from a molecule is based on the chemical structure and characteristics in the bonds.¹²⁷ Raman spectra can therefore provide information on both chemical and physical structure.

When a photon interacts with a molecule the total angular momentum in the ground state must be conserved, it therefore follows that only specific vibrational transitions are possible. Figure 2.8 shows a Jablonski diagram of these transitions showing the first vibrational states of a molecule $v=0$, $v=1$, $v=2$ and $v=3$ with respect to the vibrational energies. The diagram shows spectroscopic transitions for Raman, IR and NIR spectroscopies. Below this the energy level diagram are the Raman signals for Stokes, anti-Stokes and Rayleigh scattering corresponding to these transitions.

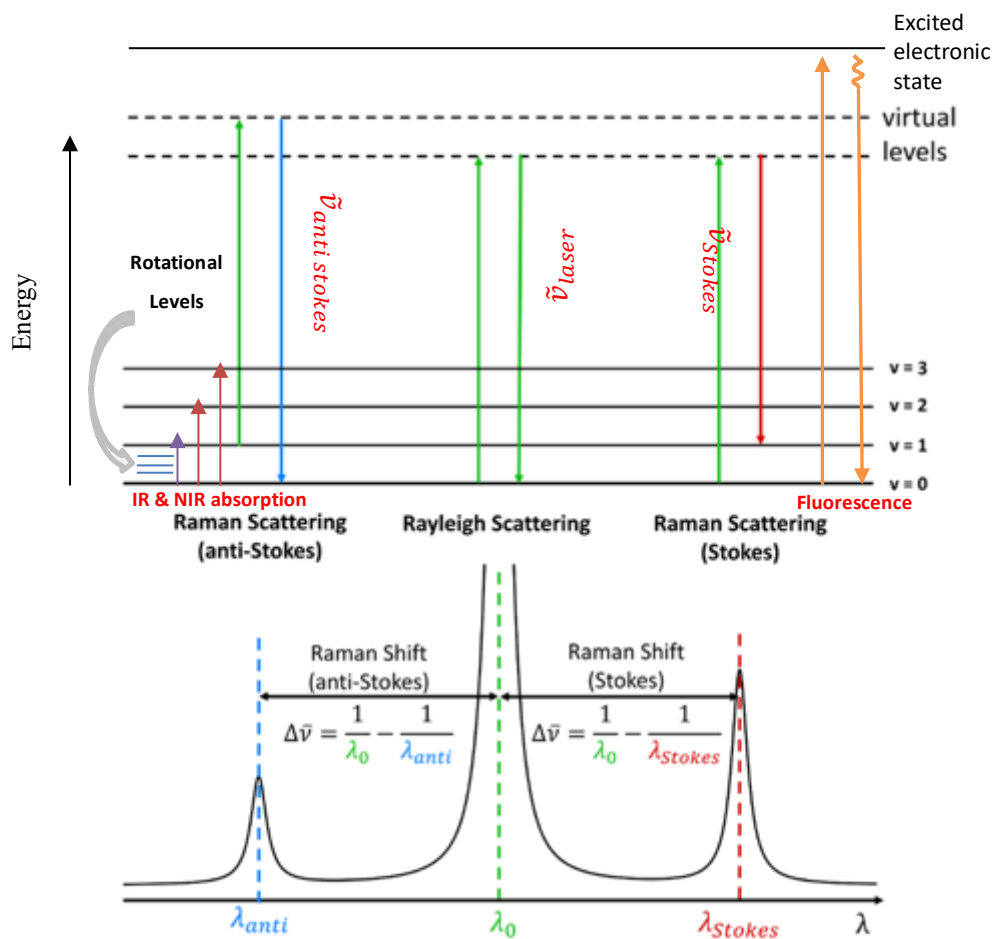


Figure 2.8 Schematic representation of spectroscopic transitions for Raman IR and NIR spectroscopies in an energy level diagram showing the interaction of light with fluorescence, Stokes, Anti-Stokes and Rayleigh scattering. ⁹⁴

Temperature can have an effect on vibrational modes and is linked to the Boltzmann distribution, (a probability distribution linked to speeds of particles within a stationary container at a specific temperature). This defines the fraction of the molecules that will be occupying a given vibrational mode at a given temperature.

Solids, liquids and gasses can produce Raman scattering but in addition to this Raman scattering can be observed from interactions between these phases. It is essential to therefore consider the properties of both of the phases being analysed.¹²⁸ Water on the

other hand is a weak Raman scatter and therefore Raman is good for analysis of analytes in aqueous solutions. Fluorescence is often encountered with Raman spectroscopy, and due to the relatively low number of Raman scattered photons compared to the efficient fluorescence process, fluorescence can often dominate the spectra. Fluorescence is observed when the energy of the incident photon is high enough to promote the molecule above the virtual energy level as described in Figure 2.8 into a vibrational energy state in the electronic energy level. Internal relaxation processes will take place before the fluorescence process occurs, which relaxes the molecule back into its ground state. Altering the laser power will reduce the intensity of the laser which can help reduce the effects of fluorescence. Light from strip lights can also affect the signal, these will appear on the spectra as sharp peaks that are quite noticeable, it is therefore essential to make sure that samples are collected in a dark room or the sampling area is covered in order to allow no light into the spectrometer. Raman scattering can provide information on the composition of the solid phase, i.e. polymorphism although several other solid-phase properties can influence Raman scattering such as particle size and shape.

P.M.A Sherwood¹²⁹ stated “*All crystal vibrations involve the entire crystal lattice and are thus lattice vibrations (a term sometimes unfortunately only applied to external vibrations). Such vibrations can be considered as a wave propagation through the crystal*”.

Unlike these normal vibrational modes of the individual molecule, the phonon is a crystal lattice vibrational wave traveling through the crystal.¹³⁰ These crystalline vibrations can be accessed with terahertz Raman spectroscopy described in the next section.

2.3.4.1 Terahertz Raman Spectroscopy

Most traditional Raman spectrometers currently utilize thin-film edge/notch filters, which remove most if not all of the low frequency signals including the entire anti-Stokes region and the Rayleigh excitation. These filters remove the entire signal produced below 200 cm^{-1} . It used to be that the only systems able to achieve both high Rayleigh attenuation and resolution close to the excitation line were large and bulky multistage spectrometer systems that were fiddly to align and difficult to operate making them unpractical and too large to be portable.

Advances in filter technologies have seen the production of new volume holographic gratings (VHG), which when used as notch filters, have a very narrow bandwidth and very high throughput. By combining a series of these new filters with a stable wavelength laser and a single stage spectrograph, a portable and affordable system capable of rapid acquisition of both Stokes and anti-Stokes Raman ($\pm 5\text{ cm}^{-1}$ to 200 cm^{-1} , or $150\text{ GHz} - 6\text{ THz}$ in the electromagnetic spectrum) has been made. An example of a LFRS system set up is shown in Figure 2.9.

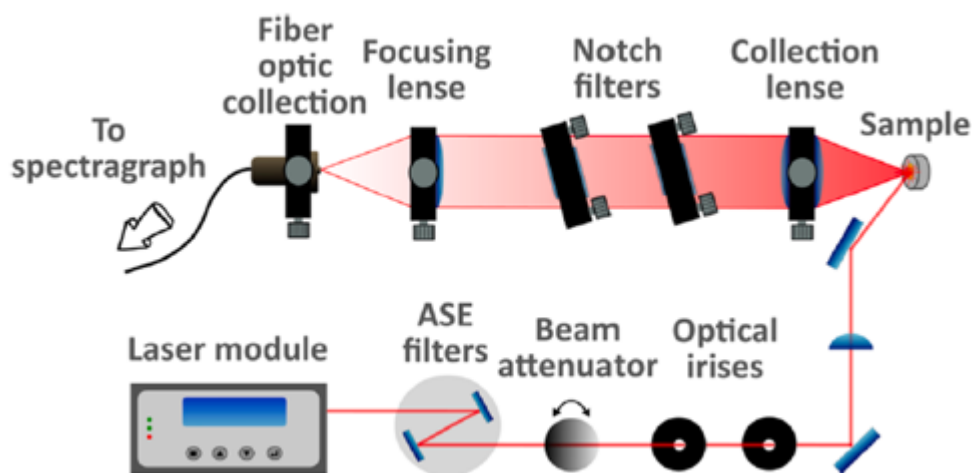


Figure 2.9 Schematic of a set up for LFRS showing the positions of the filters and lenses. ⁹⁴

Terahertz (THz) vibrations in the frequency range of $5 - 200 \text{ cm}^{-1}$ provide information on the weak intermolecular interactions in crystals such as hydrogen bonds. These interactions give strong individual characteristics in the THz region. i.e. the THz method is very sensitive to these weak interactions ¹³¹ and represents the fingerprint of the atomic crystalline lattice. The low frequency region reveals a new structural fingerprint of Raman, enabling simultaneous analysis of both molecular structure and chemical composition. Combining this information eliminates the need for multiple samples and instruments and the Raman system can be integrated with most lab grade microscopes or Raman systems with a range of excitation wavelengths (488 nm to 976 nm).

Traditional Raman spectroscopy is a “scattering” spectroscopic technique that can be associated with molecular vibrations in the spectral range of 200 cm^{-1} to 4000 cm^{-1} . It is often only reported from $200 - 1800 \text{ cm}^{-1}$ as this falls within the “fingerprint region” ($200 - 2000 \text{ cm}^{-1}$) a region where the Raman bands make it possible to distinguish and

identify the chemical composition of a substance using reference databases such as Wiley's KnowItAll¹³² spectral library and RRUFF^{TM133} mineral database.⁹⁵

ONDAX, now part of Coherent Corp's patented THz-Raman®¹³⁴ phrase which refers to the "low-frequency" Raman that corresponds to the frequency between microwaves and infrared (roughly 0.15 THz to 6 THz). This region yields valuable information on the vibrational energies associated with the molecular and intermolecular structures.¹³⁵ The THz region is shown in Figure 2.10, THz vibrations are in the frequency of 5 cm⁻¹ to 200 cm⁻¹ and give direct evidence for the formation of weak bonds such as hydrogen bonds and Van der Waals forces within crystals. These regions contain important structural information about the molecule or crystal lattice (phonon modes) which has principally been the domain of X-ray diffraction.

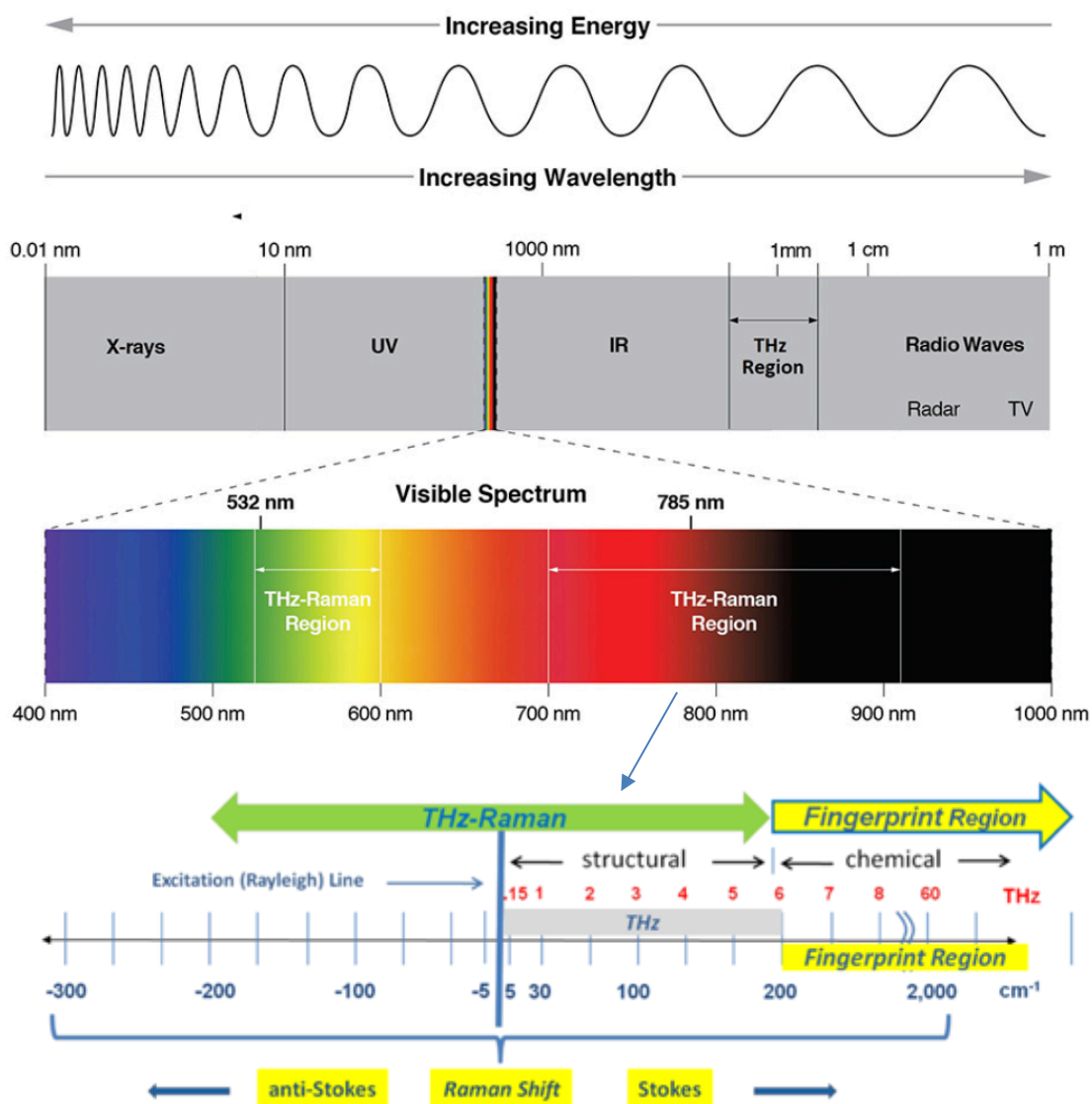


Figure 2.10 The electromagnetic spectrum above ¹³⁴ showing different spectroscopic techniques and below the THz-Raman® and Raman spectral range showing the fingerprint region, Stokes and anti-Stokes scattering¹³⁶

Raman spectroscopy gives information as annotated in the molecular structure figures and THz Raman gives the information as annotated in the packing structures.

Another key feature of THz Raman spectroscopy is the difference in the intensity between Raman and the THz Raman regions. An example of this is shown in the results from the analysis of the Sulfamerazine structural forms in Figure 2.11. The spectra demonstrate the efficiency of THz-Raman for polymorphic detection. Much like in XRPD, the amorphous forms of drugs have no distinct peaks, in the case of THz Raman the amorphous form appears as one smoothed peak from 0 cm^{-1} to 200 cm^{-1} . The difference in the intensities of the signals between the mid and low frequency Raman regions can be seen in the spectra in Figure 2.11 with the THz Region giving signals much greater. This increased sensitivity allows for much lower detection limits and better signal to noise ratio (SNR).

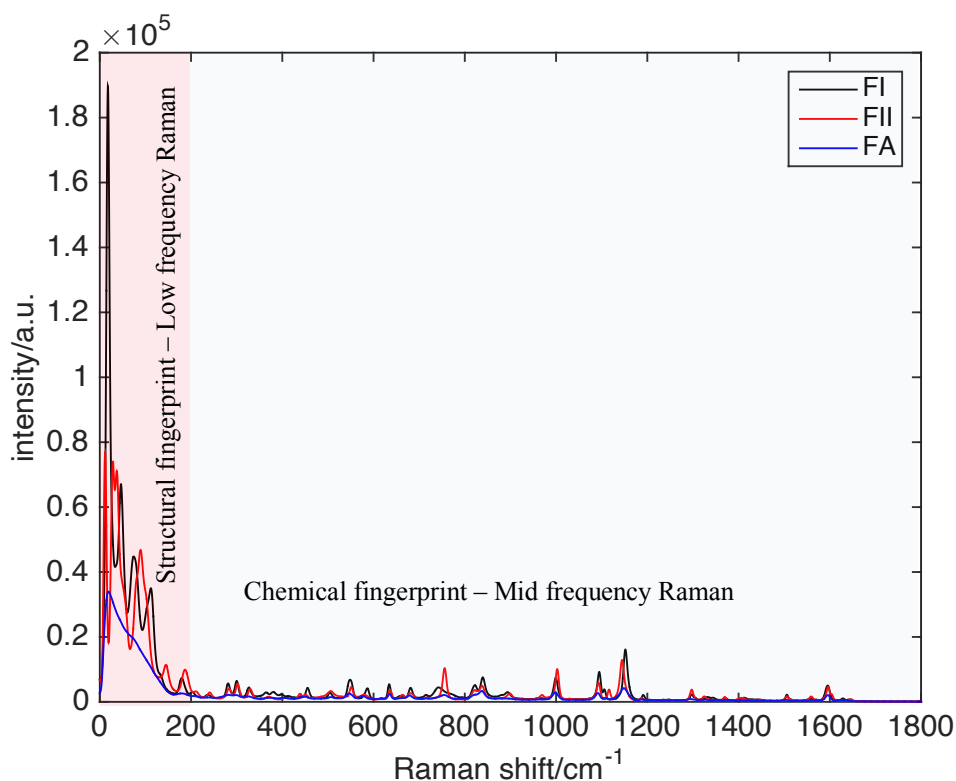


Figure 2.11 Example of Raman spectra of crystalline and amorphous solid forms of Sulfamerazine showing both the low (0 – 200 cm^{-1}) and mid (200 - 1800 cm^{-1}) frequency Raman regions.

These advantages are showing that THz Raman spectroscopy can be a very useful analytical tool across many applications in the pharmaceutical, industrial and petrochemical industries.

2.3.4.2 Other Types of Raman and Spectroscopy

It is easy to get confused between THz Spectroscopy, Raman Spectroscopy and THz Time Domain Spectroscopy below in highlighting the differences between them and the information that can be obtained by each.

Table 2.3 Overview of Terahertz and Raman Spectroscopy techniques

| Technique name and known names | Spectral/THz Region | Type of analysis | Information | Description |
|--|--|--|--|--|
| Raman spectroscopy | 200 – 4000 cm ⁻¹ | Scattering technique - Molecular vibrations. Also known as Vibrational Raman | Chemical structure, phase, polymorph identification, crystallinity and molecular interactions | Non-destructive chemical analysis technique based upon the interaction of light with the chemical molecular bonds within a material. Fingerprint region widely documented for peak assignment. |
| THz Raman | 5 cm ⁻¹ – 200 cm ⁻¹ (~ 0.15 THz to 6 THz) | Scattering technique - Intermolecular vibrations within crystals. Also known as lattice vibrational modes. | Also known as; THz Raman®, phonon Raman, Terahertz Raman. Information on molecular orientation, crystal structure (lattice modes) amorphous material, phase changes, excellent at polymorph detection | Like Raman probes the vibrational and rotational modes but with addition of Narrowband (< 5 cm ⁻¹) spectral clean up filters and Rayleigh scatter blocking filters. Allows access to LFR mode. Assignment of bands in this region not yet widely investigated. |
| THz Spectroscopy | 0.1 to 10 Hz | Different systems use different light techniques. Absorption technique. Common THz sources include the gyrotron, the far-infrared laser, quantum cascade laser, and synchrotron light sources. | Probes low frequency vibrational modes. Very good for biologicals, like THz Raman looks at the structures and dynamics of molecules. Materials characterisation, Pharmaceutical control (PAT). | Extension of far-IR (FIR) absorption spectroscopy often used in biologics: Low energy radiation able to penetrate most dry, non-metallic, nonpolar materials but not ionise atoms or molecules so safe for biologics |
| THz Time Domain Spectroscopy - THz-TDS | 0 to 10 THz (can be up to 40THz) ¹³⁷ (3.3 – 333 cm ⁻¹) | Sample probed with ultrafast (large bandwidth) short pulses of THz radiation. Sample. Measures the transient electric field rather than its intensity. Uses ultrafast pulsed laser typically titanium sapphire or mode-locked fibre lasers. ^{138 139} | Ultrashort pulsed laser used for material characterisation and process control. Great for contact free conductivity measurements for e.g. Metals and semiconductors. When coupled with density functional theory great for amino acid, peptides, drugs and explosive analysis. | THz waves generated by NIR light in semiconductor films by a process whereby the NIR is converted to THz light. NIR light emitted from short pulse laser 200 – 10 fs. ¹⁴⁰ |

2.4 Data Analysis

2.4.1 Design of Experiments

A design of experiments approach is mainly used for screening by determining the influence of a number of effects on a response, or to simplify analysis by eliminating factors that are not significant. Each of these factors are given a high and low response (e.g. screw speed, 100 and 500 rpm) and then a standard design can be formed varying each of these factors in order to create a design space. An example of a 2 level 3 factor design space is shown in Figure 2.12.

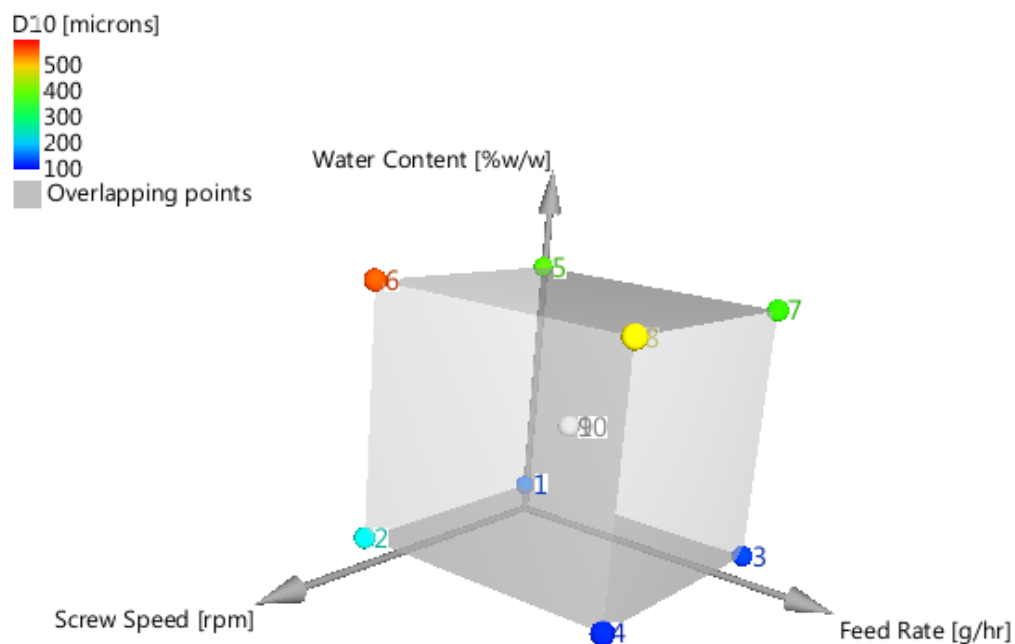


Figure 2.12 Schematic representation of a 2-level, 3-factor full factorial experimental design with 2 centre points. (Taken from experimental design in MODDE 11 Pro)

The factors can be labelled X1, X2 and X3 which, in this example are screw speed, feed rate and water content, respectively. A number of experiments are derived from these. Table 2.4 shows the method for coding of main effects where 1 and -1 denote the high and low levels, respectively, for each of the factors.

Table 2.4 Coding of the main effects – design matrix

| Expt | Screw Speed (X1) | Feed Rate (X2) | Water Content (X3) | X1X2 | X1X3 | X2X3 | X1X2X3 | Response |
|------|------------------------|----------------------|--------------------------|------|------|------|--------|----------|
| 1 | 1 | -1 | 1 | -1 | 1 | -1 | -1 | y1 |
| 2 | -1 | -1 | 1 | 1 | -1 | -1 | 1 | y2 |
| 3 | -1 | 1 | 1 | -1 | -1 | 1 | -1 | y3 |
| 4 | 1 | 1 | 1 | 1 | 1 | 1 | 1 | y4 |
| 5 | 1 | 1 | -1 | 1 | -1 | -1 | -1 | y5 |
| 6 | -1 | 1 | -1 | -1 | 1 | -1 | 1 | y6 |
| 7 | -1 | -1 | -1 | 1 | 1 | 1 | -1 | y7 |
| 8 | 1 | -1 | -1 | -1 | -1 | 1 | 1 | y8 |

The main effects of a factor are the average change in response when the factor is changes from (-) to (+). The main effects for this experiment were calculated as shown below:

In general, the main effects can be estimated from:

$$\text{Effect} = (\sum \text{response at (+)} - \sum \text{response at (-)}) / 2^{k-1}$$

where k is the number of factors:

$$\text{Effect of } X_1 = (y_1 - y_2 - y_3 + y_4 + y_5 - y_6 - y_7 + y_8)/4$$

$$\text{Effect of } X_2 = (-y_1 - y_2 - y_3 - y_4 + y_5 + y_6 - y_7 - y_8)/4$$

$$\text{Effect of } X_3 = (y_1 + y_2 + y_3 + y_4 + y_5 - y_6 - y_7 - y_8)/4$$

$$\text{Effect of } X_1X_2 = (-y_1 + y_2 - y_3 + y_4 + y_5 - y_6 + y_7 - y_8)/4$$

$$\text{Effect of } X_1X_3 = (-y_1 - y_2 + y_3 + y_4 - y_5 - y_6 + y_7 + y_8)/4$$

$$\text{Effect of } X_1X_2X_3 = (-y_1 + y_2 - y_3 + y_4 - y_5 + y_6 - y_7 + y_8)/4$$

In a 2-level design, it is assumed that the response varies linearly with each factor. It is impossible to tell whether or not there is a non-linear component in the relationship between a factor and a dependent variable if the factor is only evaluated at two points. The addition of centre points allows evaluation of the data for curvature. The centre points are set at the midway point between the high and low settings for each of the factors. If there is no curvature present in the data then the mean response at the centre point is equal to the average of the mean response of the factors at their low and high values and will lie on the plane fit through the centre point. If the mean of the centre points lies above or below the plane then this is an indication of curvature.

The addition of centre points allows the detection of curvature; they do not however provide enough information such that the curvature can be modelled. To do this, square terms are needed which means adding more points to the design as shown in Figure 2.13.

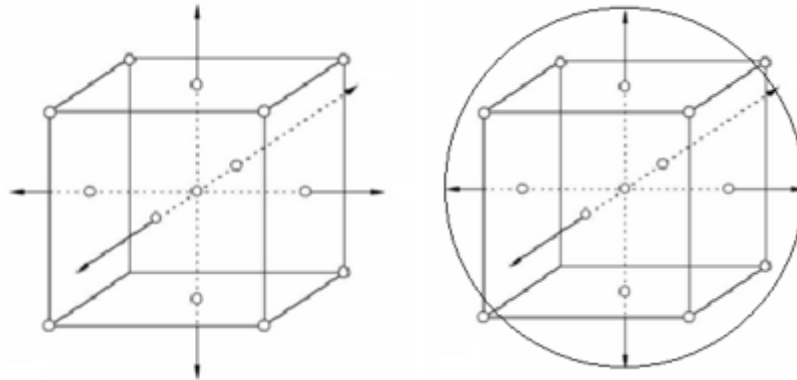


Figure 2.13 Face-centred central composite design showing sphere

This face centred central composite design allows the fitting of a quadratic model to the data. This spherical design is such that it is rotatable in the sense that all the points are equidistant from the centre. A rotatable design exists when there is an equal prediction variance for all the points at a fixed distance from the centre in any direction.

2.4.2 Pre-processing

Pre-processing algorithms are typically applied to raw spectral data before applying a chemometric model in order to remove any nuisance factors, including physical interruptions and faulty apparatus. Helping to reduce the signal to noise ratio.¹⁴¹ Non-linearities and the effects of uncorrelated sources from spectral variance such as baseline shifts and background variations. Baseline shifts are caused by the scattering of light within the sample particles.

2.4.3 Moving average

Noise is common in most analytical techniques and the background varies between each technique. Smoothing is applied in order to help reduce the noise within a spectrum.

The moving average is the average value of the data over a segmented range chosen by the analyst. The benefit of the moving average is its ability to smooth out the data from background noise or from busy data. The moving average is calculated from equation 2.4.

$$x_{mod} = \frac{x_1 + x_2 + \dots + x_{i-1} + x_i}{i} \quad (2.4)$$

Where x_{mod} is the modified data point from the moving average smoothing, and i is the range of the chosen segment.

2.4.4 Savitzky-Golay 1st and 2nd derivatives

The Savitzky-Golay algorithm is based on fitting polynomials to many small data windows (estimated by number of adjacent variables). The polynomial order and the length of the smoothing segment are chosen. 1st and 2nd derivatives were used in order to reduce baseline effects in the spectra. In spectroscopy derivatives are used to measure the rate of change in the gradient of the slope within the spectrum, which acts to resolve any overlapping peaks without losing any chemical information. The 1st derivative will remove any off-set difference between the data and the 2nd derivative will remove any slope effect in the data.

2.4.5 Standard normal variate

Standard normal variate (SNV) is used in order to eliminate the additive baseline off-set variations and multiplicative scattering effects of scattering resulting from non-uniform particles and surface area. The SNV is calculated from equation 2.5, from the mean X_i

and its standard deviation (SDV) σX_i . Each spectrum or diffraction pattern is centred and then scaled by dividing by its standard deviation. ¹⁴²

$$x_{i,mod} = \frac{x_i - (meanX_i)}{\sigma X_i} \quad (2.5)$$

The SNV assumes that multiplicative effects are uniform over the whole spectral range¹⁴³.

2.4.6 Principal component analysis

Principal component analysis (PCA) is a multivariate chemometric technique that is used to reduce the number of variables present in large data sets into much smaller set of abstract, latent variables, known as principal components (PCs). For any given matrix (X) the data can be considered as two separate component matrices, the “model” matrix (M) and associated error matrix (E); with both M and E matrices having the same dimensions as X as shown in equation 2.6.

$$X = M + E \xrightarrow{PCA} X = (TP^T) + E \quad (2.6)$$

The result of successful PCA decomposes the model matrix M, into two smaller matrices known as the scores matrix (T) and loadings matrix (P), where superscript T represents the transpose of the matrix, as is described by equation 2.7.

$$X = t_1 p_1^T + t_2 p_2^T + \dots + t_A p_{1A}^T \quad (2.7)$$

The scores matrix (T), describes any sample patterns that are present in the data set and the loadings matrix (P) describes any relationships that exist between the individual measurement variables. The number of PCs required to describe X is often far fewer than the number of measurement variables which results in a score (t_i) and loadings (p_i) vector for each PC and the residual error matrix, as is described by equation 2.8.

$$X = t_1 p_1^T + t_2 p_2^T + \dots + t_A p_A^T + E \quad (2.8)$$

Bilinear methods such as PCA are not as effective for accommodating the impact of multiplicative scattering. To minimize complex baseline variation more effectively, appropriate data-pre-treatment are needed. PCA is usually applied to data which has been mean centred, mean centring ensures the principal components are only looking at the variance within the data set and not capturing the overall mean as a variable. Mean centring the data, subtracts the mean from all observations on the variable in the dataset so that the variables' new mean is zero. In spectral data the mean spectrum is subtracted from each individual spectrum. ¹⁴⁴

2.4.7 Classical Least Squares

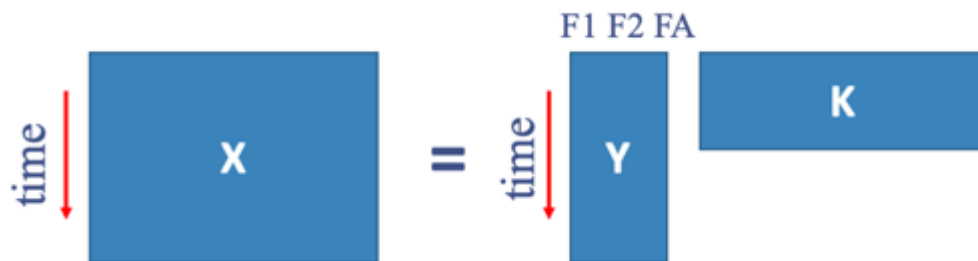
Classical least squares (CLS) regression is used to analyse mixtures of components. CLS is a quantitative analysis of these mixtures, where the individual components of a mixture are known and where the total signal of the mixture is the sum of the signals for each of the components in the mixture.

To calculate the concentrations of polymorphs e.g. F1, F2 and FA within a mixture, the information is split into vectors (like a column or row in a spreadsheet) in this case X is

the spectra of the mixtures, Y is the concentration of the individual components within the mixture and K is the matrix of the spectra of the pure components.

$$Y = XK^+$$

y for each component normalised to Y_{total}



CLS analysis makes some assumptions, it assumes that the model has linear parameter., it also assumes that the variance of residual is the same for any value of X .

Chapter Three

Dynamic Image Analysis of Twin Screw Granulation

3. Dynamic Image analysis of Twin Screw Granulation

3.1 Introduction

Continuous secondary manufacturing is rapidly becoming the first intent for production of oral solid dosage (OSD) forms of pharmaceuticals. Twin screw granulation (TSG) is the go to method these days for continuous granulation of pharmaceutical powders. Some of its benefits in comparison to traditional batch granulation include:

- Smaller quantities of materials needed – smaller inventory
- Easier scale up and atomisation
- Increased efficiency and higher but flexible throughput
- Individual excipients and API can be added separately helping to reduce risk waste materials
- The twin screw granulator handles both mixing and wetting
- Allows for the monitoring of process parameters far more easily and non-invasively

During continuous wet granulation quality attributes such as granule size can have an effect on the overall quality of the materials produced. The control of granulation processes can be challenging and currently there are limited PAT available for the monitoring and control of these processes. Some of the challenges faced with continuous twin screw granulation include the ability to control physical attributes such as granule size and shape. The morphology of the granules produced during TSG can have an effect on downstream processes such flowability, compressibility and on the final performance

and quality of the drug. Advances in PAT along with real time control can help towards a more robust process and therefore higher-quality products.

There is a requirement to develop and understand PAT's capable of on-line, real time process analysis of granules produced during TSG. This chapter explores the feasibility of using the Eyecon image analyser (Innopharma Labs, Dublin, Ireland) for this purpose. The studies in this chapter were conducted at GlaxoSmithKlein as part of a PhD industrial placement project.

The main aims of the studies in this chapter are:

- To establish methods for on-line and off-line analysis of granules produced by TSG
- To characterise granules produced by TSG by on and off-line analysis using the Eyecon image analyser.
- To evaluate the ability of the Eyecon image analyser to detect change in granule size caused by process perturbations.
- To analyse the granule size distributions of granules produced from a two level three factorial design of experiments.
- To further investigate the effects of the process parameters on granule size using multivariate analysis
- To test the ability of the Eyecon to analyse granules produced at higher powder feed rates relevant to industrial processes.

3.2 Experimental

3.2.1 Twin screw granulation set-up

A co-rotating twin screw granulator (Euro lab 16 TSG, Thermo Fisher Scientific, UK) was used for all the granulation experiments. The granulator was equipped with a gravimetric feeder (Brabender Flexwall® Feeder, Brabender-Technologies, Germany) that feeds into the powder inlet. Deionised water was fed into the liquid inlet, the volume of this was controlled firstly by a high-performance liquid chromatography (HPLC) grade pump, this was then switched for a peristaltic pump for the final experiments. Figure 3.1 shows a schematic of the experimental set up for on-line analysis of granules.

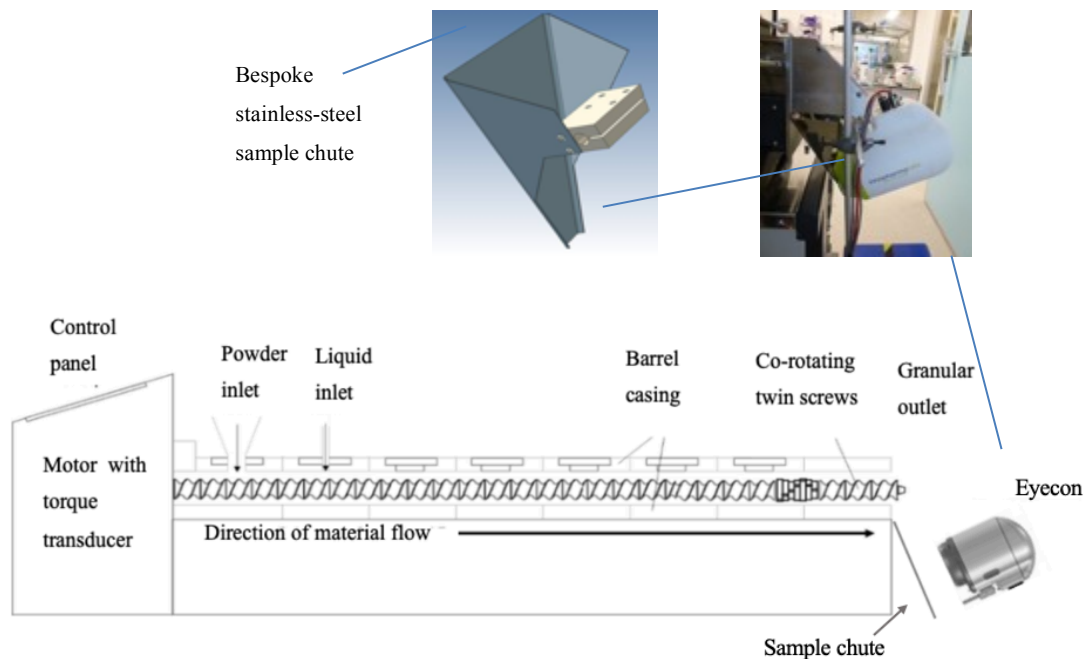


Figure 3.1 Schematic showing the twin screw granulation set up and Eyecon position with the specialised stainless-steel shoot

Water content was calibrated before every experiment and the granulator was run for five minutes before any data was captured, this was to allow for the powder to fill the twin screw barrel and for the TSG to reach steady state.

3.2.2 Screw Configuration

A picture of the screw configuration for the twin screws used in these experiments is shown in Figure 3.2. A list of the individual screw elements for this configuration are listed in Table 3.1. The configuration was labelled configuration A, and it was used throughout this chapter.

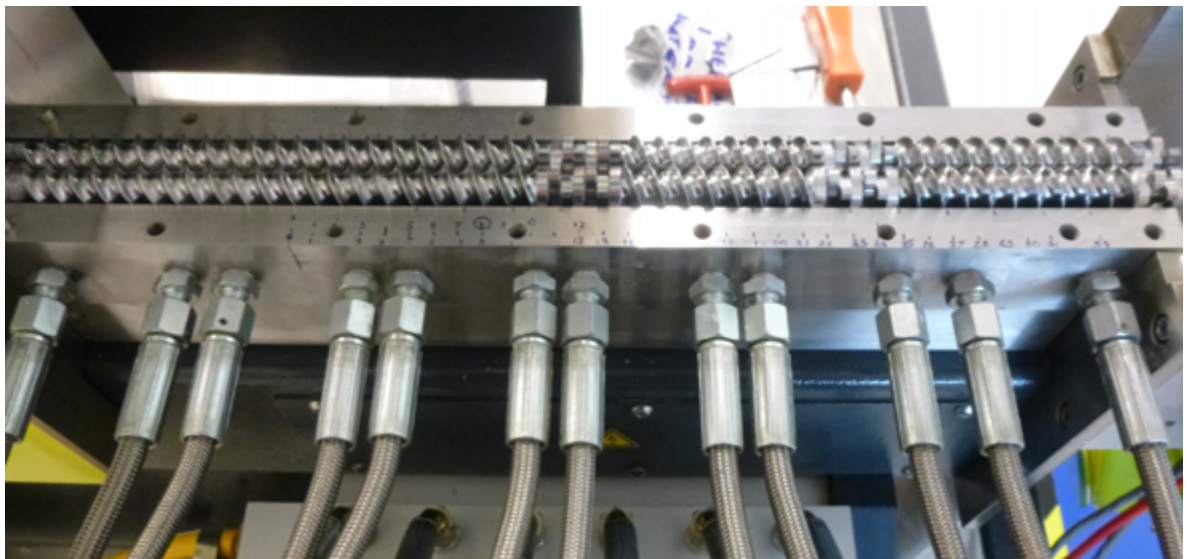


Figure 3.2 Twin screw set up in the TSG barrel showing screw configuration A with powder flow left to right.

Table 3.1 Screw elements for configuration A

| Number | Type & Description |
|--------|----------------------------|
| 9 | 1D conveyors |
| 7 | 0.25 bilobes at 60 degrees |
| 4 | 1D conveyors |
| 7 | 0.25 bilobes at 60 degrees |
| 7.5 | 1D conveyors |
| 3 | 0.25 bilobes at 90 degrees |

3.2.3 Materials

3.2.3.1 Off-line analysis of granules

Granule were produced using a 16 mm Twin Screw Granulator (Thermo Scientific™) with screw configuration A (see Table 3.1) and formulation A listed in section 3.2.3.2.1.1. The granules were collected and dried overnight in an oven at 40 °C, these were then sieved using two 1 mm and one 0.5 mm sieves. The three sieves were stacked on top of each other so that four sieved fractions were collected. Table 3.2 lists an approximate size range for the granules.

Table 3.2 Granule properties for off-line analysis.

| Nomenclature | Size |
|--------------|-----------|
| Large | < 3000 µm |
| Medium | ≥ 2000 µm |
| Small | > 1000 µm |
| Fines | < 1000 µm |

3.2.3.2 On-line analysis

3.2.3.2.1.1 Formulation

A placebo formulation, labelled Formulation A, composed of lactose monohydrate (Pharmatose 200M), 73.5 % w/w, microcrystalline cellulose (Avicel PH101), 20 % w/w, Hypromellose 2910 (Pharmacoat 603) 5 % w/w and Croscarmellose sodium (Ac-Di-Sol) 1.5 % w/w was used in this study. Material was blended in batches of 700 g using a Willy Bachofen Turbula Blender T2F 2 litre at 34 rpm for 10 minutes.

3.2.4 Methods

3.2.4.1 Off-line analysis

Off-line analysis of granules

A uniform dispersion of each sample was placed into the sample tray, the sample tray was then placed onto the sample stage in the measurement field below the camera. The Eyecon was set to bench top mode and images were captured continuously as the sample stage was moved through the analysis points. The images were then processed using software provided with the Eyecon (Innopharma Labs) and the data was saved as a CSV file, for further analysis in Excel using a macro supplied by Innopharma Labs. The macro calculates the particle volume, number and size distributions from the images collected.

3.2.4.2 On-line analysis

Effect of water content on Granule size

The Eyecon was set up on-line as shown in Figure 3.1. Images were captured every two seconds for one minute at each water flow rate; the data was then exported into csv files for further analysis. Granules were produced from formulation A and screw configuration A at three different water flow rates 1.5, 2.0 and 3.0 mL/min. All other parameters were fixed and are summarised in Table 3.3.

Table 3.3 Experimental parameters for liquid to solid ration on-line study

| Parameter | Fixed/Varied | Set point |
|-----------------|--------------|--------------------------|
| Powder Feed | Fixed | 1 kg/h |
| Screw Speed | Fixed | 150 rpm, |
| Water Feed Rate | Varied | 1.5, 2.0 and 3.0 mL/min. |
| Formulation | Fixed | Formulation A |

Investigation of feed rate, screw speed and water content at feed rates of 1 and 3 kg/h

The effect of varying powder feed rate, screw speed and water content on the size of granules produced was explored using a 2 level full factorial design with 2 centre points. The experiments performed with a feed rate centre point of 1 kg/h are given in Table 3.5. The water flow rate required to give a water content of 10, 15 and 20% w/w at powder feed rates of 800, 1000 and 1200 g/h was calculated using the calibration graph shown in Figure 3.3; the calculated water flow rates are given in Table 3.4. A second 2 level 3

factor full factorial design was used to investigate the effect of feed rate, screw speed and water content on granule size at a higher feed rate (centre point of 3 kg/h); the experiments performed are given in Table 3.6.

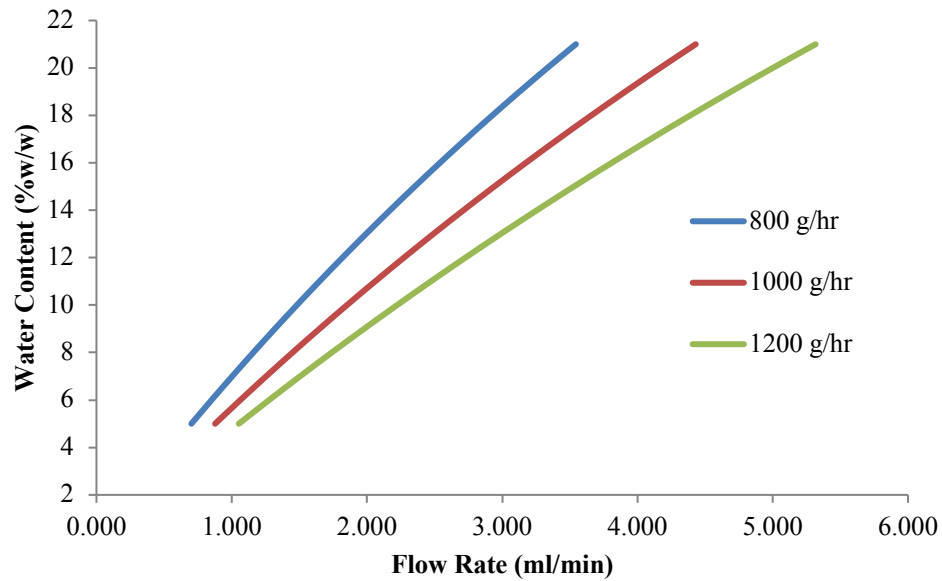


Figure 3.3 Calibration graph for calculation of the water flow rate required to produce granules with a given water content at powder feed rates of 800, 1000 and 1200 g/h.

Table 3.4 Calculated water flow rates (mL/min) required to produce granules with water content of 10, 15 and 20% w/w at powder feed rates of 800, 1000 and 1200 g/h

| Water content (% w/w) | Feed rate g/hr | | |
|-----------------------|----------------|------|------|
| | 800 | 1000 | 1200 |
| 10 | 1.48 | 1.85 | 2.22 |
| 15 | 2.35 | 2.94 | 3.53 |
| 20 | 3.33 | 4.17 | 5.00 |

Table 3.5 2 level 3 factor full factorial design, with two centre points, used to investigate the effect of screw speed, feed rate and water content on granule size where the powder feed rate of the centre point was 1 kg/h

| Expt Number | Screw Speed (rpm) | Feed Rate (g/hr) | Water Content (%w/w) | Flow rate (ml/min) |
|-------------|-------------------|------------------|----------------------|--------------------|
| 1 | 100 | 800 | 10 | 3.33 |
| 2 | 200 | 800 | 10 | 3.33 |
| 3 | 100 | 1200 | 10 | 5.00 |
| 4 | 200 | 1200 | 10 | 5.00 |
| 5 | 100 | 800 | 20 | 2.22 |
| 6 | 200 | 800 | 20 | 2.22 |
| 7 | 100 | 1200 | 20 | 1.48 |
| 8 | 200 | 1200 | 20 | 1.48 |
| 9 | 150 | 1000 | 15 | 2.94 |
| 10 | 150 | 1000 | 15 | 2.94 |

Table 3.6 2 level 3 factor DoE full factorial design, with two centre points, used to investigate the effect of screw speed, feed rate and water content on granule size where the powder feed rate at the centre point was 3 kg/h

| Expt Number | Screw Speed (rpm) | Feed Rate (g/hr) | Water Content (%w/w) |
|-------------|-------------------|------------------|----------------------|
| 1 | 100 | 1000 | 10 |
| 2 | 500 | 1000 | 10 |
| 3 | 100 | 3000 | 10 |
| 4 | 500 | 3000 | 10 |
| 5 | 100 | 1000 | 20 |
| 6 | 500 | 1000 | 20 |
| 7 | 100 | 3000 | 20 |
| 8 | 500 | 3000 | 20 |
| 9 | 300 | 2000 | 15 |
| 10 | 300 | 2000 | 15 |

Each experiment was performed for 5 minutes, during these 5 minutes the Eyecon was set to capture an image every 0.5 s. After 5 minutes, image acquisition was stopped and the experimental parameters were changed. This procedure was repeated so that images were captured of granules produced using the experimental conditions given in Table 3.5 and Table 3.6. Samples of granules were also collected for off-line analysis. 20 g of the wet granules collected were weighed out into crystallising glass bowls, covered and placed in the oven at 40 °C overnight to dry in a vacuum oven. The samples were then analysed off-line using the Eyecon instrument. More information on the weight of the granules before and after drying along with some observations during analysis and screw feeder calibrations can be found for the 1 and 3 kg/h studies in Appendix A.

3.2.4.3 Data Analysis

The experimental designs were produced and data analysis were carried out using MODDE (Umetri AB, Sweden). The effect of screw speed, feed rate and water content on granule size was evaluated using the D values extracted from the images.

3.3 Results and Discussion

3.3.1 Off-line analysis of granules

The size ranges obtained using sieve analysis for samples of granules are shown in Table 3.7 and the corresponding images captured for each of these samples are shown in Figure 3.4.

Table 3.7 Granule properties obtained via sieve analysis.

| Nomenclature | Size |
|--------------|---------------------------|
| Large | > 3000 μm |
| Medium | \leq 2000 μm |
| Small | > 1000 μm |
| Fines | < 1000 μm |

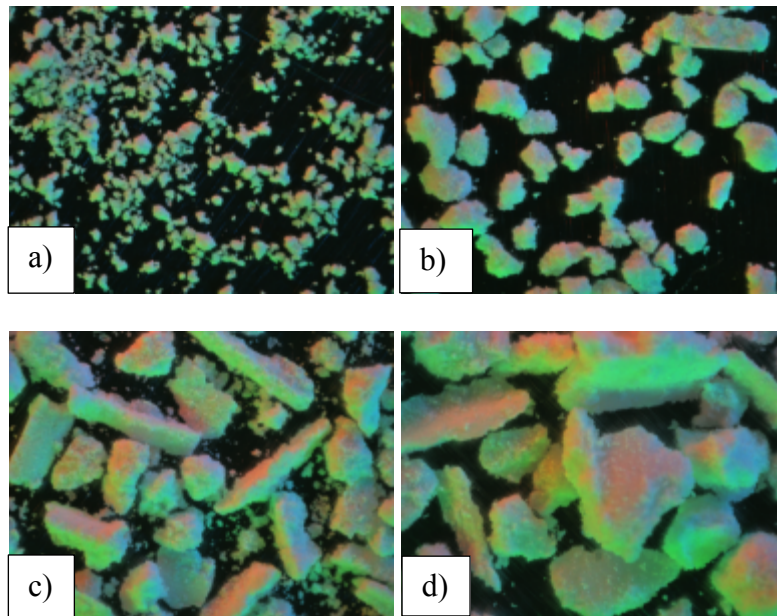


Figure 3.4 Off-line Eyecon images of granules with a size of a) $< 1000 \mu\text{m}$ (fines), b) $> 1000 \mu\text{m}$ (small), c) $\leq 2000 \mu\text{m}$ (medium) and d) $> 3000 \mu\text{m}$ (large)

The off-line images show quite clearly the texture of the granules, and it is obvious from Figure 3.4 a) and c) that there are lots of finer particles present within these samples. For the samples comprising smaller particles (such as that shown in Figure 3.4 a), it was very hard to present the samples in a monolayer; Figure 3.5 shows a good example of this.

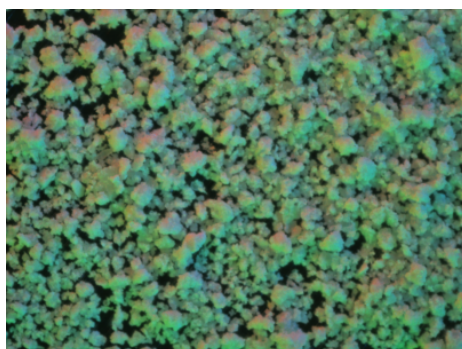


Figure 3.5 Example of an off-line Eyecon image obtained of a sample showing granule overlap

The particle count obtained from off-line image analysis of each of the sieved samples was plotted against size and is shown in Figure 3.6. This shows that there are a huge number of fines in the smallest sieve fraction, but also a surprising number in the small, medium and large fractions.

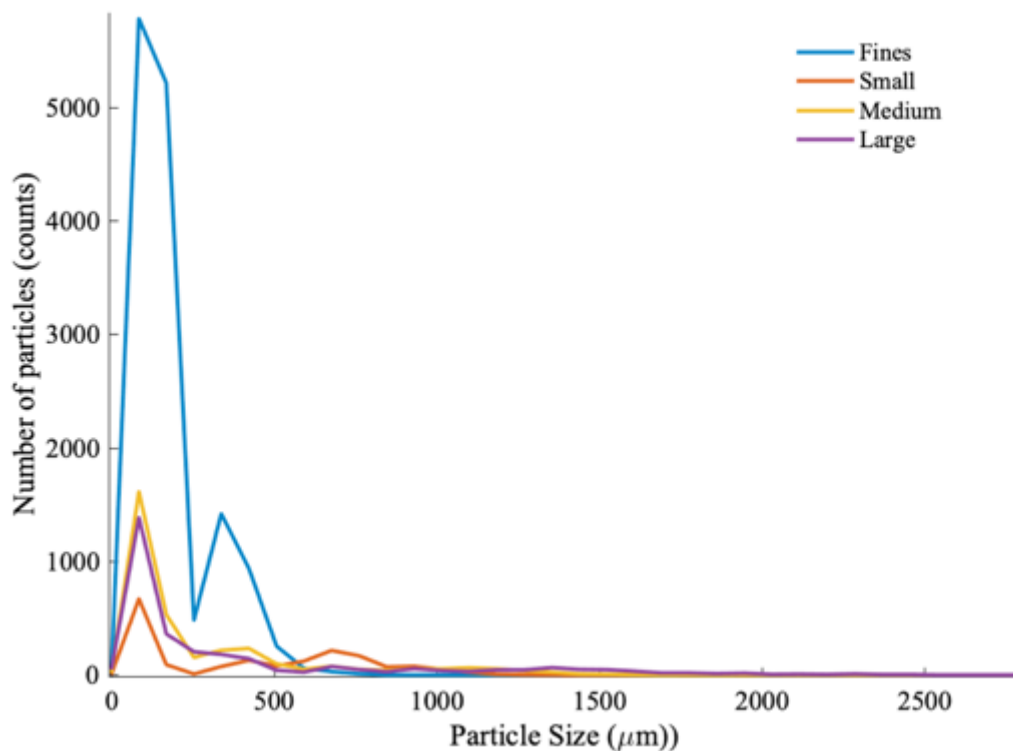


Figure 3.6 Particle size distribution of granules from off-line analysis with Eyecon image analyser

The volumetric particle size distribution data (Figure 3.7) confirms that there is a broad range of particle sizes present in each of the granule samples.

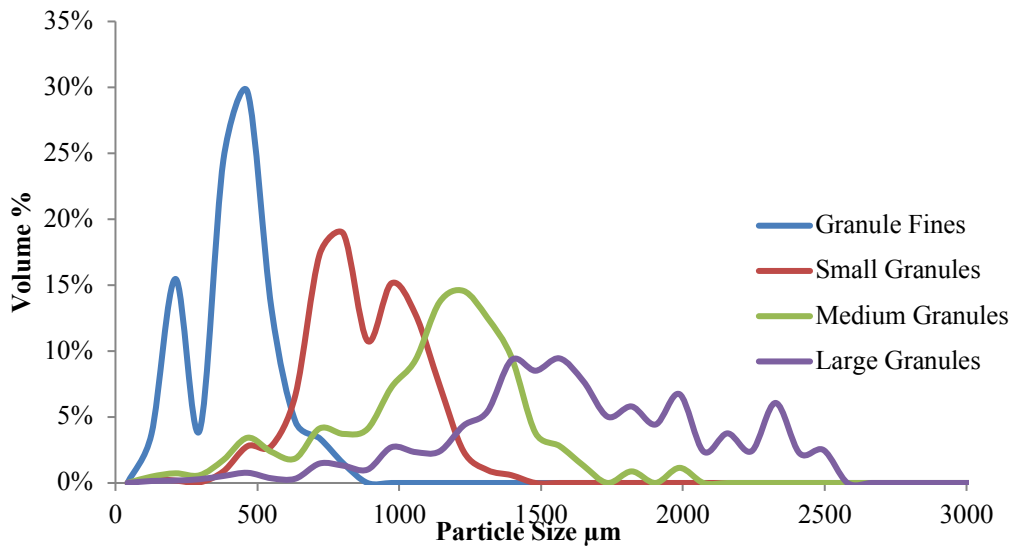


Figure 3.7 Volumetric particle size distribution obtained from off-line Eyecon image analysis of sieved granule fractions

The sample labelled Granule Fines shows primarily a bimodal distribution containing a large volume of particles are around 500 μm and a smaller amount that are close to 200 μm. These are all below 1000 μm which fits with the sieve fraction. There are a higher number of smaller particles here but the larger particles are taking up a bigger volume. The Small Granules sieve fraction shows a slight trimodal distribution with a very small volume at about 500 μm and the rest of the sample split between 800 and 1000 μm. The last two sieve fractions Medium and Large both show broad distributions across a large size range from > 500 up to about 2500 μm. This could be due to insufficient separation of the sample during sieving.

The cumulative particle sizes based on volume are plotted on Figure 3.8, and the corresponding D values, calculated from this are shown in Figure 3.9. These two methods for granule size analysis are a much easier way to visualize the trends in results.

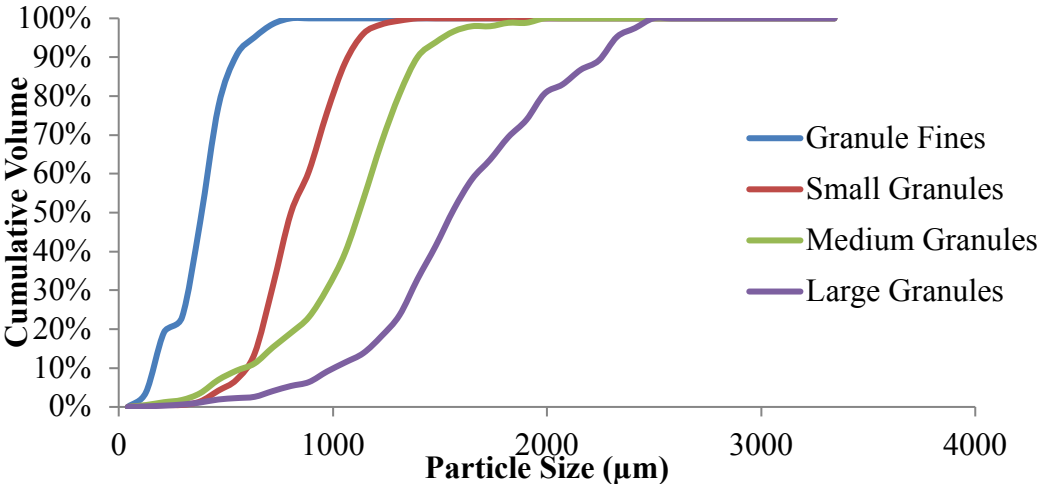


Figure 3.8: Cumulative particle size of sieved granule fractions calculated from images acquired off-line using the Eyecon image analyser

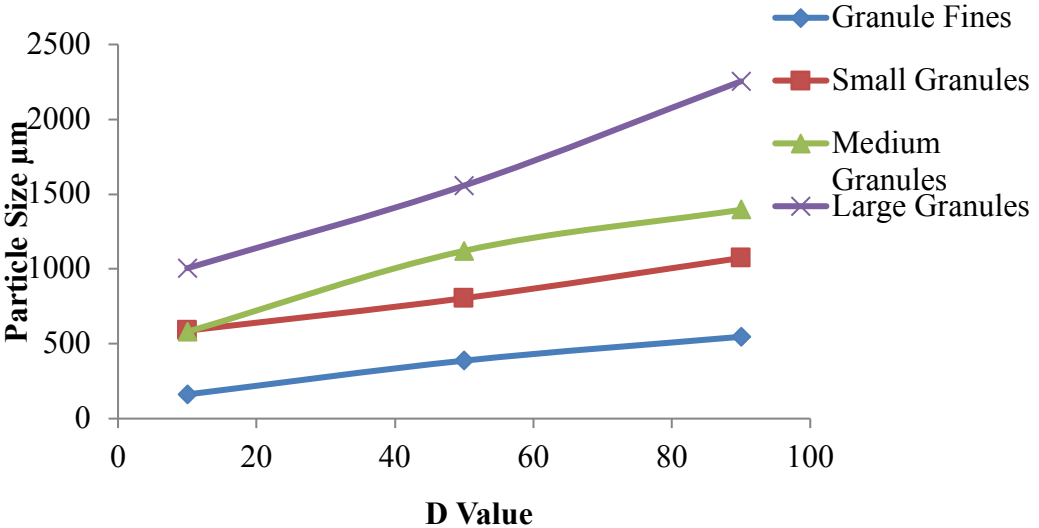


Figure 3.9 D10, 50, and 90 values of sieved granule fractions calculated from images acquired off-line using the Eyecon image analyser

The D10 values for both the small and medium particles both sit about 5800 μm whereas all of the other values differ for each of the sieve fractions. As the graph shows the D10, D50 and D90 values are given by the X values in Figure 3.8. Which is the particle size at 10 %, 50 % and 90 %. D values are commonly used in particle sizing techniques due to their convenience and easy to understand definition. A single number is good for quality control purposes and therefore the use of D values is common practice. ¹⁴⁵

3.3.2 On-line monitoring of twin screw granulation

3.3.2.1 Effect of liquid to solid ratio

Figure 3.10 (a) – (c) show example images acquired on-line of a granulation process performed at three different water feed rates; the images show an increase in particle size but a decrease in particle number as the water feed rate is increased.

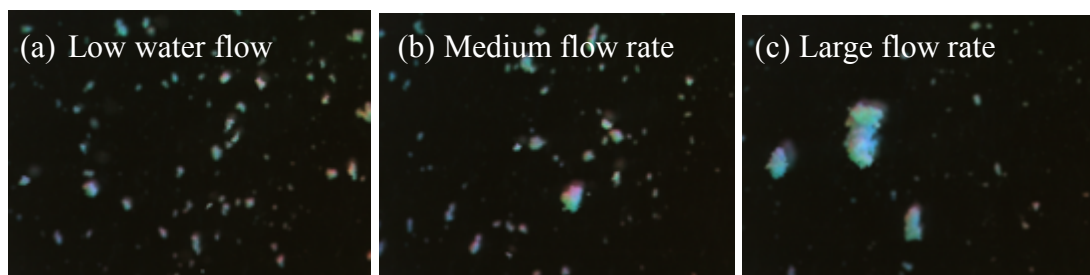


Figure 3.10 Eyecon images acquired on-line of a granulation process performed at water feed rates of (a) 1.5, (b) 2.0 and (c) 3.0 ml/min

The images presented clearly show a difference in the size and number of particles. However, there was quite a variation between the images taken throughout the analysis and it

would be hard to determine what was going on in terms of granule size by looking at the images alone.

One of the key advantages of dynamic image analysis over conventional methods such as laser diffraction and sieve analysis is the information that can be obtained from images. The RGB light system also gives the Eyecon technique an advantage over other imaging techniques as the colour feature provides improved edge detection and the ability to detect overlapping or touching particles. The software is also programmed to only detect particles that are in focus and within the image boundaries which is great for on-line analysis of fast flowing granules. Another advantage of having the images when it comes to irregular shaped particles such as granules is the ability to calculate the best fit ellipse from the maximum and minimum diameters and therefore be able to estimate the particle volume and the corresponding D10, D50 and D90 values.

The particle size distribution based on particle count in Figure 3.11 shows a change in the number of fines ($<500 \mu\text{m}$) for each of the L/S ratios. It would be expected at the highest water flow rate that there be a decrease in fines and an increase in larger granules. This is not evident from the particle count and again as discussed earlier this could have been affected by the number of images analysed for each experimental run. Figure 3.12 however, shows the expected change in distribution that would be expected from an increase in the L/S ratio, i.e., a decrease in fines and an increase in larger particles. This is because these results are based on volume and not count of particles.

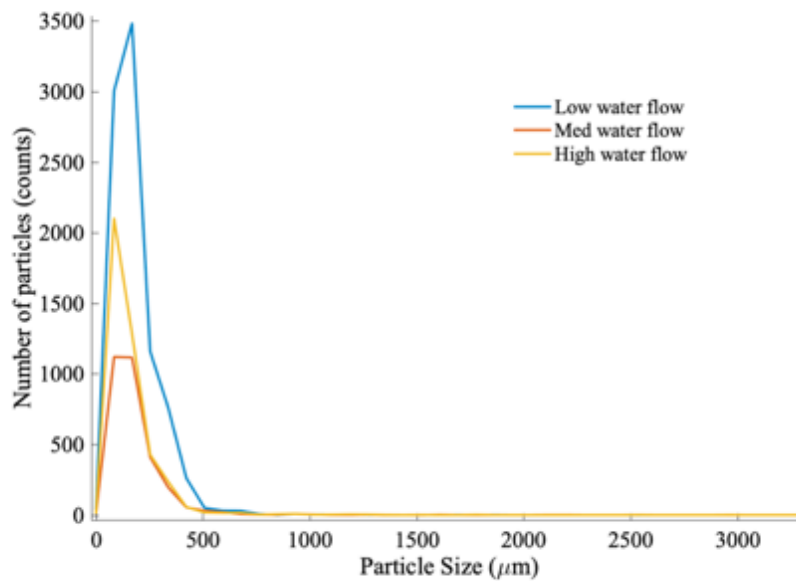


Figure 3.11 Particle size distribution calculated from data taken from 100 images captured on-line by the Eyecon of granulation processes performed at water feed rates of 1.5 (low), 2.0 (medium) and 3.0 mL/min (high).

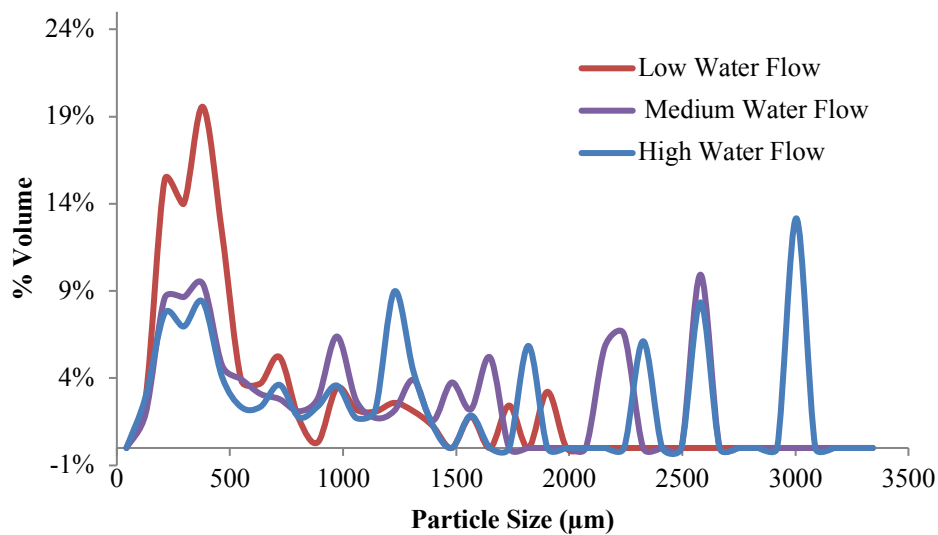


Figure 3.12 Volumetric particle size distribution of granules calculated from data taken from 100 images captured on-line by the Eyecon of granulation processes performed at water feed rates of 1.5, 2.0 and 3.0 ml/min

Figure 3.13 shows the calculated D10, D50 and D90 values. These results show the change in particle size through the D values for each of the different water flow rates. As the liquid content is increased the granule size increases as shown in the increase in D10, D50 and D90 values.

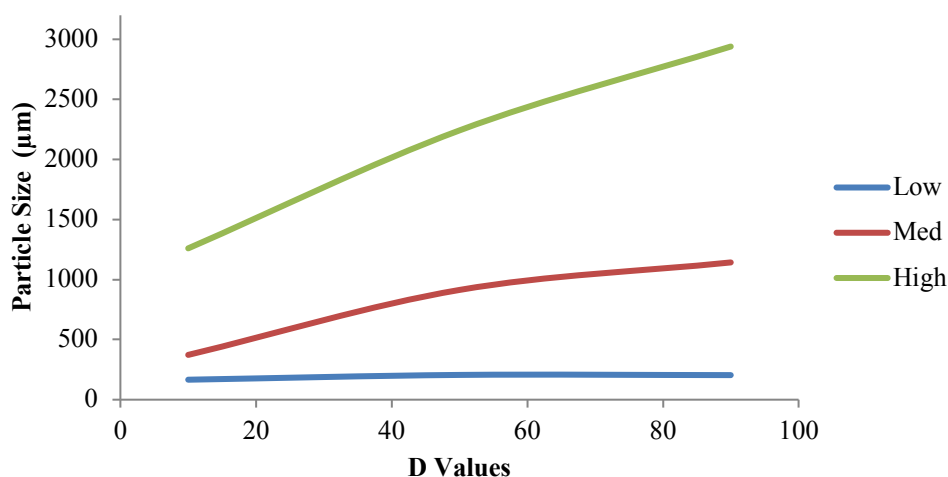


Figure 3.13 D10, D50 and D90 values calculated from data taken from 100 images captured on-line by the Eyecon of granulation processes performed at water feed rates of 1.5 (low), 2.0 (med) and 3.0 (high) ml/min⁻¹.

In the pharmaceutical manufacturing of tablets, the presence of excessive fines can lead to tablet defects such as capping and lamination, however some fines are needed in order to fill the interstitial spaces between the larger particles. The granule size distribution (GSD) will also affect other production processes such as flow and the filling of a tablet die and can also cause unwanted dust, which is not good in good manufacturing (GMP) environments.^{113, 115}

It is thought that the link between a high L/S ratio and large granule size is due to the amount of surface wetting caused by the large liquid distribution. This was the case in a number of studies^{102, 115} but it has been found that the shape of the granules can cause the average granule size to decrease with an increase in L/S ratio.¹¹³ It has been found that there are many factors that can contribute to granule size such as binder addition¹¹⁵ excipient grade e.g. Lactose¹¹⁵ and screw configuration¹⁰⁹ to name a few.

In one study, the number of fines was found to decrease and the distribution narrowed as the water concentration was increased.¹¹⁵ This paper also found that the size distribution of the granules was bimodal and that lumps and ungranulated powder were formed at low water concentrations. As the liquid content was increases, the number of granules increased at the expense of fines and a narrower distribution was observed. These findings are consistent with research conducted by Dhenge et al.¹¹³ One thing to note is that the granule size is also dependent on the screw configuration, formulation and on the binder used. It is also possible, at high L/S ratios, to produce granules that are too large to be used directly for tableting.^{113, 115, 146} The next section looks into the effects of varying more than one parameter on the GSD monitored by dynamic image analysis using the Eyecon.

3.3.3 Design of Experiments: powder feed rate at the centre point 1 kg/h

3.3.3.1 Analysis of on-line images

A number of difficulties were encountered in performing the granulation experiments according to the DoE given in Table 3.5: these are summarised in Table 3.8 below. The Eyecon software crashed a few times during the analysis but each time the system was

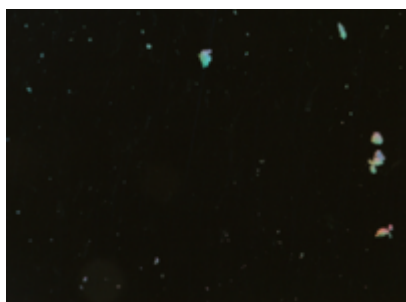
rebooted and the data collected. Experiments 6 and 10 were performed twice with the second experiment labelled 6.2 and 10.2, respectively. The results from the repeat experiments are reported here.

Table 3.8 Observations during the analysis

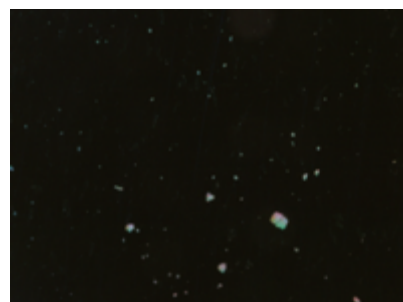
| Experiment No. | Start Time | Stop Time | Notes |
|----------------|------------|-----------|------------------------------|
| 1 | 15:15:59 | 15:21:02 | |
| 2 | 15:24:55 | 15:29:58 | |
| 3 | 15:34:06 | 15:39:14 | Eyecon crashed and fouling |
| 4 | 15:44:36 | 15:49:38 | |
| 5 | 15:53:09 | 15:58:13 | |
| 6 | 16:02:29 | 16:05:14 | Eyecon crashed (excluded) |
| 6.2 | 16:11:48 | 16:17:01 | Eyecon crashed |
| 7 | 16:20:50 | 16:25:58 | |
| 8 | 16:28:58 | 16:33:22 | |
| 9 | 16:37:23 | 16:42:26 | |
| 10 | 16:45:34 | 16:48:29 | Granulator ran out of sample |
| 10.2 | 16:55:07 | 17:00:10 | |

Example images picked at random from each of the experiments are shown in the Figure 3.14 below.

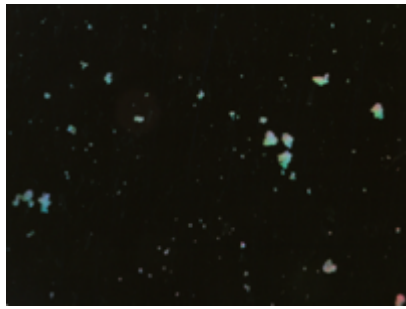
1 a)



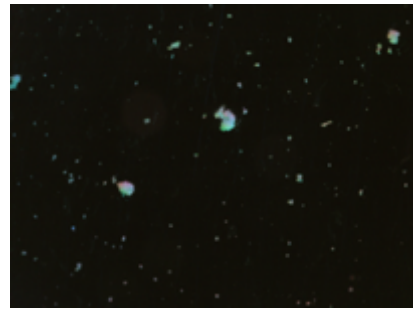
b)



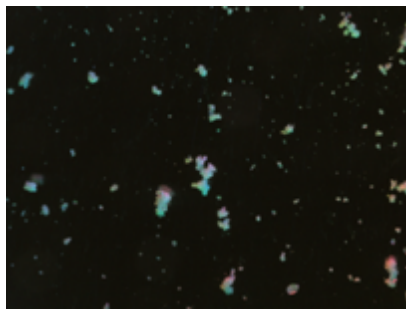
2 a)



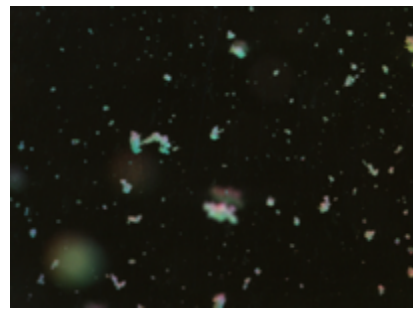
b)



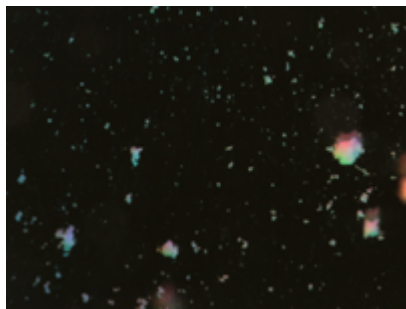
3 a)



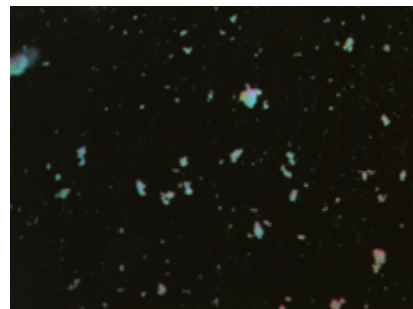
b)



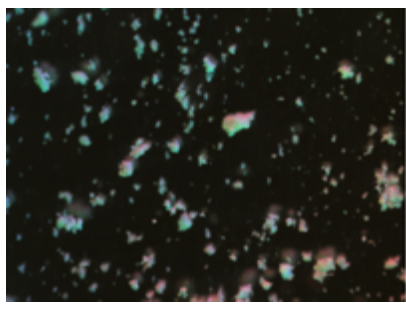
4 a)



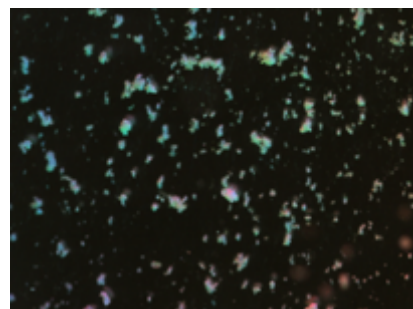
b)



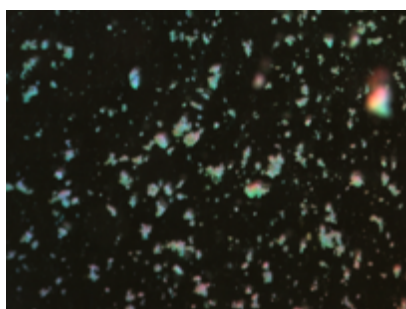
5 a)



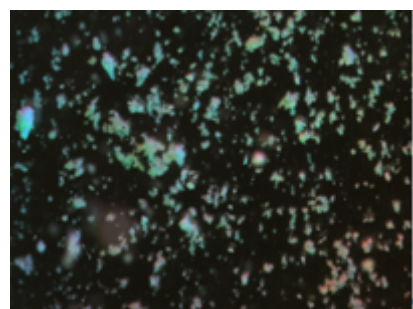
b)



6 a)



b)



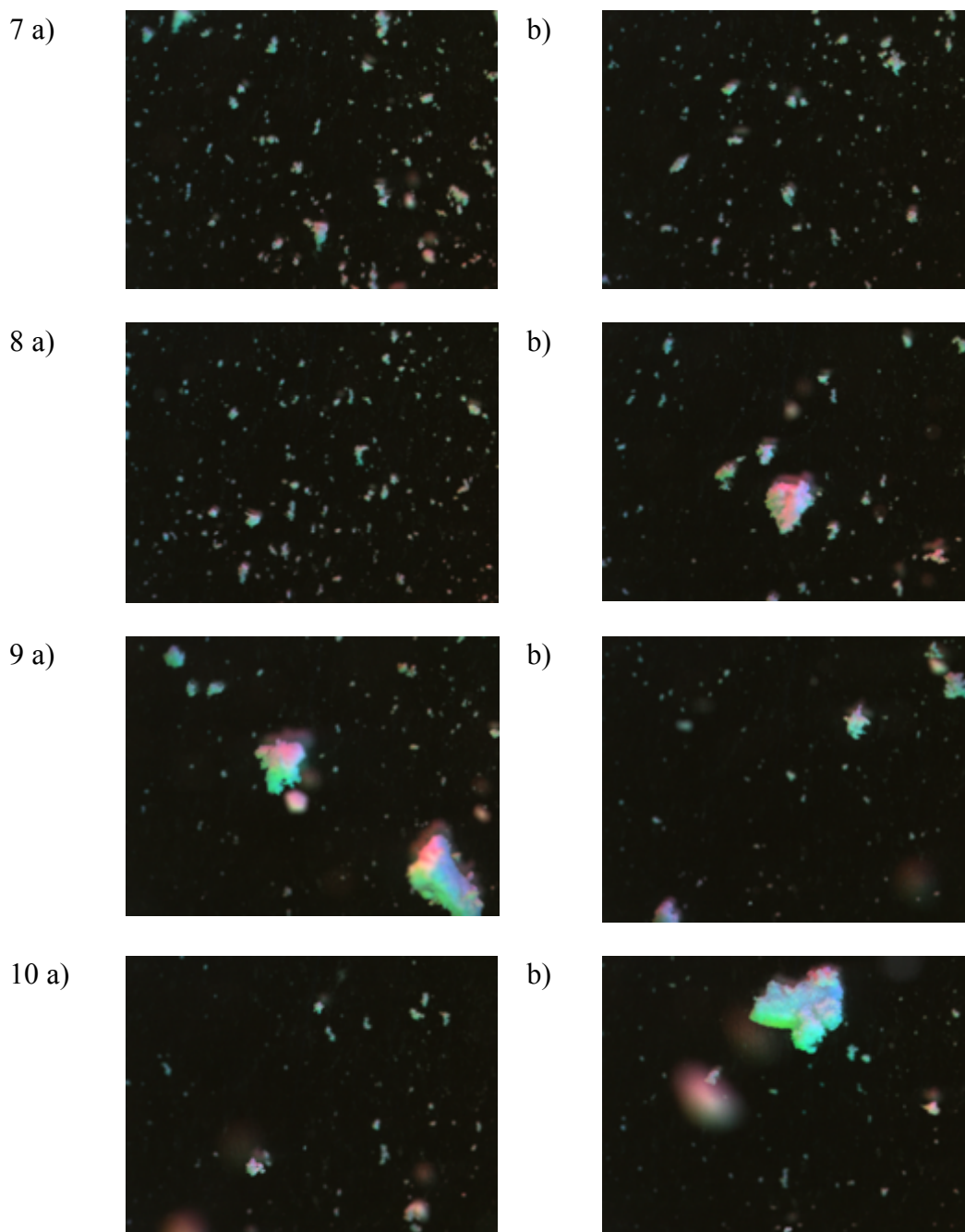


Figure 3.14 Example images all on the same scale taken by the Eyecon from on-line analysis of granules obtained from a DoE with a centre point powder feed rate of 1kg/h. Two images from each experiment are shown and are labelled with the experiment number followed by a) then b).

The particle count was calculated from 100 images from each experimental run, this was done to eliminate any errors due to variations in analysis time. The calculated number of particles is given in Table 3.9. From observation of the images, it is very clear that there is a large variation in the number of particles being analysed, with experiments 5 and 6 showing the largest number of particles and one and ten the least. This is also reflected in the data shown from the particle count.

Table 3.9 Total particle count calculated from 100 images captured by the Eyecon during experiments 1 to 10.

| Experiment | No particles analysed |
|------------|-----------------------|
| 1 | 39601 |
| 2 | 42221 |
| 3 | 50531 |
| 4 | 78839 |
| 5 | 197470 |
| 6 | 104114 |
| 7 | 86640 |
| 8 | 72602 |
| 9 | 45852 |
| 10 | 21550 |

There is a good correlation between the number of particles observed in images 1 – 10 and the number of particles counted during the analysis. The volume weighted D values calculated from the analysis are plotted in Figure 3.15.

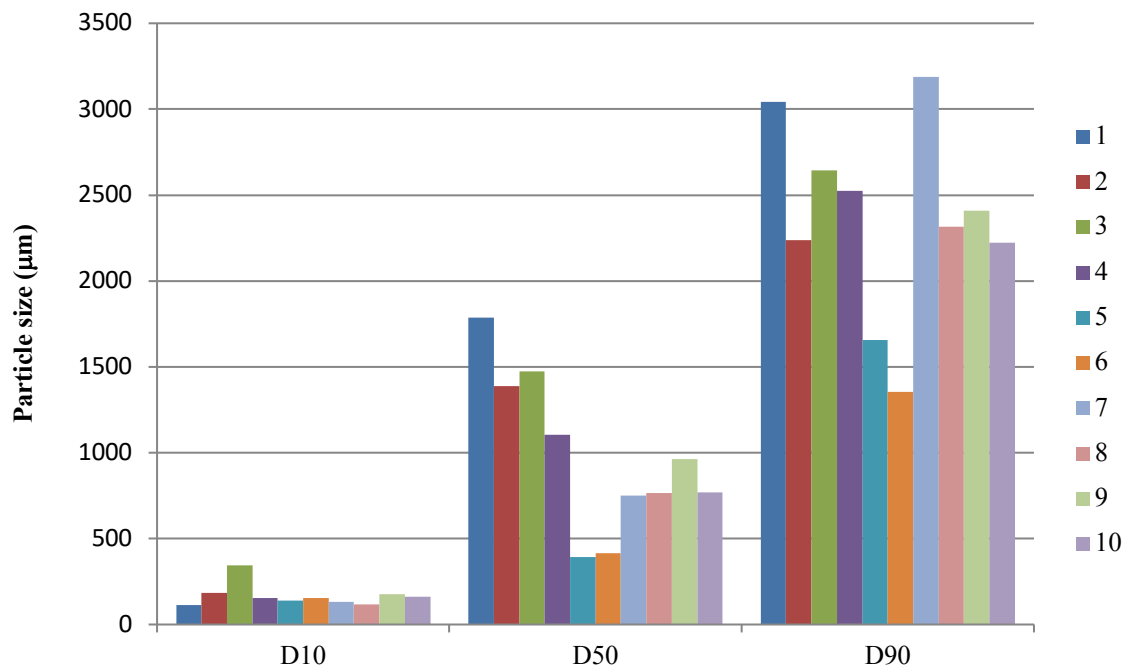


Figure 3.15 A summary of the calculated D10, D50 and D90 values from on-line analysis of granules produced during Experiment 1 to 10 of DoE with feed rate centre point at 1kg/h

The Eyecon software claims to exclude particles that are out of focus and those which lie over the boundaries of the images, so technically it should exclude these some examples of large out of focus granules were observed in some of the images some examples of these are shown in Figure 3.16 with a picture of the fouling observed in Figure 3.17.



Figure 3.16 Three images from the analysis of experiment three. This experiment was run with a screw speed of 100 rpm feed rate of 1200 and a water content of 10 % w/w.

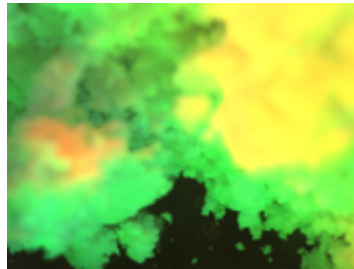


Figure 3.17 Image of the fouling that occurred in experiment three

The screw speed is a critical factor in determining the barrel fill level, and at mid flow limits it has been reported to have a minor effect on the granule properties.^{84, 113} However, at higher and lower barrel feed levels the properties of the granules were found to be determined by barrel fill level.¹¹⁴ A lower screw speed and high powder feed rate content would cause a high level of barrel fill and potentially a peak in the torque, which could cause an increase in the granule size. Experiment three was performed with a relatively low water feed rate; at low water feed rates, there is less liquid to form the liquid bridges to bind the material to form stronger granules. TSG has the advantage of still being able to granulate at lower L/S concentrations in comparison to other wet granulation techniques.^{84, 99, 146}

Figure 3.18 shows the volume weighted distributions for all of the experimental runs. It is very hard to get clear information out of this as there are such a broad range of granules through the distributions. However some information can be retrieved, the plot shows

that experiments 5 and 6 have a high volume of fines which correlates with the images from these experiments shown in Figure 3.14 (images no 5 and 6 a) and b)). It also shows that there might have been some granules produced outside the limits of detection as there is a clear cut off at 3500 μm .

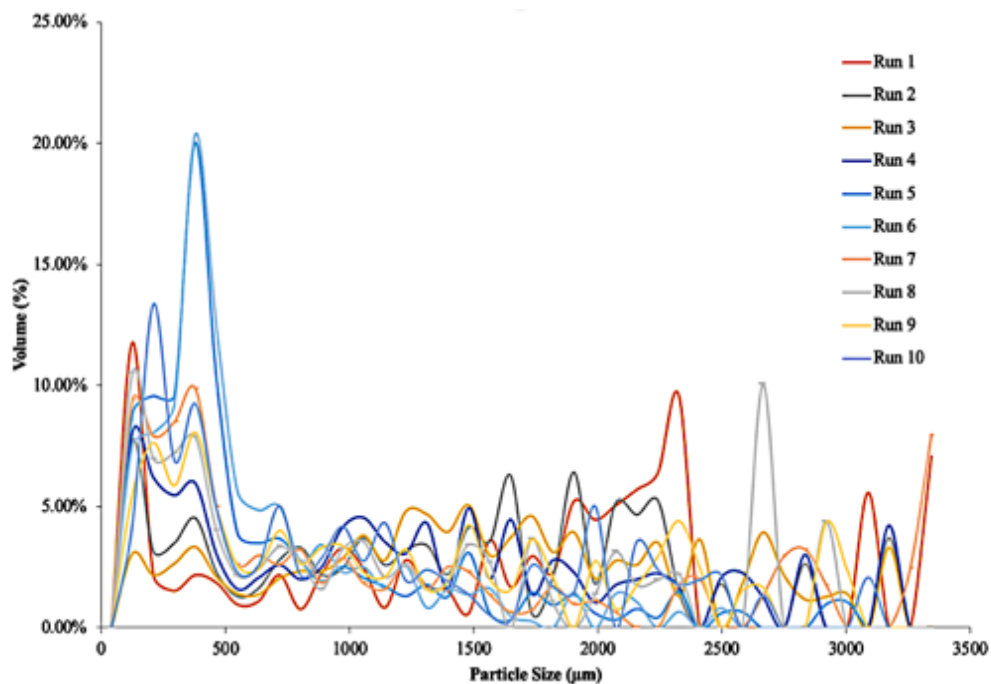


Figure 3.18 Volume weighted particle size distribution of granules produced during Experiments 1 to 10 of DoE with a feed rate centre point at 1kg/h.

Although it is hard to get clear information from the volume weighted distributions when there are multiple experiments it is good to be able to look at the range of data produced from the Eyecon as each builds a picture of what is going on in the experiment. Some example images of larger granules are shown in Figure 3.19.

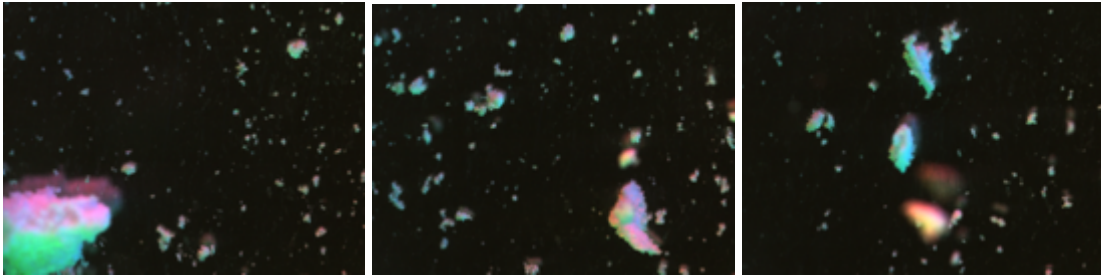


Figure 3.19 Examples of large particles from experiments with large D90 values that may skew the results.

These images were left in the analysis as the idea was to be able to analyse in real time to apply to a continuous manufacturing process, the software doesn't offer any image pre-processing so these images would have to have been removed manually after the experiments had been run.

3.3.3.2 Analysis of on-line image data using MODDE software

The main effects and interactions were calculated from the D values in Table 3.11 and are shown in Figure 3.11.

Table 3.10 D values taken from images captured by the Eyecon image analyser rounded to the nearest significant figure

| Number | D10 | D50 | D90 |
|--------|--------|---------|---------|
| 1 | 562.81 | 1256.82 | 1987.44 |
| 2 | 385.60 | 1064.46 | 1635.86 |
| 3 | 371.48 | 971.55 | 1546.99 |
| 4 | 482.66 | 1067.89 | 1604.19 |
| 5 | 118.03 | 480.59 | 1708.55 |
| 6 | 127.06 | 444.67 | 1929.14 |
| 7 | 140.17 | 606.35 | 1836.74 |
| 8 | 241.33 | 839.15 | 1476.33 |
| 9 | 365.92 | 1102.36 | 1543.22 |
| 10 | 371.48 | 971.55 | 1546.99 |

Table 3.11 Calculated main effects and interactions for the response values D10, D50 and D90

| Factor | Term | D10 | D50 | D90 |
|------------------|--------|--------|---------|---------|
| Screw Speed | X1 | 96.52 | 106.65 | -42.11 |
| Feed Rate | X2 | -59.06 | -167.82 | -37.82 |
| Water Content | X3 | 292.60 | 530.19 | -45.01 |
| Screw*Feed | X1X2 | -42.66 | -105.93 | -37.70 |
| Screw*Water | X1X3 | 50.46 | -27.71 | 248.39 |
| Feed*water | X2X3 | 9.15 | 92.30 | -200.13 |
| Screw*Feed*Water | X1X2X3 | 12.43 | -7.49 | -107.61 |

A summary of the model fit based on the D10, D50 and D90 response values is shown in Figure 3.20. The summary of fit shows the R^2 value, which is a statistical measure that represents the proportion of variability in the response explained by the model. Q^2 is an estimate of the future prediction precision; if this value is significant it should be greater than 0.1 as in D10, a value greater than 0.5 shows a good Q^2 as in the D50 results.

For a good model, R^2 and Q^2 should have a difference of less than 0.3.¹⁴⁷ It is apparent from Figure 3.20 that the model fit is best for the D50 value, which is a metric that is commonly used to represent the size of particles and will be done so in this analysis. The model validity is a test of the diverse model problems, in the case of this model the D50 shows the best R^2 , Q^2 and model validity. It also has a good reproducibility score (although lower than that observed for the D10 and D90 models) and so overall, the model fit based on D50 is the best. During the experiments it was noted that the larger particles were sometimes bouncing out of the field of view. This may have had an effect on the data obtained for larger particles and could explain the poor fit of the D90 model. In order to find a solution to the interfacing and segregation of particles the sample chute a plastic barrier was cut to size and placed into the top of the Eyecon™ window in an attempt to prevent granules from bouncing past the analytical window. A protective screen to prevent particles escaping was put into place for further experiments. An image of the barrier in place is shown in Figure 3.21.

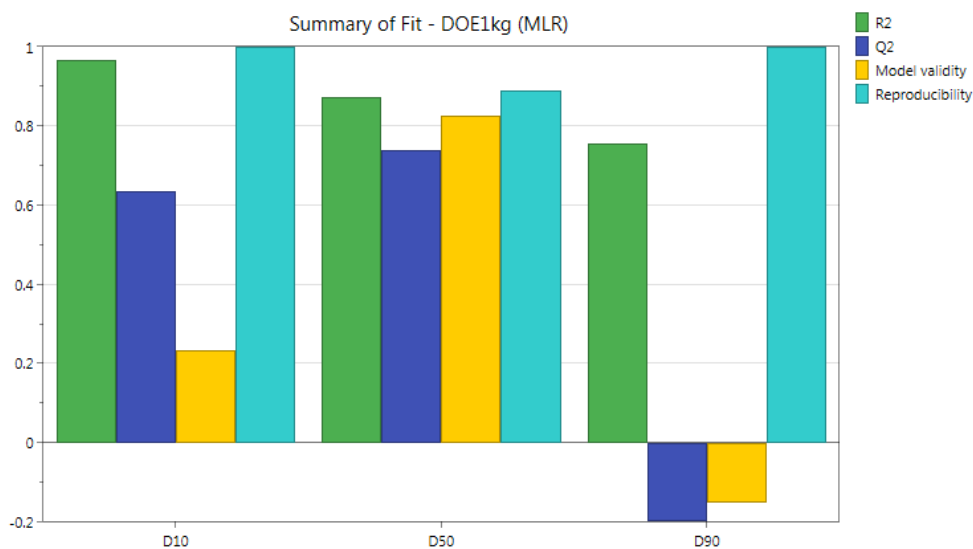


Figure 3.20 Summary of fit for D10, D50 and D90 values extracted from the analysis of images taken during TSG process using Eyecon image analyser.

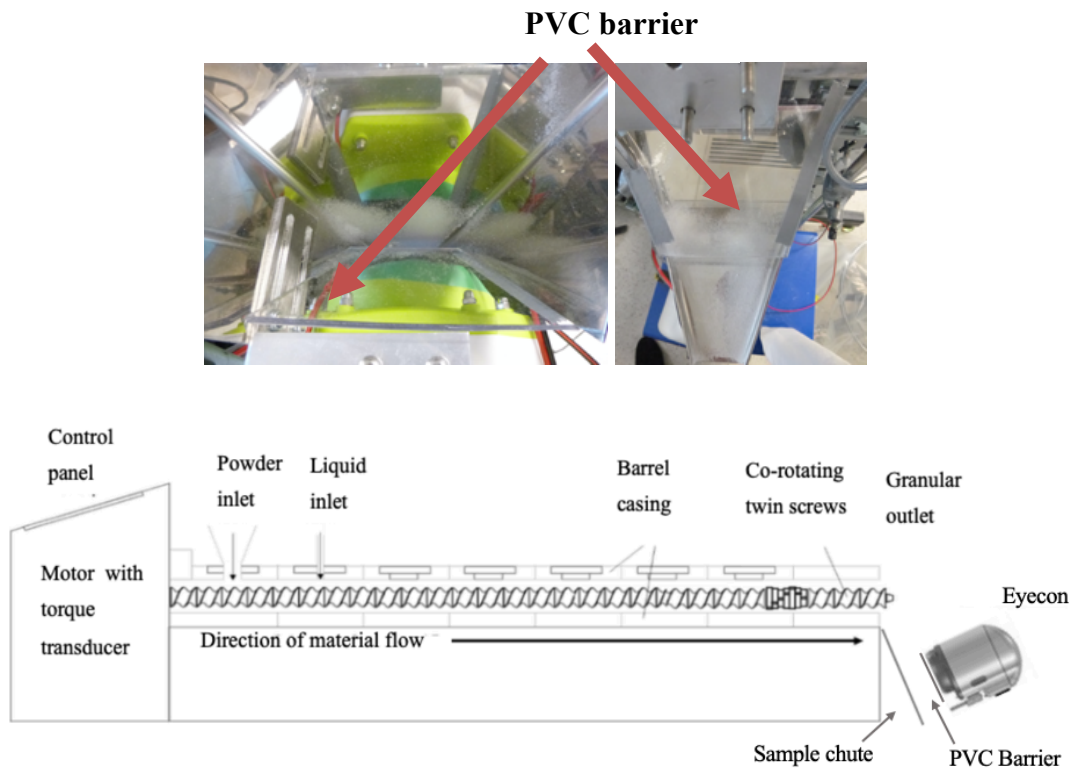


Figure 3.21 Picture showing the sample shoot from above (left) and looking at the front (right) of a PVC barrier that was put into place to stop the escape of large particles. Along with a schematic of barrier placement

Figure 3.22 shows the calculated coefficients for the main effects and interactions obtained using the D50 values from on-line image analysis of granules. The coefficient plots display the coefficients, when changing from 0 to high, for the selected response with the confidence interval as error bars. Therefore, it can be taken that the significance of the model coefficients is indicated by the error bars as shown in the figure, was used for tuning of the model. It can be seen that water concentration has the biggest impact on the D50 of the granules obtained, with an increase in water content from 10 to 20% w/w resulting in an increase in the size of granules produced. Screw speed and feed rate have much smaller influences on granule size and according to the coefficient plot are 8er5feed

rate from 1200 to 800 g/h causes an increase in particle size. Screw speed has the smallest influence on the granule size, with a small increase in granule size observed when the screw speed is increased from 100 to 200 rpm. The interaction terms show that a reduction in both screw speed and feed rate will have a negative effect on the granule size whereas an increase in feed rate and water content will have a positive effect. However, the interaction terms are insignificant and therefore these effects will be minor. The interaction between water and screw speed is negligible. As the interaction terms were deemed to be statistically insignificant in the model, the model was recalculated using only the main effect terms with the coefficients obtained shown in Figure 3.23.

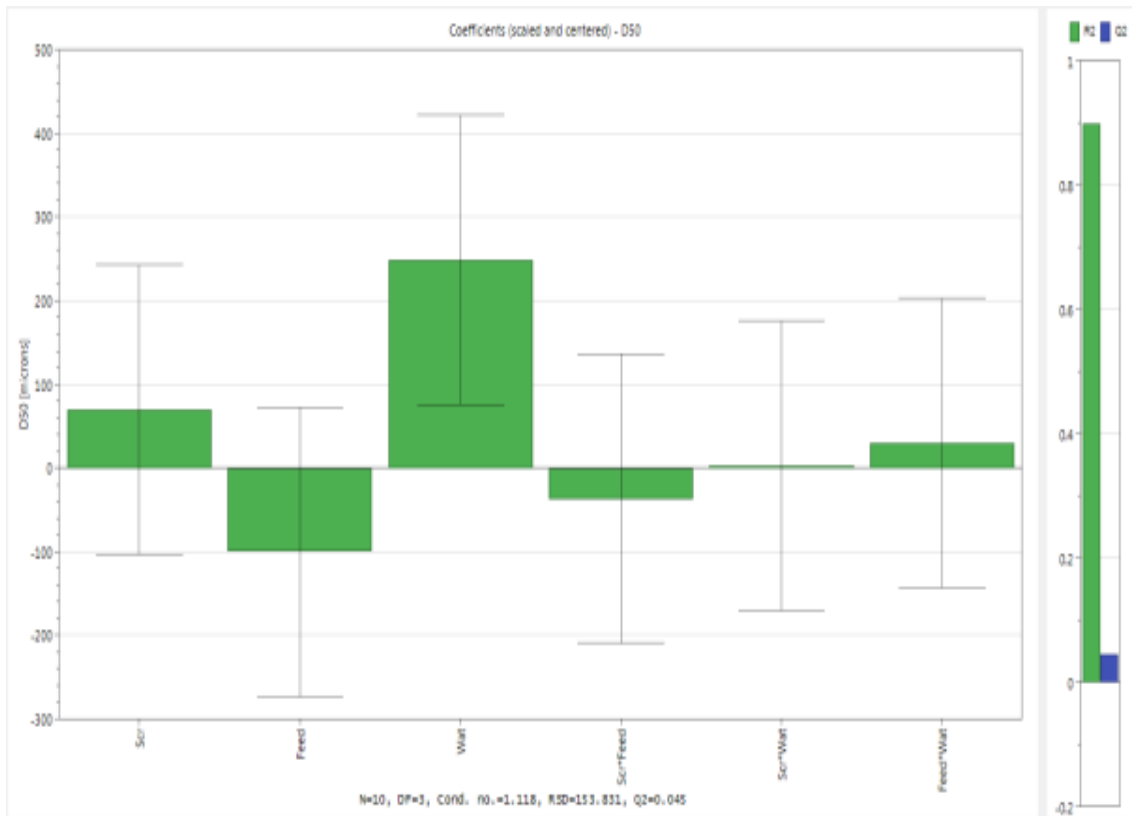


Figure 3.22 Coefficients calculated from the D 50 values calculated from Eyecon images taken from on-line analysis of granules during a DoE investigating the effect of screw speed, powder feed and water content on granule size.

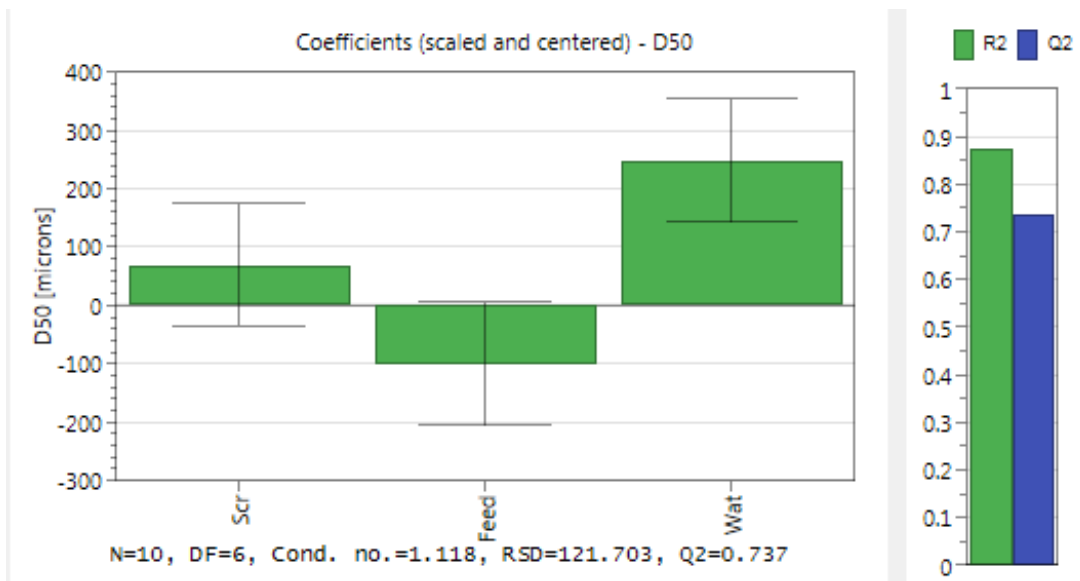


Figure 3.23 Model containing the main effects: screw speed, water content and feed rate calculated from the D50 value of granules produced by a TSG process for a DoE labelled DoE 1kg.

In doing this, a much higher Q^2 value was achieved and the model fits the data much better. A 4D contour plot (Figure 3.24) of water content, feed rate and screw speed show that to obtain larger particles at screw speeds of 100, 150 and 200 rpm, a high-water content and a lower feed rate is required and that the largest granules are produced at a screw speed of 200 rpm. These results are consistent with those found in the literature,^{102, 148, 149} the theory behind this is that as the ratio of water to powder increases, more wetting of the granulation powder occurs. The extra moisture allows for a big wet mass of nuclei which then consolidates, coalesces and finally breaks into granules. If there is too much water, a slush is formed; if there is too little water present, no granulation occurs.

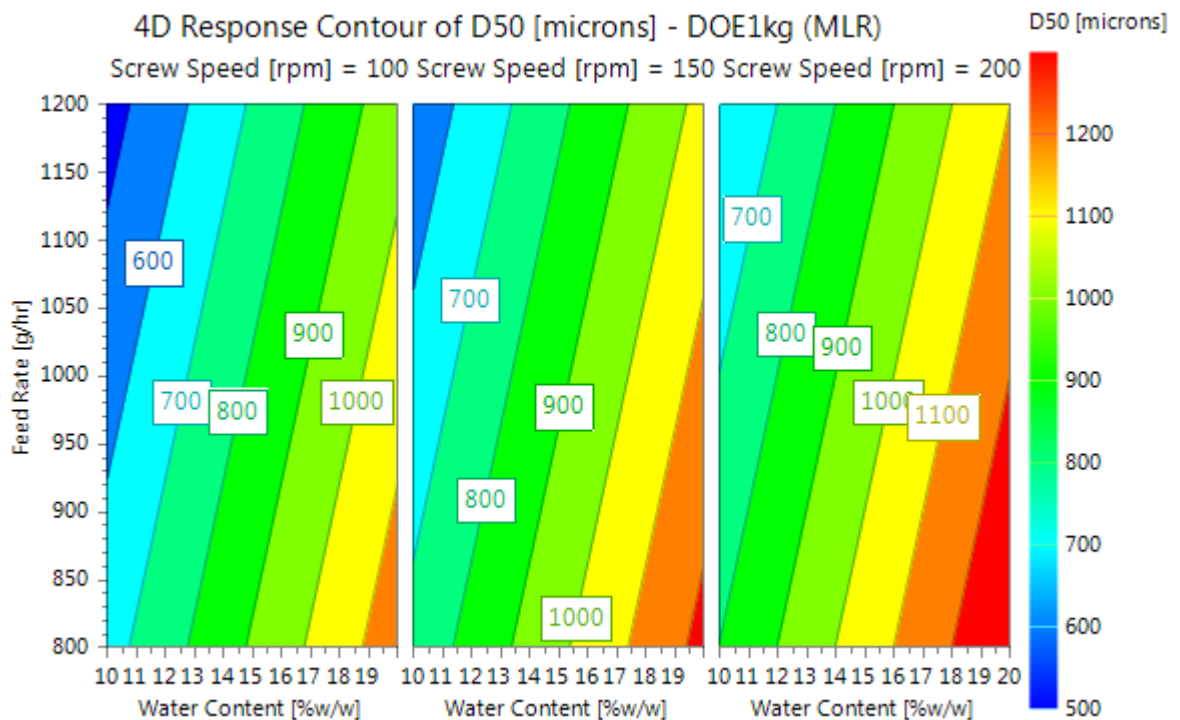


Figure 3.24 4D contour plot of the effect of screw speed, water content and feed rate on the granule size from on-line analysis of granules produced in a twin-screw granulation process.

The effect of powder feed rate on the granule size is minor in this case, which could be due to the low powder feed rates of the granulator. The 16 mm TSG can operate at powder feed rates of up to 20 kg/h. The extent of fill of the granulator barrel depends on three factors: screw and barrel geometry, screw speed and powder feed rate.¹⁵⁰ The higher the fill rate, the denser the powder and hence the compaction level increases in the barrel. Torque is thought to be a good indication of barrel fill level,^{114,151} but unfortunately it was not possible to monitor this parameter in this study. In contrast to the results obtained here, Djuric et al.¹⁴⁹ found that the median granule size increased with increased powder feed but this could be due to a difference in screw configuration. Keleb⁸⁴ used one way

ANOVA to analyse the effect of water concentration, feed rate and screw speed on granule properties, and found that the screw speed (200 – 450 rpm) and feed rate (5.5 - 9.5 kg/h) had no significant effect on granule properties in a twin screw granulation process.

3.3.3.3 Off-line Analysis of Granules with Eyecon Image analyser

As a conformational analysis for the experiments, samples were analysed off-line with the Eyecon. The D values were calculated and plotted in Figure 3.25.

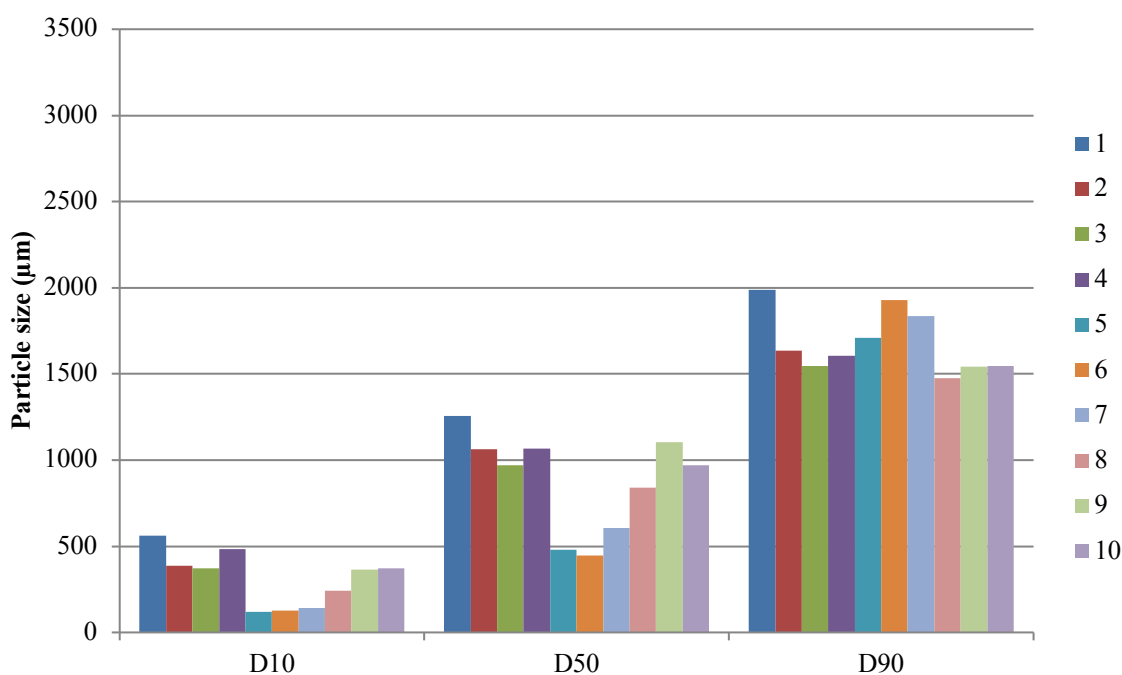


Figure 3.25 A summary of the calculated D10, D50 and D90 values from off-line analysis of granules collected from experiments 1 to 10 in the design of experiments with feed rate centre point at 1kg/h

The trends in D10 and D 90 are very different for the on and off-line results. It is thought that this could be due to the software over estimating the number or volume of large particles present from the images; this could also be due to the number of particles analysed off-line in comparison to on-line. A study by Sayin et al. into the use of the Eyecon for analysis of granules on a smaller 11 mm TSG found that the size parameter and particle count were much more reliable than the D values for analysis due to the inherent variability during analysis, even when the process was in steady state. ⁷⁵

Data captured from off-line image analysis of granules collected from the experiments in section 3.3.3.1 are listed in Table 3.12.

Table 3.12 D values from off-line Eyecon analysis

| Experiment Number | D10 | D50 | D90 |
|-------------------|-----|------|------|
| 1 | 133 | 749 | 3187 |
| 2 | 123 | 914 | 2618 |
| 3 | 153 | 413 | 1355 |
| 4 | 137 | 397 | 1705 |
| 5 | 186 | 1387 | 2237 |
| 6 | 114 | 1786 | 3044 |
| 7 | 349 | 1468 | 2651 |
| 8 | 153 | 1103 | 2524 |
| 9 | 177 | 964 | 2407 |
| 10 | 163 | 769 | 2223 |

Figure 3.26 shows the coefficients from a model based on the D50 values obtained from off-line analysis of samples of the granules showing the main effects from the analysis.

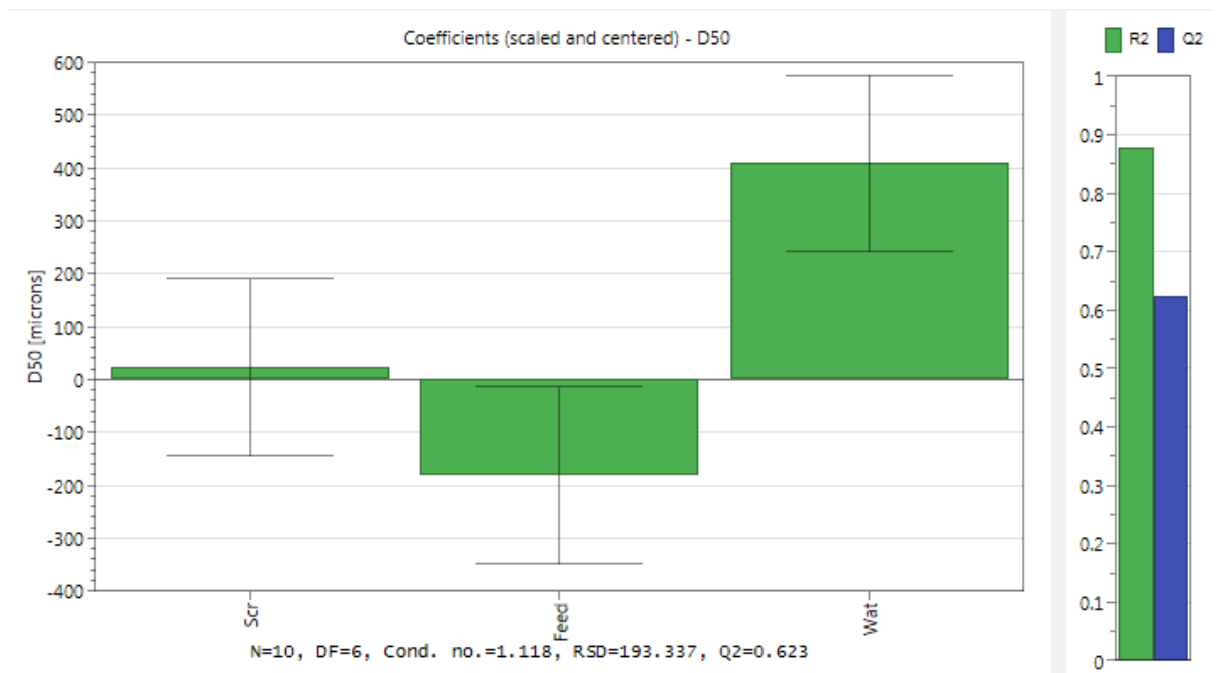


Figure 3.26 Coefficients for the main effects during off-line analysis of granules produced by TSG for a DOE investigating the effect of screw speed, feed rate and water content on granule size distribution.

In terms of coefficients, the error bars from the on-line analysis are very similar to those for off-line analysis. Both of the models predict that water is the most significant term and that screw speed and feed rate still have a slight effect on the D50 (median) granule size. An overlay of the D50 results from both on- and off-line analysis of the granules (Figure 3.27) shows good agreement of the D50 values obtained for experiments 4 to 10, with poorer agreement observed in experiments 1 to 3. This could be due to the granules being dried overnight before being analysed off-line. It may also have something to do with analysis of larger granule sizes and the imaging technique.

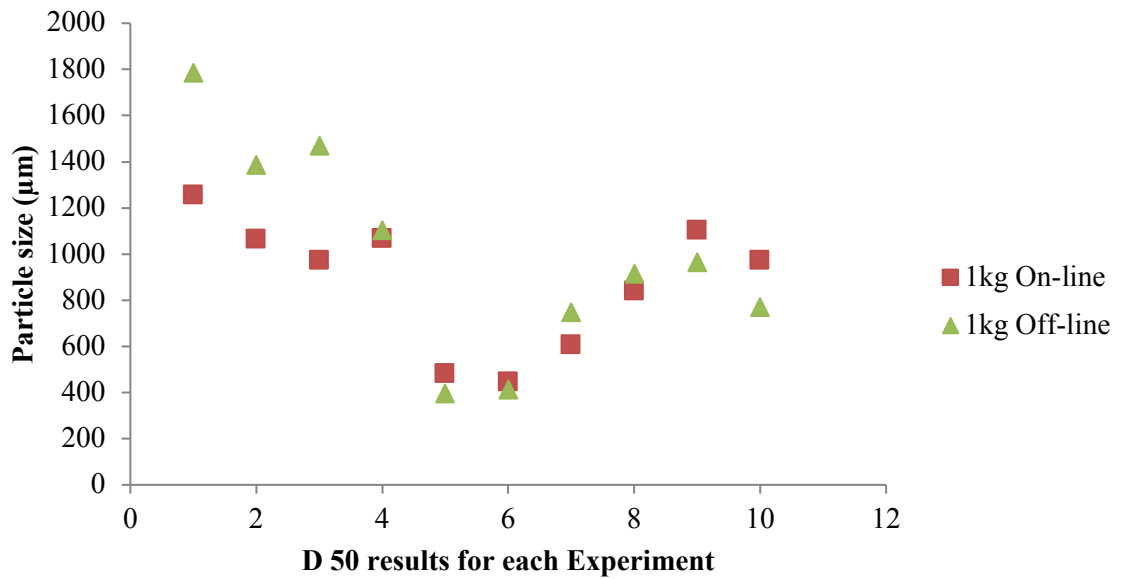


Figure 3.27 Overlay of the D50 results taken from both on and off-line analysis of granules produced by twin screw granulation for a design of experiments investigation for feed rates up to 1kg/h.

Example off-line images of the granules produced in experiments with the largest (experiment 6) and the smallest (experiment 4) D50 values are plotted in Figure 3.28. The corresponding size distribution plots are shown in Figure 3.29. As the D50 value increases there appears to be a decrease in the size of granules in the range 250 – 600 µm and an increase in the size of granules between 1800 and 2400 µm with an increase in the number of fines.

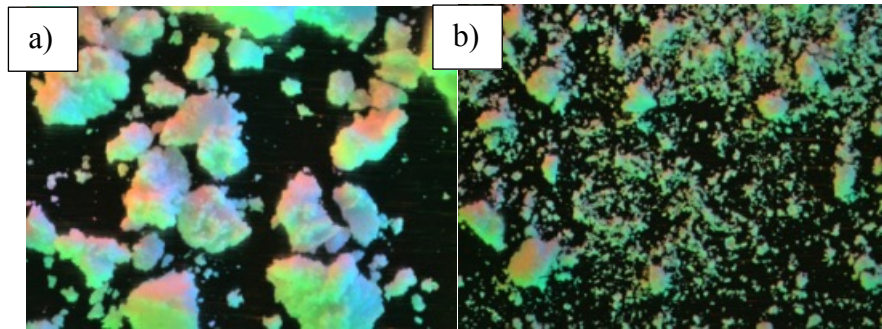


Figure 3.28 Images taken from dried granules collected from experiments a) 6 where the largest D50 values were observed and b) 4 where the smallest D50 values were observed.

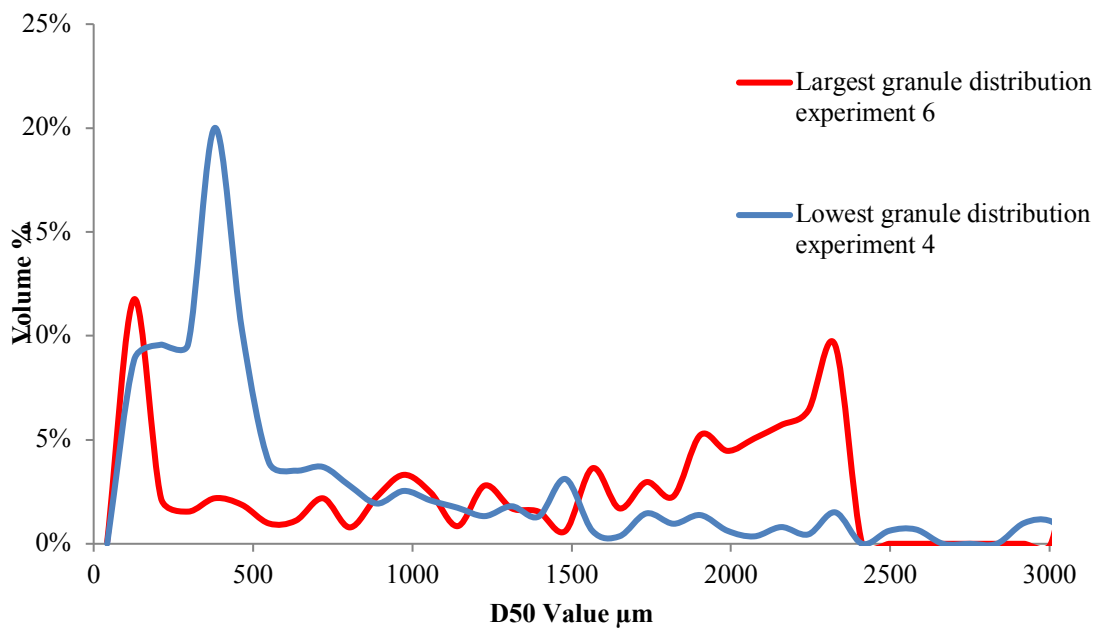


Figure 3.29 Overlay of the D50 values taken from experiments 4 – lowest D50 values produced for the experiment and 6 – highest D50 values produced. (The parameters set for experiment 4 were: screw speed 200 rpm, powder feed rate 1200 g/h and a water content of 10 %w/w while experiment 6's were: screw speed 200 rpm, powder feed rate 800 g/h and water content 20 % w/w)

El Hagrasy¹¹⁵ reported that different grades of lactose showed similar growth behaviour occurs at different L/S ratios and granule size analysis demonstrated a bimodal distribution for all the formulation grades with the presence of lumps and un-granulated fines even at the lowest L/S concentration. However, the number of fines decreased and the distribution narrowed as the L/S ratio increased. The presence of fines was thought to be due to poor liquid distribution inside the granulator. The same study found that the addition of the binder to the liquid instead of as a solid form helped to decrease the number of resulting fines.

Section 3.3.4 further studies the effects of process parameters on the granule size distributions. This study looks at much higher throughput rates in order to try and simulate feed rates more typical of industrial processes and to further test the abilities of the Eyecon to be able to capture data at higher throughputs.

3.3.4 Design of Experiments: powder feed rate at the centre point 3 kg/h

Higher powder feed rates were explored as these are more typical of industrial granulation processes. The main effects and interactions calculated from the D10, D50 and D90 values given in Table 3.13 are shown in Table 3.14

Table 3.13 D values taken from images captured by the Eyecon image analyser during 3 kg/h study rounded to the nearest significant figure

| Experiment Number | D10 | D50 | D90 |
|-------------------|--------|---------|---------|
| 1 | 133.17 | 748.69 | 3187.3 |
| 2 | 122.78 | 914.05 | 2618.17 |
| 3 | 152.86 | 413.23 | 1354.94 |
| 4 | 137.14 | 396.84 | 1705.09 |
| 5 | 185.79 | 1386.53 | 2236.84 |
| 6 | 113.57 | 1786.33 | 3044.29 |
| 7 | 349.31 | 1468.10 | 2651.21 |
| 8 | 153.19 | 1102.8 | 2523.95 |
| 9 | 176.63 | 964.18 | 2407.34 |
| 10 | 163.00 | 769.17 | 2223.41 |

Table 3.14 Calculation of the main effects and interactions for DOE 3kg for D10, D50 and D90 results calculated from on-line image analysis using an Eyecon image analyser.

| Factor | Term | D10 | D50 | D90 |
|------------------|--------|---------|---------|---------|
| Screw Speed | X1 | 12.07 | -11.08 | 66.03 |
| Feed Rate | X2 | -152.71 | -592.50 | -723.04 |
| Water Content | X3 | 74.71 | 411.01 | 352.92 |
| Screw*Feed | X1X2 | -15.12 | 3.04 | -207.02 |
| Screw*Water | X1X3 | 18.88 | 104.47 | 200.28 |
| Feed*water | X2X3 | -12.53 | 97.24 | 275.97 |
| Screw*Feed*Water | X1X2X3 | -38.74 | -119.64 | 194.56 |

The bar plots of the main effects and interactions in Figure 3.30 and the dominant main effects Figure 3.31 shows that the effect of powder feed rate is the dominant effect for

D50 results although it is not significant, a decrease in feed rate shows an increase in D50 of the granules. Water concentration however has a positive effect on the D50 value whilst the effect of screw speed appears negligible. The interactions between the factors are minor and insignificant with the greatest interaction existing between the screw speed and water content which is positive. The main interaction for this DoE is the effect of feed rate on the granule size. Large granules are produced at low feed rates and high-water contents irrelevant of screw speeds between 100 and 500 rpm.

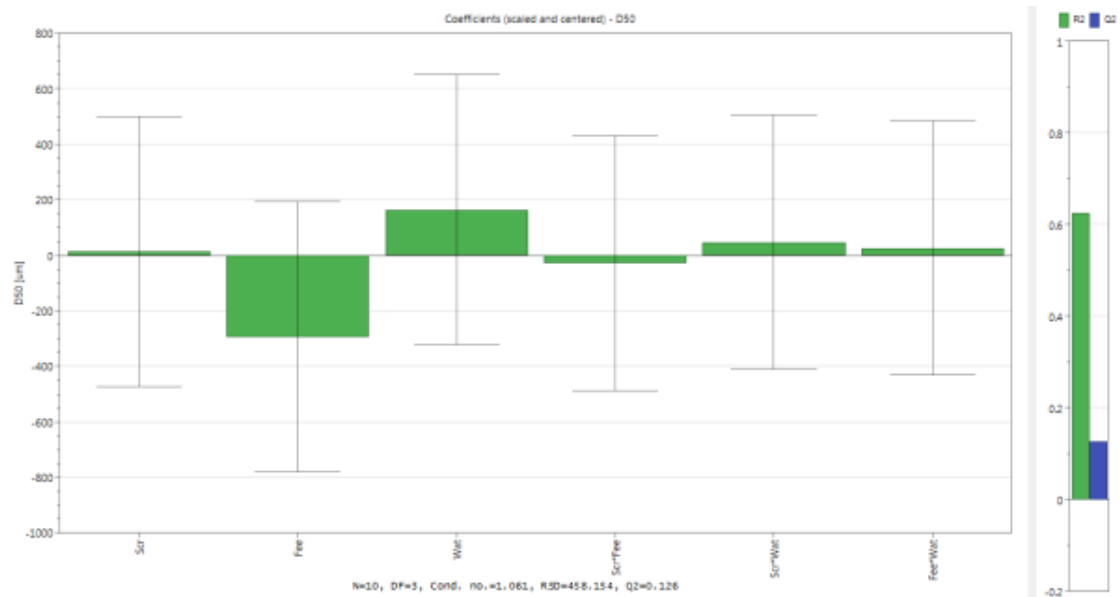


Figure 3.30 MODDE Coefficients plot of the main effects and interactions between the factors for a DoE for the D50 results obtained in-line by Eyecon image analysis.

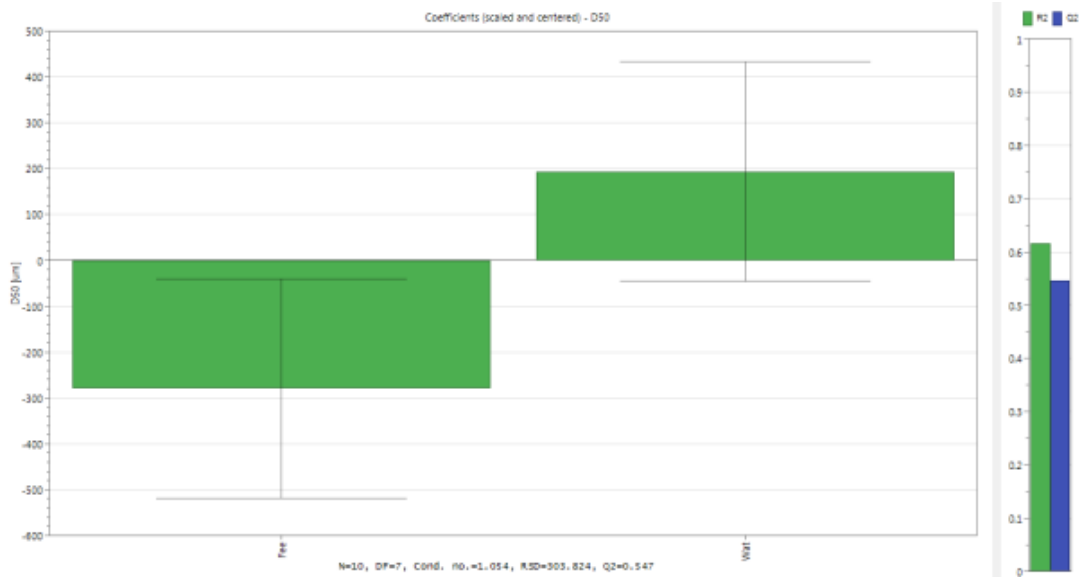


Figure 3.31 Main effects for 3kg DoE results for the D50 values obtained by Eyecon image analysis from a TSG process.

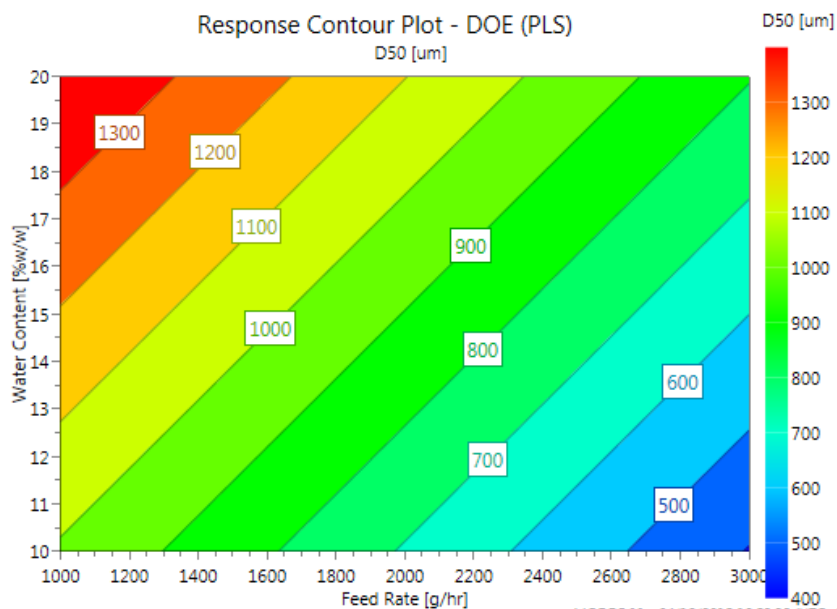


Figure 3.32 Contour plot of powder feed rate vs water concentration for the D50 values obtained during a DoE of with feed rates of up to 3 kg/h.

A comparison of the results produced from the two DoE experiments, that of the lower powder feed rates (800 - 1200 g/h) and screw speeds (100 - 200rpm) with that of higher powder feed rates (1000 - 3000 g/h) and screw speeds (100 - 500 rpm), show differences in that water does not appear to have as much of an effect on the granule size for powder feed rates between 1000 and 3000 g/h as it does for those between 800 and 1200 g/h. Feed rate however has more of an effect although according to the model this is not significant. There are many theories as to why an increase in powder feed rate may cause a reduction in particle size, Dhenge et al ¹¹⁴ suggested that a higher fill level at higher feed rates leaves less room in the barrel for individual particle movement due to the close packing of particles, leading to an increase torque and a decrease in residence time. Lower feed rates (2 kg/h) produced a bimodal distribution of larger granules while higher feed rates >2 kg/h showed more monomodal distributions which narrowed with increasing feed rate.

3.4 Conclusions

3.4.1 Off-line analysis

Sample presentation was very important so as to form a monolayer with minimal overlap. The physical analysis of movement of the sample stage through the twenty-five-stage pattern took a bit of getting used to but with practice this improved and so care must be taken in order to stay in sequence and not step out of sample position which was easy to do. There was also the issue of representative sampling, when sampling for off-line analysis samples should be passed through a riffler or other separating method.

3.4.2 On-line analysis

Both on-line and off-line analysis of granules produced during TSG processes performed using the parameters in the first DoE, (feed rates 800 - 1200 g/h), show good agreement in terms of the D50 results. There is also a correlation between the main effects and interactions of different factors on the D50 values of the granules calculated from on and off-line image analysis. This demonstrates the ability of the Eyecon for on-line analysis despite the dense flow of particles from the granulator. The results show that water concentration during granulation is the dominant factor when it comes to the effect on granule size, screw speed and powder feed rate are insignificant and there is almost no effect from any interactions. The largest granules are produced at screw speeds of 200 rpm, at low powder feed rates, 800 g/h and at a water content of 20%w/w, these settings also produced a large number of fines. The smallest granules were produced at screw speeds of 200 rpm, powder feed rates of 800 g/h and water content of 10%w/w. It is thought that screw speed and feed rate had little effect due to the level of barrel fill and compaction within the granulator. Eyecon images proved to be a useful tool for visualizing whether sufficient number of granules were produced or not and allow for easier determination of optimization of parameters.

Overall the Eyecon proved to be a useful tool for both off and on-line analysis of physical properties of granules at feed rates of 1 kg/h. The data obtained from the analysis was able to provide information on size and volume of granules produced and the D values were an easy way to look at the trends in the data. However, at 3 kg/h feed rates more relevant to industrial processing the Eyecon struggled to analyse granules without issues of fouling of the analytical window.

Chapter 4

Dynamic Image Analysis Industrial Scale Study of Twin Screw Granulation

4. Dynamic Image Analysis Industrial Scale Study of Twin Screw

Granulation

4.1 Introduction

An experiment was set up to investigate the ability of the Eyecon to monitor a twin-screw granulation process over an elongated period of time at steady state. It is important to ensure that the PAT can generate reliable results over a long period especially for a continuous process as prolonged analysis relates more to an industrial setting where processes are run continuously for long periods of time. A process perturbation was then put in place to assess the ability of the PAT to detect a response. This experiment was then repeated with two different screw configurations, each with their own formulation, the torque produced was measured for both experiments and the results of the experiments were compared.

It is known that when the screw speed of the granulator is reduced the speed at which the powder is conveyed down the barrel is reduced. This causes an increase in barrel fill level resulting in an increase in torque. It is thought that the increase in torque is related to particle size. The following studies investigate the connection between torque, screw speed and the size of granules produced. Two different screw configurations were used, one was known to cause high shear and the other low shear; each should have a different effect on the torque produced and therefore potentially the granule size. Two formulations were also used throughout these experiments to look at the effect on granules produced. This chapter also looks into two novel techniques for the resolution of fouling issues caused at high granulation powder feed rates.

The main aims of this chapter are:

- To test the Eyecon image analyser to detect process perturbations during long process times and high throughput
- To determine if the Eyecon would be able to be implemented for industrial analysis

4.2 Experimental

4.2.1 Materials

Formulations

Two formulations were used throughout this chapter. These are labelled formulation A and Formulation B and are found in Table 4.1 and Table 4.2. The formulations were blended using a Turbular blender at 34 rpm for 10 minutes in batches of 700 g.

Table 4.1 Powder blend formulation A

| Material | Function | MSDS CAS Number | Formula (%w/w) |
|---|-----------------|------------------------|-----------------------|
| Lactose Monohydrate (Pharmatose 200M) | Filler | 64044-51-5 | 73.5 |
| Microcrystalline cellulose (Avicel PH101) | Filler | 9004-34-6 | 20.0 |
| Hypromellose 2910 (Pharmacoat 603) | Binder | 9004-65-3 | 5.0 |
| Croscarmellose sodium (Ac-Di-Sol) | Disintegrant | 74811-65-7 | 1.5 |
| Water | Liquid Binder | | 17.5 |

Table 4.2 Powder blend formulation B

| Material | Function | MSDS CAS Num- ber | Formula (%w/w) |
|---|-----------------|----------------------------------|---------------------------|
| Lactose Monohydrate (Pharmatose 200M) | Filler | 64044-51-5 | 51.0 |
| Microcrystalline cellulose (Avicel PH101) | Filler | 9004-34-6 | 40.0 |
| Hypromellose 2910 (Pharmacoat 603) | Binder | 9004-65-3 | 5.0 |
| Croscarmellose sodium (Ac-Di-Sol) | Disintegrant | 74811-65-7 | 4.0 |
| Water | Liquid Binder | | 32.5 |

4.2.2 Equipment

4.2.2.1 Granulator set up

The same twin-screw granulation set up was used as in section 2.2.1.1 in the previous chapter (figure 2.1). Raman spectroscopy was implemented into the first experiment as an attempt to try and obtain some chemical information from the granules coming directly out of the granulator twin screw heads. Unfortunately, the Raman analysis was unsuccessful, details of these experiments can be found in Appendix B.

4.2.2.2 Screw Configuration

The following screw configurations were used throughout the experiments, these have been labelled Configuration A (low shear) and B (high shear). The set ups for both are listed in Table 4.3 and Table 4.5.

Table 4.3 Screw configuration A (low shear)

| Number | Type & Description |
|--------|----------------------------|
| 9 | 1D conveyors |
| 7 | 0.25 bilobes at 60 degrees |
| 4 | 1D conveyors |
| 7 | 0.25 bilobes at 60 degrees |
| 7.5 | 1D conveyors |
| 3 | 0.25 bilobes at 90 degrees |

Table 4.4 Screw configuration B (high shear)

| Number | Type & Description |
|--------|--------------------------------------|
| 3 | 0.25D bilobes at 60 degrees forwards |
| 10 | 1D conveyors |
| 2 | 0.25 bilobes at 60 degrees forwards |
| 4 | 1D conveyors |
| 7 | 0.25 bilobes at 60 degrees forwards |
| 3 | 1D conveyors |
| 1 | 0.25D distributive mixer |
| 2 | 1D conveyors |
| 3 | 1D cut conveyors |

4.2.3 Methods

4.2.4 Determination of torque

The twin screw granulator has a ConsiGma-25 system built and keeps track of parameters during the granulation process. The torque values were captured by a sensor, every 5 s and extracted into csv files. The torque was taken as the amount of work or power input needed to rotate the screws in order to feed the powder through the barrel and therefore

an indication of the amount of shear and compaction forces experienced by the powder in the barrel. The torque was measured in Nm.

4.2.5 Off-line sieve analysis

Granules collected from the experiments were firstly spread out onto trays and oven dried at 40 °C for 24 hours. For representative sampling, samples were split using a sample splitter/riffler (Laval Labs Inc, Canada). For sieve analysis, a known amount of sample from each experiment was placed into the top sieve of the sieve shaker. The sieves were stacked from 45 µm up to 2 mm in a $\sqrt{2}$ series. The sieves were shaken for an initial 10 minutes and the fractions obtained individually weighed and recorded. The sieves were then shaken for a further 5 minutes and the weights of each sieve fraction recorded. This was repeated until the results obtained for every sieve were within 2% of the previous weighed fraction. From the final results the cumulative population and the population of each sieve fraction were calculated and plotted.

4.2.6 Long Run Perturbation studies with Eyecon Image analyses

The TSG was set to operate with a powder feed rate of 1 kg/h, a screw speed of 150 rpm, and a water feed rate of 2.95 ml/min. Before data was collected, the granulator was operated at these conditions for ten minutes in order for the system to reach steady state. After ten minutes, images were collected on-line with the Eyecon camera and data collected by the TSG software. After about 45 minutes a system perturbation was introduced, this was an increase of water and powder feed to 5 ml/min and 1.2 kg/h, respectively. Samples were taken for off-line sieve analysis; the first sample was taken

at ten minutes and then further samples were taken every 15 minutes, six samples in total were collected.

This experiment was repeated with two different screw configurations the first was with screw configuration A (Table 4.3) and the second was with Screw configuration B (Table 4.4). Eyecon images were collected on-line every second, the D values were calculated from the images by the Eyecon software, CSV files were exported and a moving average of 60 was calculated for the torque values and for the D10, D50 and D90 values. These were then plotted against time and feed rate for the two experiments.

4.2.6.1 Torque studies at powder feed rates of 1, 2 and 5 kg h⁻¹

The granulator was set up with screw configuration A and formulation A. All of the granulation parameters were fixed except for the screw speed, these were set as follows 500, 300, 150, 60 and 40 rpm, the feed rate was set to 1 kg/h and the resultant torque was recorded. The TSG was operated at 10 min at each screw speed to reach steady state before on-line image analysis of the granules commenced. This experiment was then repeated with powder feed rates of 2 and 5 kg/h.

4.2.7 Fouling issues and interface development

As higher feed rates were being analysed it was essential to come up with a method for prevention of fouling of the analytical window. An external examination of the sample chute and Eyecon window was carried out whilst the granulator was turned on. It was

discovered that the fouling issue was being caused by water droplets forming on the sample chute and Eyecon window. Two potential solutions to this problem were investigated:

1. Hydrophobic coatings
2. Temperature control of the interface

Four substances were trialled as potential surface barriers in order to try and prevent water droplets and hence powders from sticking to the surface of a piece of polished stainless steel. The coatings were chosen due to their hydrophobic properties. The chosen coatings were:

1. Halfords Silicone Lubricant
2. Nikwax Tx. Direct Spray on water proofer
3. WD-40 Dry PTFE Coating
4. Rain X

The sheet of steel was separated into 5 sections as shown in Figure 4.1(a), one for each of the coatings and one control. The sections were labelled and then carefully sprayed individually with as even a coat as possible of each of the relevant coatings (Figure 4.1(b)). Each was allowed to dry before it was covered and the next was applied. Spraying of the coatings was carried out in a ventilated fume cupboard. Once all the coatings were dry, the granulator was switched on at a low flow rate and powder was allowed to pass over the metal sheets. The coatings were labelled on the steel sheet from left to right as follows:

1. Nikwax Tx. Direct Spray on water proofer
2. WD-40 Dry PTFE Coating
3. Control – no coating
4. Silicone Lubricant
5. Rain-X



Figure 4.1 Hydrophobic coatings used to try and prevent fouling of the sample chute

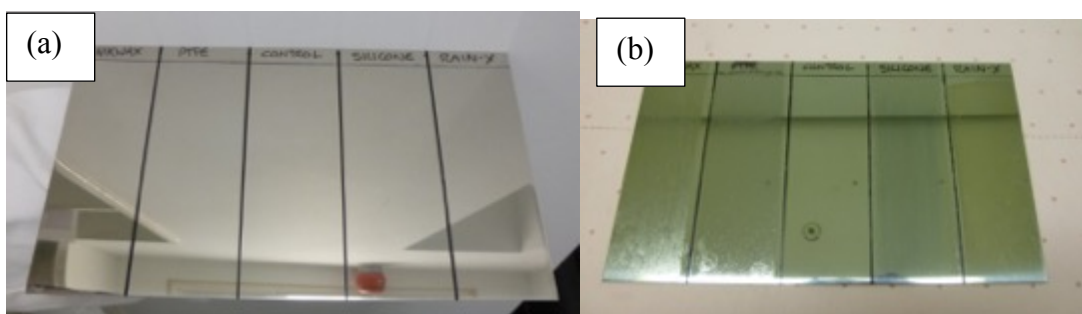


Figure 4.2 Labelled steel plate without (a) and with (b) the hydrophobic coatings.

The second avenue to explore was that of a heating element, a hand held infrared digital gun was used to look at the temperature gradient between that of the exiting granules and the sample chute.

A prototype heating element for both the sample chute and the Eyecon glass was built in order to bring the temperature of these elements to that of the granules exiting the granulator.

The resistive heater was made from the following components:

- Resistance Wire
- Power Source
- Electrical Tape
- Insulating Material

Firstly, the back of the sample chute was insulated by carefully adding a layer of black insulation tape (Figure 4.3 a)). Resistive wire was then snaked from the top to the bottom of the chute with a gap between the metal wire coils (Figure 4.3 b)), the wire was then covered with another layer of electrical tape and then insulated with a layer of cork material (Figure 4.3c)). A heating element was then coiled around the front of the Eyecon camera glass with a finer coated resistive wire; this was attached with clear tape as shown in Figure 4.4 in order not to interfere with LED lights and camera.

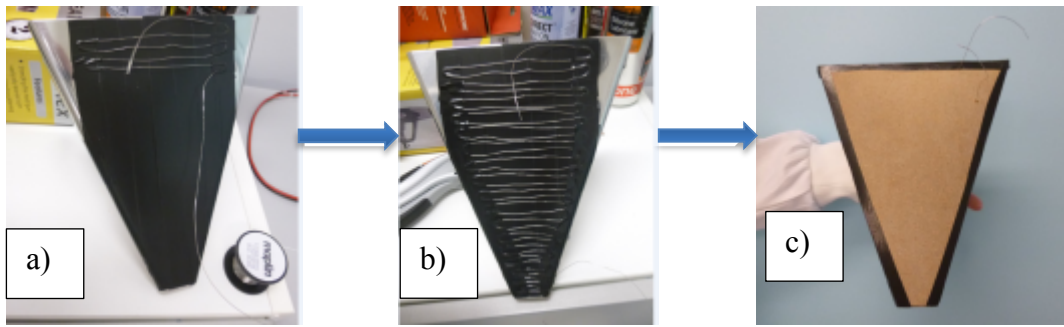


Figure 4.3 Steps to building the resistive heater on the back of the sampling chute showing a) black insulation tape layer, b) resistive wire running down the sample chute c) insulation of the resistance wire on the sample chute

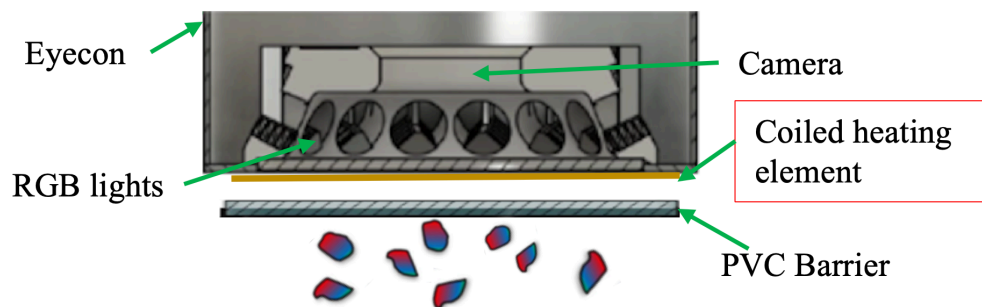
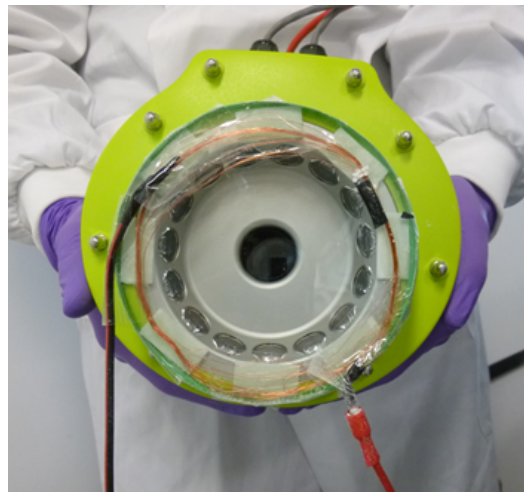


Figure 4.4 Eyecon camera with the attached heating element made from resistive wire and schematic showing the placement of the wire

The following studies were carried out in order to test the ability of the heating element to prevent fouling.

4.2.8 Torque studies at powder flow rates of 3 and 6 kg/h with heating element

A flow rate of 3 kg h⁻¹ was chosen to test out the prototype. Formulation A and screw configuration A were used in this experiment, no torque measurements were taken as this was mainly to see if fouling occurred. The system was continuously operated throughout the measurements and the parameters were changed without turning off the granulator. Each screw speed setting was allowed to run for 5 minutes before 5 minutes of data was then captured for each of the following screw speeds: 500, 300, 250 and 200 rpm totalling a granulator running time of 40 minutes. The granulator was then operated with a powder feed rate of 6 kg h⁻¹. The parameters for this experiment are shown in Table 4.5.

Table 4.5 Parameters set for 6 kg powder feed twin screw granulation study

| Parameter | Fixed/Varied | Setting |
|---------------------|--------------|-----------------------------------|
| Powder Feed Rate | Fixed | 6 kg h ⁻¹ |
| Water Content | Fixed | 17.5 g/min |
| Screw Speed | Varied | 500, 470, 400, 350, 300 & 230 rpm |
| Formulation | Fixed | Formulation A |
| Screw Configuration | Fixed | Configuration A |

As before, the granulator was allowed to operate for ten minutes to equilibrate before data was then captured with the Eyecon for roughly 5 minutes at screw speeds of 500, 470, 400, 350, 300, 270, 250 and 230 rpm.

4.3 Results and discussion

4.3.1 Development of the heating element

4.3.2 Long Run Perturbation studies with Eyecon Image analyses

4.3.2.1 Screw configuration A

Eyecon images from the long run with screw configuration A are shown in Figure 4.5. It can be seen that clear images were obtained for 0 – 30 mins ((a) and (b)). However, it is evident in the images collected after X mins that fouling of the chute occurred ((c) - (e)) although in the final image collected at X mins ((f)), material that had adhered to the sample chute had cleared.

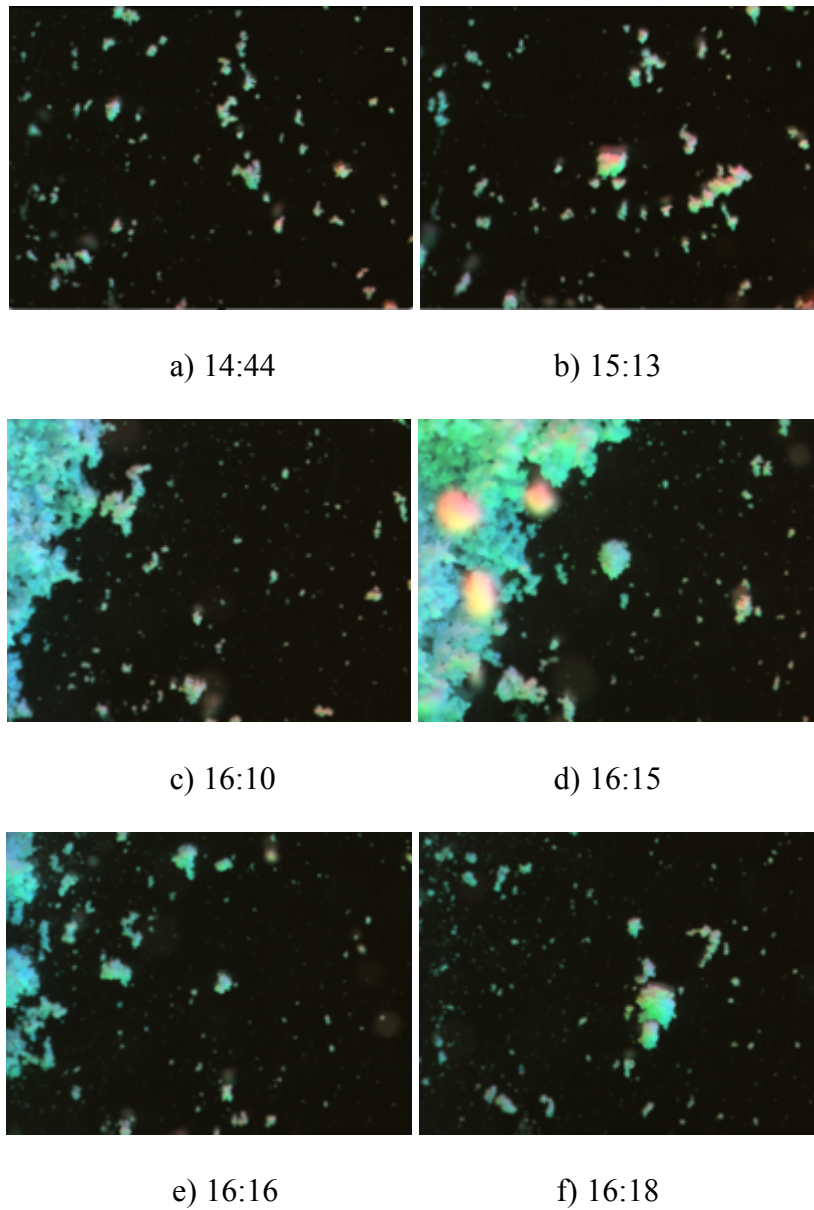


Figure 4.5 Eyecon Images captured from the on-line analysis of the long run experiment showing clear images in a) and b), the onset of fouling in b), c) and d) it then clearing up in e)

The corresponding D values were calculated by the software from the images. A moving average of 60 for each of the D values and for the torque was calculated in order to see any trends observed in the results more clearly. These results are plotted in Figure 4.6

along with the feed rate, showing a change in feed rate at 15:56:28 (hh:mm:ss) from 1kg/h to 1.2kg/h. The sharp spike in the results at approximately 16:10 is indicative of the fouling of the analytical window as shown in images c) and d) in Figure 4.5. The fouling was resolved by simply brushing the particles away from the window with a long handled fine brush, this was done twice, once at 15:37 and again at 16:15 (hh:mm). Another peak in the D10, 50 and 90 results appear after the fouling had been cleared, images from this are shown in images d) and e) in Figure 4.5. These images show that there were some granules still stuck on the sample chute which may have caused this, image e) shows that the bulk of this cleared itself but some smaller granules were still stuck on the sample chute.

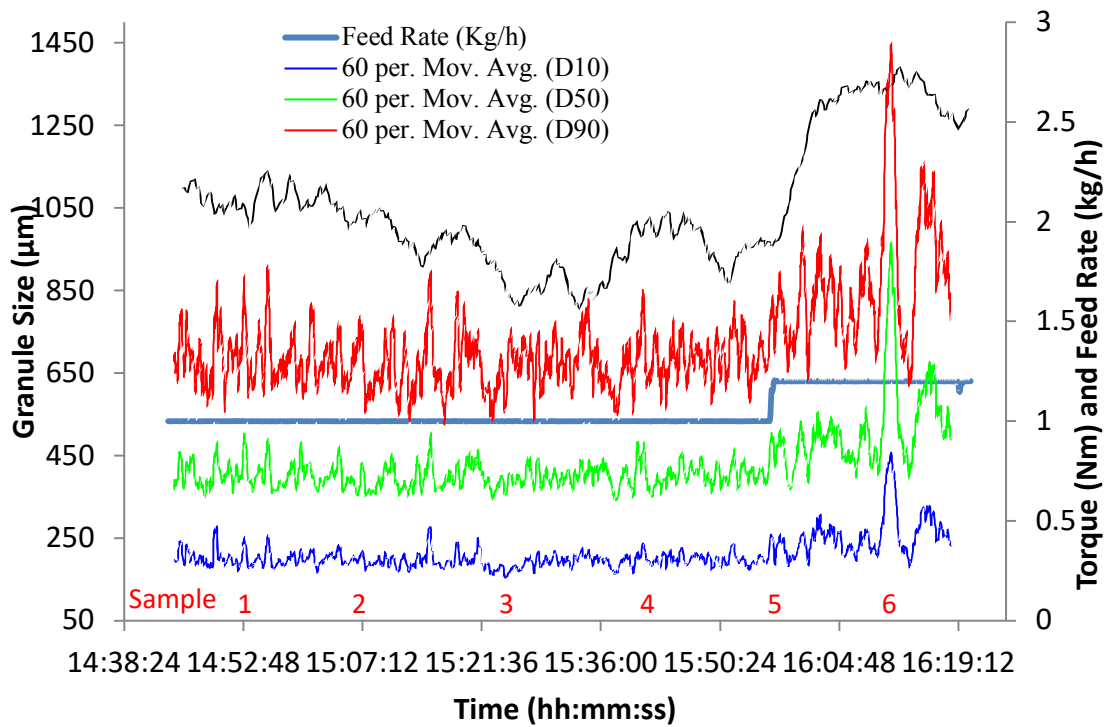


Figure 4.6 1kg/h study with screw configuration A showing an overlay of the moving average of the torque, D10, 50 and 90 values of granules with feed rate. The change in feed rate shows the change in process conditions.

Despite the fouling issues, it was found that an increase in powder feed rate from 1kg/h to 1.2 kg/h caused an increase in torque (an indication of powder compaction in the granulator), which resulted in an increase in the moving average of the D10, D50 and D90 values. The results from sieve analysis of samples taken at each of the sample points indicated on the plot above have been plotted in Figure 4.7.

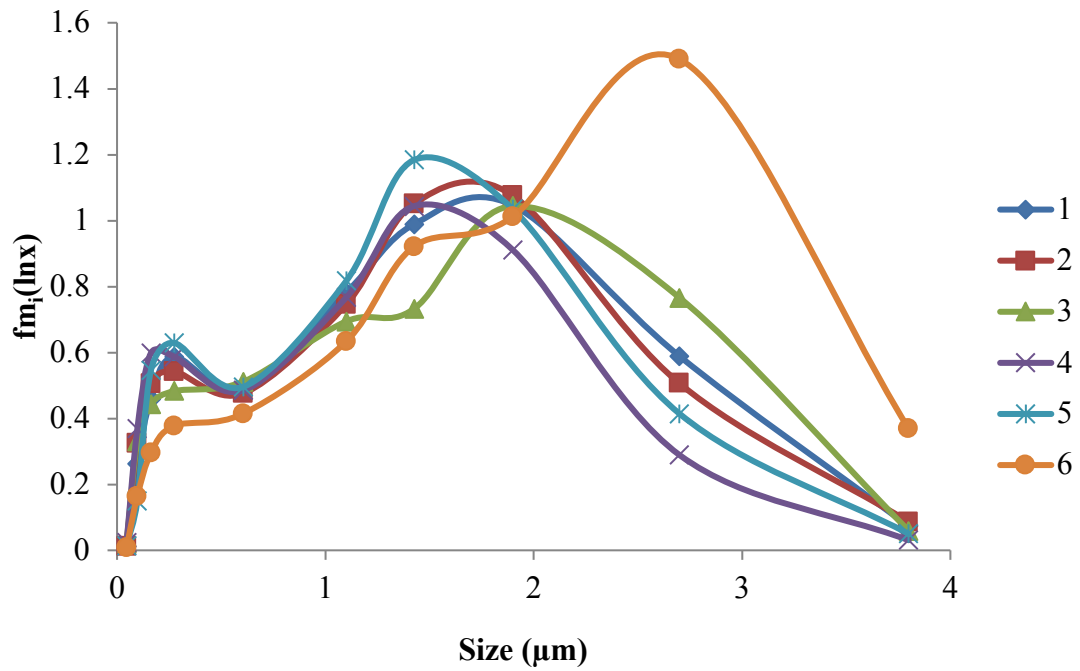


Figure 4.7 Particle size data from sieve analysis of granules obtained with screw configuration A

The sieve analysis results show a bimodal distribution for samples 1 to 5 collected before the perturbation; sample 3 shows a slightly different distribution. The results from sample 6 show a reduction in the number of fines $>0.5 \mu\text{m}$ and an increase in granules $>2 \mu\text{m}$. This sample was retrieved at the higher powder feed rate (1.2 kg h^{-1}) when there was an increase in torque. There is a clear difference between this sample and those taken beforehand which is in good agreement with the moving average of the D values shown in Figure 4.6.

4.3.2.2 Screw configuration B

This experiment was then repeated as above but with screw configuration B; the results are plotted in Figure 4.8. Off-line sieve analysis of the six collected samples are plotted in Figure 4.9.

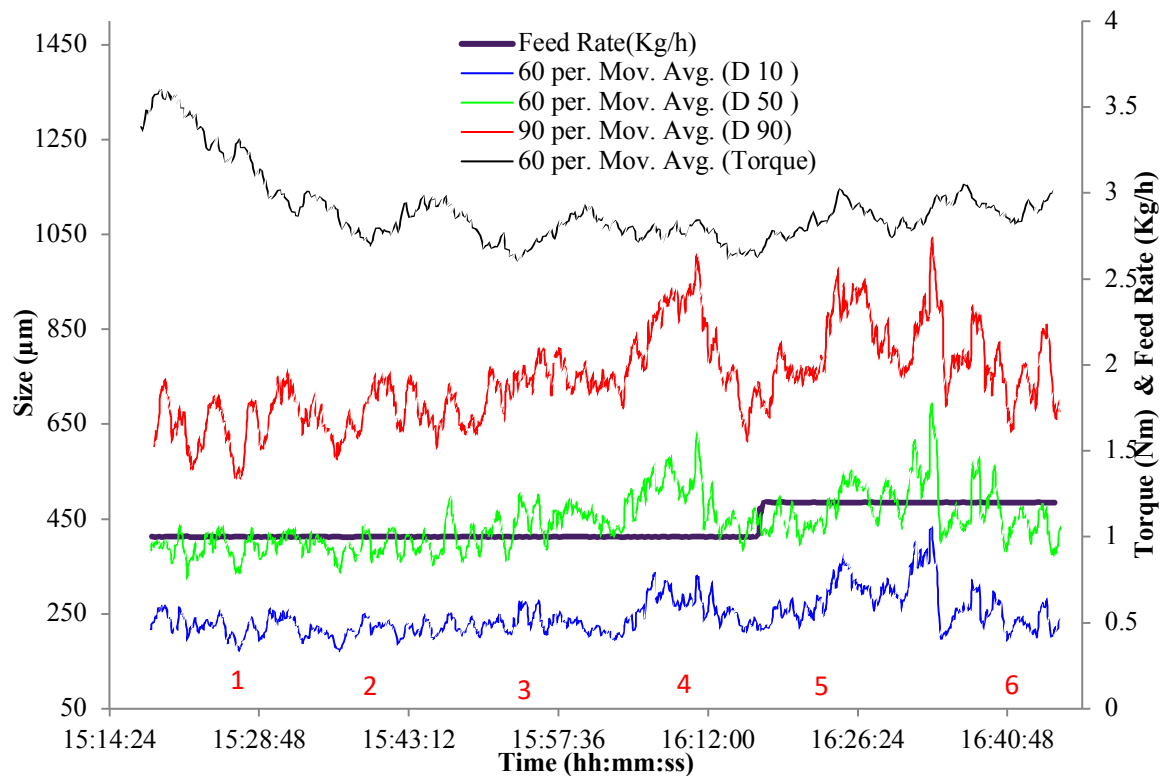


Figure 4.8 1kg/h study with screw configuration B showing an overlay of the moving average of the torque, D10, 50 and 90 values of granules with feed rate. The change in feed rate shows the change in reaction conditions.

These results show a very different trend in the torque, showing an initial decrease in torque over the first ten minutes, the torque then does not appear to change significantly with a change in flow rate as seen in the previous results presented in section 4.3.2.1.

The on-line particle size analysis shows a slight incline towards the end but is not correlated with a change in feed rate. The off-line sieve analysis of the collected granules shows that samples 1, 5 and 6 contain a greater portion of larger granules than the other samples collected. The large torque value could be the cause of the larger granules produced in sample 1. There is a slight change in the trend of the size values towards the end, starting about 16:05:00 until roughly the end of the run. If this was linked to an increase in particle size then sample 4 should show a similar result in the sieve analysis as those for samples 5 and 6. This however is not the case and so this change in moving average cannot be linked to a change in particle size.

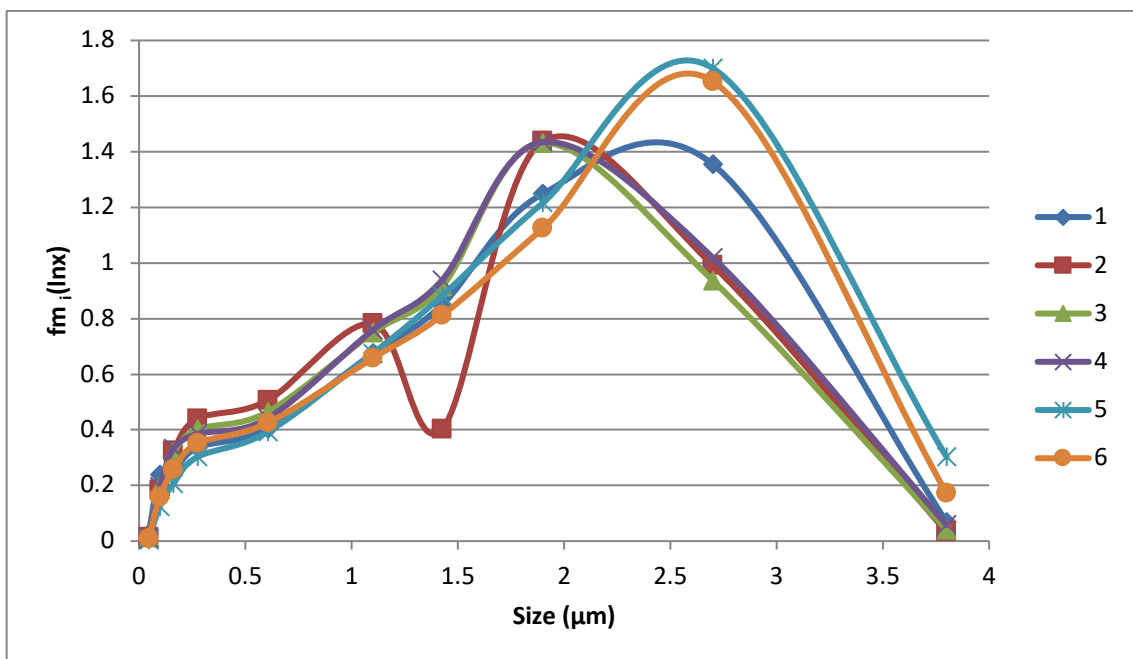


Figure 4.9 Particle size data from sieve analysis of granules obtained with screw configuration B

A direct comparison of the torque produced in each experiment (Figure 4.6 and Figure 4.8), shows that a higher torque was produced with screw configuration B. Thompson and Sun¹⁵² discussed the increase in torque caused by the addition of mixing and kneading elements. Configuration A contains no mixing elements whereas configuration B contains one mixing element. The mixing element in B would be likely to cause an increase in torque, however this is only one mixing element so the jump in torque must also be contributed by the divide of the bilobes across the shaft.

4.3.3 Torque studies at a powder flow rate of 1 kg h⁻¹

The results obtained when the screw speed was changed at a powder flow rate of 1 kg h⁻¹ are plotted below in Figure 4.10

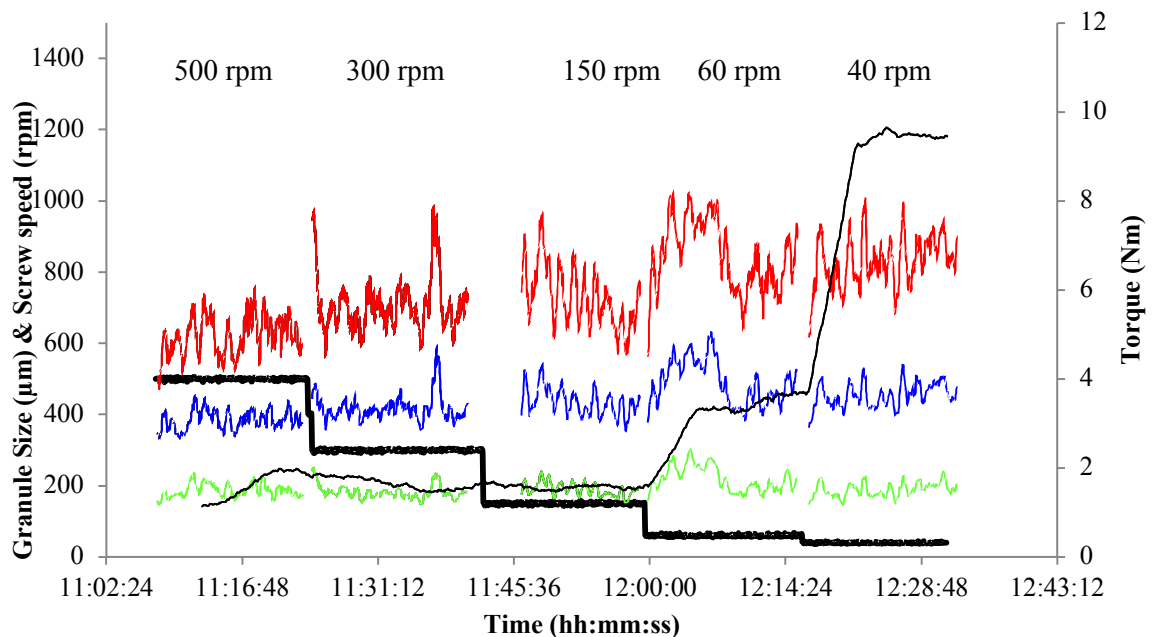


Figure 4.10 A plot of a moving average of 60 for each of the D values captured from Eyecon image analysis: D10 (green), D50 (blue) and D90 (red) values and torque (thin black line) obtained at screw speeds of 500, 300, 150, 60 and 40 rpm

At higher screw speeds there is a lower level of torque, this is believed to be due to the barrel fill level as the powder is being conveyed through the granulator much more quickly. As the screw speed is reduced there is a build-up of powder in the granulator resulting in an increase in barrel fill, this is confirmed by the change in torque at 60 and 40 rpm. This change in torque is followed by a slight change in granule size which can be seen in the particle imaging results.

4.3.4 Torque studies at powder flow rates of 2 and 5 kg h⁻¹

When screw speed was varied at a powder feed rate of 2 kg h⁻¹, fouling was observed at the sampling window at all screw speeds (500, 300, 150 and 120 rpm). From inspection of the images from the 500-rpm study and a look at the sample chute it can be seen that build-up of powder on the window appeared to be caused by water condensation formed from the wet granules expelled from the granulator. The images shown in Figure 4.11 are from the initial 500 rpm study where the “fogging” of the window took approximately ten minutes to develop.

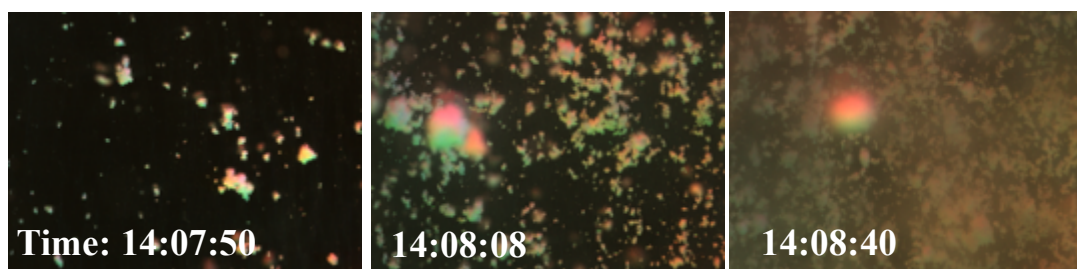


Figure 4.11 Fogging of sampling window at a screw speed of 500 rpm and a powder feed rate of 2 kg/h

The same fouling issue was experienced during the 5kg/h study, experiments had to be stopped until the fouling issues had been addressed. Potential solutions to these are studied in the next section.

4.3.5 Fouling issues and interface development

4.3.5.1 Coating results

The end results from the powder contact with the steel plate are shown in Figure 4.12. It is quite clear straight away that the best results come from the middle panel which was that of the control and that by applying a layer of coating to the steel actually aided the fouling of the steel. This was possibly due to the change in texture of the surface caused by the uneven coating of each of the samples.

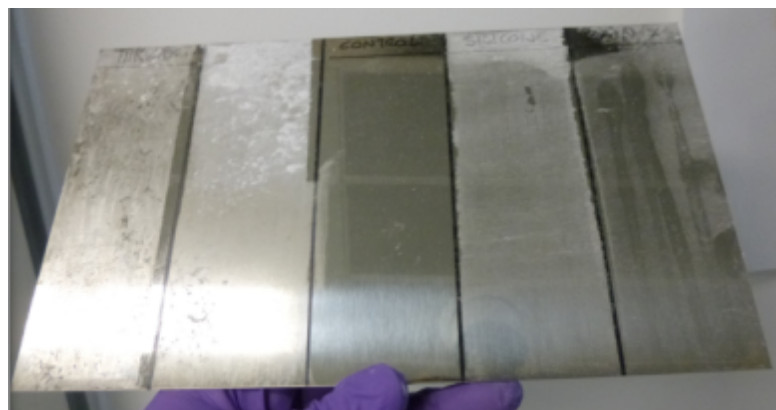


Figure 4.12 Resulting powder attachment from the coating experiment

It was concluded from this that it was not possible to apply a coating smooth enough to the surface of the steel in order to prevent the granules/powder from sticking and that this

was not a feasible route to go down for the actual sample chute. Further work on a smoother coating professionally applied may help prevent fouling and could be further investigated. Nanoscale technologies are mainly used in the coating industries and could be used for future experiments on fouling issues but the investigation of these is out of the scope of this work.

It was found that the temperature of an average of three measurements of the granules upon exiting the TSG was 43 °C and the average temperature of the steel chute was 24 °C. This large temperature gradient appeared to be the cause of the problem. A heat gun was then applied to the steel chute to see if this would have an effect on the number of particles sticking to the surface. Images of before (a) and after (b) are below in Figure 4.13 a) and b).

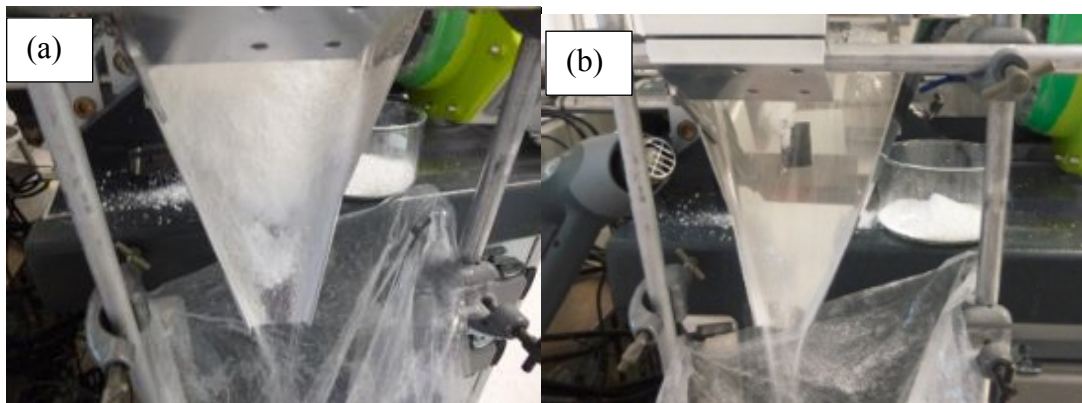


Figure 4.13 Fouling of the sample chute (a) before heat was applied and (b) after applying heat with a heat gun.

4.3.6 Evaluation of heating element solution at high power feed rates

All of the experiments from this point forward were done with the heating element implemented.

4.3.6.1 Torque study at a powder feed rate of 3 kg h⁻¹

The granulator was operated successfully for the full 50 minutes with no fouling at all. The images produced during this experiment were clear, sharp and a good indication of how successful the heating devices were. There was no sticking of granules at all to any of the surfaces that were heated. Figure 4.14 illustrates the fouling that occurred over a short period of 50 seconds during an experiment with a powder feed rate of 2 kg h⁻¹. The covering of the analytical window was so bad that analysis at this feed rate was unable to be achieved. Figure 4.15 on the other hand shows images from the start right through to the end of a 40-minute analysis that show no signs of fouling at all.



Figure 4.14 Fouling over 50 seconds of running at 2 kg h⁻¹ 400 rpm

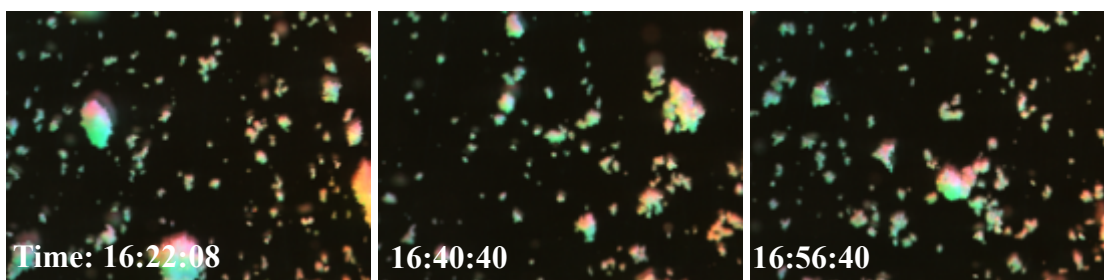


Figure 4.15 No sticking of particles to the analytical window throughout a 40-minute run at 3 kg h^{-1} 300 rpm.

The effect of change in screw speed on the granule D values is illustrated as a bar chart in Figure 4.16.

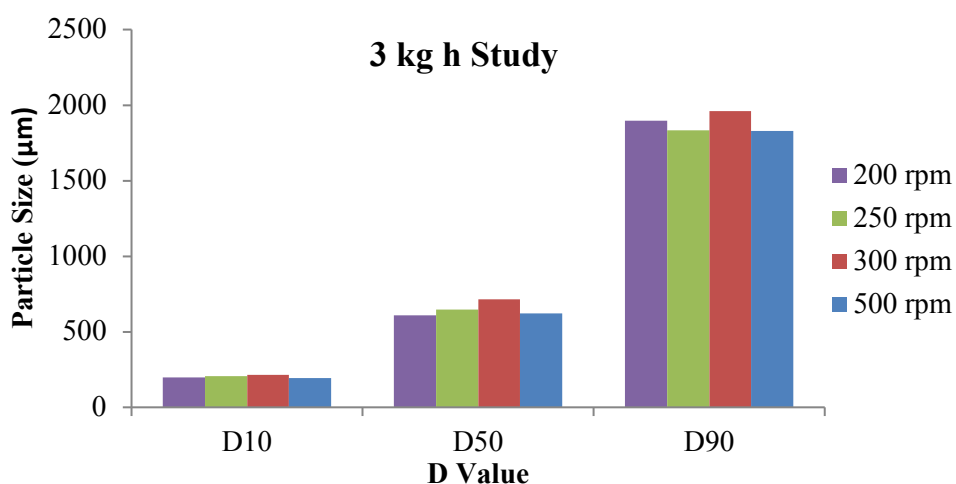


Figure 4.16 D10, 50 and 90 values for 5 different screw speeds during a 3 kg h^{-1} study

The results show very little difference between the granule sizes obtained for all four screw speeds. The main thing to note from this study was that there was no fouling throughout the experiment and analysis was able to now be carried out at higher flow rates and for longer time periods.

4.3.6.2 Torque study at a powder feed rate of 6 kg h⁻¹

Throughout the whole experiment there were no signs of fouling of the analytical window; analysis was able to be carried out trouble free. A bar chart of the D values from the analysis is shown in Figure 4.17.

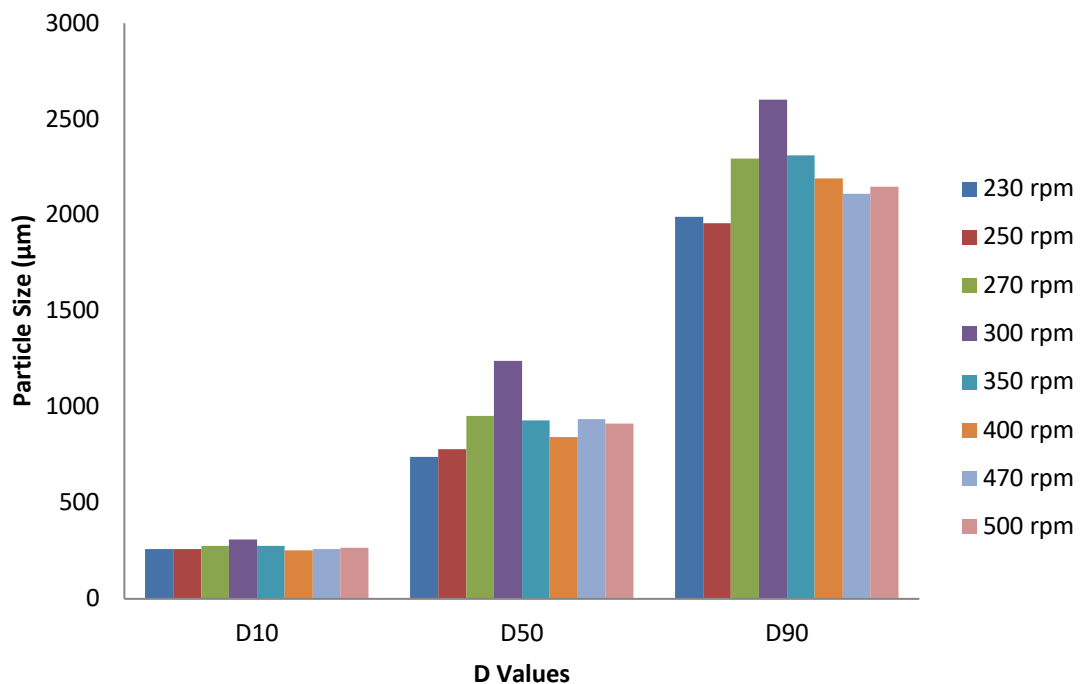


Figure 4.17 D values for 6 kg/h torque study

The bar chart shows that a screw speed of 300 rpm produces the largest granules. It also shows that as the screw speed is increased the overall size values for D10, D50 and D90 also increase with a maximum at 300 rpm, this then decreases again mainly in the D90 value, this can be seen more clearly in the plot shown in Figure 4.18. Figure 4.19 is an overlay of the trend lines produced from a calculated moving average of 60 for each of the D values calculated from the individual images captured over time for the eight

different screw speeds. On top of the D values, the moving average for torque has been calculated and plotted.

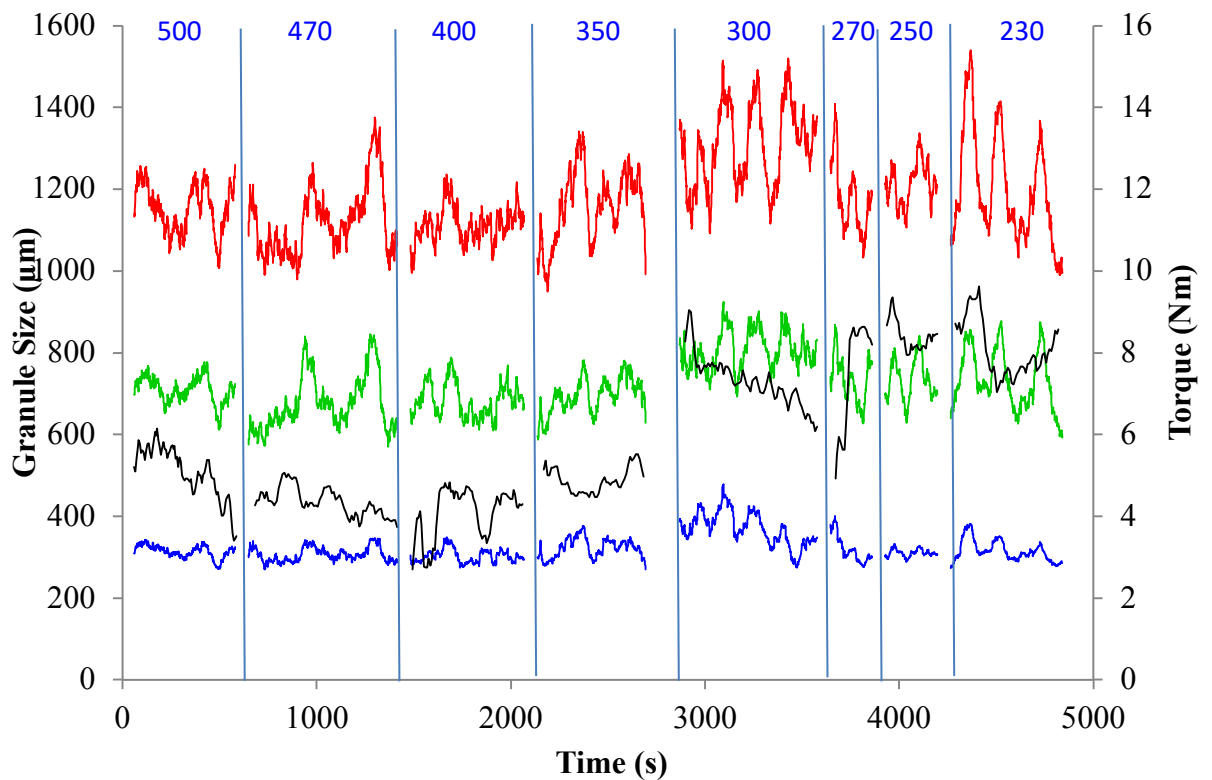


Figure 4.18 A moving average of 60 has been calculated for each of the D10 (blue) D50 (green) and D90 (red) values and torque (black) for each of the screw speeds as labelled.

Further smoothing has been achieved in Figure 4.19, which shows the average D10, D50, D90 and Torque values plotted for each of the different screw speeds.

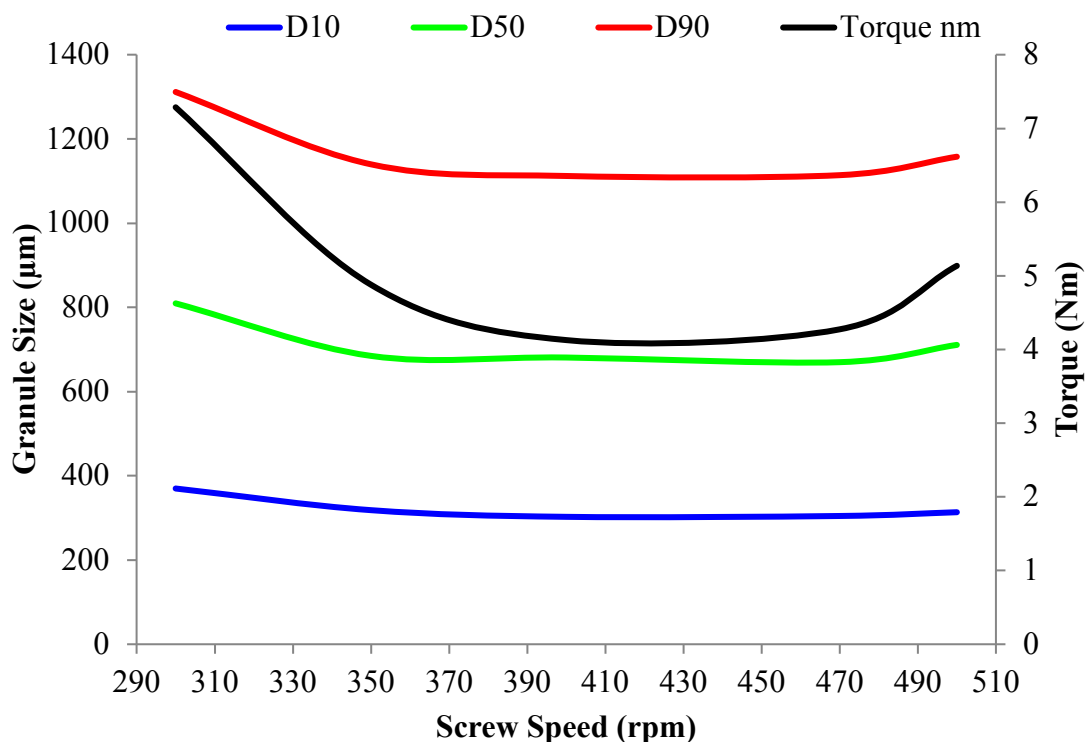


Figure 4.19 Overlay of D10, D50, D90 and torque values for a powder feed rate of 6 kg h⁻¹

There is more of a trend between the torque and the D50 and D90 values than that of the D10. An increase in throughput should result in a higher filling degree and therefore a higher amount of energy required for rotating the screws in the barrel, yielding higher torque values.

4.4 Conclusions

On-line analysis initially proved to be a challenge at powder feed rates of roughly 1.2 kg h⁻¹. This was due to build-up of powder obscuring the analytical window of the Eyecon™. Results were unable to be obtained for flow rates above 1.2 kg h⁻¹ where most of the rest of the research was to take place. Hydrophobic coatings were attempted as a

solution to water condensation build up on the sample chute that was occurring due to a temperature gradient between the warm granules and the cold sampling chute. The hydrophobic coatings actually proved to worsen the fouling of the steel and were abandoned for a successful resistive heater element design. A simple barrier solution was able to prevent granule segregation and further improve analysis. The heating elements put in place allowed for much clearer image analysis and sharper images from which more representative data could be gathered and for analysis of flow rates above 1.2 kg h^{-1} . The heating elements eradicated the fouling issue for even long runs up to an hour at flow rates as high as 6 kg h^{-1} . The 3 kg h^{-1} study showed that screw speed had little influence on the granule size for screw speeds ranging from 500 – 200 rpm.

Chapter 5
Terahertz Raman analysis of Hot Melt Extruded
Amorphous Solid Dispersions

5. Terahertz Raman analysis of Hot Melt Extrusion Amorphous Solid Dispersions

5.1 Introduction

Paracetamol (PCM) or acetaminophen, is an antipyretic compound that is clinically used as an analgesic.¹⁵³ Currently there are three fully characterized polymorphic crystalline forms (forms I, II and III) and two high pressure polymorphs with unknown crystal structure (forms IV and V).¹⁵⁴ These reported crystalline forms include; the most stable monoclinic crystal (form I) and its metastable orthorhombic form (form II) and the elusive highly metastable polymorph (form III), which is hard to isolate in sufficient quantities for long enough periods to enable analysis.

It is relatively straightforward to supercool the melt of PCM and prepare an amorphous form which is the least stable of all PCM solid forms. The amorphous form has been found to possess a low glass transition temperature T_g at circa 25 °C which suggests a high tendency for recrystallisation under room conditions. Many amorphous forms show stability around T_g whereas others show rapid crystallisation below T_g and so there is real uncertainty as to the predictability of amorphous forms to recrystallise into crystalline forms. This unpredictability extends to the kinetics and the crystalline structure of the recrystallised product. The key to the ability to understand the kinetics and transitions is to be able to analyse these spontaneous events in real time and in-situ. Many analytical techniques take time to collect the data and by that time the recrystallisation or change in polymorphic form may have happened. One of the key benefits of HME is the ability to be able to change processing parameters such as extrusion temperature, screw speed, feed

rate and screw configuration. Each has its own function and the options of variations is endless, each one correlating with the other in order to control the whole process.¹⁵⁵

The physical stability of ASD-based products remains one of the major challenges in their development. The instability involves the separation of the drug and the polymer, leading to the crystallisation of the drug which may have an effect on the solubility and dissolution of the drug and remove the benefits of creating an ASD. Moreover, the drug may recrystallise into unwanted polymorphic forms and compromise the safety of the end product.¹²³ The ideal ASD will remain homogeneously dispersed during its shelf life. The phase behaviour of the drug during its storage is a governing step in the physical stability of the drug and is defining factor in the determination of a products shelf life. Extensive research has been done on the effects of different polymer excipients, the use of co-crystals,¹⁵⁶ and optimisation of process parameters, to name a few, all in order to develop more stable ASDs for poorly soluble drugs.^{40, 123} Three of the main analytical techniques to look at ASDs are compared to THz Raman spectroscopy for the analysis of solid form and for a study into the homogeneity of the ASDs. The first study looks at the stability of the ASDs over a five-month period and the ability of THz Raman to detect crystalline and amorphous material. The ASDs were firstly studied immediately after extrusion, DSC, XRPD and Raman analysis is compared to THz Raman as a feasibility study for the detection of crystalline material. The results for these are then followed by a more extensive analysis of the materials at 5 months to look at the stability and homogeneity of the ASD over time.

The study looks at the effects of process parameters including screw speed, barrel temperature, screw speed and drug loadings of paracetamol with affinisol. A study into the homogeneity of ASD of these samples is also investigated with THz Raman spectroscopy with PCA of spectra taken across and within the extruded samples. The study then focuses on in-line analysis of the extrusion of paracetamol with affinisol and then the application of this technique to solve an industrial problem involving stearic acid, a plasticizer used as a processing aid for HME and as a lubricant in TSG. This study was carried out in order to look into solving issues occurring with the blockage of the HME process when stearic acid is used the plasticiser.

The specific aims of this chapter are:

1. To be able to characterise solid dispersions of paracetamol and Affinisol (PCM-AFF) prepared by hot melt extrusion using both on-line and off-line using THz Raman spectroscopy.
2. To compare XRPD, DSC and THz Raman for solid state analysis of ASDs.
3. To investigate the stability of amorphous solid dispersions to monitor the effect of temperature of hot melt extruded stearic acid by both in and off-line analysis using THz Raman Spectroscopy.
4. To prove THz Raman spectroscopy to be a reliable method for solid dispersion analysis of HME ASDs.

5.2 Experimental

5.2.1 Materials

5.2.1.1 Active pharmaceutical ingredients and polymers

Crystalline pharmaceutical grade (98.0-102% powder) granular paracetamol (PCM) and amorphous hydroxypropyl methylcellulose grade Affinisol (HPMC) were purchased from Sigma-Aldrich. The chemical structure of all materials is displayed in Figure 5.1. All compounds were used as obtained, without further purification.

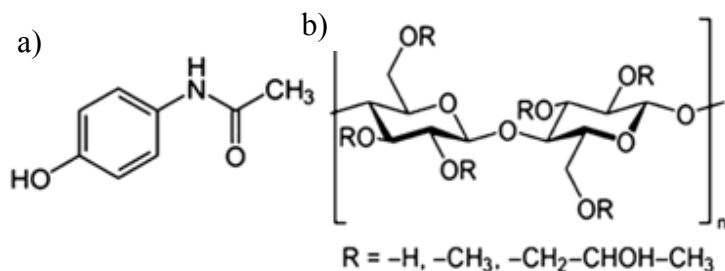


Figure 5.1 Chemical structure of a) paracetamol and b) Affinisol-hydroxypropyl methylcellulose

Hypromellose (HPMC) is a hydrophilic polymer widely used in pharmaceutical dosage forms. Due to their high T_g available grades of HPMC are difficult to process during HME. Affinisol, is a modified grade of HPMC used because of its improved thermal properties for HME. Affinisol has a much lower T_g and melt viscosity making it much better for HME processes.¹⁵⁷

Amorphous solid dispersions (ASDs) from four HME experiments, performed by Muhammad T. Islam at Strathclyde University were provided for analysis. The ASDs were provided as pellets and extrudes collected from experiments shown in Figure 5.2. The

experiments were performed as in Table 5.1, the table shows each of the parameters set for each sample set within each of the four experiments.

Table 5.1 Hot Melt Extrusion Experimental Conditions for PCM-AFF

| Experiment No | Sample No | API Concentration (% w/w) | Combined API/Polymer feed rate (kg/h) | Processing temperature (barrel sections 4-10 (°C)) | Screw Speed (rpm) |
|---------------|-----------|---------------------------|---------------------------------------|--|-------------------|
| 1 | 1 | 10 | 1 | 180 | 200 |
| 1 | 2 | 20 | 1 | 180 | 200 |
| 1 | 3 | 30 | 1 | 180 | 200 |
| 1 | 4 | 40 | 1 | 180 | 200 |
| 1 | 5 | 50 | 1 | 180 | 200 |
| 2 | 6 | 10 | 1 | 160 | 100 |
| 2 | 7 | 20 | 1 | 160 | 100 |
| 2 | 8 | 30 | 1 | 160 | 100 |
| 2 | 9 | 40 | 1 | 160 | 100 |
| 2 | 10 | 50 | 1 | 160 | 100 |
| 3 | 11 | 10 | 1.5 | 160 | 300 |
| 3 | 12 | 20 | 1.5 | 160 | 300 |
| 3 | 13 | 30 | 1.5 | 160 | 300 |
| 3 | 14 | 40 | 1.5 | 160 | 300 |
| 3 | 15 | 50 | 1.5 | 160 | 300 |

| | | | | | |
|---|----|----|---|-----|-----|
| 4 | 16 | 15 | 1 | 160 | 125 |
| 4 | 17 | 30 | 1 | 160 | 125 |
| 4 | 18 | 45 | 1 | 160 | 125 |
| 4 | 19 | 60 | 1 | 160 | 125 |

Samples 1, 2 and 3 were supplied pelleted, as a pelletizer was used in the production process for these three samples, extrudes were not therefore available for these three samples. An example of these are shown in Figure 5.2 (left), the right figure shows some manually cut pellets used for analysis of samples 4 – 19 as pellets. Before the extrudes were pelleted they were provided as extrudes as shown in Figure 5.3.



Figure 5.2 Example of pellets produced by a pelletizer for samples 1,2 and 3 (left) and example of manually cut pellets used for pellet analysis of samples 4 – 19 (right).

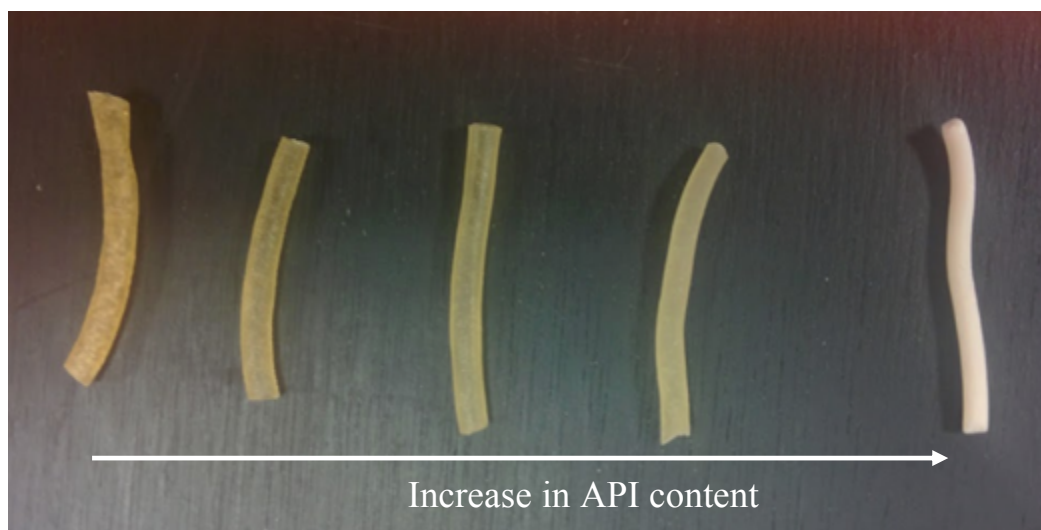


Figure 5.3 Example of extrude samples produced by HME supplied for THz Raman analysis with increasing API concentration from left to right.

The ASDs were analysed with XRPD, DSC and THz Raman as soon as they were received this was labelled as 0 months but samples were produced slightly before then. and they were then stored at 25 °C and 60 % relative humidity and were analysed with XRPD and THz Raman again after 5 months. Details of these experiments are described in the methods section below.

5.2.2 Stearic acid analysis

Pharmaceutical grade stearic acid, was supplied by industry, the original source of the material was unknown.

5.3 Methods

5.3.1 Off-line analysis of amorphous solid dispersions - comparison of XRPD and Terahertz Raman spectroscopy for characterisation of amorphous content

5.3.1.1 Differential Scanning Calorimetry

ASDs samples at 0 months old were analysed by DSC. All DSC /TGA data were collected simultaneously from samples using a NETZSCH Jupiter STA 449C Instrument under nitrogen atmosphere using NETZSCH software. Samples were placed in a 25 μ L aluminium crucible with a pierced lid and analysed at a heating rate of 10 K/min in the range 10 – 180 °C.

5.3.1.2 X-ray powder diffraction

XRPD analysis was carried out on a Bruker D8 Advance II (Priscilla) GX002103, with materials mounted onto 25 mm Kapton tape. Materials presented as pellets were mounted directly onto the tape, whereas extrude filaments were cut to the required length and loaded parallel to the longest axis of the wells. Several of the filaments were thicker than the depth of the sample well and such a variable height across the collected samples was unavoidable. Data were collected from each sample in the 2Θ range of 4 – 35° with a step size of 0.015° and 0.1 sec. step⁻¹ count time. Samples were oscillated ± 0.5 mm in the x-y plane at a speed of 0.3 mm sec⁻¹ throughout data collection to maximize particle sampling and minimise preferred orientation effects. Pellets were analysed at 0 and 5 months old and compared to DSC and THz Raman results. Identification of the

crystalline form was made by comparison to results in the literature and compared to CSD crystalline forms I, II, and III (HXACAN27, HXACAN31 and HXACAN29, respectively) using Mercury software (version 3.1).

5.3.1.3 Terahertz Raman spectroscopy

A Terahertz-Raman probe (Ondax. Inc, USA) coupled with an RXN1 Kaiser Raman spectrometer (Kaiser Optical Systems, Ann Arbor, MI, USA) was used with different probes/optics depending on the experiment. Spectra were captured with an excitation wavelength of 785 nm at 70 mW power over the wavelength range of 0 – 1800 cm^{-1} . Data was acquired with Holograms (version 4.1) and saved as SPC or CSV files to be further analysed in MATLAB (version R2016b (9.1.0) MathWorks, Inc., USA). Off-line THz Raman spectra were collected of extrudes and pellets using a short focus optic. Preliminary experiments determined that the best signal was observed when the sample was positioned 9 mm away from the optic, these can be found in Appendix A.

5.3.1.4 Raman spectroscopy

Off-line Raman spectra were collected using a Raman RXN2 spectrometer (Kaiser Optical Systems, Ann Arbor, MI, USA), equipped with a PhAT probe and 250 mm F1 and 6 mm spot size. All spectra were recorded from 50 to 1800 cm^{-1} . Extruded samples were acquired with a 10 s exposure time and 1 accumulation, pelleted samples were acquired with a 5 s exposure time and 1 accumulation. Data acquisition was made using Holograms (version 4.1) and HoloReact (version 2.0.0.0 Kaiser Optical Systems, Inc.). A dark spectrum was taken at the start of analysis and the cosmic ray filter was on. Files were converted to SPC files and analysed using both MATLAB and Origin Pro.

5.3.2 Content uniformity study of amorphous solid dispersions - extrudes and pellets

The samples from Table 5.1 were analysed off-line by firstly Raman with the PhAT probe and then a comparison of Raman and THz Raman for the analysis of pellets and extrudes using principal component analysis was carried out. Details of these experiments are as are below.

5.3.2.1 Raman analysis RXN2

Raman spectra were collected using the Kaiser Raman Rxn2 spectrometer set up as described in section 5.3.1.4 The spectrometer was equipped with a 6 mm PhAT probe. The samples were analyzed as they were received: 1 - 3 were analyzed as pellets and 4 - 19 as extrudes. Spectra of the pelleted samples were acquired with a 5 s exposure time and 1 accumulation, the extrude samples were acquired with a 20 s exposure time and 1 accumulation. A single spectrum for each sample was acquired.

5.3.2.2 Content uniformity study - THz Raman and Raman comparison

Samples were analysed as extrudes and as pellets. Multiple spectra for the same sample were acquired using both Raman and THz Raman. The samples were analysed along the extrude as shown in

Figure 5.4 a) and within the pellets shown in b). The extrudes were cut using clean wire cutters into pellets for samples 4-19.

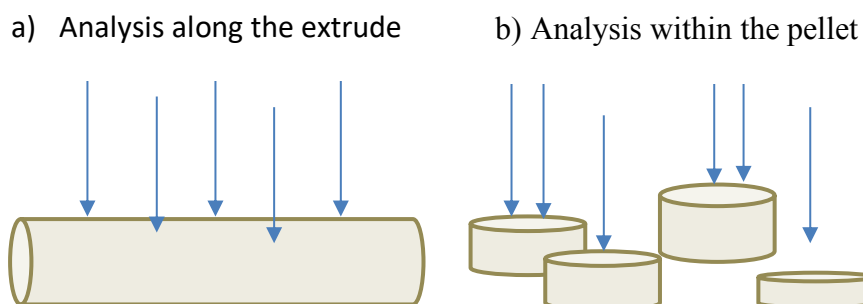


Figure 5.4 Schematic showing example analysis points with Raman and Terahertz Raman of amorphous solid dispersion extrudes and pellets produced by HME.

The experimental set up as seen in Figure 5.5 shows the THz Raman probe on the left and Raman probe on the right. Both samples were analysed from above, the room lights were switched off and an area around the sample was covered with foil in order to prevent any room lights from reaching the detectors. THz Raman analysis was carried out as described in section 5.3.1.3 with the short focus optic the Raman analysis was carried out as in section 5.3.1.4 with the MR probe and short focus optic.

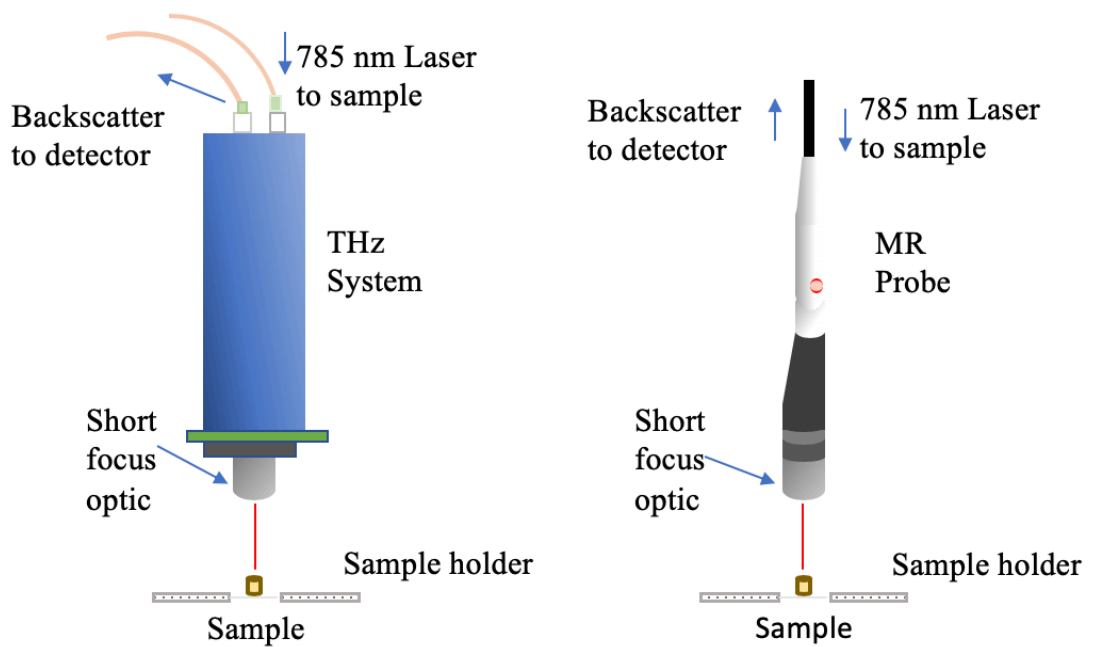
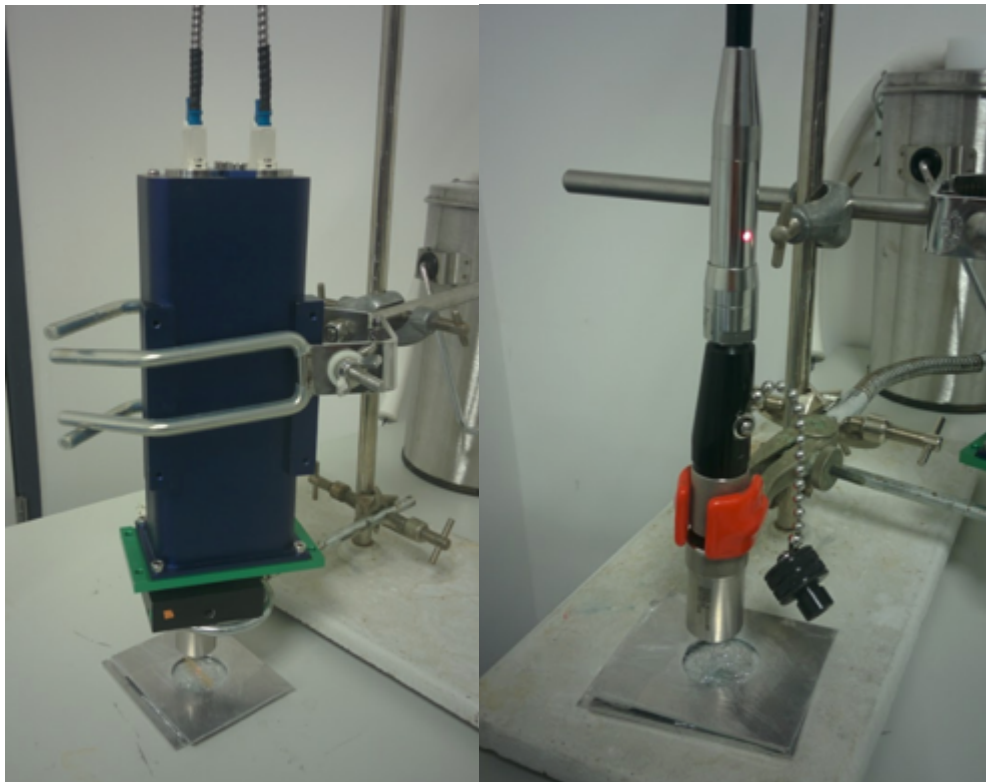


Figure 5.5 Above pictures of the probes set up for analysis of samples by both THz Raman on the left and Raman with the MR probe on the right with the same optic. Below are the corresponding schematics for each technique

5.4 In-line terahertz Raman analysis of hot melt extrusion of PCM-AFF

5.4.1 Hot met extruder set up for in-line analysis

The hot melt extrusion experiments were all carried out on a co-rotating Eurolab 16 Twin screw extruder (Thermo Fisher Scientific™, Karlsruhe, Germany) equipped with two DDW-M FW20 gravimetric feeders and a vertical crammer hopper (Brabender Technologies, Germany). The extrudes were prepared by varying the API content, which was set by the powder feed rates of the API and polymer. The feed rates were combined to give the desired API – polymer ratios. The screw speeds, feed rates and temperatures of the corotating screws were set within the control unit. For all experiments, barrel zone 1 was operated at 20 °C and barrel zones 2 and 3 were controlled at temperature set points of 50 and 100 °C, respectively, to prevent powder melting and blockage of the feeding zone. Product melt zones 4 to 10 and the die zones were controlled at the same temperature, these varied for each experimental method as were the screw speed, feed rates and API content. Each of these parameters is stated within each method below. A schematic of the HME set up showing the position of the heating zones, PAT placement and screw configuration is shown in Figure 5.6.

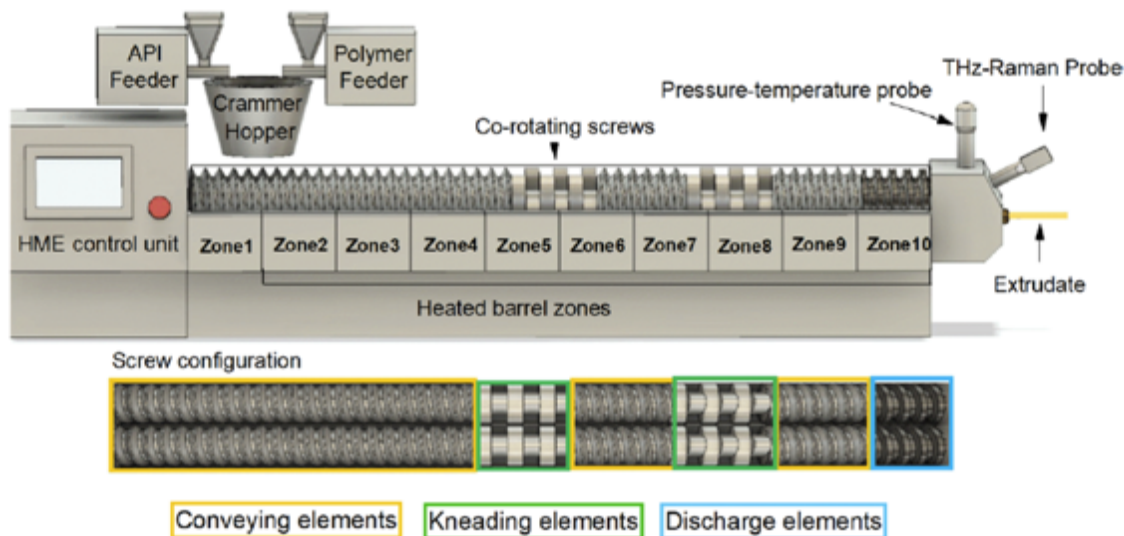


Figure 5.6 HME schematic showing the screw configuration and HME set up for in-line analysis ⁹⁷

5.4.2 In-line Terahertz Raman of hot melt extrusion of PCM - AFF

Solid dispersions containing 0%, 10, 30, and 50 and 100 wt % paracetamol in Affinisol were prepared by hot melt extrusion. Samples were collected, pelleted and analysed off-line by XRPD, Raman and THz Raman spectroscopy.

In-line analysis of HME was carried out using a metal probe adapted for the HME, as shown in Figure 5.7. Affinisol and Paracetamol were extruded at a temperature of 175 °C, a screw speed of 300 rpm and with the following drug loads: 0:100, 10:90, 20:80, 30:70, 40:80 and 50:50 % w/w of paracetamol to Affinisol, respectively. THz Raman spectra were acquired every 10 s with an exposure time of 7 s and 1 accumulation. Spectra were recorded from -5 to 1800 cm^{-1} .

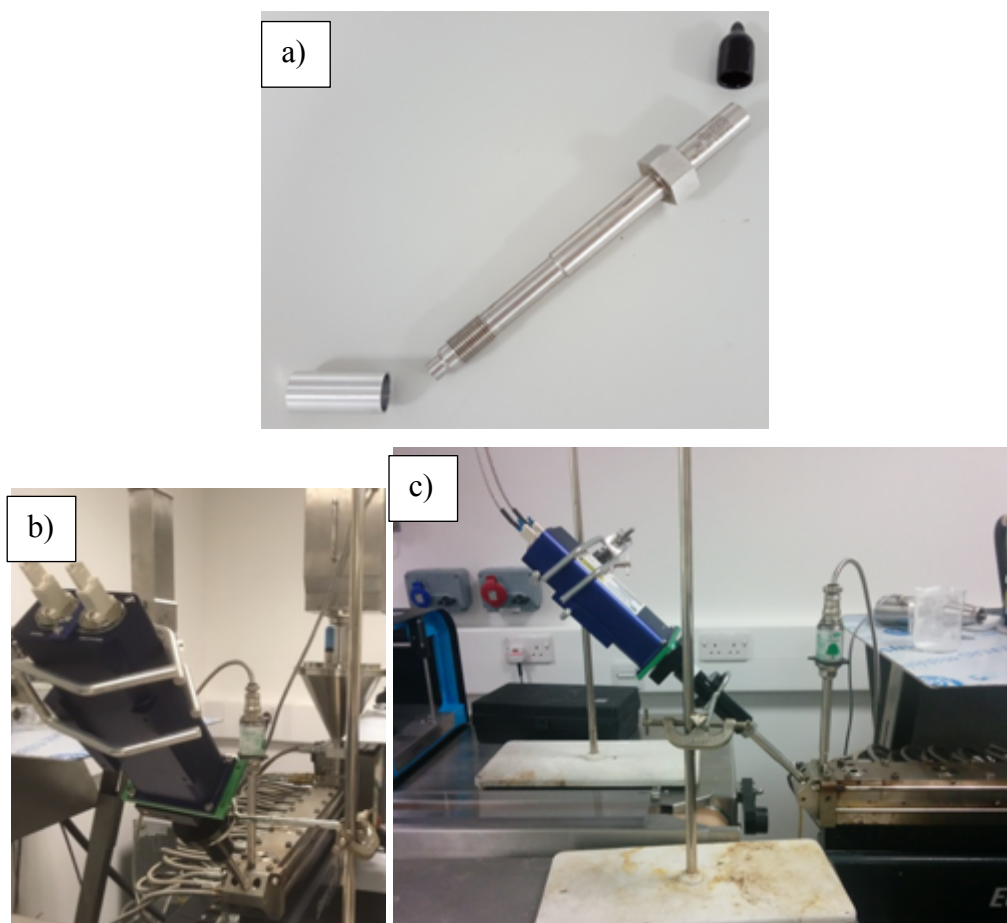


Figure 5.7 In-line Terahertz Raman spectroscopy of HME showing a) the probe used for THz analysis of HME b) the probe in-line looking down the extruder and c) the probe in-situ looking from the side

Samples were collected at each of API concentrations for off-line analysis. The data was analysed in Excel and MATLAB, the 2nd derivative of intensity (with a filter width of 35 points) was calculated for the THz peak at 9.8 cm^{-1} , this was plotted along with PCM powder feed rate vs time.

5.4.3 Off-line analysis of extrudes of PCM - AFF

Samples were collected from 5.4.2 for off-line analysis with XRPD as in section 5.3.1.2 and THz Raman as in 5.3.1.3.

5.4.4 Off-line analysis of stearic acid with THz Raman

0.01g of Stearic acid was melted at 90 °C and then placed onto a flat surface and allowed to cool. The melt – crystalline transition was recorded with THz Raman spectroscopy with a 2 second exposure time and 1 accumulation. Spectra were acquired every 10 s. Spectra were obtained of the raw material, the extruded material and the melt.

5.4.5 In-line analysis of HME Stearic acid with THz Raman

Pure stearic acid was added to the HME via one of the feeders at a powder feed rate of 2 kg/h and a screw speed of 250 rpm, the temperature of barrel in zones 4-10 was varied in two sets of experiments. In the first experiment, the temperature was set to 90 °C, which was then allowed to drop to 60 °C before being increased to 75 °C. In the second experiment, the temperature started at 90 °C and was dropped to 70 °C where it was held until the extrusion had finished. Spectra were acquired every 30 s each with an exposure time of 27 s and 1 accumulation.

5.5 Data Analysis

5.5.1 Principal component analysis

Principal component analysis (PCA) was applied to data sets in order to simplify the data and look at the effects of the key parameters. Each set of data was subject to pre-processing before PCA was carried out. Standard normal variate was applied first then the Savitzky–Golay algorithm was used to calculate the first derivative spectra, this removes the baseline offset, a filter width of 15 points and a 1st order polynomial was used for XRPD, Raman and THz Raman analysis. Finally, for all PCA the data were mean centred.

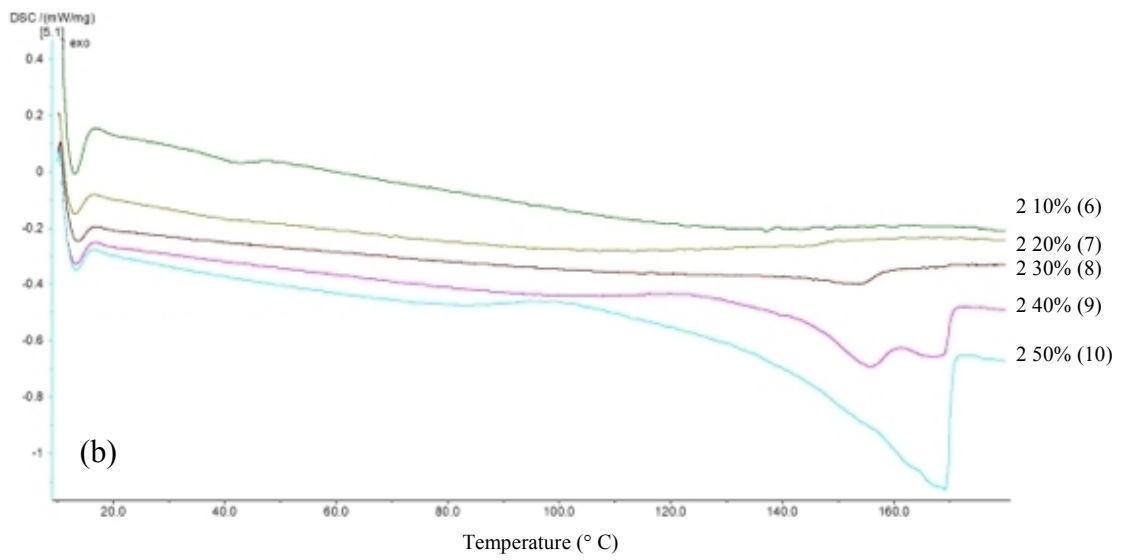
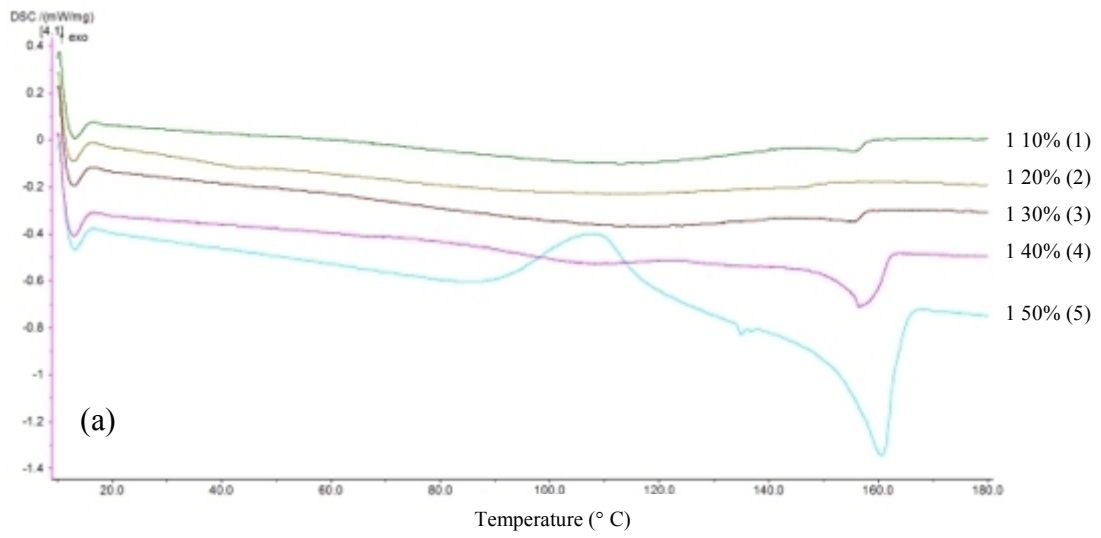
5.6 Results and Discussion

5.6.1 Off-line analysis of amorphous solid dispersions - comparison of DSC, XRPD and Raman spectroscopy with THz Raman for solid state analysis.

5.6.1.1 Results from analysis immediately after production

DSC results

DSC thermograms of PCM-AFF extruded samples analysed immediately after analysis are shown in Figure 5.8 a) to d). The DSC data was compared with that in the literature in order to determine the solid state of PCM present within the samples. A summary of physical transformations of paracetamol by S.Qi et al,¹⁵⁸ described the reported exothermic and endothermic transformation temperatures of PCM by DSC analysis, a summary of this shows that the melting point for Form I was mainly reported to be between 169 to 172 °C^{159 160,161}, but a T_m as low as 157 °C was observed in one study.¹⁶² The T_m for Form II was reported to sit between 157 – 160 °C but some reports are as high as 167 °C.⁵⁸ The T_m for Form III had been reported as 158 - 140 °C. Transitions from the amorphous (A) form were seen at 76, >70, 78–83, 76–79 and 70 °C. Transitions of Form II–Form I were observed at the following temperatures: 156, 161, 122, 120, 115–126 °C. Transition from Form III–Form I was at 130 °C and finally the transition from Form III–Form II was observed at 70–120, 120–130, 125–140 °C. This information was used to study the DSC results.



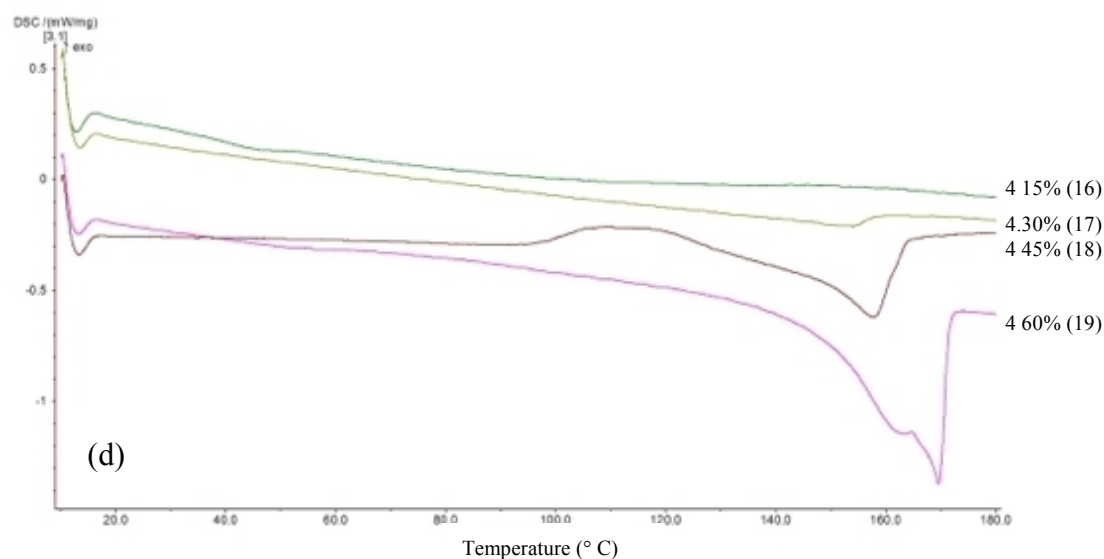
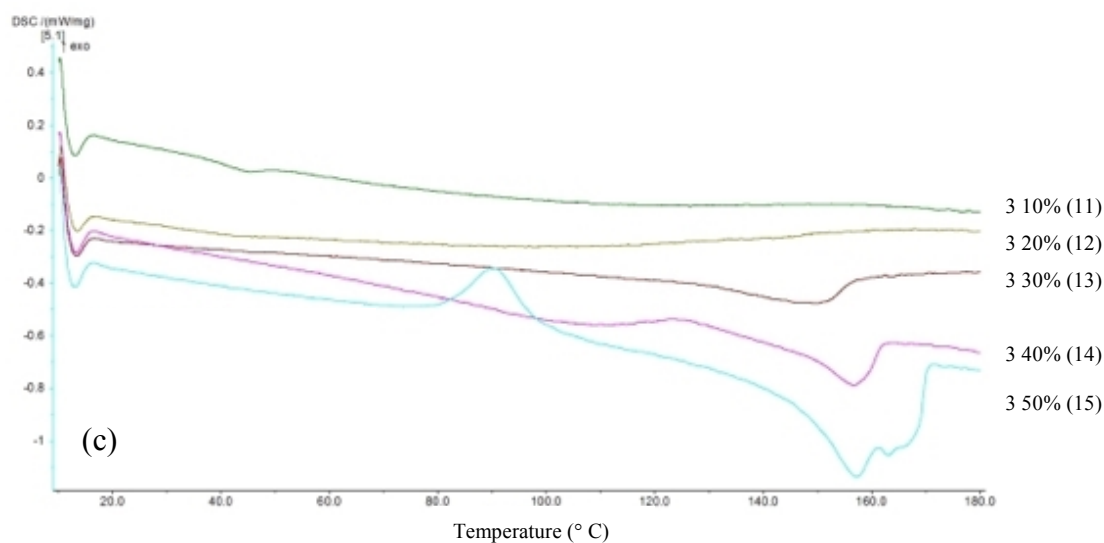


Figure 5.8 DSC thermographs of samples 1 to 19 immediately after analysis (0 months) showing a) experiment 1, samples 1-5 b) experiment 2 samples 6- 10, c) experiment 3 samples 11-15 and d) experiment 4 samples 16-19

T_g can be seen in samples 2, 6, 7 and 11 suggesting the formation of the amorphous form. Samples 2, 6, 7, 11, 12 and 16 all show smooth curves with no endothermic events because of the melting of crystalline material. These smooth curves with absence of exotherms and endotherms is indicative of amorphous material or material with no crystalline. Exotherms present in 5 (110 °C) 15 (90 °C) and 18 (116 °C) are indicative of

amorphous material recrystallising/reordering through the heating process. A few samples with higher drug loadings > 40 wt % show double endothermic peaks. These are present in samples 9, 15 and 19, (40, 50 and 60 wt %, respectfully). Double endotherms indicate that there may be two polymorphs present, the two peaks represent the melting of each of the polymorphs. The exothermic peak for PCM Form II is showing first at 157-158 °C and then for Form I it shows between 168- 169 °C, the endotherm at < 158 °C in sample 15 may be indicative of the presence of Form III. Samples 1, 3, 4, 5, 7, 13, 14, 17 and 18 all appear to show the melting of Form II PCM as they have endothermic peaks between 157 and 158 °C.

XRPD analysis

The XRPD results show in Figure 5.9 were used along with those in the CCSD for analysis of the experimental XRPD results in order to determine the presence of different polymorphs. The main distinctive peaks for FI, FII and FIII observed in the XRPD pattern are given in Table 5.2. These peaks are consistent with the literature and those on the CCSD.^{163, 164}

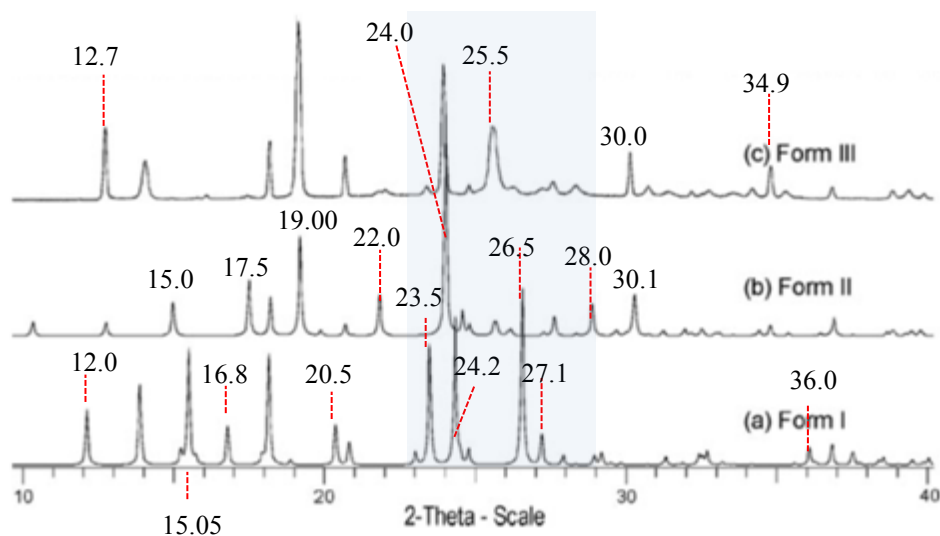


Figure 5.9 XRPD of the known forms of Paracetamol a) Form I, b) Form II, c) Form III taken from the literature highlighting the area with the most differences ¹⁶³

Table 5.2 Distinctive polymorphic XRPD pattern peaks for paracetamol

| Solid form | 2 – Theta |
|------------|--|
| FI | 12.0, 15.5, 16.7, 20.5, 23.5, 24.2, 27.1, 36.0 |
| FII | 15.0, 17.5, 19.00, 22.0, 24.0, 28.0, 30.1 |
| FIII | 12.7, 25.5, 30.0, 34.9 |

The experimental results from the XRPD analysis of the extrudates immediately after extrusion are shown below in Figure 5.10 a) to d).

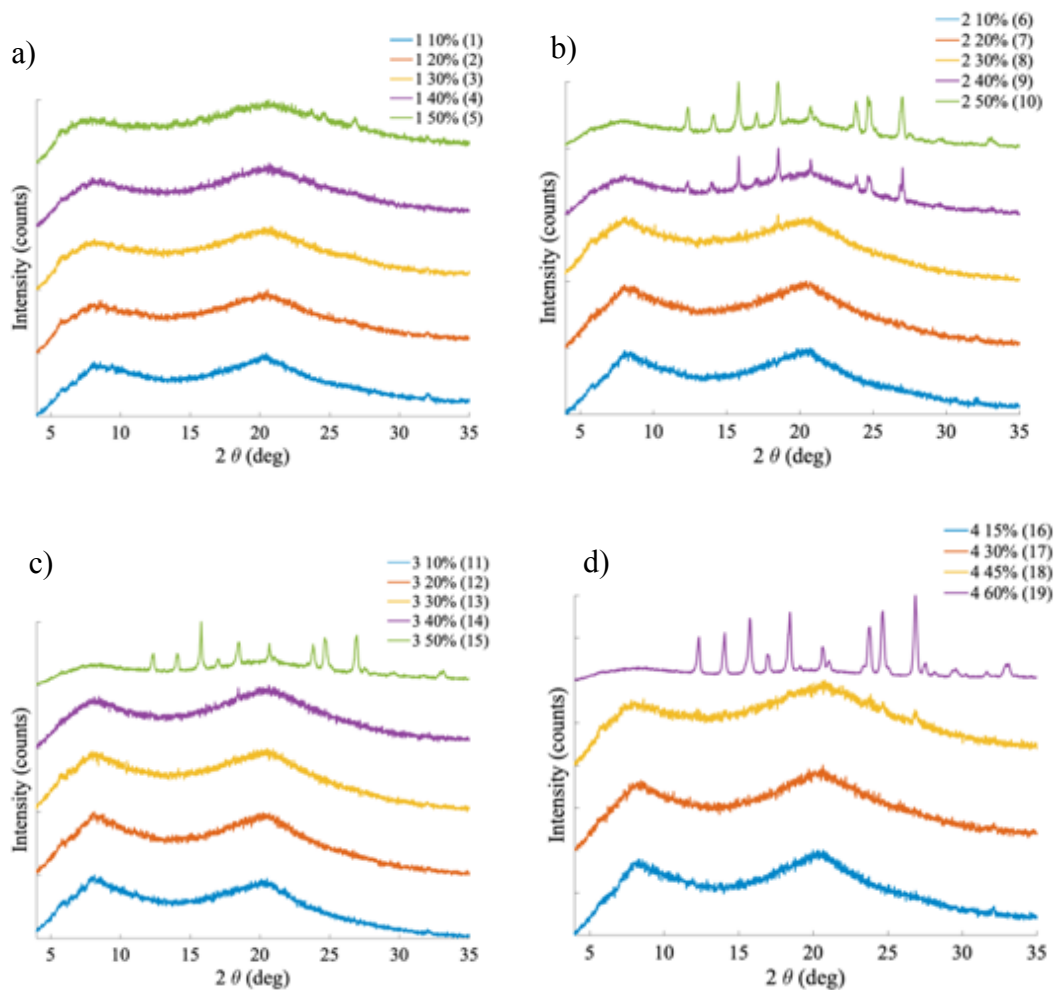


Figure 5.10 Results of XRPD analysis of hot melt extruded PCM-AFF samples immediately after analysis (0 months) showing a) experiment 1, samples 1-5 b) experiment 2 samples 6- 10, c) experiment 3 samples 11-15 and d) experiment 4 samples 16-19

Crystalline material is present in the higher drug loadings, with sample 1 showing almost negligible peaks, similar to those in sample 18, it is assumed that these are mostly amorphous material. Experiment 1 samples were extruded at the highest temperature and a mid to high screw speed. At 0 months the XRPD results show crystalline peaks in samples 9, 10, 15 and 19, with small crystalline peaks evident for sample 5. From comparison with the results in the literature and the XRPD results in Figure 5.9, the crystalline

samples show peaks distinctive of FI but in sample 9 (experiment 2 with 50 wt % drug loading) the peak indicative of FI at 24.2 ° is showing a split at the top which could indicate the presence of the FII peak at 24 °, these are very close to each other so the presence of both forms could be hard to detect with a lack of defined peaks, however the lack of presence FII peaks at 17.5, 19.0 and 15.0 ° suggests that FII may not be present. It is also unknown what the effect that AFF has on the XRPD pattern. Samples 2 - 5, 8 - 10, 13-15 and 17- 19 with low drug loadings (30 wt %) all show amorphous content with some negligible peaks present in sample 18.

Overall, samples extruded in experiment 1 showed the least crystalline material present across all drug loadings of PCM, these experiments were performed with the highest barrel temperature at 180 °C and a screw speed of 200 rpm. Whereas the samples extruded in experiment 2 showed the most crystalline content across the drug loadings, these were produced at 1kg/h feed rate, 160 °C and the lowest screw speed of 100 rpm.

PCA on the XRPD data shown in Figure 5.10 was carried out in order to try and simplify the information from the analysis. The scores plot of PC1 vs PC2 is plotted in Figure 5.11. PC1 and PC2 describe 92.64% of the variance in the data.

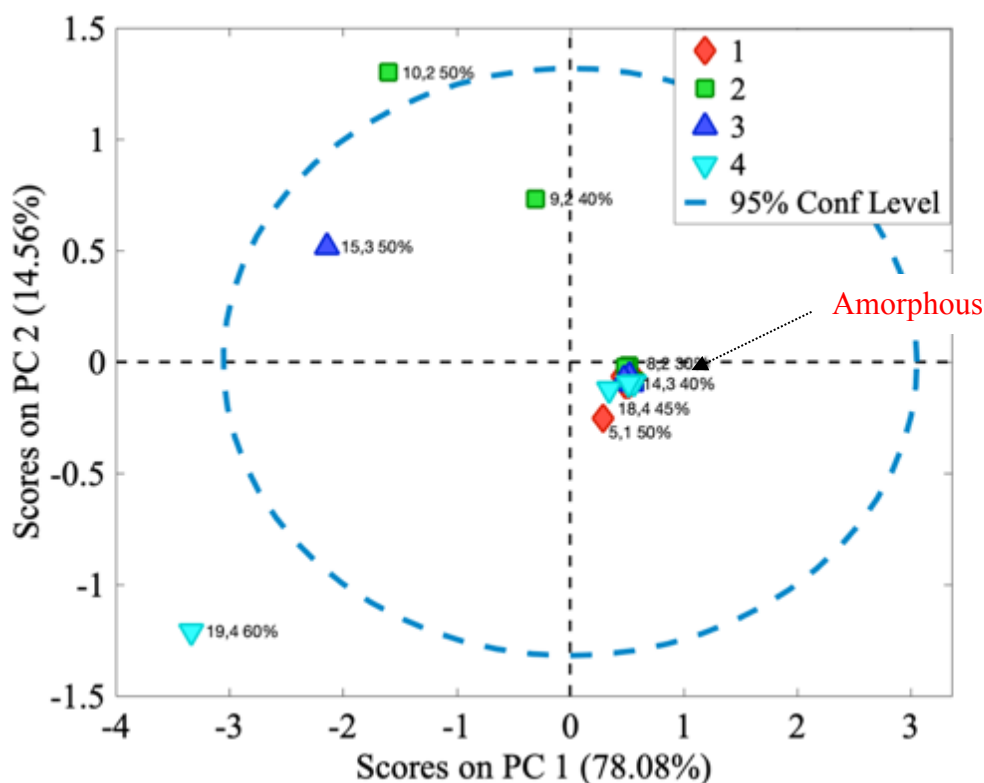


Figure 5.11 PCA scores plot for XRPD analysis of HME solid dosage forms obtained immediately after production.

The PCA results show that the amorphous samples have a similar PC1 and PC2 score (close to zero) while the crystalline samples have negative PC1 scores and vary in terms of their PC2 score. Samples 9 and 10 were both produced under the same experimental conditions (experiment 2) and have the highest PC2 scores. These were produced at the lowest screw speeds, medium an and therefore would have the longest residence time within the extruder. Sample 15 from experiment 3 was produced at the highest feed rate and screw speed with the set point temperature this has a positive PC2 score but a negative PC1. The biggest outlier is sample 19 from experiment 4, this had the highest drug loading at 60% and was also produced with set point feed rates and processing

temperature with a low-mid screw speed. Sample 19 also shows the most intense and sharpest crystalline peaks in the XRPD results.

The XRPD results were in good agreement with the DSC results in terms of absence of crystalline material, but the presence of different polymorphic forms was not detected for any of the samples showing crystallinity. The presence of these in the DSC analysis are thought to be thermally induced by the heating involved in DSC analysis, as reported by Bordos et al.⁹⁷

THz Raman Spectroscopy

THz Raman spectroscopic analysis of the samples immediately after extrusion are shown in Figure 5.12. The initial study was to look at the THz region to see the response in comparison to the results shown in Figure 5.10 as a direct comparison of THz with XRPD for the analysis of the ASDs for the potential of THz as an alternative, fast real time analysis. The full Raman spectral range is analysed later in this chapter.

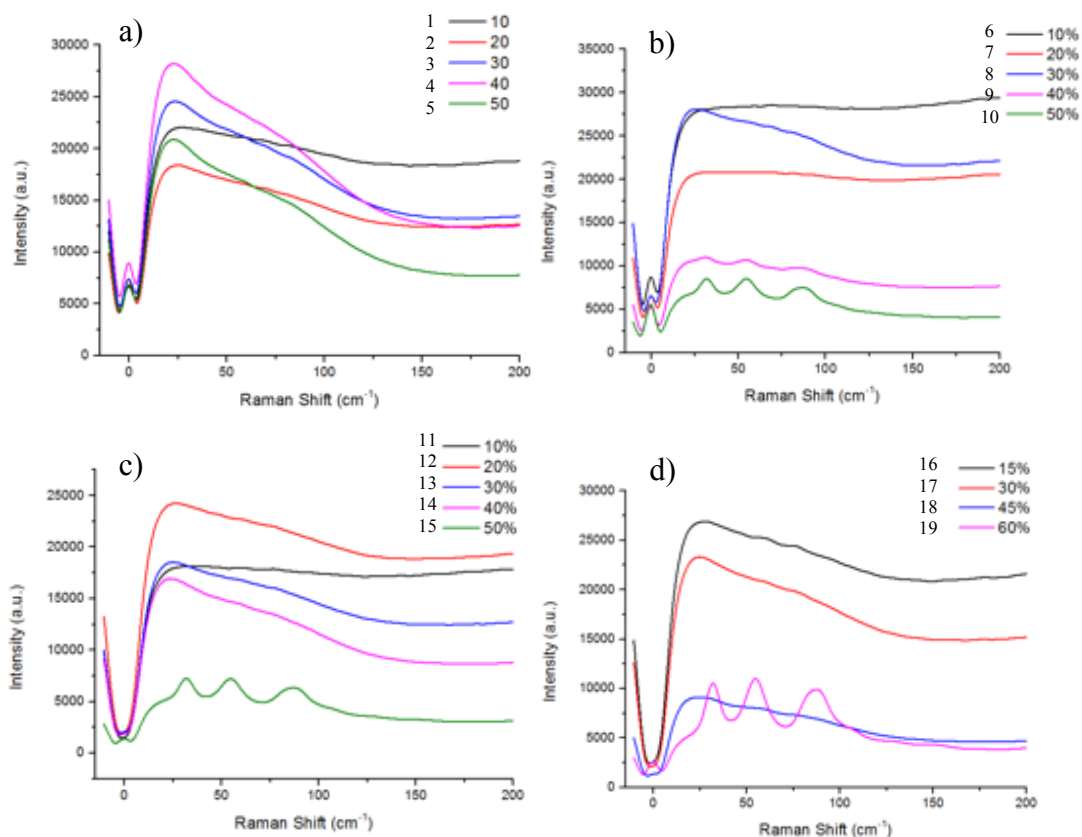


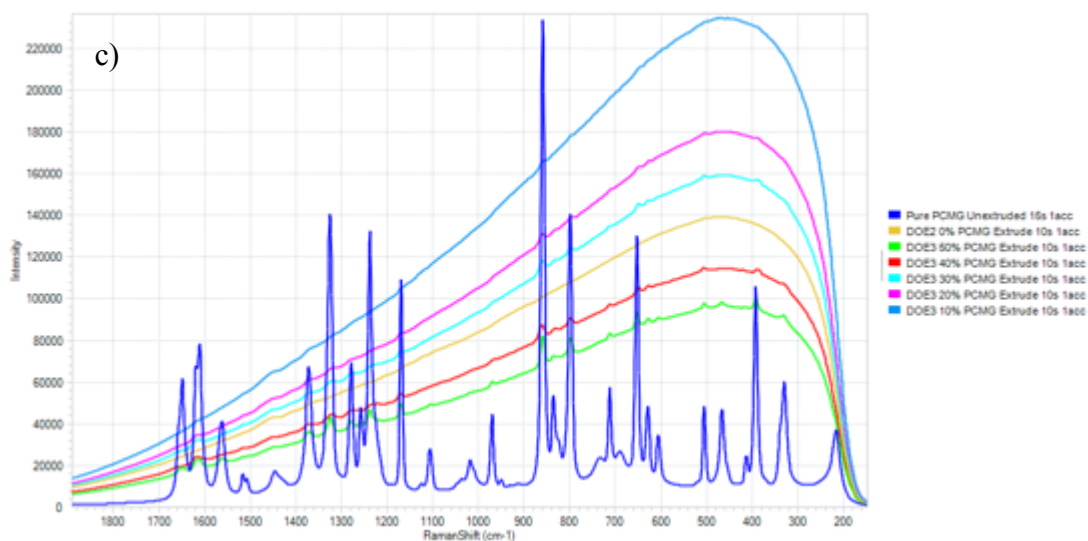
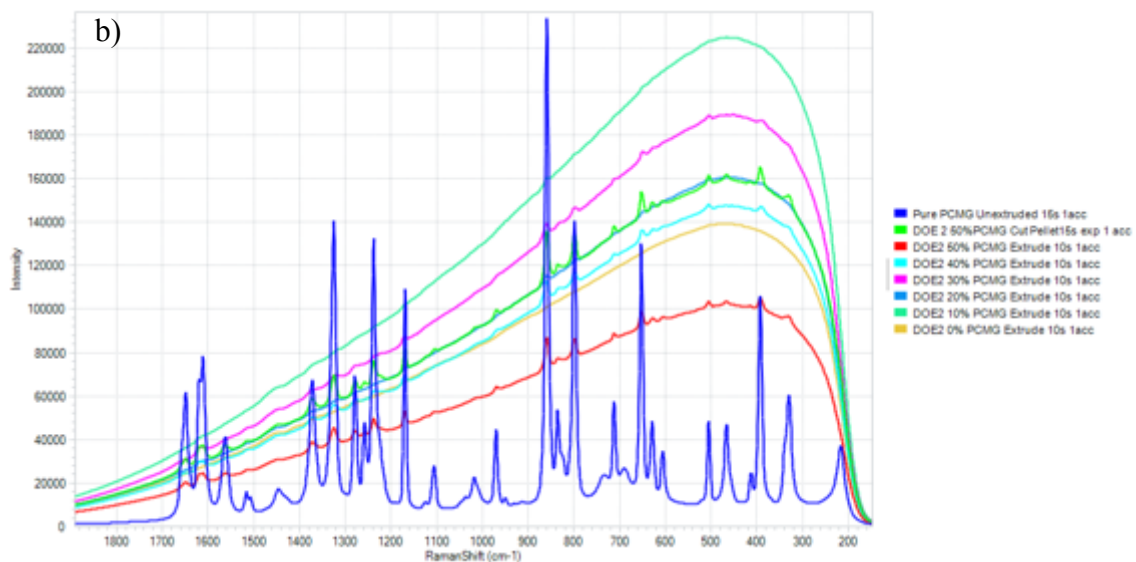
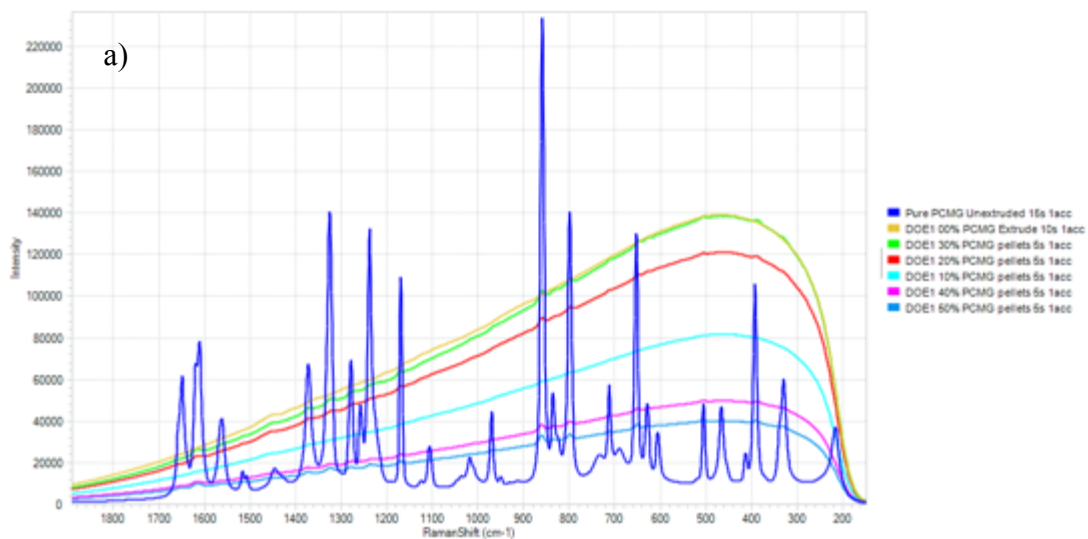
Figure 5.12 THz Raman spectroscopic analysis of pelleted samples 1 to 19 immediately after analysis (0 months) showing a) experiment 1, samples 1-5 (10-50% respectively) b) experiment 2 samples 6 - 10 (10 to 50 % respectively) , c) experiment 3 samples 11 - 15 (labelled 10 to 50% respectively) and d) experiment 4 samples 16-19 (labelled from 15-60 % respectively)

Three peaks in the THz region appear when there is crystalline material present, these are at 32, 56 and 89 cm^{-1} and are indicative of the presence of form I PCM.¹⁶⁵ The small amount of crystalline material present in the XRPD analysis of sample 5 from experiment 1 is not as obviously detectable in this case by THz Raman spectroscopy, the results for all the samples in experiment 1 show smooth peaks indicative of amorphous material. Crystalline peaks are however present in samples 9, 10, 15 and 19 which is in good agreement with the XRPD results. The amorphous content appears in the THz Raman region

as a smooth curve and the presence of crystalline material shows as the formation of peaks. The peaks are not as sharp as those present in the XRPD results but provide a good indication of the presence of crystalline material. The XRPD results for each of the samples takes about 25 minutes to complete whereas the THz Raman results can be produced in a few seconds, moreover THz Raman can be implemented on-line and in-line very easily. One of the most popular methods for in and on-line analysis is Raman spectroscopy, although not shown in this section, both the mid and low frequency Raman spectral ranges are acquired with the Ondax THz Raman probe, showing again the benefit of this method for analysis. In the next section the samples were analysed off-line with Raman spectroscopy in order to look at the ability to detect amorphous and crystalline materials.

5.6.1.1.1 Raman analysis

Raman analysis of pellets for experiment 1 and extrudes for 2-4 immediately after extrusion are shown in Figure 5.13 a) to d).



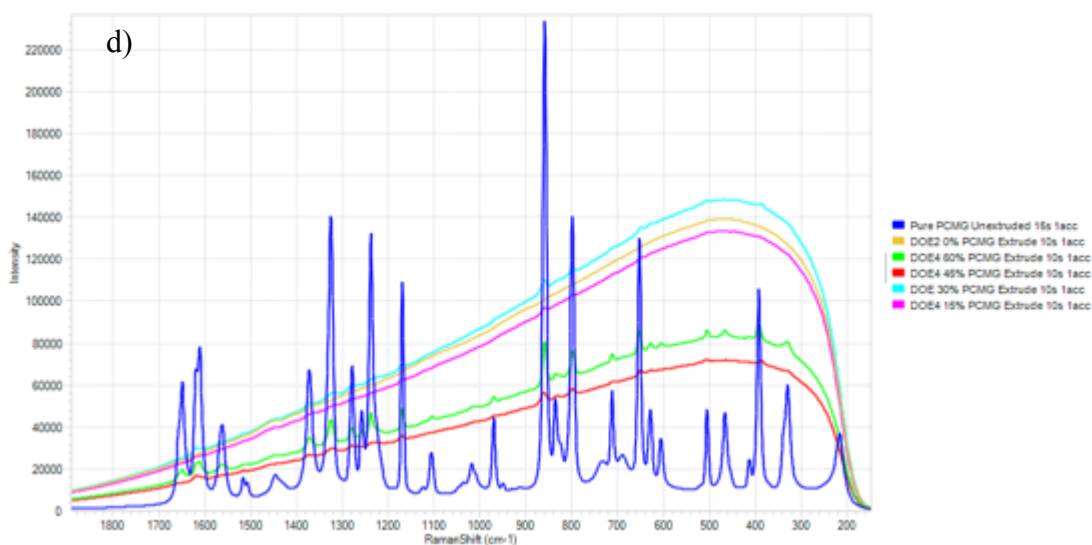


Figure 5.13 Raman spectra of samples 1 to 19 0 months after production showing a) experiment 1, samples 1-5 b) experiment 2 samples 6- 10, c) experiment 3 samples 11-15 and d) experiment 4 samples 16-19.

The mid frequency Raman spectroscopy (MFRS) results show structural peaks in the higher drug loading samples. Amorphous peaks are not as obvious to spot within mid Raman “fingerprint” region and in this case, it appears as if the structural peaks are masked by fluorescence from the affinisol. Amorphous material usually presents as broader peaks rather than being absent as in THz Raman. This is because the information in the THz region comes from the phonon mode vibrations which give information on the crystallinity whereas as the peaks in the Raman fingerprint region comes from the vibrational modes within the molecule. From comparison to the PCM Raman spectra for form I powder plotted with each sample it appears that all those samples with small peaks contain Form I of PCM although it is hard to be sure in this case due to the lack of defined structural peaks, the presence of AFF appears to be masking a lot of the signal form the PCM. In experiment 2 there are two spectra for the sample with the drug loading of 50%, one of these is of the extrude and the other is of the same sample but cut into a pellet.

The peaks in the pelleted sample appear to be a little more intense than those of the extrude, this was done as a test experiment to see if there would be a difference in the results and formed the basis of the homogeneity study described later in this chapter.

5.6.1.2 Analysis of aged amorphous solid dispersions samples

The higher energy of the amorphous state in ASDs leads to instability with aging much more than crystalline dispersions, it is therefore essential to understand the crystalline behaviours of the solid forms within these dispersions for the design and development of more safer and stable products.^{166 167}

There has been some research on the stabilities of amorphous solid dispersions and their analysis. Yang et al.¹⁶⁶ used XRPD, ATR-FTIR, and imaging techniques (SEM, AFM and thermal analysis) to observe the physical stabilities of the surfaces of ASDs produced with 10 – 90% drug loadings of felodipine-EUDRAGIT® E PO. The ASDs were produced using spin coating and HME, and samples were aged over 10 months. It was found that the API in samples produced at high drug loadings (50 to 90%) by HME crystallised out shortly after preparation and that the spin coated material had significantly higher surface stability. This stability was thought to be attributed to the increased process related apparent drug–polymer solubility and reduced molecular mobility due to the quenching effect from the rapid solvent evaporation in spin coating. Benefits of HME are that it is solvent free, continuous and has the ability to process high volumes of material, whereas spin coating is more of a laboratory-based method.

5.6.1.2.1 XRPD analysis of aged samples

XRPD results from the samples that had been stored for five months are shown in Figure 5.14 a) to d).

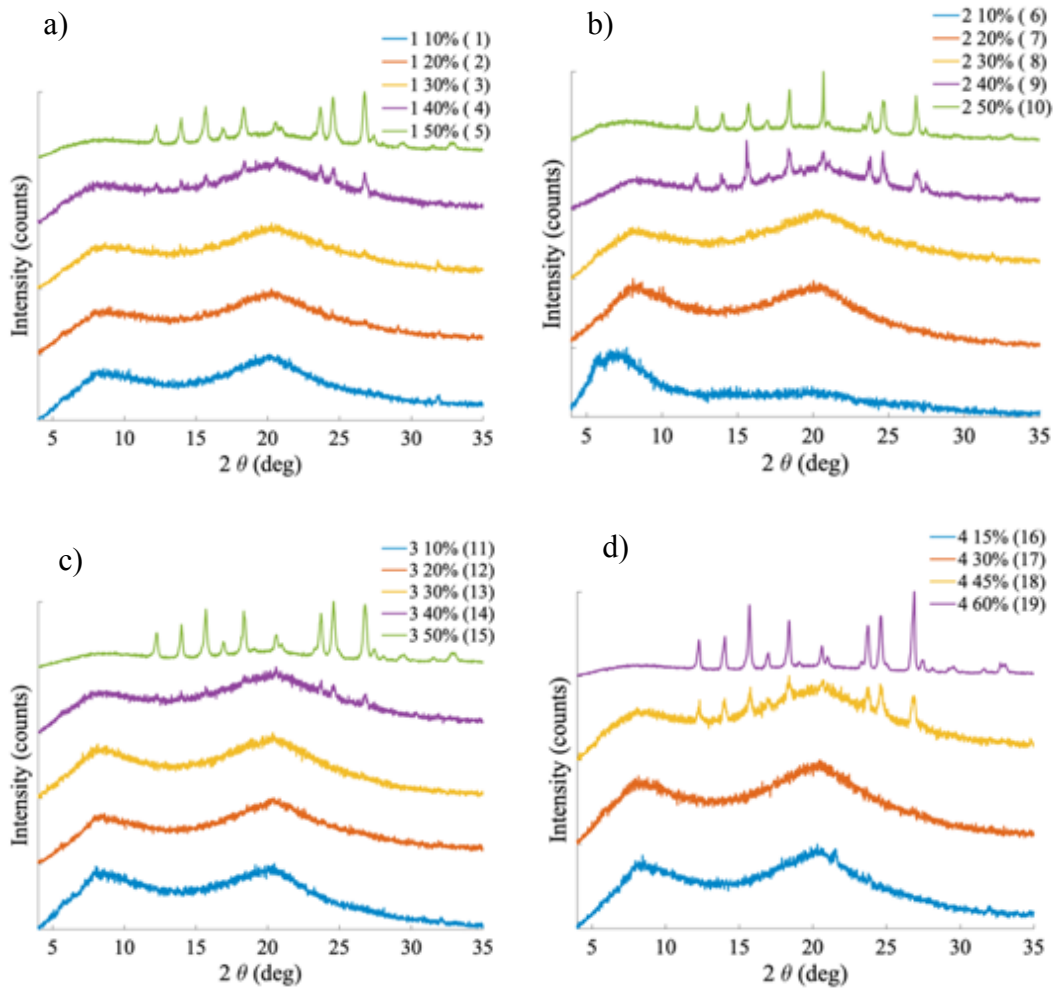


Figure 5.14 Results of XRPD analysis of hot melt extruded PCM-AFF samples after 5 months showing a) experiment 1, samples 1-5 b) experiment 2 samples 6- 10, c) experiment 3 samples 11-15 and d) experiment 4 samples 16-19

The XRPD results obtained in experiments 1 to 4 for those samples exhibiting crystalline content immediately after extrusion (labelled 0) and five months post extrusion (labelled

5) are plotted for 40 and 45 wt % drug loadings in Figure 5.15 and for 50 and 60 wt % drug loadings in Figure 5.16.

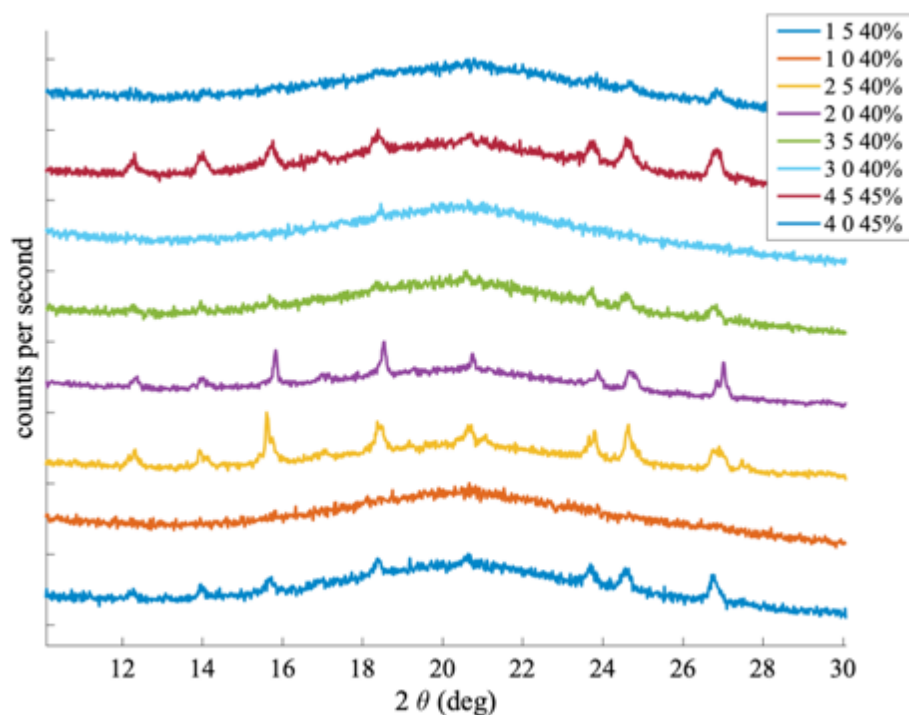


Figure 5.15 Offset XRPD results for 40 and 45% drug loadings of HME samples analysed immediately after analysis (labelled 0) and five months post extrusion (labelled 5) for samples 4 (experiment 1 - 40 wt %), 9 (experiment 2 - 40 wt %), 14 (experiment 3 - 40 wt %) and 18 (experiment 4 - 45 wt %)

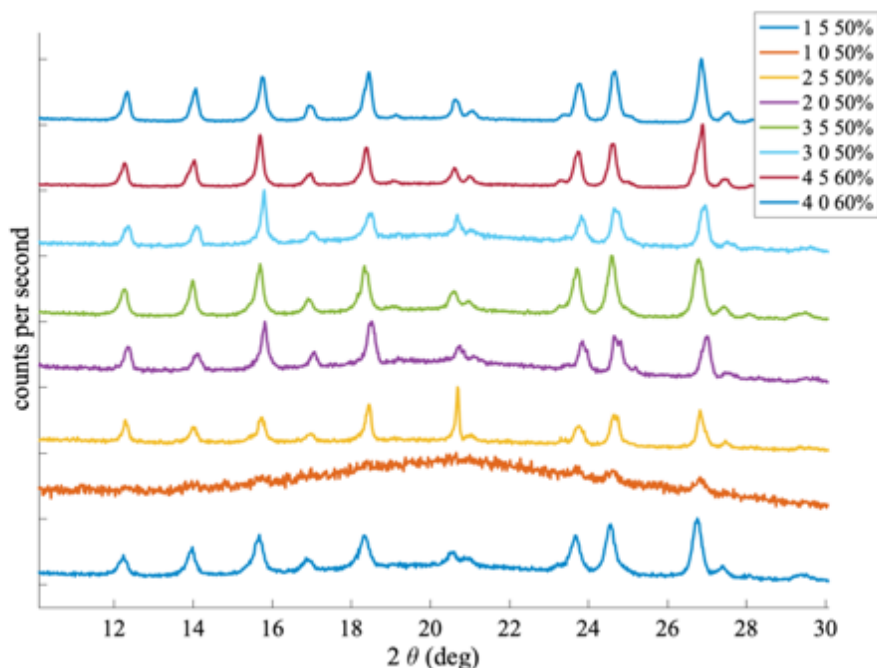


Figure 5.16 Offset XRPD results for 50 and 60% drug loadings of HME samples analysed immediately after analysis (labelled 0) and five months post extrusion (labelled 5) for samples 5 (experiment 1 - 50%) , 10 (experiment 2 - 50%) 15 (experiment 3 – 50%) and 19 (experiment 4 – 60%)

The XRPD results show an overall increase of crystalline material present after 5 months in storage when compared to those analysed immediately after production (Figure 5.10). An increase in peak height is indicative of an increase in crystalline content. Samples with high drug loadings > 40 wt % all show an increase in peak height. The sharp peak in sample 10 at 20 degrees has been compared¹⁶³ to XRPD results for other polymorphic forms of PCM, it appears to only contain Form I despite this unusually high peak. There is a similar peak present in Form III PCM but the lack of other significant peaks for Form III makes this unlikely. PCA was carried out on the XRPD results to try and determine the differences between the samples analysed immediately after extrusion (0 months) and 5 months after storage. The results for these are listed in the next section. Experiment 1

was extruded at the highest temperature at 180 °C. Samples containing PCM concentrations of 40% and above showed an increase in crystalline content after being stored for 5 months. This suggests that extrudates containing higher concentrations of PCM are less stable than those containing lower concentrations of PCM or that XRPD analysis was unable to detect crystalline material at these concentrations. Minimal crystalline PCM was evident in samples containing PCM at concentrations less than 40 wt %.

The scores plot from PCA of the XRPD results of the 5-month-old samples are shown in Figure 5.17. PC1 and PC2 describe 89.24% of the variance in the data.

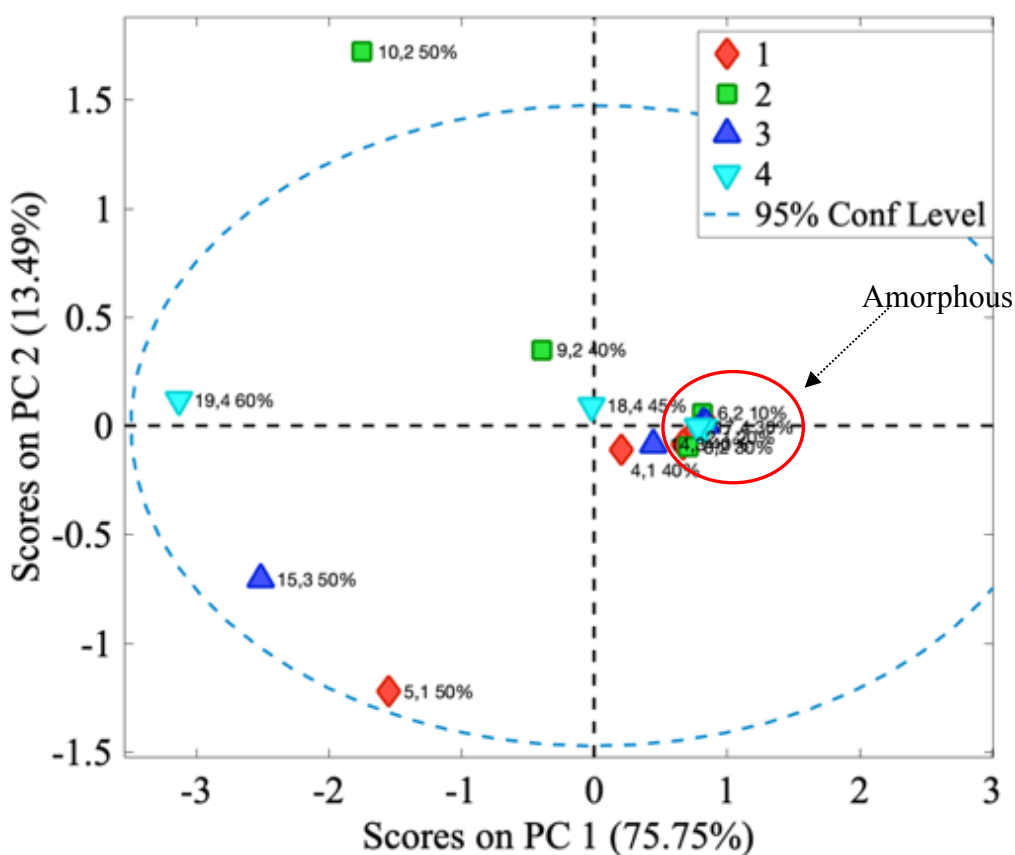


Figure 5.17 PCA scores plot for XRPD analysis of HME solid dosage forms obtained 5 months post extrusion

The PCA results show similar trends to those in Figure 5.11 in that the amorphous samples all have similar PC1 and PC2 score (close to zero) while the crystalline samples have negative PC1 scores and vary in terms of their PC2 score. Sample 10 (experiment 2 at 50 wt % drug loading) is out with the 95% confidence level and is the sample that shows the largest peak around 21°.

PCA of the XRPD results from 0 and 5 months was carried out in order to do a direct comparison. The scores plot of PC1 vs PC2 is shown in Figure 5.18. PC1 and PC2 describe 86.48% of the variance in the data.

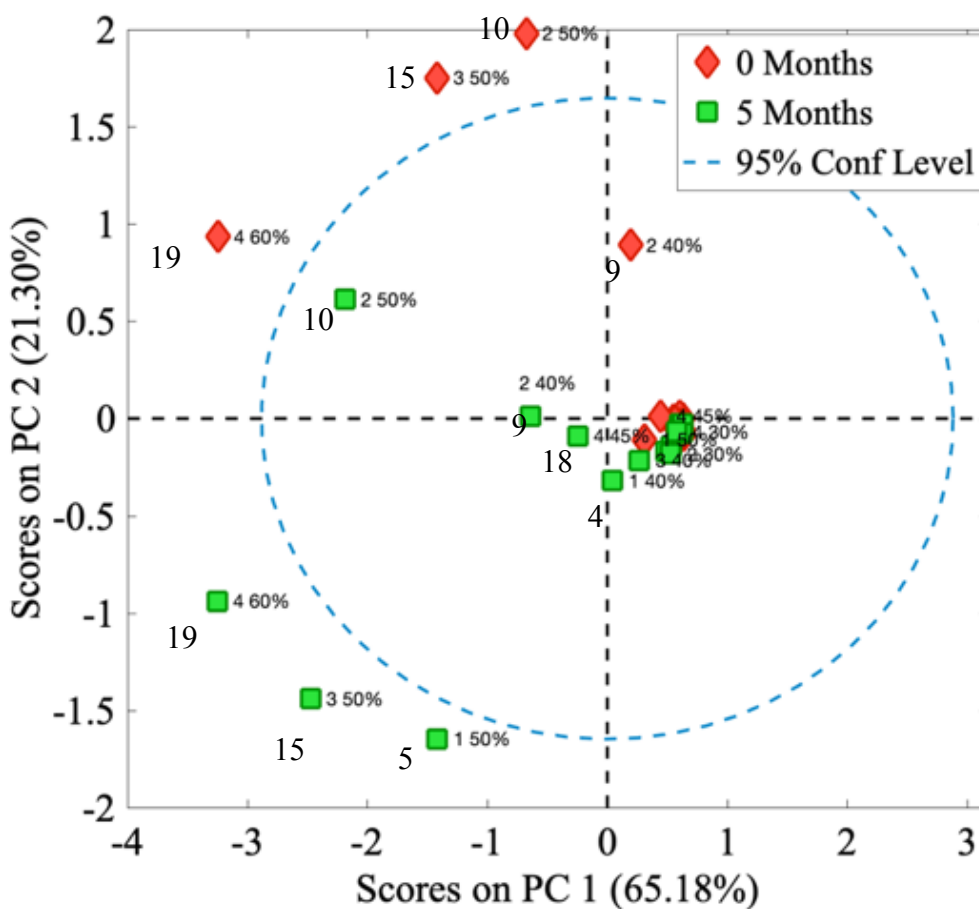


Figure 5.18 PCA scores plot for XRPD analysis of HME samples obtained immediately after extrusion and 5 months post extrusion, labelled by experiment number and API concentration with the sample numbers added.

Again, the amorphous samples are grouped together with PC1 and PC2 scores close to 0. In this case, a clear divide can be seen between the samples at 5 months old and those at 0 months. Looking at the loadings for PC1 and PC2 in Figure 5.19 shows that PC1 is mostly describing an increase in the crystalline peaks, while PC2 describes a change in the peaks for the higher diffraction angles and the differences between the peaks.

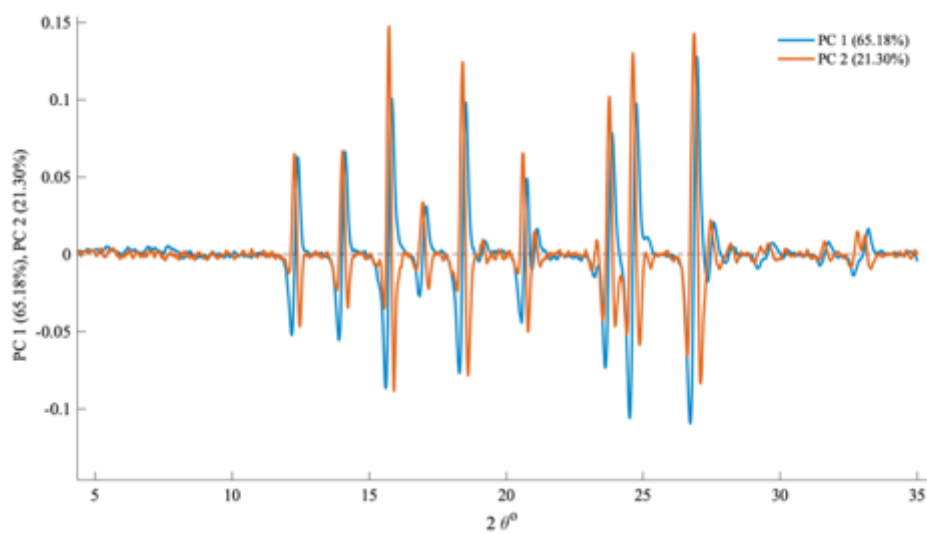
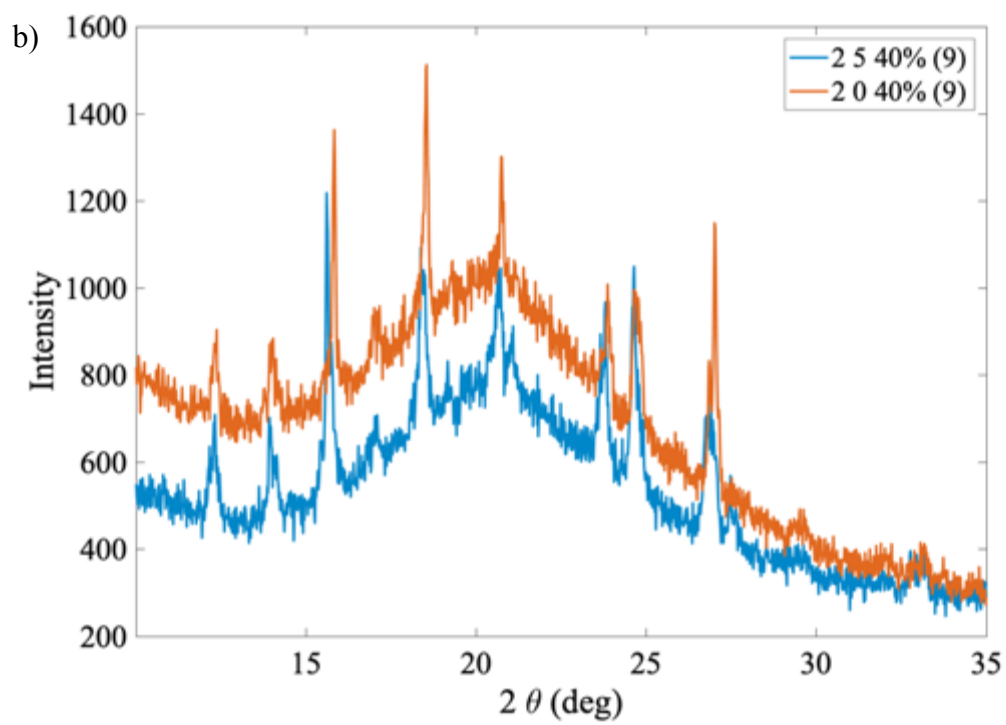
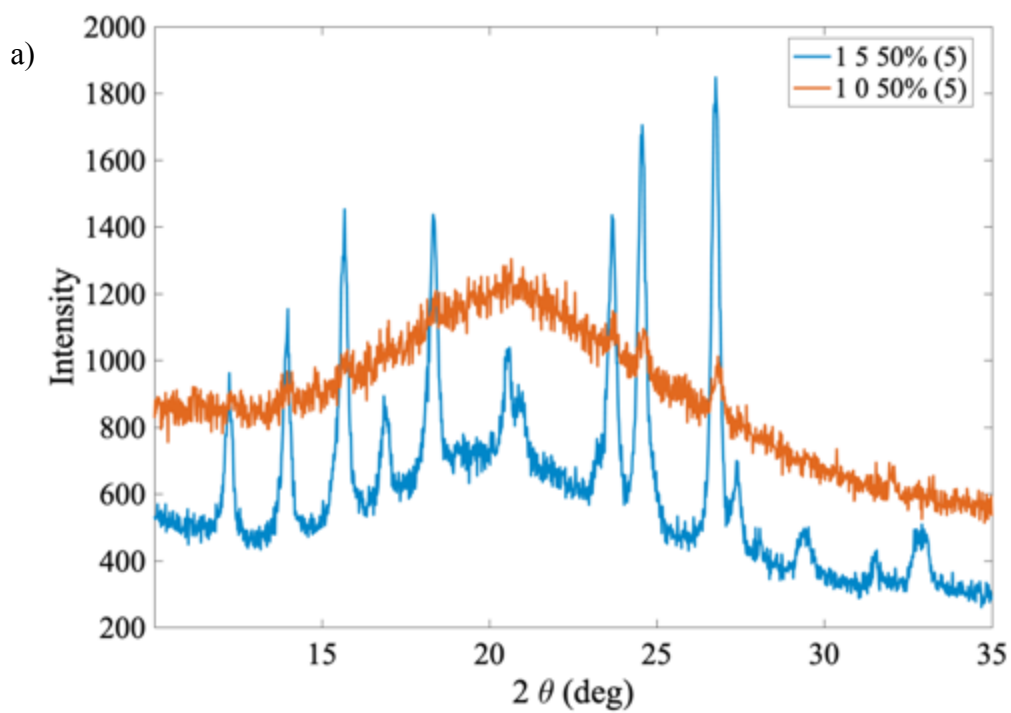
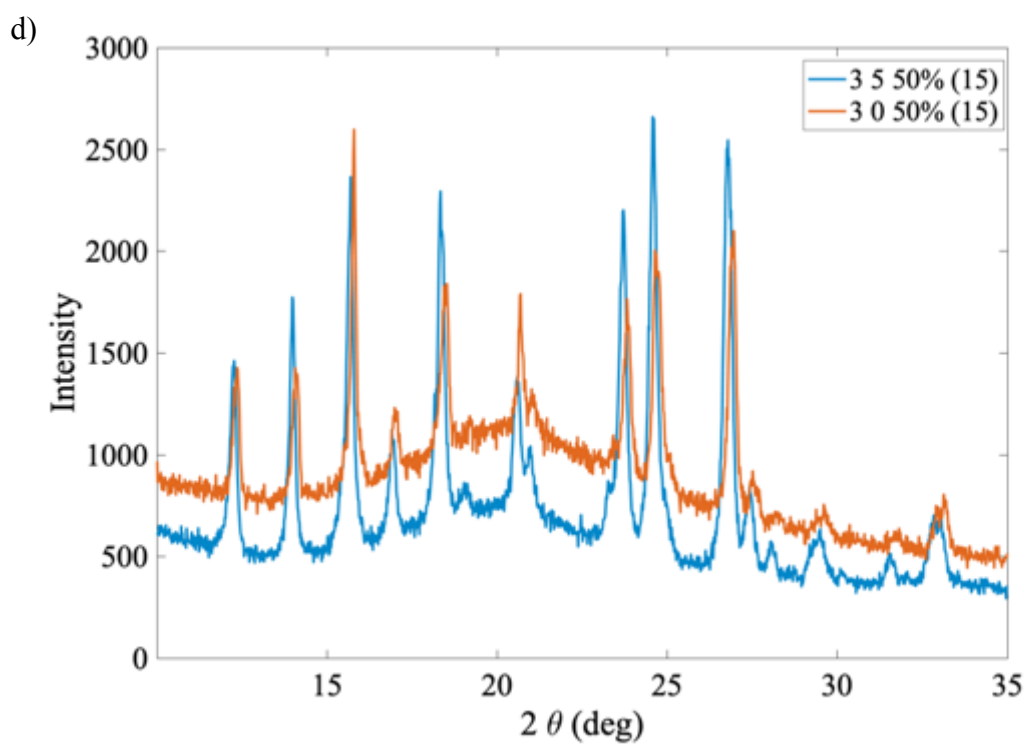
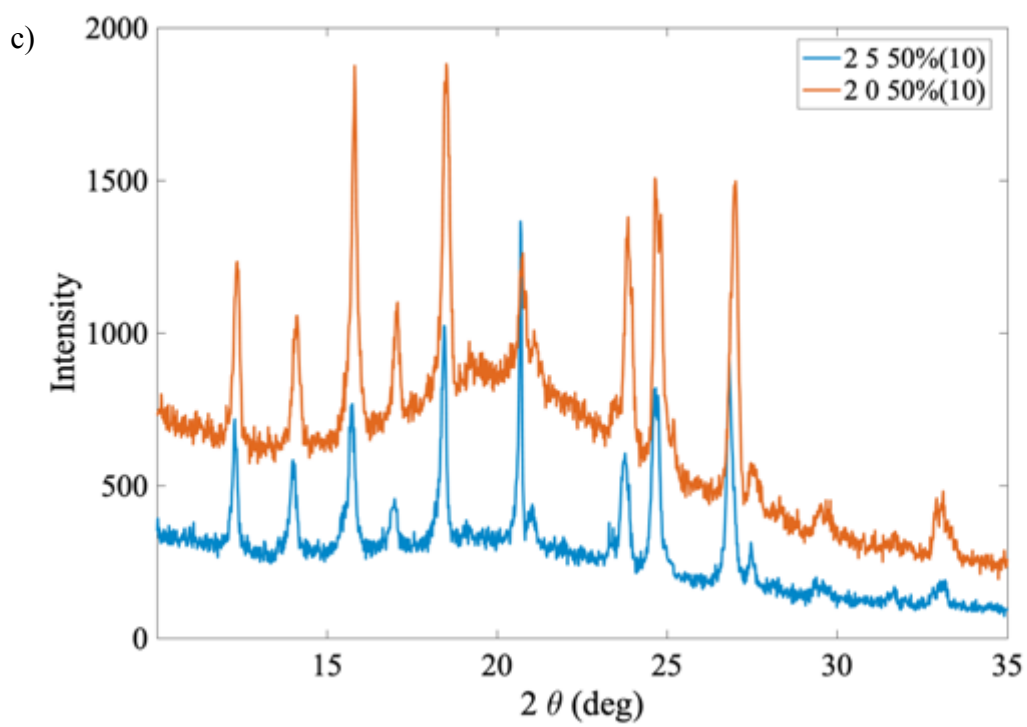


Figure 5.19 Loadings of PC1 and PC2 for PC analysis of XRPD results for 0 and 5-month-old HME samples.

Overlay of the XRPD patterns for samples with a negative PC1 score (5, 9, 10, 15 and 19) at 0 and 5 months are shown in Figure 5.20.





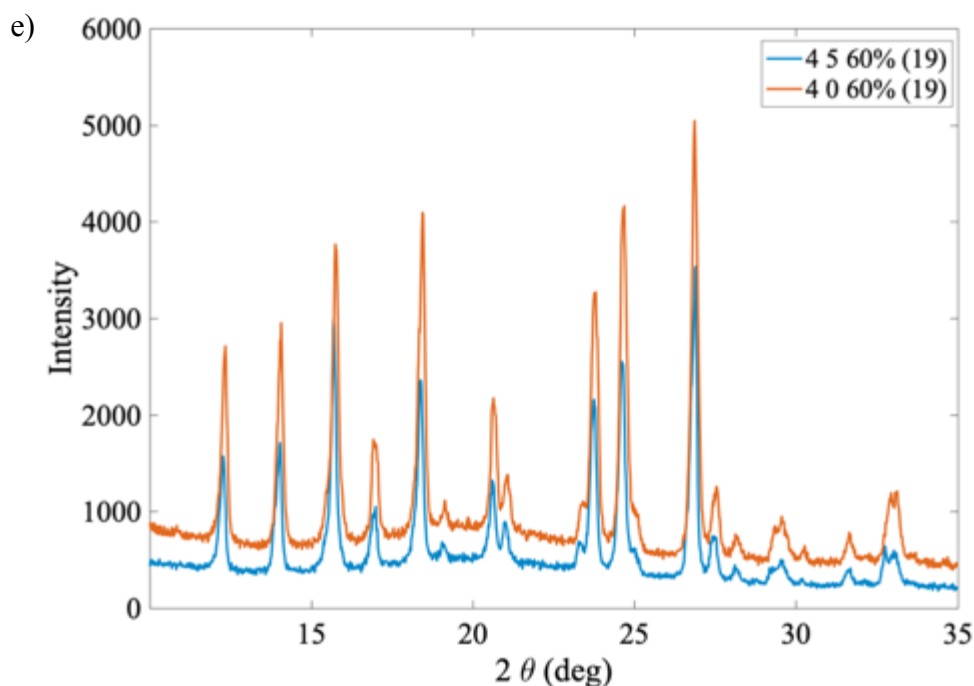


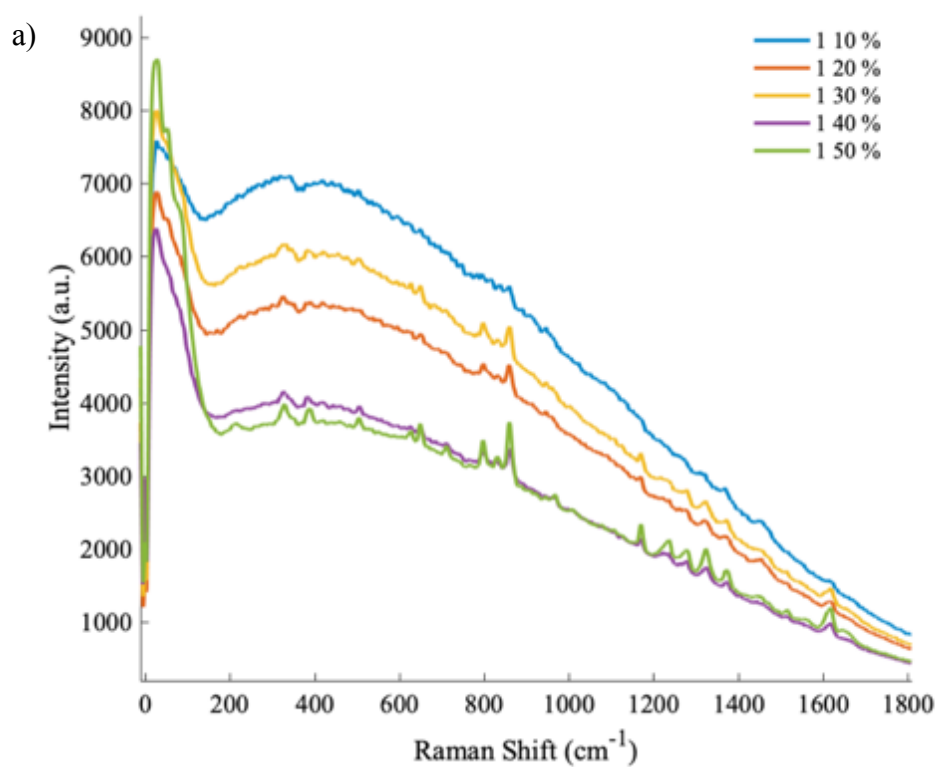
Figure 5.20 Overlay of XRPD patterns for samples 5, 9 10, 15 and 19 (a) to e) sub-jectively) showing in each the sample at 0 months in red and 5 months in blue.

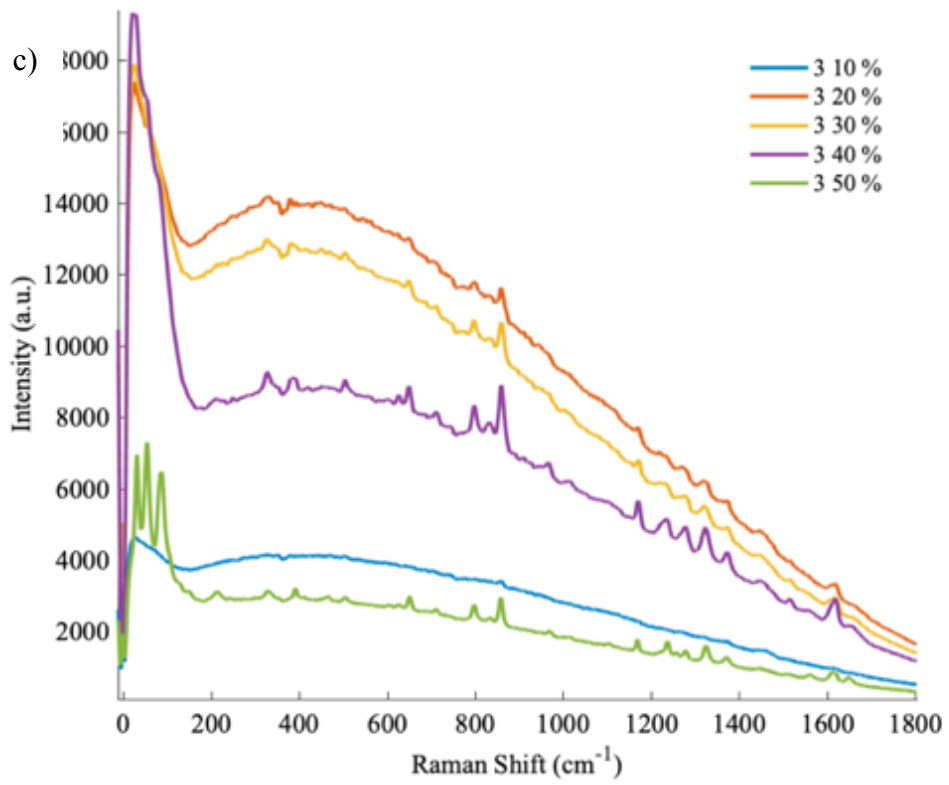
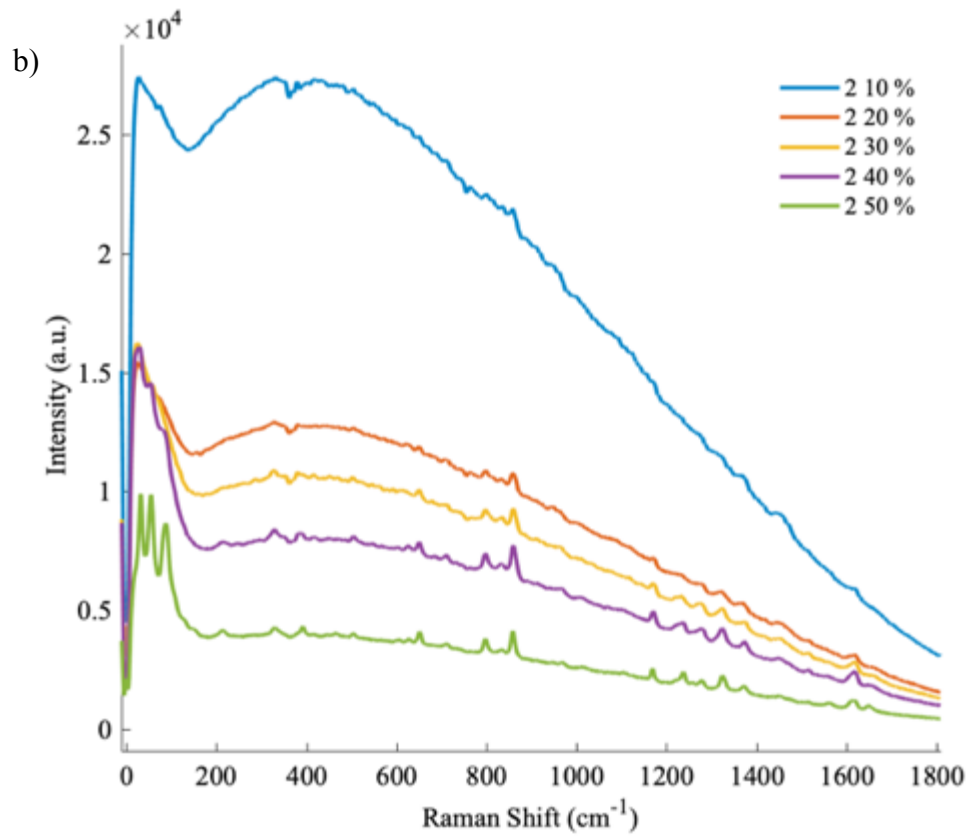
As the samples have aged there is more crystalline API present, those with a higher crystalline content have negative PC2 scores except for sample no 10 (experiment 2 at 50 wt % drug loading) this sample is the outlier in the XRPD plots shown in Figure 5.16 with a sharp peak around 21°. More defined crystalline peaks give rise to more negative PC2 scores so as the samples crystallise with time their PC2 score becomes negative. Those that appear amorphous within the XRPD show the same grouping as in Figure 5.11 and Figure 5.17. THz Raman analysis of the samples was carried out in order to try and better understand the differences between the samples observed from PCA of the XRPD data and to compare with the XRPD plots of the aged samples. Instrument error was excluded as the cause of the peak shift, the XRPD results were obtained with the same experimental

conditions on the same instrument, also not all the peaks in the XRPD patterns are shifted as would be expected if there was an instrument error.

5.6.2 THz Raman analysis

THz Raman spectra were collected from pelleted samples five months post extrusion. Example spectra from multiple pellets measured for each of samples are plotted showing the full low and mid-frequency Raman spectra ($0 - 1800 \text{ cm}^{-1}$) are shown in Figure 5.21 plots a) to d).





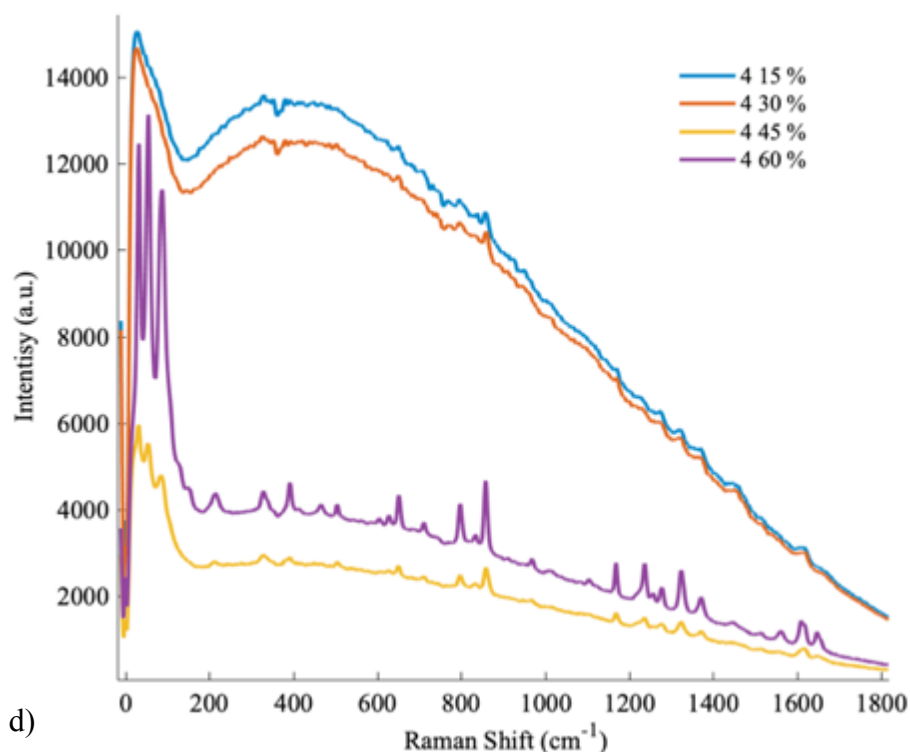


Figure 5.21 Low and mid-frequency Raman spectra of pelleted extrudes from samples at each of the drug loadings for the four different experiments showing a) experiment 1, b) experiment 2, c) experiment 3 and d) experiment 4.

For experiment 1 (see Figure 5.21 a)) all of the samples with drug loadings below 50 wt % appear to be amorphous, the sample with 50 wt % drug loading is showing small number of crystalline peaks suggesting this sample contains a small amount of crystalline material but is mostly still amorphous. The XRPD results for experiment 1 suggest that both drug loadings of 40 and 50 wt % contain crystalline material. For the other three experiments (see Figure 5.21 b), c) and d)) samples with loadings < 30 wt % all appear amorphous and drug loadings above that contain some crystalline material i.e. semi amorphous. The Raman peaks that are present across the spectra for all experiments all appear to only contain Form I of PCM. The increase in drug loading causes a drop in the

fluorescence background and the appearance of peaks, indicating that less affinisol is present in the sample and more intense crystalline peaks. There are large variations in the intensities of spectra of samples of similar concentrations and this is thought to be due to the slight variations in the distances of the samples from the laser and the degree of crystalline material present in the laser spot.

XRPD and THz Raman spectroscopy both show peaks that indicate that solid form material is present. XRPD has sharper more defined peaks than the THz region, XRPD also has a lot more information on the structure of the molecule, this is due to affinisol masking the fingerprint region in the Raman spectra in this case. THz Raman proved to be a good alternative for the determination of amorphous and crystalline content in HME extrudes. DSC results were in good agreement with the amorphous content of extrudes but multiple polymorphs appeared not to be present within the thermal analysis that were not detected in low (THz) and mid frequency Raman or XRPD. Raman analysis is not a good technique for determination of amorphous material.

5.6.3 Homogeneity study of amorphous solid dispersions - extrudes and pellets with THz Raman

The development of homogeneous amorphous solid dispersions offers the possibility to obtain valid sustained release. The following experiments are to look at the homogeneity of crystalline material within each of the extrude samples as pellets and to monitor the surfaces of the extruded samples. The samples that are analysed are those that have been stored for 5 months.

It is well known that the properties of materials at the surface can vary significantly to that present in the bulk.¹⁶⁶ It is necessary to have a full understanding of the content of the drug within the ASD. It is well known that the solid state of a drug may exist in a number of physical states within the polymer including crystalline dispersions, molecular dispersions, amorphous dispersions and eutectics (where the drug and polymer are co-dispersed as small crystallites).¹¹⁸ Most studies focus on the physical stability of the surfaces of materials and the homogeneity as a whole. Traditional methods for these studies are time consuming and usually involve multiple techniques such as DSC, XRPD, Raman and FT-IR analysis. Surface studies of samples are usually done by SEM¹⁶⁶ or Raman mapping, although there are also reports of the use of THz Raman imaging.¹⁶⁵ With THz Raman, the possibility of quick analysis along the surface of the extrude and within the sample is possible. Multiple spectra were obtained along the surface of the extrude and compared to multiple spectra taken within the sample. These were then analysed by PCA in order to determine any differences between the results.

There are very few reports of LFRS studies of paracetamol, an early report in 2009 by Al-Dulamimi et al.¹⁶⁸ used “phonon-mode” Raman spectroscopy for the analysis of milligram quantities of the three polymorphs and the amorphous form of PCM obtained by hot stage microscopy. They reported that the spectra in the “fingerprint region” for all forms are very similar but have minor differences around 1600 cm^{-1} with peaks arising from the amorphous form being broader than those arising from the crystalline form, but in general the spectra are very similar. In contrast they found that the LFR region for the crystalline forms were dramatically different and that the lack of peaks in the amorphous

material confirmed that the intermolecular vibrations for amorphous content are not measured.

5.6.3.1 Pre-processing of spectra

For each of the samples, multiple spectra were captured for both the pellets and the extrudes. These were then analysed by PCA and spectra that appeared to be outliers were plotted to determine why they were out with the confidence interval. These were plotted and are shown in Figure 5.22 below.

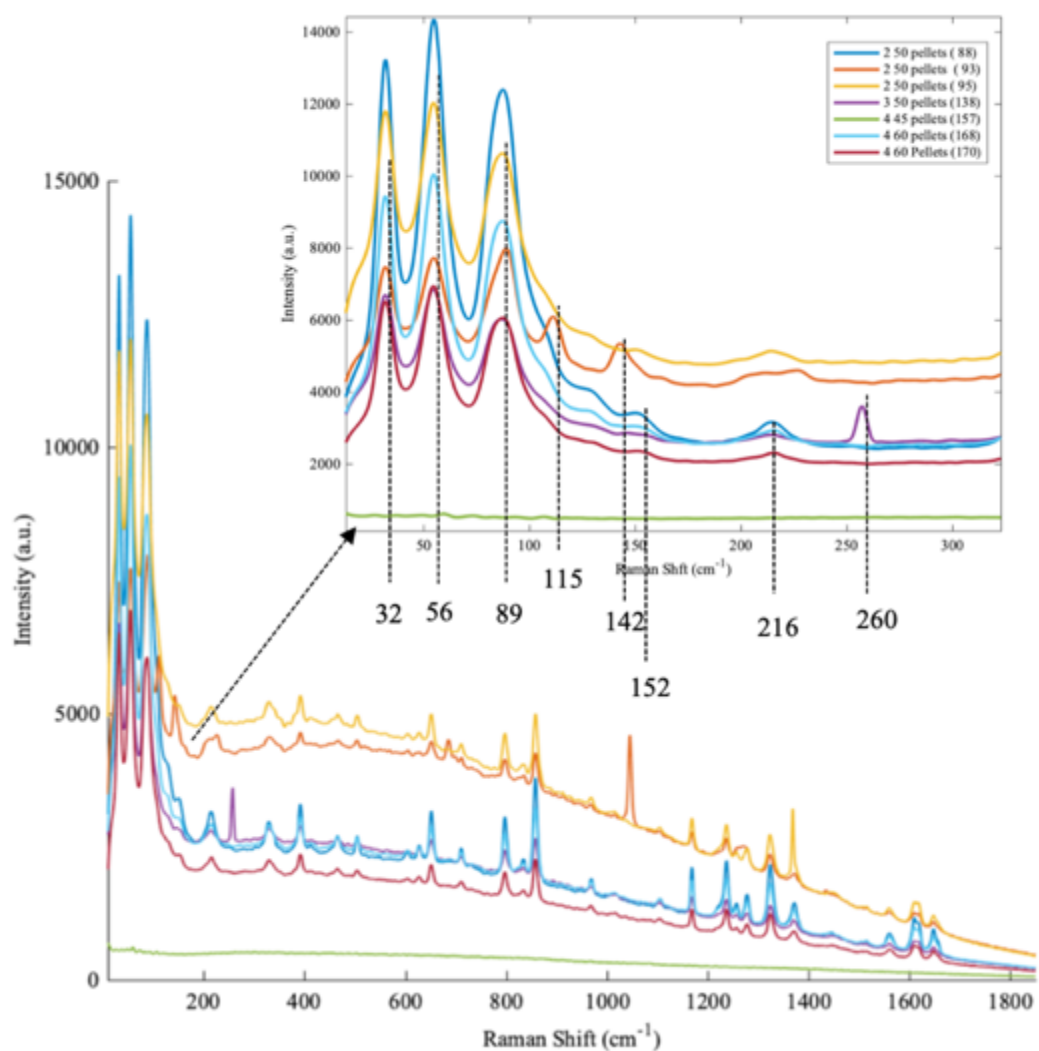


Figure 5.22 Outliers from analysis of THz Raman spectra from pellets of HME solid dosage forms showing variations in the spectra

All of the outliers in the analysis came from the pelletised samples, they also all showed the peaks present in Form I of PCM at 32, 56 and 89 cm^{-1} with the exception of sample 93, which also showed peaks at 115 and 142 cm^{-1} in the THz Raman region. Sample 93 shows subtle spectral differences across the entire spectral range, a sharp peak at 1050 cm^{-1} and a broad peak a 1270 – 1280 cm^{-1} . All the spectra were compared with the different polymorphic forms of PCM and there were no similarities to any of these except

for Form I. It was therefore thought that the spectral changes in sample 93 may have been due to contamination, cross contamination could have happened in the cutting of the pellets. The lack of peaks and low intensity of the spectrum for sample 157 suggests that the spectrometer laser missed the sample. The spectrum for sample 138 has a sharp peak at approximately 250 cm^{-1} , which is thought to be from the effects of room lights. Therefore, the data for samples 157 and 93 were removed prior to further analysis of the data set by PCA. The variations within these spectra really highlight the sensitivity of THz Raman for analysis, the number of spectra that are able to be obtained in quick succession allows for these variabilities to be easily detected, something that would take a lot of time with other analytical methods. The next study focuses on the variations along and within the extruded samples, looking at the homogeneity of each of the samples.

5.6.3.2 PCA of Pellets and Extrudates

The loadings for PC1 and PC2 from PCA of low and mid-frequency Raman spectra ($10 - 1800\text{ cm}^{-1}$) obtained from multiple points along the extrude (E) and multiple points within the sample as a pellet (P) are shown in Figure 5.23. PC1 and PC2 describe 87.63% of the variance in the data. PC1 and PC2 scores are plotted in Figure 5.24. There are two plots, each with samples coloured according to sample type (pellets and extrudes) and drug loadings for each experimental set.

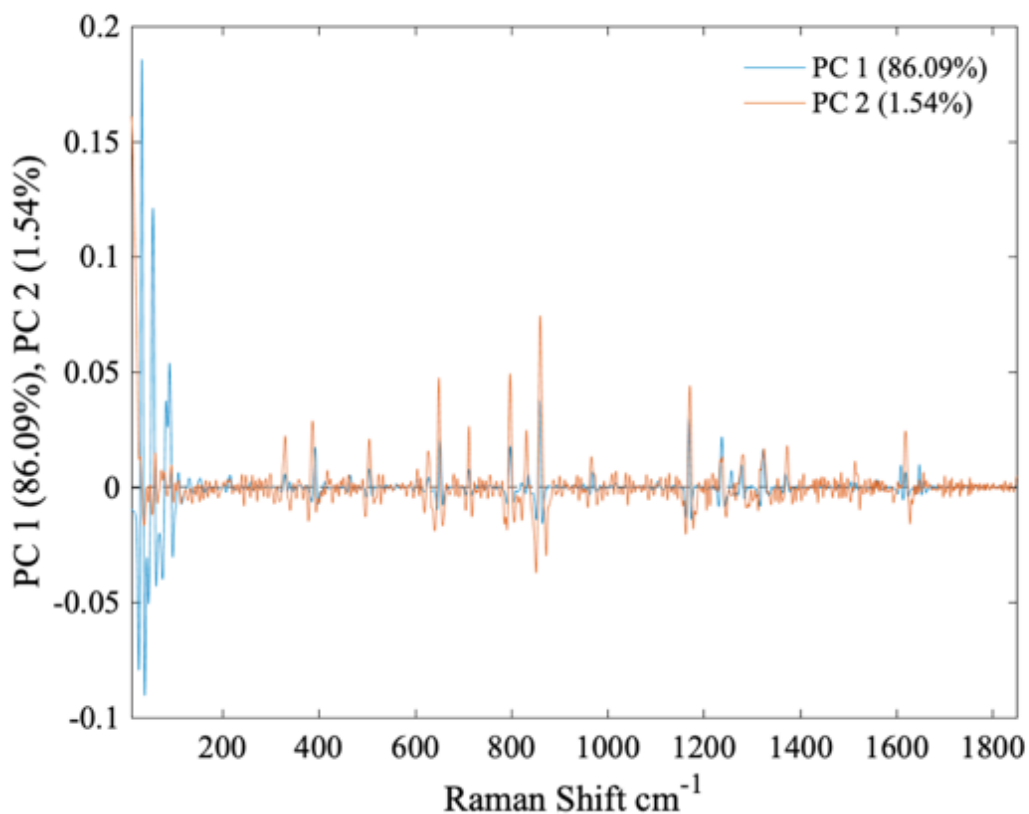


Figure 5.23 PC1 and PC2 loadings from PCA of low and mid-frequency Raman spectra (10 - 1800 cm^{-1}) obtained from multiple points along the extrude and multiple points within the sample as a pellet.

PC1 is describing mostly differences occurring in the THz Raman region while PC2 describes mostly information in the MFR region. The results suggest that PC1 is describing the variation in the degree of crystallinity and amount of amorphous material present and PC2 describes small variations in molecular structure.

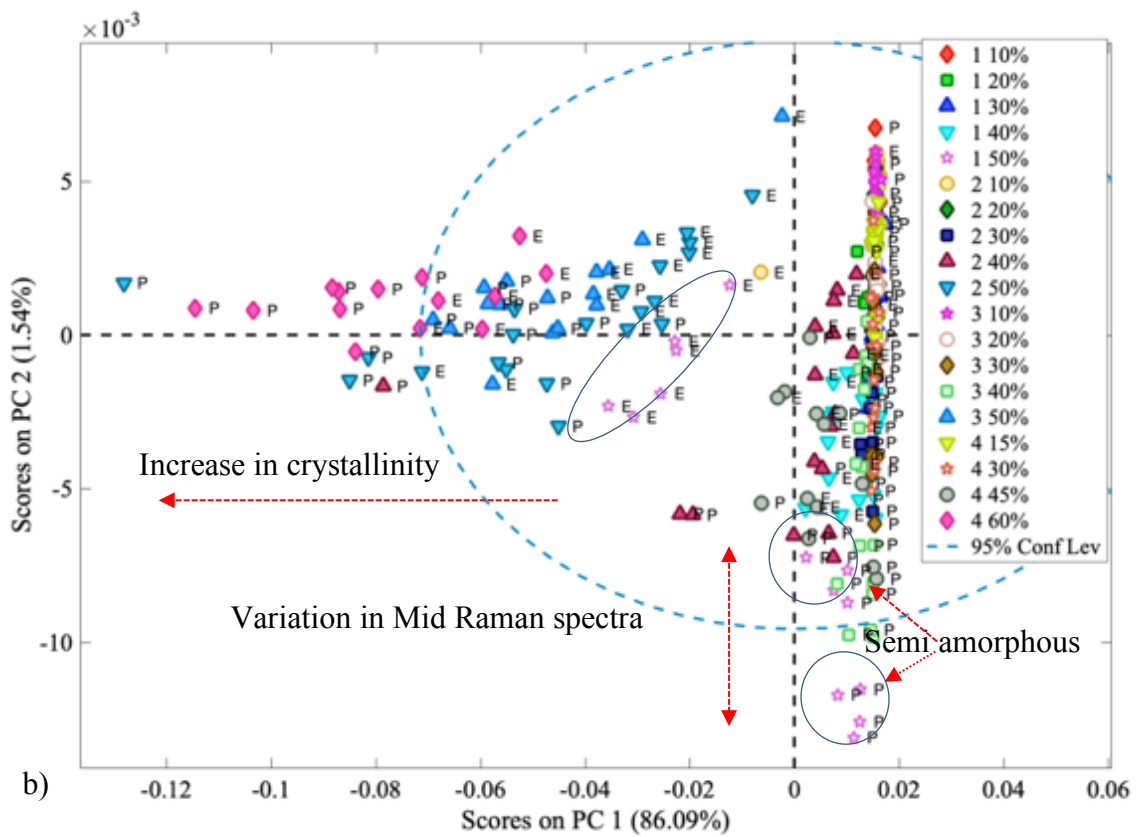
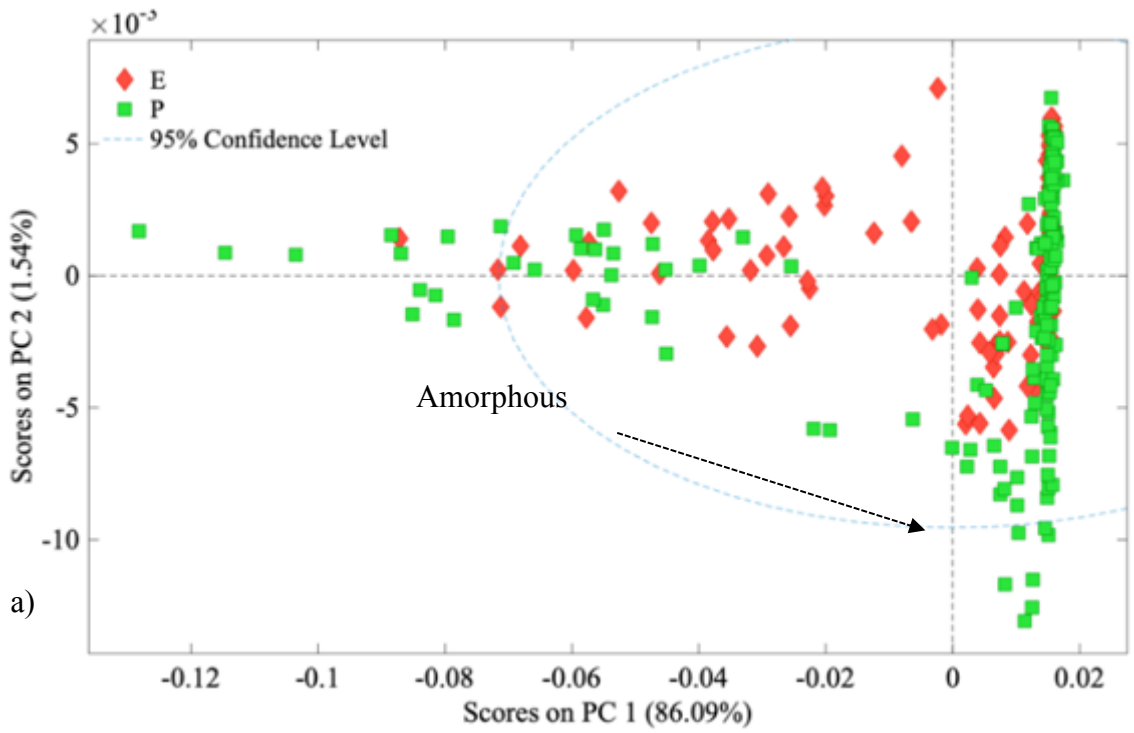


Figure 5.24 Scores plots for PCA of pellets and extrudes analysed by low and mid frequency Raman spectroscopy with different labelling. The scores plot in a) is classified by sample type (pellet and extrude) and b) is classified by drug loading

The low drug dosage pellets and extruded samples are mostly in the amorphous zone with PC1 scores close to 0.02. For the higher drug loading samples, there is more variation in the PC1 scores for spectra acquired within the samples (P) than for those acquired on the surface of the sample (E). The PC 2 scores for spectra acquired of the 60% wt sample in experiment 4 are quite similar for the pellets and extrudes suggesting that they mostly vary in the amount of crystalline content. This is also the case for spectra acquired of the 50 wt % PCM sample in experiments 2 and 3 but they have more variation in the PC2 scores. Figure 5.25 shows the PC1 scores for each of the samples, the degree of crystallinity increases with decreasing PC1 score.

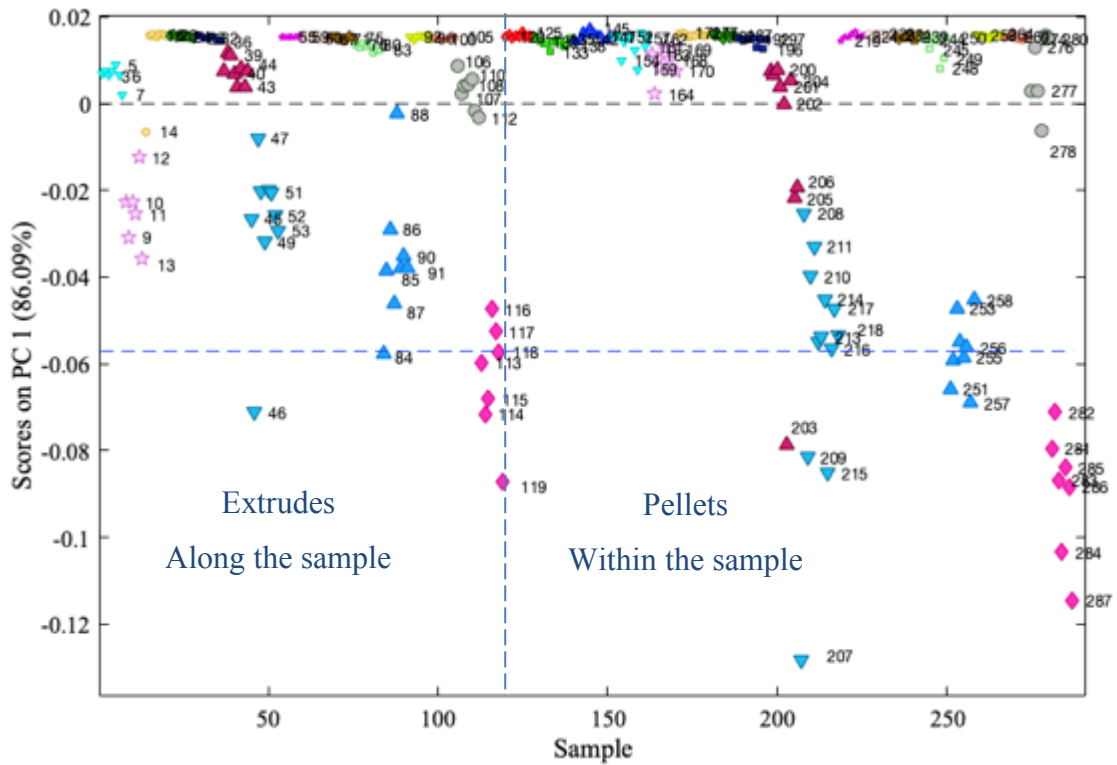


Figure 5.25 PC1 scores for pelleted and extruded samples from PCA

The extrude samples 1 – 7 experiment 1 40 wt % PCM have been plotted with their corresponding pelleted samples 152 – 161 in Figure 5.26 a) and b). Figure 5.27 shows a plot of Y scaled Extrudes and Pelleted samples from Experiment 1 with a drug loading of 50 wt %.

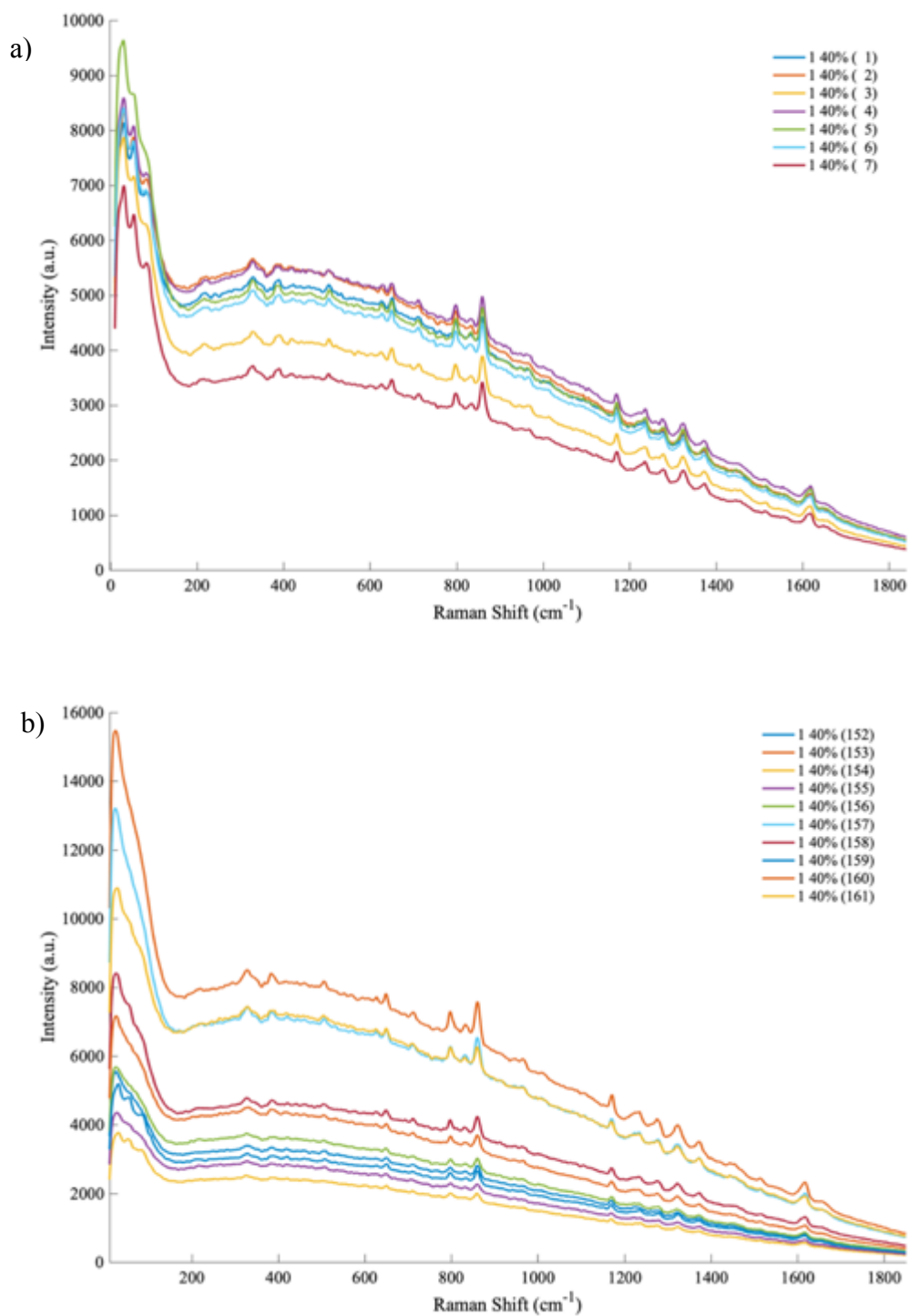


Figure 5.26 Low and mid-frequency Raman spectra acquired along the extruded sample a) (Extrudes samples 1-7) and within the extruded samples (pellets samples 152 – 161)

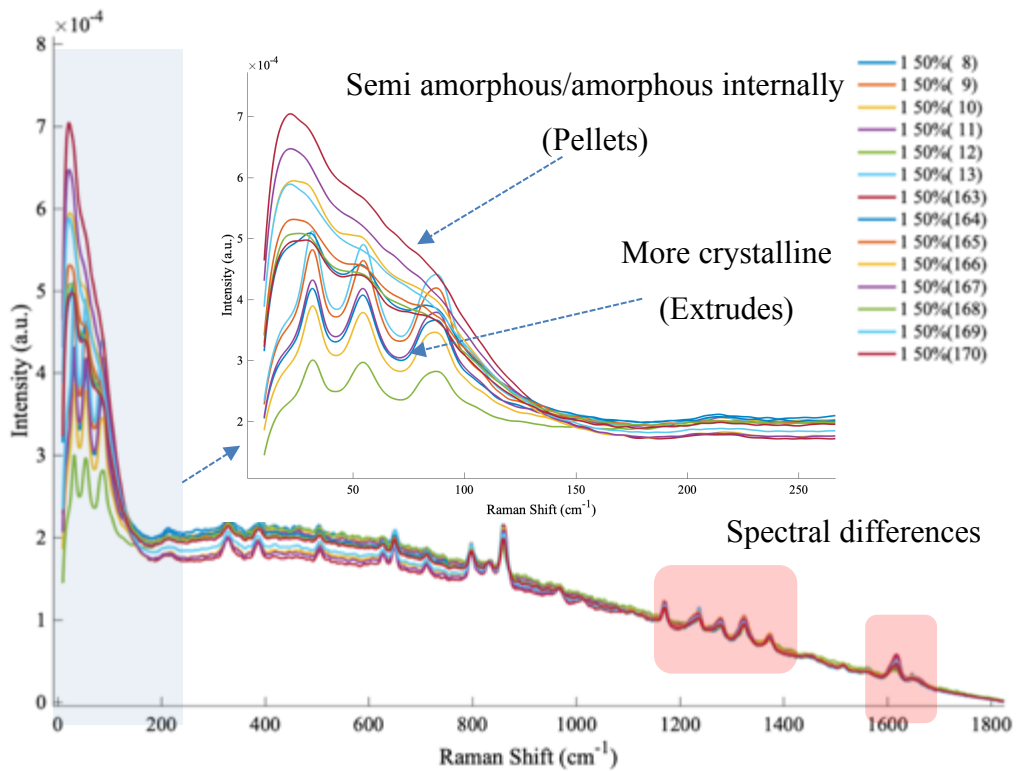


Figure 5.27 Plot of Y scaled Extrudes and Pelleted samples from Experiment 1 with a drug loading of 50 wt %

The MFR spectra for Experiment 1 50 wt % drug loadings are plotted in Figure 5.28, some differences in the spectra were observed explaining the groupings of these samples in the PCA plot shown in Figure 5.29.

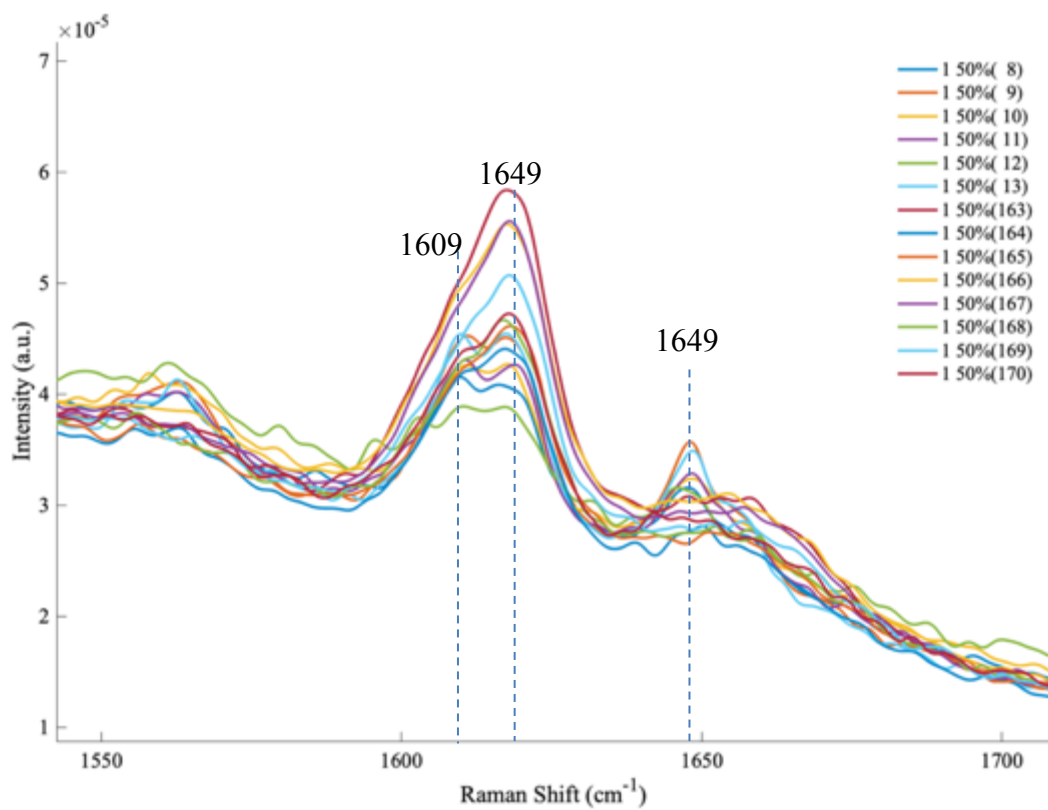
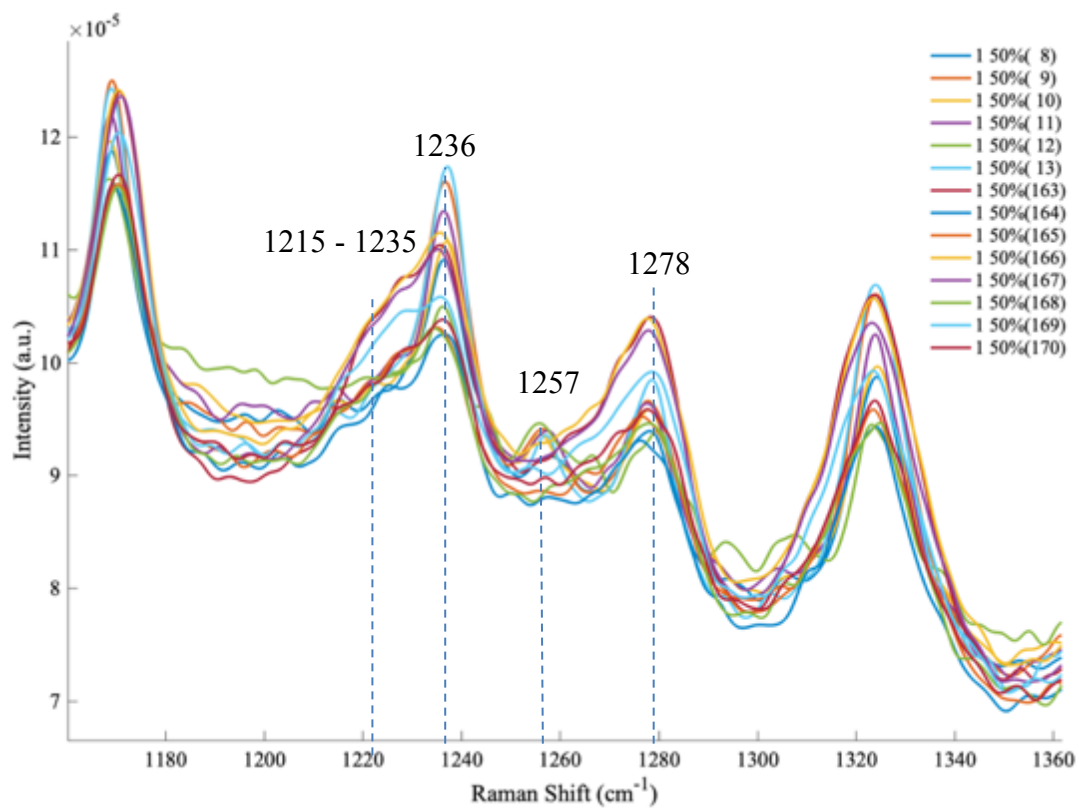


Figure 5.28 Raman spectra showing slight differences in the spectra between pellets and extruded samples from experiment 1 with 50 wt % PCM drug loadings

A double peak is present in samples 8 - 13 at 1609 and 1649 cm^{-1} , which is indicative of the presence of form II paracetamol; this peak at 1650 cm^{-1} is also seen in PCM form II.^{130, 168} It may be that the presence of PCM form II is not seen in the THz Raman region due to the degree of amorphous content in the sample. These samples are highlighted in the scores plot in Figure 5.29

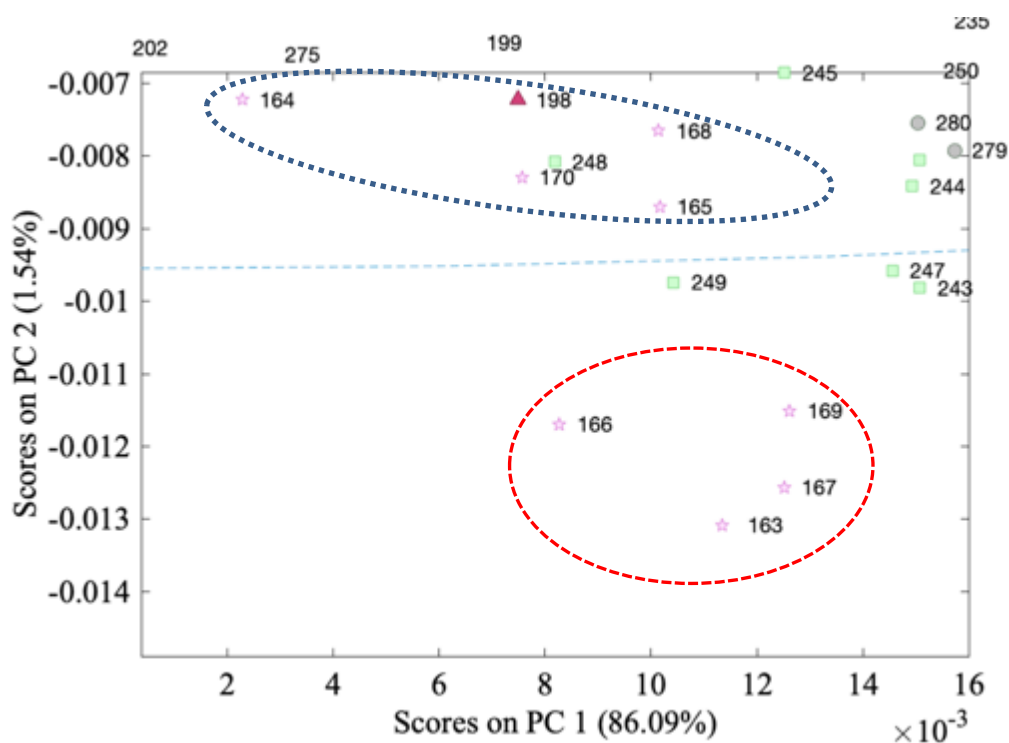


Figure 5.29 Scores plot showing the sample numbers from the PCA of THz Raman results

The pelleted samples numbered 163, 166, 167 and 169 are thought to be form I PCM, samples 164, 165, 168 and 170 are mixtures of FA, FI and FII and the extrusion samples 8 - 13 are thought to contain FA and FII.

PCA highlights the differences in the crystalline content between the samples with high drug loadings for both the pellets and the extrudes. There is less variation between the pellets and extruded samples for experiments 2-4 but a large variation in those from experiment 1. Experiment 1 was extruded at the highest temperature at 180 °C which is above the melting point of PCM, the presence of Form II PCM was also detected in the mid Raman spectral region but not the THz Raman region. The next step in the analysis was to look at the response of the extrusion of PCM-AFF within the HME.

5.6.4 In-line Terahertz Raman of hot melt extrusion of PCM-AFF

The analysis of the HME of PCM-AFF was studied with in-line THz Raman, the results from the study (10 – 1800 cm^{-1}) were plotted as the raw spectra with time in the waterfall plot in Figure 5.30. The THz Raman region (10 – 200 cm^{-1}) is focused on in Figure 5.31. During the process, an initial experiment was performed with 50% PCM to calibrate the spectrometer., this was then set to 0% PCM and then gradually increased through, 10, 30, 50 and 100% PCM in AFF, the barrel temperature was set at 175 °C.

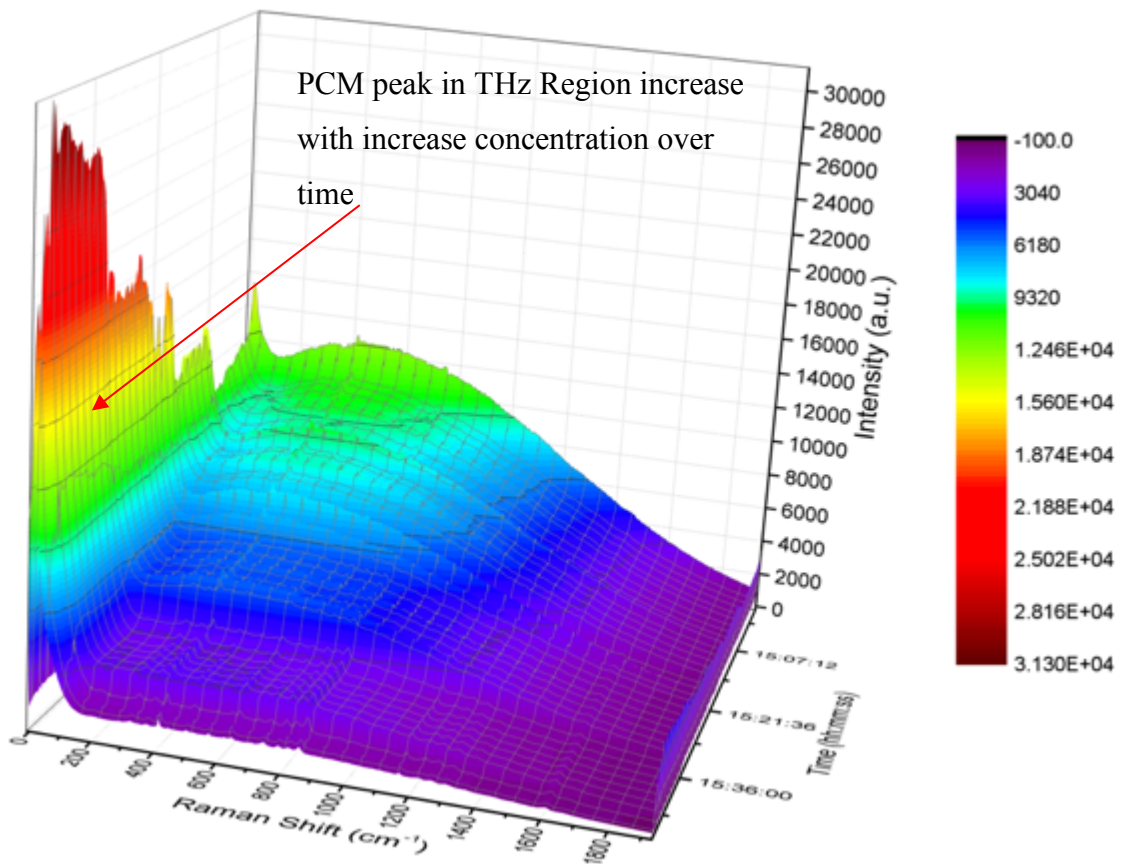


Figure 5.30 Low and mid frequency Raman spectra waterfall plot from in-line analysis of HME, PCM-AFF

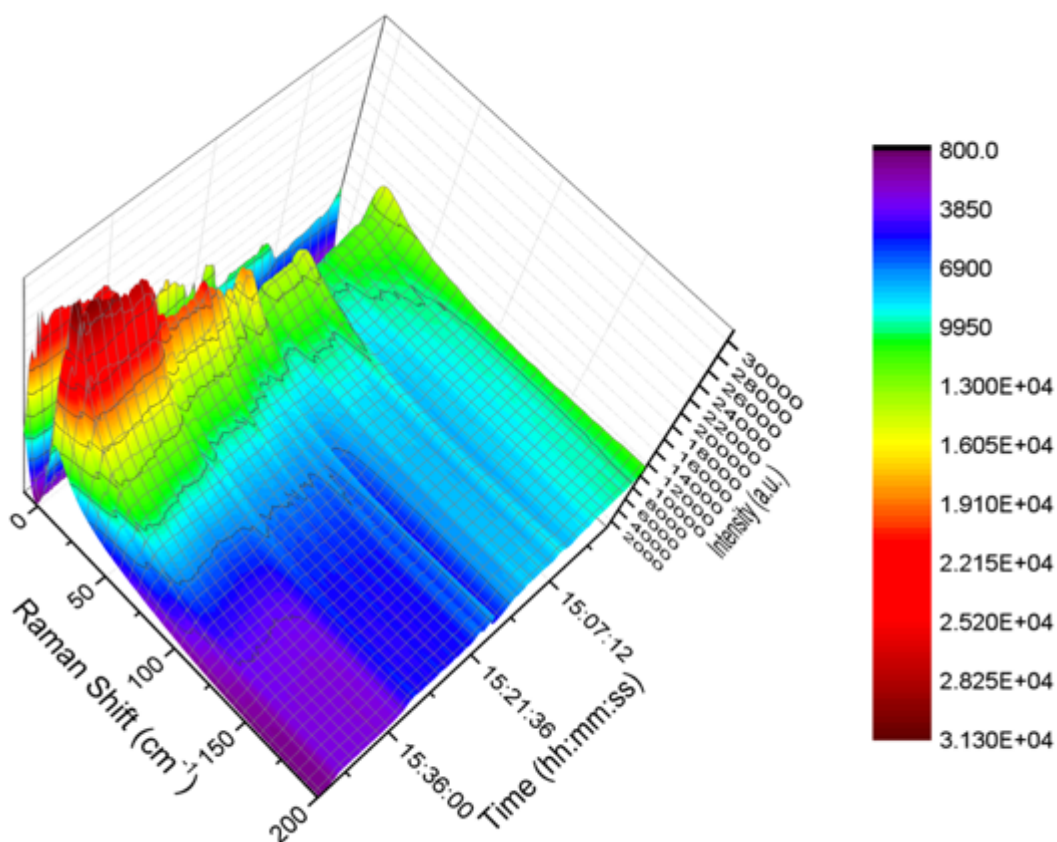


Figure 5.31 THz Raman region of HME PCM-AFF from - 10 to 200 cm^{-1}

The in-line results show an intense broad peak in the THz Raman region for the HME process suggesting that the PCM has dissolved completely in the polymer matrix, this is expected at such high processing temperatures of 175 °C. A study into the solubility of PCM in AFF showed that crystalline peaks disappear at around 130 °C for drug loadings of 30-70 wt % during the HME process.⁹⁷ In this study they found that as the temperature of the extrusion process approached the saturated solution temperature (T_s) (145 °C in PCM-AFF 30-70 wt %), the drug progressively dissolves in the polymer and the peaks associated with the lattice mode vibrations disappear as the API becomes amorphous. The change in the 2nd derivative of the main peak at 9.8 cm^{-1} with feed rate concentration is plotted in Figure 5.32. The powder feeder ran out of material just after 15:19:00,

represented by the drop-in feed rate. This was also detected in the Raman response. While in this case, no crystalline/amorphous transitions were observed within the THz Raman region, it is good to explore its response to process perturbations.

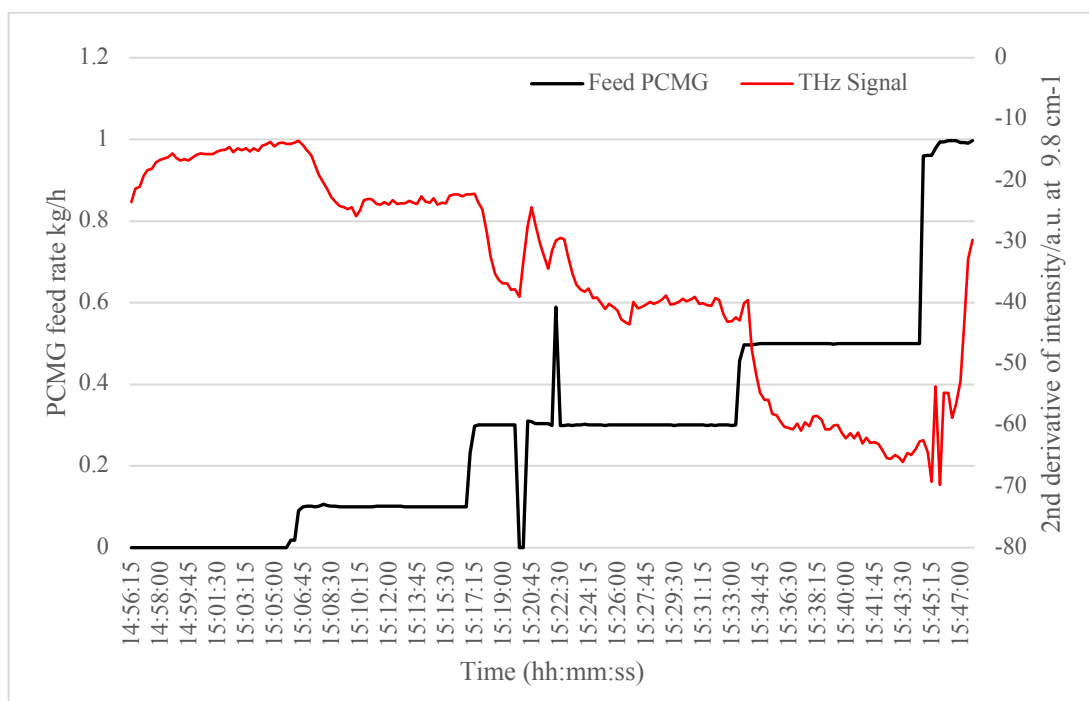


Figure 5.32 Change in peak height at 9.8 cm^{-1} with time plotted with the feed rate of paracetamol kg/h.

Another study looking into the HME of stearic acid at varying temperatures was then carried out.

5.6.5 Terahertz Raman spectroscopy analysis of hot melted stearic Acid

An industrial process involving the extrusion of stearic acid was studied, as this material was causing issues during a HME process. The process was creating very high torque measurements and the HME process was jamming during production causing the production of the product to stop. It was not fully understood why the HME process was

jamming so a study of the effect of temperature during HME was carried out. In-line analysis of the LFRS of extruded stearic acid were monitored over varying temperature profiles. The initial experiments were conducted off-line.

Stearic acid was melted on a hot plate to observe the melt amorphous material and observe its change with time. This was then moved to in-line analysis of HME of stearic acid to look at the effect of varying barrel temperatures with the resultant torque produced. The off-line THz Raman spectra for the extruded, amorphous liquid and the crystalline stearic acid are shown in Figure 5.33.

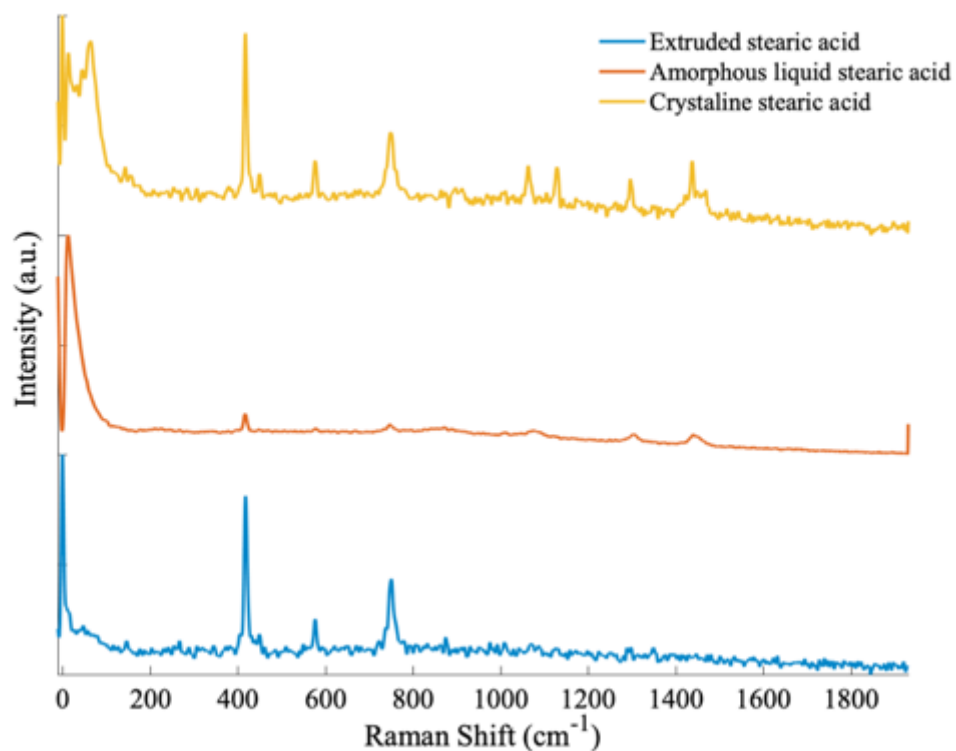


Figure 5.33 Low and mid frequency Raman spectra of stearic acid in the solid form (yellow), melt liquid (red) and extruded stearic acid (blue)

The crystalline stearic acid sample (yellow) shows sharp peaks in both the LFR and the MFR regions, the liquid melt spectrum (red) however shows very smoothed out spectra typical of amorphous material, which is lacking any long-range order, the last spectrum (in blue) shows pure stearic acid that has been extruded. Typically, extruded samples contain API and a polymer carrier like stearic acid. However, in this case there is no API and therefore no polymer-API interactions causing the change in structure in the LFR region, suggesting the extrusion process has caused changes to the physical structure during the heating process. A study by Luiz et al.¹⁶⁹ looked at the effects of solvent polarity on polymorphism of stearic acid. This study looked at LFR and XRPD analysis, two polymorphs were found one of which is the same as the crystalline powder but the other does not resemble the extruded sample.

The spectra obtained from the cooling crystallisation of the melt of stearic acid are shown in Figure 5.34.

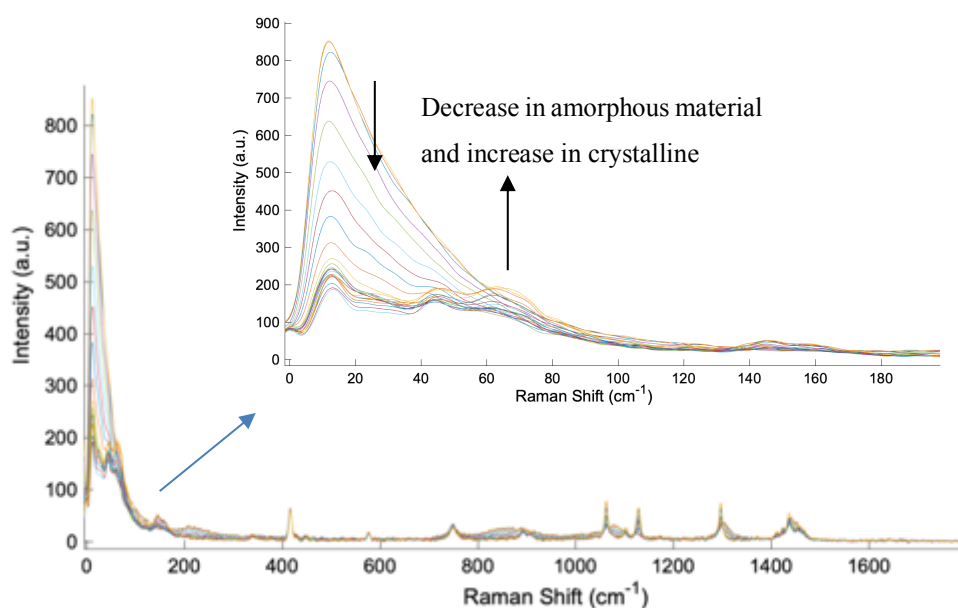


Figure 5.34 Low and mid-frequency Raman spectra of the cooling crystallisation of the melt of stearic acid

Stearic acid transitions from an amorphous melt material into a crystalline material as it cools over time. The amorphous peaks lower in intensity and form more defined peaks as the sample crystallises.

5.6.5.1 In-line analysis of Stearic acid

In the first experiment, the experiment was pushed to the limits to see at what temperature the extruder was becoming jammed. This was achieved by letting the temperature decrease over time until the extruder stopped. Figure 5.35 shows the increase in torque resulting from the drop-in temperature, the corresponding THz Raman spectra in Figure 5.36 ($0 - 200 \text{ cm}^{-1}$) show that the increase in torque corresponds to an increase in the degree of crystalline material present.

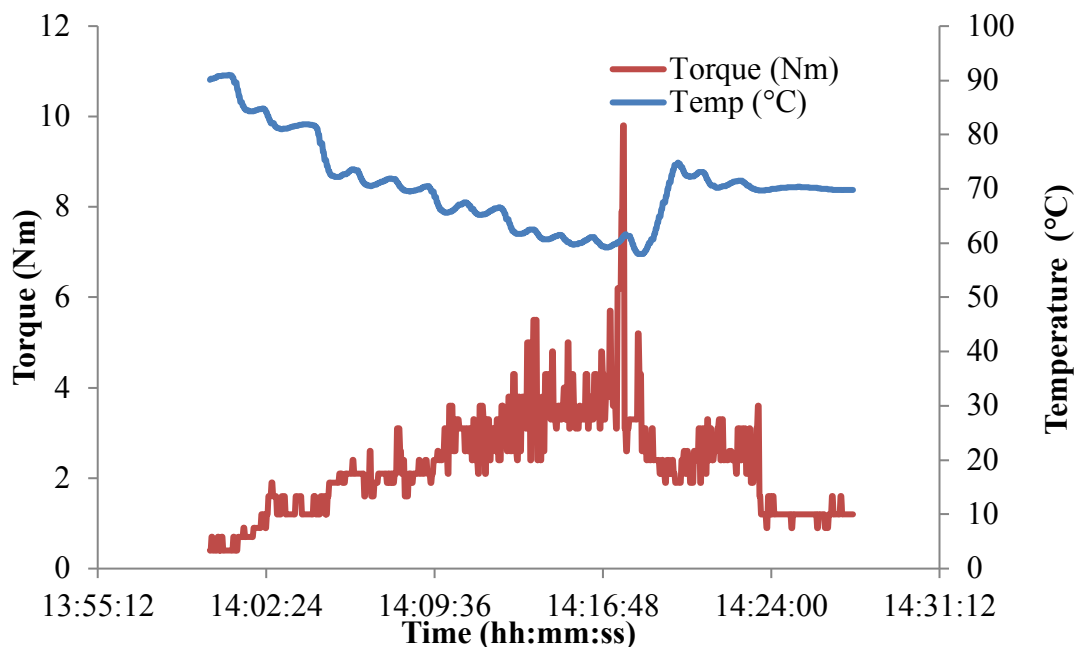


Figure 5.35 Overlay of the change in temperature with the torque for hot melt extrusion of stearic acid at 2 kg/h and 250 rpm.

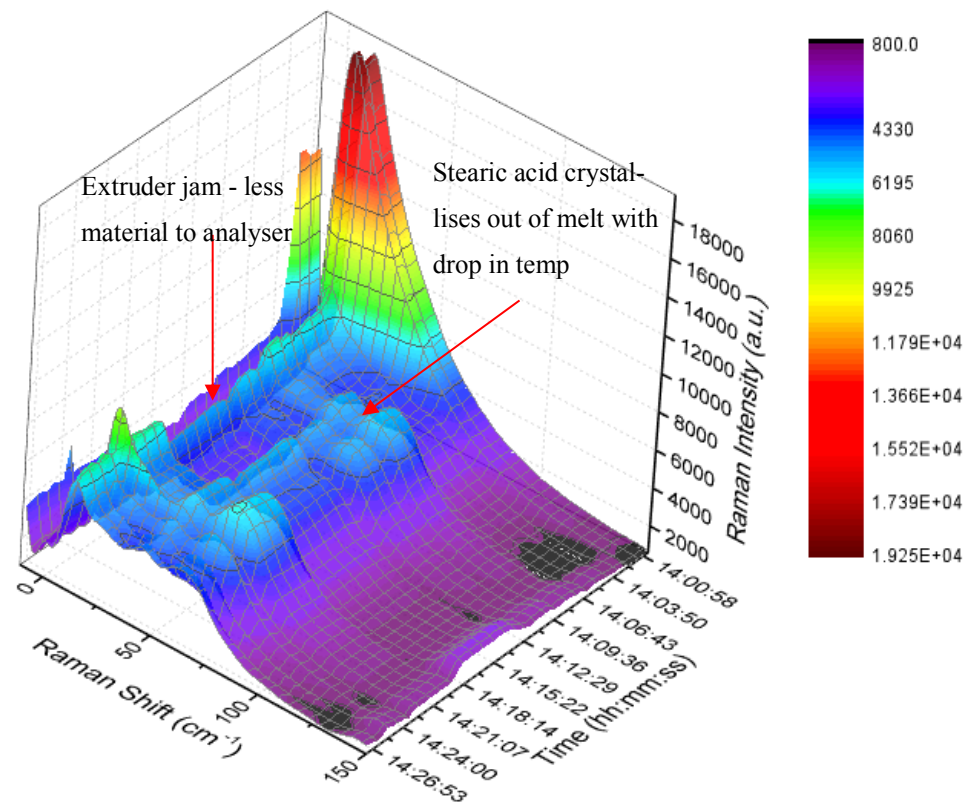


Figure 5.36 Waterfall plot of change in intensity with time in the THz Raman region. Samples were collected every 30s with 1 accumulation and an exposure time of 27 s. The screw speed was set to 250 rpm and feed rate 2 kg/h.

In the second experiment, the temperature was allowed to drop from 90 to 70 °C where it was held for just over ten minutes to allow the system to reach steady state. The results of the change in torque with temperature is shown in Figure 5.37 and the corresponding THz Raman spectra in Figure 5.38.

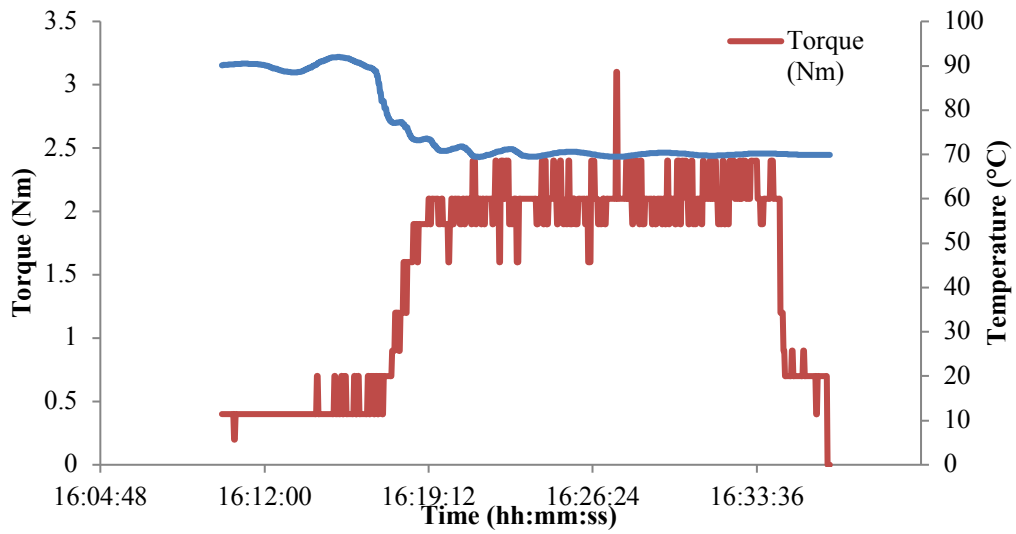


Figure 5.37 Overlay of the change in temperature from 90 to 70 °C with the resultant torque for hot melt extrusion of stearic acid at 2 kg/h and 250 rpm

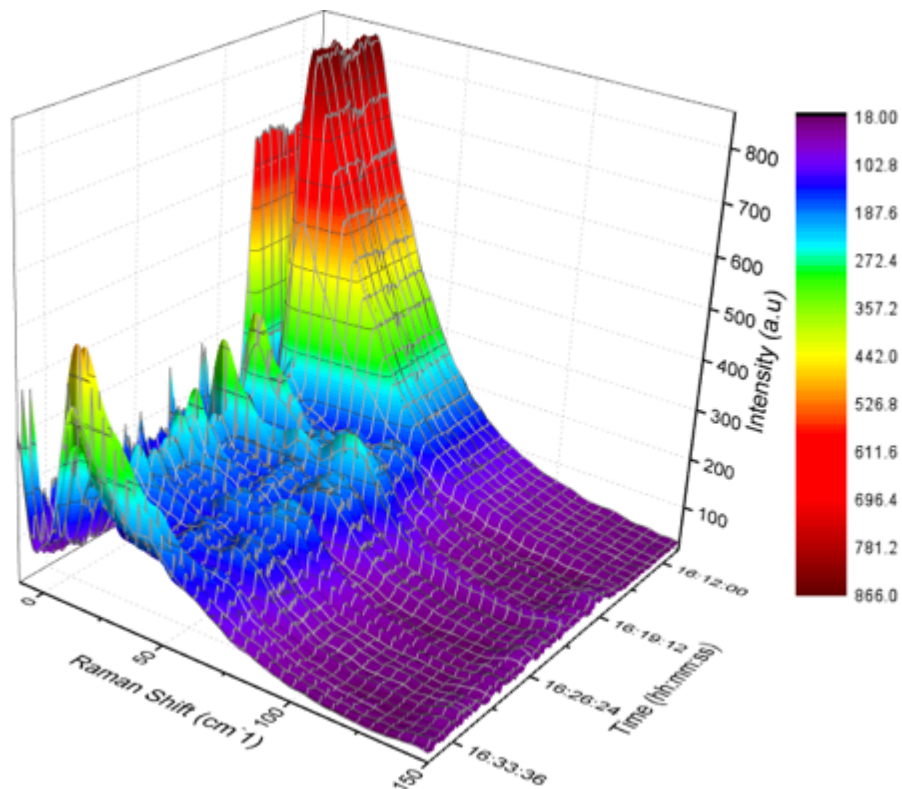


Figure 5.38 THz Raman region of peak change with time during the hot melt extrusion of stearic acid.

Stearic acid is used as a polymer and in this case no API was dissolved in the polymer matrix. This study was to look at the feasibility of monitoring in-line the degree of crystalline- amorphous material and to determine why the HME was jamming for stearic acid.

5.7 Conclusions

These studies have been good stepping stones onto further analysis in that they have proved that THz Raman is an excellent tool for quick and easy analysis of HME ASDs and a great alternative to XRPD, DSC and MFRS. The results showed that DSC analysis of HME samples was the most sensitive for detection of crystalline material, although some of the results appeared to show mixtures of polymorphic forms that are thought to be heat transformations induced by the heating during DSC analysis. XRPD analysis of samples immediately after extrusion were in good agreement with the LFRS analysis of the samples, showing that THz Raman spectroscopy analysis is as sensitive as XRPD for detection of amorphous material. Stability studies using XRPD showed that at 0 months samples in experiment 1, 1 kg/h, 180 °C and screw speed of 200 rpm were the most amorphous. This was thought to be due to the high processing temperature above the T_m of paracetamol (169 °C) causing complete miscibility of the polymer/API in the extruded samples. Experiment 2 showed the most crystalline peaks at 0 months in XRD analysis with peaks in 40 and 50 wt % drug loadings. Experiments 4 and 5 contained crystalline peaks in drug loadings above 50 wt % and negligible peaks below this. In PCA, the amorphous samples all had similar PC1 and PC2 scores (close to zero) while the crystalline samples have negative PC1 scores and vary in terms of their PC2 score.

The LFRS results gave similar results to the XRPD for these samples with only slight differences in the ability to detect amorphous material. It was however harder to determine any differences between the polymorphs of the samples in the LFRS for PCM polymorphs whereas there were some slight differences in the peaks observed in the XRPD analysis. Raman analysis of the samples showed little differences in the spectra thought to be due to the samples being masked by affinisol.

XRPD analysis of samples 5 months post extrusion showed that the API had crystallized out of the ASD in Experiment 1 40 and 50 % drug loadings. There was a slight change in the peak shapes in experiment 3. An increase in crystallinity was observed in Experiment 3 50 % drug loadings, negligible peaks were present at 40 % drug loadings. Experiment 4 showed an increase in crystalline material at 45 wt % drug loading. PCA of XRPD data at 0 and 5 months again show grouping of the amorphous samples. Samples analysed at 0 months mainly have positive PC2 scores and those extruded at 5 months have negative PC2 scores, this is thought to describe the changes in the peaks of the XRPD analysis and PC1 describes the degree of crystallinity in the samples.

A homogeneity study of the samples using THz Raman spectroscopy showed quite a lot of variation along and between the samples mostly in the higher drug loadings. Experiment 1 looked to contain FI and FII along with FA of PCM. The extruded samples were the most crystalline and this was thought to be due to API crystallising out on the surface of the extrudate. The internal analysis still showed variation but appeared to contain more amorphous material.

In-line analysis of HME process using THz Raman Spectroscopy was really promising, changes in the concentration of API were able to be detected in the HME of PCM and AFF at different drug loadings showing that API is fully dissolved in the polymer carrier and that the material is amorphous during HME. THz Raman was also able to detect change in amorphous to crystalline material in the extrusion of stearic acid at varying temperatures and was able to determine the onset of crystallisation in a melt cool crystallisation of stearic acid.

Chapter Six

Analysis of Sulfamerazine Solid State Transitions
with THz Raman Spectroscopy

6. Solid State Analysis of Sulfamerazine solid forms with Terahertz

Raman Spectroscopy

6.1 Introduction

Sulfamerazine SMZ, (4-amino-N-[4-methyl-2-pyrimidinyl] benzenesulfonamide), is a widely used sulfonamide antibacterial drug. Antibiotics are neutral compounds that are synthesised by living organisms to inhibit the growth of harmful micriorganisms. Sulfonamides have a bacteriostatic effect by inhibiting bacterial folic acid synthesis. Sulfonamides such as Sulfathiosol, are generally a highly polymorphic class of antibacterial drug. This is due to the presenece of various hydrogen bond donors and acceptors in their molecular structures leading to variability in H bonding in the solid state. Sulfamerazine on the other hand has been harder to understand. For sulfamerazine three polymorphic forms have so far been reported; Forms I and II are enantiotropically related such that form II is more thermodynamically stable at room temperature whereas form I is more stable at higher temperature. Forms I and II have been obtained in several studies,^{38, 170-172} Form III was discovered more recently in 2006 by G Hossain,¹⁷³ this is a far less known polymorph, which is hard to isolate, and therefore is not covered here. Forms I and II along with the amorphous form will be the focus of this study.

Form I and Form II polymorphs have the same hydrogen bond connectivity patterns but different secondary structures. In both polymorphs the repeating motif is a dimer, pseudocentrosymmetric in FI and centrosymmetric in FII.¹⁷⁴ The ladder crystalline structure and slip planes of FI allow for an easy conversion into FII by application of mechanical shear. The transformations of Form I by room temeratiure milling and cryogenic milling are described in Figure 6.1

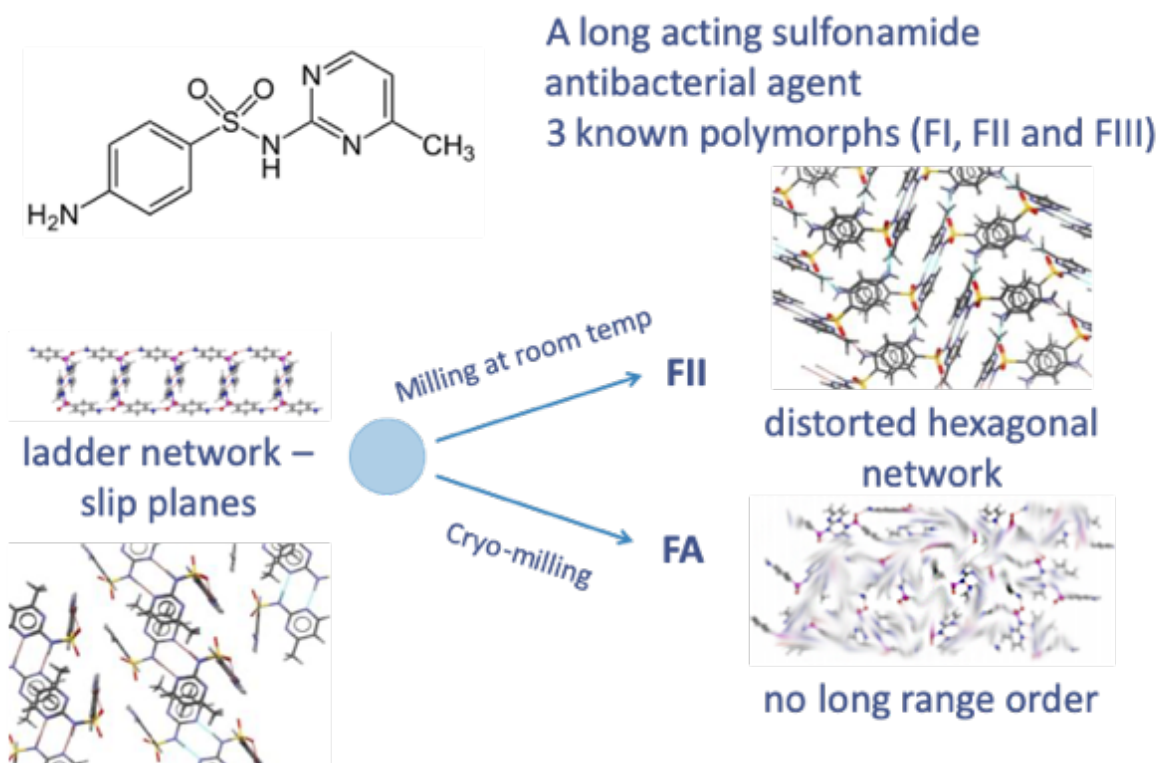


Figure 6.1 Schematic explaining the polymorphic transitions of sulfamerazine caused by room temperature milling and cryogenic milling of form I.

Because of the ability of SMZ to transform easily between solid states it was chosen as a model compound for analysis with THz Raman spectroscopy in order to try and better understand these transitions. This work stemmed from Pol MacFhionnghaile's studies³⁷ on sulfamerazine, a fellow CMAC researcher. The main aims and objectives of this work are:

- To further investigate the fundamental principles and understanding of LFRS via observation of the varying dimensionality of the sulfamerazine polymorph crystal lattices.
- To create FII of SMZ by mechanical milling of FI
- To develop a method for crystallisation in order to create a bulk mixture of FII

- To obtain the amorphous form (FA) of SMZ by cryogenic milling of FI
- Evaluation of the stability of the solid forms produced using THz Raman spectroscopy
- To isolate and characterize solid forms using THz Raman spectroscopy and compare them to XRPD.
- To investigate ternary mixtures of these with LFRS

6.2 Experimental

6.2.1 Materials

Sulfamerazine was purchased from Sigma-Aldrich with a purity of >99.0%, this was confirmed to be form I by comparison of XRPD results (CCDC code: SLFNMA02) and by comparison of those in the literature^{175,170}. Seeds of FII SMZ was produced by room temperature milling of FI SMZ, these were then used to make bulk FII via a solvent mediated phase transformation. Details of these experiments are explained in the experimental section below. SMZ FII was also confirmed on the CCDC (SLFNMA01), Raman spectroscopy and FT-IR analysis.

6.2.2 Methods

6.2.2.1 Milling and cryo-milling

An oscillatory ball mill (Retsch (MM 400) GmbH Haan, Germany) was used for all room temperature milling experiments. Initial experiments were carried out at room temperature with a 4 x 5 mL stainless steel sample holder, each containing a 2 mm diameter steel

ball bearing, later experiments were then carried out using a 25 mm stainless steel sample holder with a 15 mm diameter steel ball bearing.

Cryo-milling was carried out on a Retsch cryomill equipped with the 25 mm stainless steel sample holder and 15 mm ball bearing. During milling a supply of liquid nitrogen was constantly fed to the cryoMill via a large liquid nitrogen tank.

6.2.2.2 Fourier transform infrared (FT-IR)

FT-IR measurements were obtained on a Tensor II FTIR spectrometer (Bruker Optics). Off-line spectra were acquired at a resolution of 4 cm^{-1} . 16 scans were accumulated with a measurement time of 15 seconds; data was collected from $400 - 4000\text{ cm}^{-1}$.

6.2.2.3 Differential Scanning Calorimetry

All experiments were performed on a DSC 214 Polyma differential scanning calorimeter (Netzsch-Geratebau GmbH, Germany). Samples of 3 to 5 mg were weighed out accurately and crimped in 25 μL aluminium pans with pierced lids. These were then subject to heating to heat-cool-heat cycles under a helium environment (purge 1 = 40 mL/min, Purge 2 = 60 mL/min).

6.2.2.4 X-ray powder diffractometry

X-ray powder diffraction patterns were collected on a Bruker D8 Advance II Discover diffractometer working in the Bragg-Brentano geometry using CuK_α radiation with a step size of 0.05° and a 2 s counting time per step. Two analysis methods were used, the first was a standard method with the diffraction patterns recorded between 5° and 35° (2θ) taking approximately 25 minutes. In the second method, the same parameters were

employed but diffraction patterns were only recorded between 5° and 18° resulting in a shorter analysis time of 40 minutes to capture the amorphous form. The diffraction patterns were received as RAW files and converted in MATLAB.

6.2.2.5 Raman Spectroscopy

A Kaiser Raman RXN2 Spectrometer equipped with either the PhAT probe or a filtered remote MR probe was used in the experiments. The PhAT probe shown Figure 6.2 a) is a wide area non-contact probe with the options of either a 3, 4, 5 or 6 mm spot size sample lens, the 6 mm was used for the analysis in this chapter b) shows the off-line sample holder that comes with the instrument and c) shows a schematic of the set up for the off-line experiments. The MR probe shown in Figure 6.2 d) was used with an in-line immersion optic for analysis in the Easymax mixer during the solvent mediated phase transformation of SMZ.

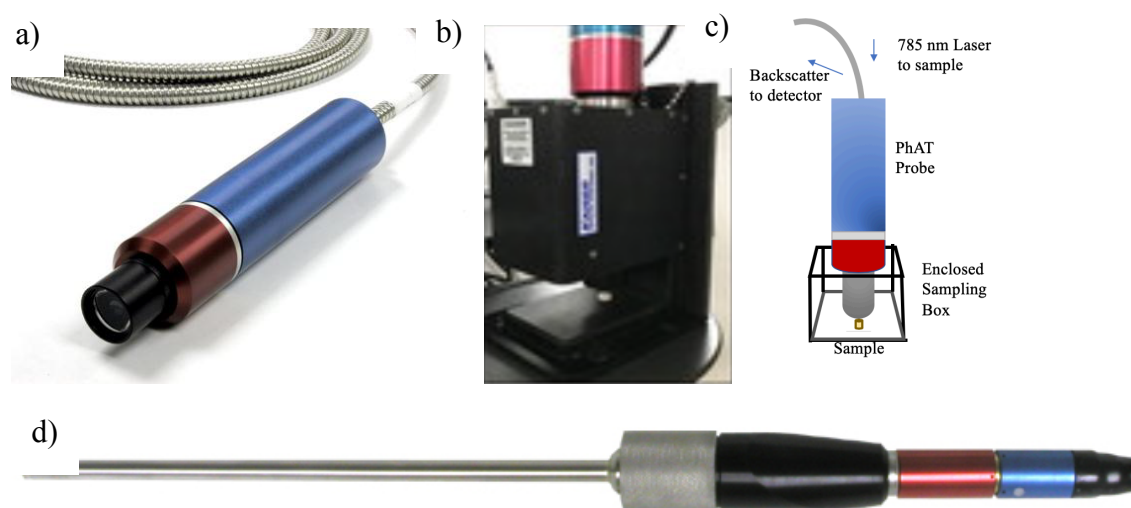


Figure 6.2 Kaiser PhAT Probe above a) the sample holder for off-line Raman analysis b) a schematic of the set up for analysis c) and the Immersive MR probe below d)

Spectra were acquired with an exposure time of 15s and 1 accumulation, spectra were taken every 5 minutes. Off-line analysis was acquired at 5 to 10 s exposure times depending on the sample and each analysis comprised 1 accumulation.

6.2.2.6 THz Raman Spectrometer

Spectra were collected as in the previous chapter. Exposure times were varied according to the sample.

6.2.2.7 Focussed beam reflectance measurement

The FBRM probe was used to analyse the solvent mediated phase transformation particles. It was set to acquire data every 20s. Information on chord length for the following size ranges was obtained: <10, >100, 10-50, 150-130, 300-100, 50-150 μm . The data was then plotted in Excel.

6.2.2.8 Preparation of form II Sulfamerazine by mechanical milling of form I

Initial experiments were carried out with approximately 0.3 g of FI of sulfamerazine in 2 x 5 mL stainless steel sample containers each containing a 2 mm stainless steel ball bearing. The samples were milled at 25 Hz for different time increments up to 120 minutes, breaks of 15 minutes were taken every 30 minutes to avoid overheating of the sample. Samples were taken at 0, 5, 10, 20, 30, 40, 45, 50, 55, 60, 90 and 120 minutes. A larger 25 mL stainless steel sample container was then used. 1g of FI of sulfamerazine was added to the jar with a larger 15 mm diameter stainless steel ball bearing. The sample

was then milled using the same procedure as that described with the 5 mL jar above. The milled samples were analysed with FT-IR spectrometry to confirm the identity of the material produced.³⁷ Milled samples were also analysed with Raman spectrometry XRPD and THz Raman spectrometry in order to compare the findings from different analytical techniques.

6.2.2.9 Preparation of bulk form II Sulfamerazine by solvent mediated phase transformation

After some method development, discussed in 6.3.1, the best method for the production of bulk FII was as follows: Sulfamerazine FII was prepared from an aqueous acetonitrile solution. 2.5 g of SMZ form I was added to 100 mL H₂O: acetonitrile (20:80) in a 100 mL Easymax reactor. Seeds of FII were then added to the mixture and it was stirred at 400 rpm for 13 h the stir rate was then gradually increased to 600 rpm and left to run for 24 h. The sample was then filtered leaving a slurry which was left to dry overnight. The resulting samples were then further analysed with XRPD, DSC and Raman spectrometry.

6.2.2.10 Preparation of the amorphous form of sulfamerazine via cryo-milling of FI.

Cryo-milling was performed on SMZ FI powder for 70, 120 and 160 minutes. The pre-cool time was set initially at 5 minutes at 5 Hz, then milling cycles were set to mill for 5 minutes at 25 Hz then cryo-mill for 5 minutes for 5Hz. These cycles were repeated until the required period of time had passed.

6.2.3 Data analysis

Data was analysed in MATLAB, Microsoft Excel and Origin Pro. Classical least squares regression was used to analyse mixtures of solid forms of SMZ.

6.3 Results and Discussion

6.3.1 Method development for production of bulk form II

sulfamerazine

Multiple methods, shown in Table 6.1, were reviewed for the preparation of bulk FII sulfamerazine to determine the best method for production.

Table 6.1 Review of methods for bulk production of sulfamerazine form II

| Reference | Method | Time | Apparatus | Conformation analysis |
|---|---|-----------|---|---|
| Roy et al. ²⁹ & Caira et al. ^{174, 176} | 50 g FI suspended in 250 mL of acetonitrile at room temp and stirred vigorously. After several hours 0.75 g of FII was added. The slurry was then left at room temperature for 15 days wrapped with foil to prevent photodegradation. | 15 days + | Magnetic stirrer Flask Hot plate | Seeded crystallisation DSC and XRPD |
| MacFhionn ghaile et al. ³⁷ & Zhang et al. ¹⁷⁰ | In a 1 L round bottom flask on a hot plate. 800 mL solution H ₂ O-acetonitrile 20:80, containing 5 g of SMZ was heated to 60 °C for to ensure complete dissolution. Seeds of FII were added and the solution was stirred over night at 300 rpm using a magnetic stirrer. The solvent removed and the slurry was led to dry under vacuum. | 24 h + | 1 L round bottomed flask Hot plate | Seeded crystallisation. XRPD patterns with simulated ones in CSD |
| Kurotani et al. ¹⁷⁷ | The desired amount of SMZ to create a supersaturated solution was added to 200 mL of MeCN in a flat-bottomed flask. The contents were stirred and heated to 50 °C and maintained for 3 h. The solution was then cooled to 21 °C at a rate of 10 °C /h. An ultrasonic probe was then immersed in the solution and it was ultrasonicated at 6.8 W for a determined period up to 360 s. Form II was observed at irradiation times of 180 and 360 s supersaturation (S ₀) of 1.2 and 1.3), whereas at 90 s irradiation time FII was seen only in the lower S ₀ of 1.2. Unfortunately, FI and FII mixtures were produced but FI is likely to change to FII over time. | 20h | 300 mL flat bottomed glass vessel, magnetic stirrer, UH-50 ultrasonic homogenizer | Ultrasonic induced phase transformation. XRPD Microscopy |
| Lee et al. ²³ | A comparison of an Rushton Mixing Tank (MT) and Couette-Taylor (CT) crystalliser for phase transformation of SMZ was | MT 60h | CT crystalliser | Seeded crystallisation |

| | | | | |
|---------------------------|---|--------------------|---|-------------------------------------|
| | carried out. In the MT crystalliser 3000 rpm SMZ dissolved in acetonitrile the process took 60 h but using a CT crystalliser the process was 3-7 h with 300-1000 rpm. It was found that increasing the rotation of the of the CT significantly enhanced the phase transformation and that adding water to the solvent increased the solubility which was a driving force for the transition. 80% ACN and 20% water was found to be a good mixture. Lowering of temperature also had a significant impact on phase transformation, increase in temperature reduced phase transformation rate by decreasing the solubility difference. CT crystalliser proved to be much better due to the turbulent fluid motion in the Taylor vortex. | CT crystalliser | and MT crystalliser | Morphology and XRPD |
| Park et al. 171 | Followed on from the previous study by Lee et.al. Here they refined the findings from above. Seeds were pretreated by three methods, grinding of FI crystals, grinding of FII crystals and washing of ground FII crystals. The best results were from ground seed crystals due to the increase in surface area. Washing didn't seem to increase the transformation times. Increasing the fraction of FII in the seed samples increased the reaction time in the MT crystalliser but had little effect on the CT crystalliser. Morphology samples showed distinct differences in shape for each polymorph. FI was a rectangular shaped crystal whereas FII was a distorted. | MT 3.5h CT 1.5h | CT and MT crystallisers 700 and 100 rpm respectfully | Cooling crystallisation FT Raman |
| Sun et al. 178 | Two batches of FII were prepared, 250 g of raw material (FI) were suspended for 2 weeks with 1 g of seed crystals of FII in 1.2 L of acetonitrile. One batch was stirred with a magnetic stirring bar in the bottom of the flask the other with a three-blade stirrer., samples were mixed at 231 rpm. The flasks were covered in aluminium foil to prevent degradation of and the mixture filtered and analysed by XRPD. | 2 weeks | 2 L Erlenmayer flask, magnetic stirrer and three-blade stirrer | Seeded crystallisation XRPD |
| Gong et al | A study into the effect of impurities in SMZ on SMPT was XRPD investigated, 80:20 mix acetonitrile/water was stirred for 3 days at room temperature in a conical flask covered in foil It was found that three out of four of the samples were not able to be converted into FII. | 8h | Conical flask | Raman RXN1 |

A lot of the methods were time consuming^{176, 179-181} one taking up to 30 days. There was a common realisation in a few other studies that an increase in the agitation of the slurry seemed to enhance the phase transformation. Agitation has been introduced via ultrasound,¹⁸² another was able to achieve agitation through the formation of a Taylor vortex,

achieved by hydrodynamic fluid motions of a Couette-Taylor (CT) crystalliser.²³ This cut down the crystallisation times to as low as 3 – 7 hours from the use of a Rushton mixing tank (MT), which took up to 60 h. Another study was able to enhance the phase transformation by a drop in the temperature after complete dissolution of FI seeds from just above 50 to 10 °C at a rate of 30 °C/h.¹⁷¹

In an initial study, the method reported by MacFhionnghaile et al³⁷ was attempted in a Radley reactor instead of a 1000 mL round bottom flask. This used 800 mL H₂O-acetonitrile (20:80) containing 5g of SMZ. The solution was heated to 60 °C in order to dissolve the SMZ, seeds of FII SMZ were then added and the solution was stirred overnight at 300 rpm. Repeating this method found that the high temperatures caused the solvent to evaporate overnight, another attempt but with a condenser attached was also unsuccessful, neither showed any signs of FII. It was thought that potentially a change in the solvent from volatile acetonitrile might help with the SMPT. Further analysis of the literature looking at solvent selection was carried out. Figure 6.3 highlights the importance of solvent selection when trying to crystallise a specific polymorph. A screening of polymorph selection of sulfamerazine in three solvents,¹⁸³ water, acetonitrile and methanol, showed that the energy barrier of form I is lower in the three selected solvents than it is for form II. This is depicted in a direct observation of Ostwald's rule of stages and Stansky Totomanow conjecture.

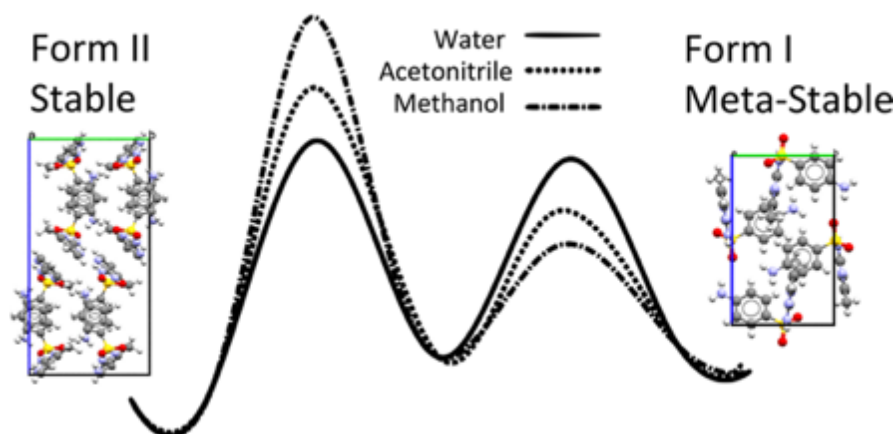


Figure 6.3 Schematic showing the energy barriers for forms I and II in three solvents; water, acetonitrile and methanol ¹⁸³

An increase in the water content and reduction in the acetonitrile was explored, but according to Blanco-Márquez et al.¹⁸⁴ SMZ does not dissolve well in pure water potentially due to the structuring of water being close to the non-polar groups of SMZ.

Lee et al.²³ found that the addition of water to acetonitrile really enhanced the form transformation as the solubility difference between the two polymorphs was a key driving force. Increasing the temperature of the solvent also increased the solubilities of the FI and FII. It was found that agitation was important and that a Taylor vortex CT crystalliser promoted better alignment for the nucleation of the stable form. A change in temperature and addition of water to the solvent had an effect on the solubility difference between the two polymorphs. The reduction in temperature increased the solubility difference.

For the next experiment an increase in the acetonitrile content from 80 to 85% in order to try and increase the solubility of SMZ without having to elevate the temperatures was then explored. Agitation was introduced in order to try and resemble the that observed in

the Taylor cortex and CT crystalliser studies. This was achieved by the addition of 3 x baffles and an increased stir speed. It was also decided to reduce the temperature instead of elevate it, the following conditions were used:

100 mL of H₂O-acetonitrile (15:85) was cooled to 10 °C and allowed to equilibrate for 10 minutes before 20 g of SMZ FI was added to the solution. This was then stirred at 500 rpm for roughly 12 hours. This method was scaled down and repeated in the Easymax reactor: 2.5 g of SMZ FI was added to 100 ml H₂O-acetonitrile (15:85). This was left to stir overnight at 400 rpm, the stir rate was then increased to 500 rpm and finally 600 rpm to encourage FII to crystallise. The filtered and dried samples were then analysed.

6.3.2 X-ray powder diffraction of sulfamerazine polymorphs

Predicted XRPD patterns obtained from CCSD are plotted against those obtained experimentally for Forms I and II in Figure 6.4.

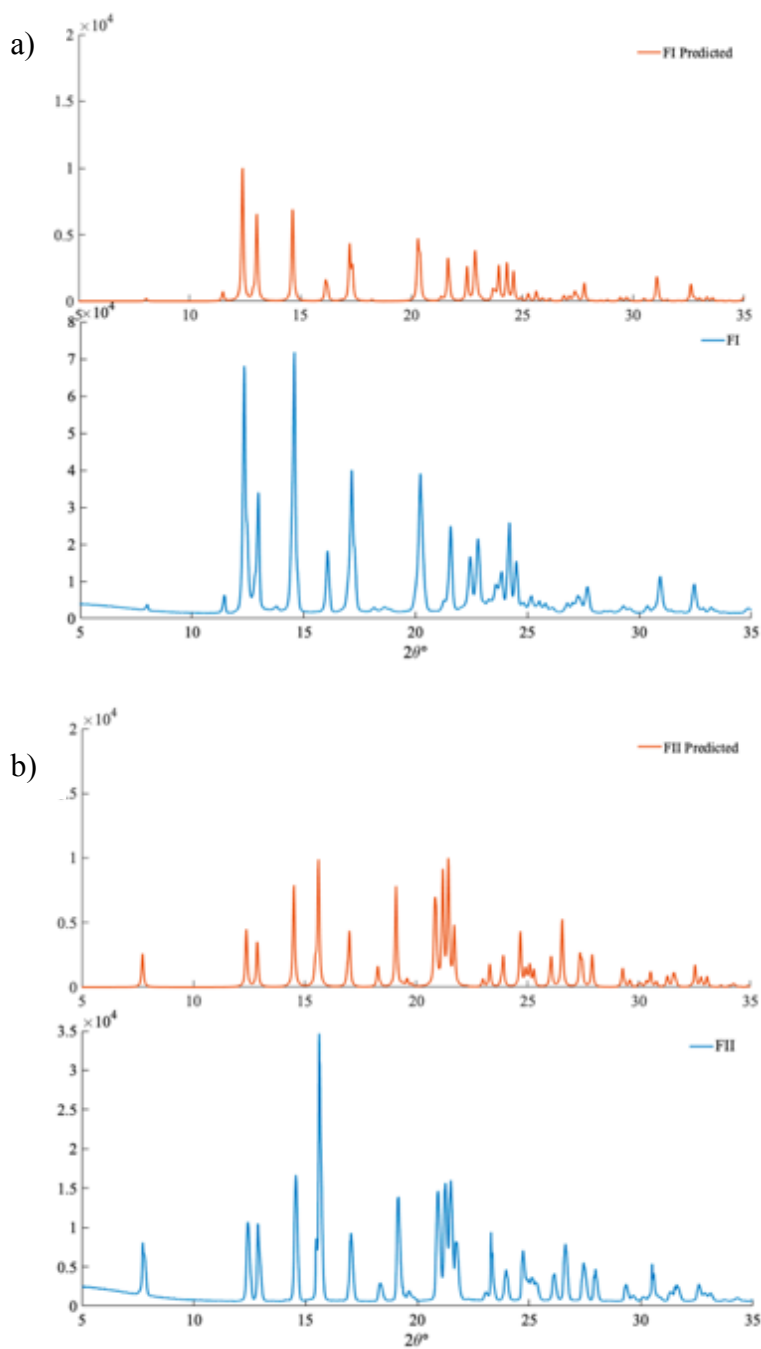


Figure 6.4 XRPD results of the theoretical taken from CCSD and experimental patterns from a) Form I and b) form II of sulfamerazine.

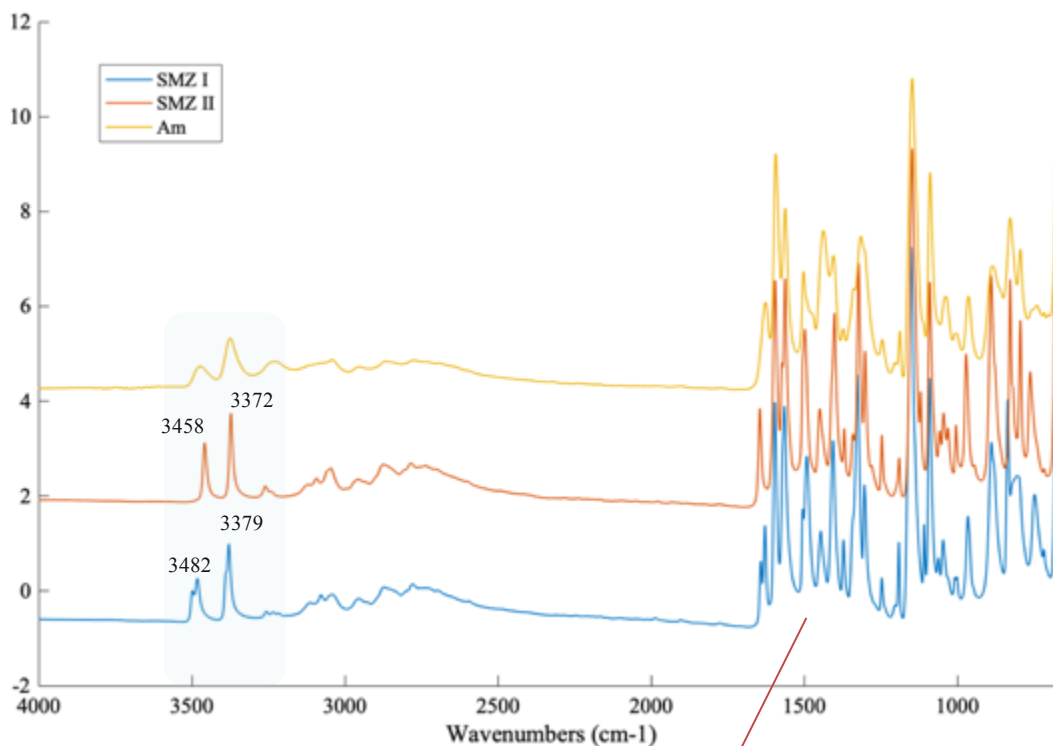
The main distinct peaks from the XRPD analysis for both FI and FII are shown in Table 6.2.

Table 6.2 Diffraction peaks representative of FI and FII in XRPD patterns

| Solid Form | XRPD 2 θ peaks (°) |
|------------|--|
| FI | 8.00, 11.05, 12.35, 13.00, 14.60, 16.10, 17.20, 20.25, 21.60, 22.50, 23.90, 24.35, 27.75, 31.00, 32.55, 38.15 |
| FII | 7.70, 12.35, 12.85, 14.50, 15.60, 16.95, 18.25, 19.05, 21.40, 23.25, 23.90, 24.65, 26.50, 27.85, 29.25, 30.50, 32.50 |
| FA | No distinct peaks |

6.3.2.1 FT-IR characteristics of FI, FII and FA

FT-IR analysis of the solid forms are shown in Figure 6.5 highlighting the peak differences between the solid forms.



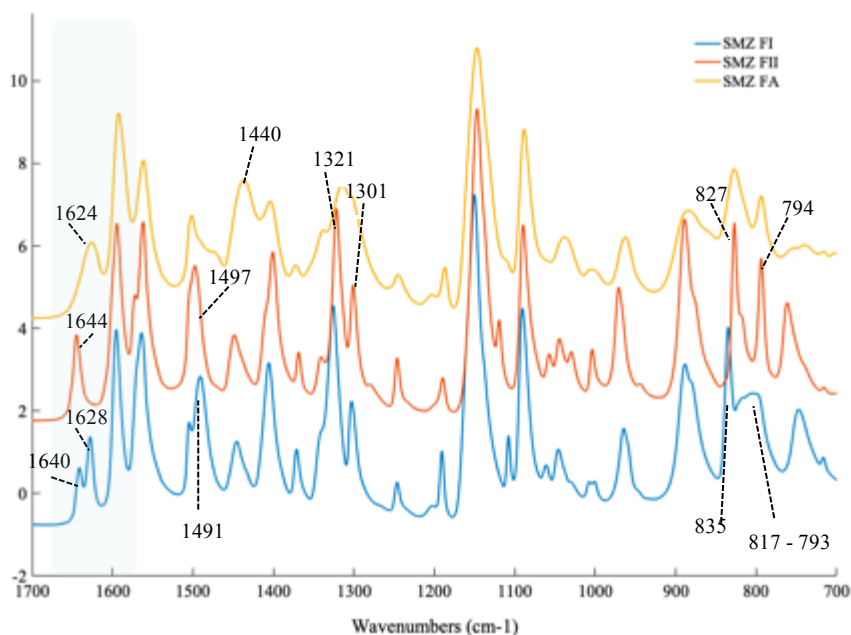


Figure 6.5 Comparison of FT-IR spectra showing the distinct characteristics of forms I (blue), II (red) and the amorphous form (yellow) of sulfamerazine.

Assignment of the main peaks has been reported in the literature.³⁷ The main differences between FI and FII are highlighted in the IR spectra and tabulated in Table 6.3,

Table 6.3 Main defining peaks for sulfamerazine FI, FII and FA from FT-IR analysis

| Solid Form | Defining peaks (cm ⁻¹) |
|------------|---|
| FI | 3482, 3379, 1640, 1628, 1491, 835, 817 - 793 |
| FII | 3458, 3372, 1644, 827, 794 |
| FA | 162, Broadening of most peaks, 1440 broad double peak |

6.3.2.2 Raman Analysis

The full spectra and those from the THz region are shown in Figure 6.6. Below this the wavenumbers of the main polymorphic peaks in the LFR and MFR spectra were assigned, these are tabulated in Table 6.4.

Table 6.4 Polymorphic peaks of forms I and II of Sulfamerazine from THz Raman analysis

| Sulfamerazine Forms | Defining LFR peaks cm^{-1} | Defining MFR peaks cm^{-1} |
|------------------------|-------------------------------------|--|
| Form I | 16, 45, 75, 112 | 999, 1092, 1105, 1151, 1191 |
| Form II | 13, 29, 36, 84, 145, 186 | 968, 1001, 1092, 1115, 1143, 1188 |
| Amorphous Form | One broad smooth peak | Smoothed peaks depending on what forms present |

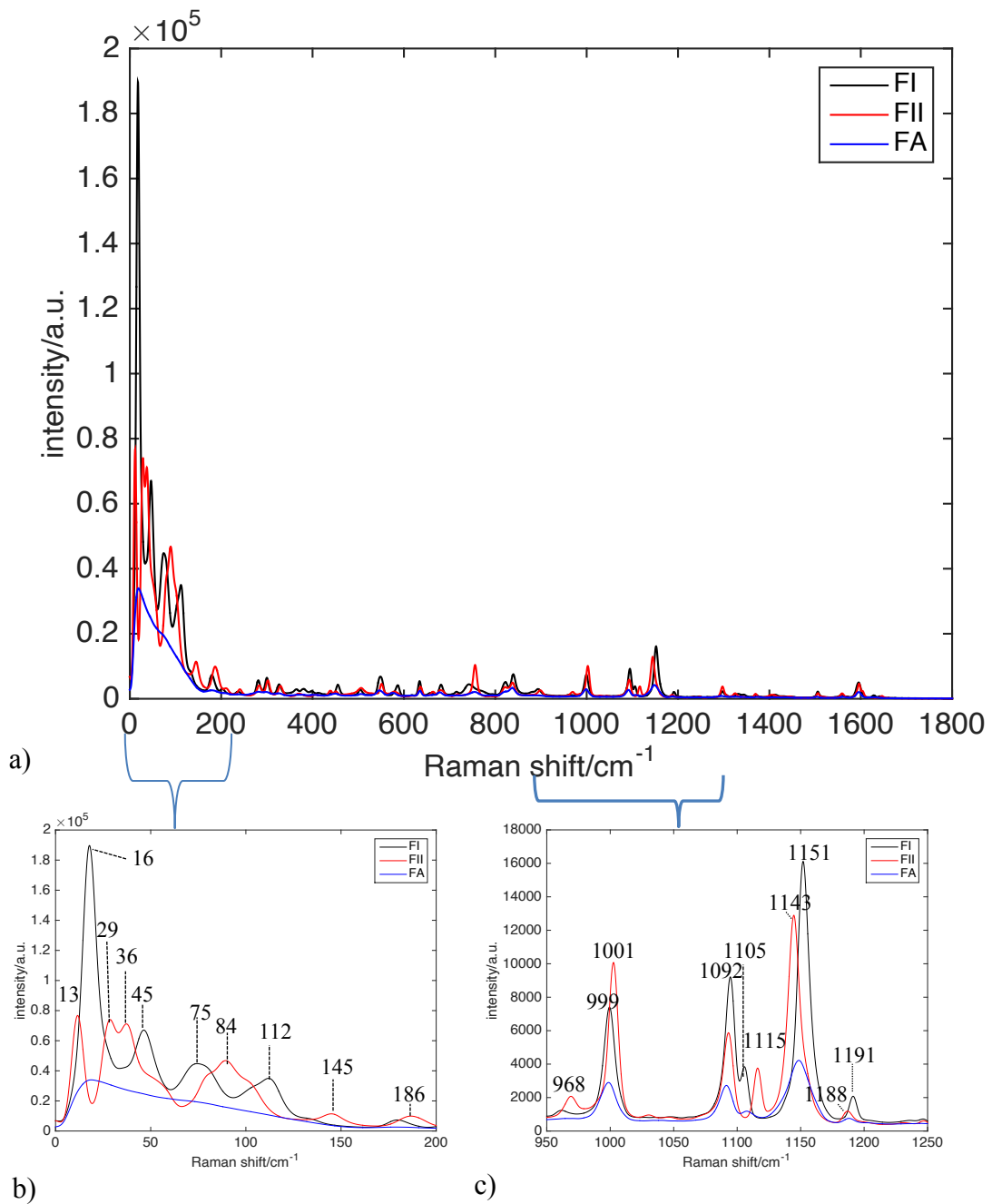
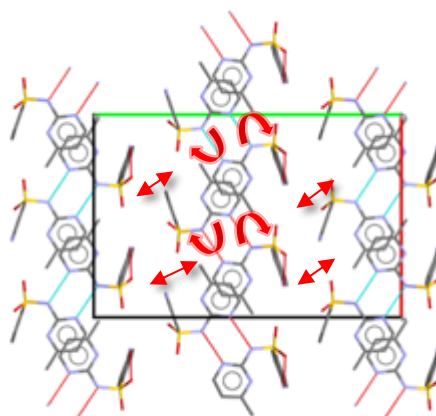
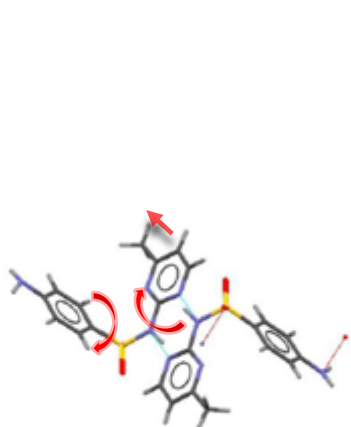


Figure 6.6 Raman spectra of sulfamerazine FI, FII and the amorphous forms showing a) the full spectral range, b) the low frequency Raman and c) the mid frequency Raman spectral regions

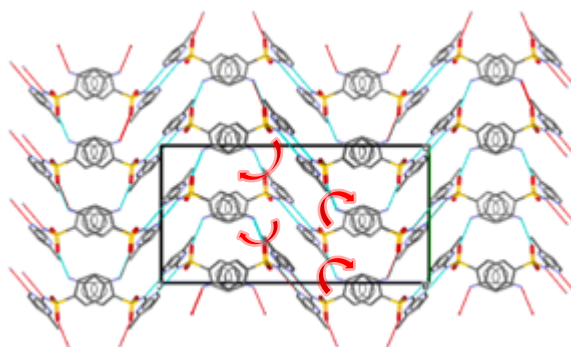
It can be easier to visualise where the different spectroscopic peaks come from by looking at the difference between molecular vibrations in the MFR (left) and lattice vibrations in the LFR (right) annotated by the red arrows in Figure 6.7.

Molecular Structure

Packing Arrangement



a) Form I (two molecules)



b) Form II

Figure 6.7 The molecular and crystalline packing structures of sulfamerazine a) Form I and b) Form II generated from Mercury software from reported structures.^{173, 174, 185} The blue and red lines indicate H bonding. The arrows represent an indication of molecular vibrations (left) and and lattice vibrations (right).

In the case of sulfamerazine, the distinctive differences between polymorphs in the LFR region makes THz Raman spectroscopy an ideal method studying polymorphic transitions in sulfamerazine.

In a study into SMZ Roy et al ¹⁷⁶ reported that its crystal structure played an important role in the in vitro release of the drug, they reported that FII tablets dissolved much faster than FI. This was explained to be due to FI possessing slip planes within its structure. Furthermore, FI exhibited much better tablet-ability and compressibility compared to FII crystals resulting in much harder tablets of FI. This is also reported in a study by Sun et al.,¹⁷⁸ in this study FII was produced in two batches as described in which the two batches differed mainly in particle size and tensile strength. It was found that FII with the lower particle size had higher tensile strength. It was concluded that FI crystals had greater plasticity and therefore greater compressibility and tablet ability over both batches of FII. It was also concluded that larger crystals in the same polymorph led to slightly lower tablet ability and slightly compressibility and therefore lower compact ability. While polymorphic form and particle size play a role there are also other factors in these studies that can be considered such as the interactions between the polymorph ¹⁷⁶ and the excipient.

6.3.3 Preparation of form II sulfamerazine by mechanical milling of form I

Figure 6.8 shows the Raman spectra, obtained using the Ondax probe with the Kaiser RXN1 Raman spectrometer, of samples milled in the 5 mL sample vial. As expected, the

THz spectral range shows much stronger and more distinct peaks than those in the traditional Raman fingerprint region.

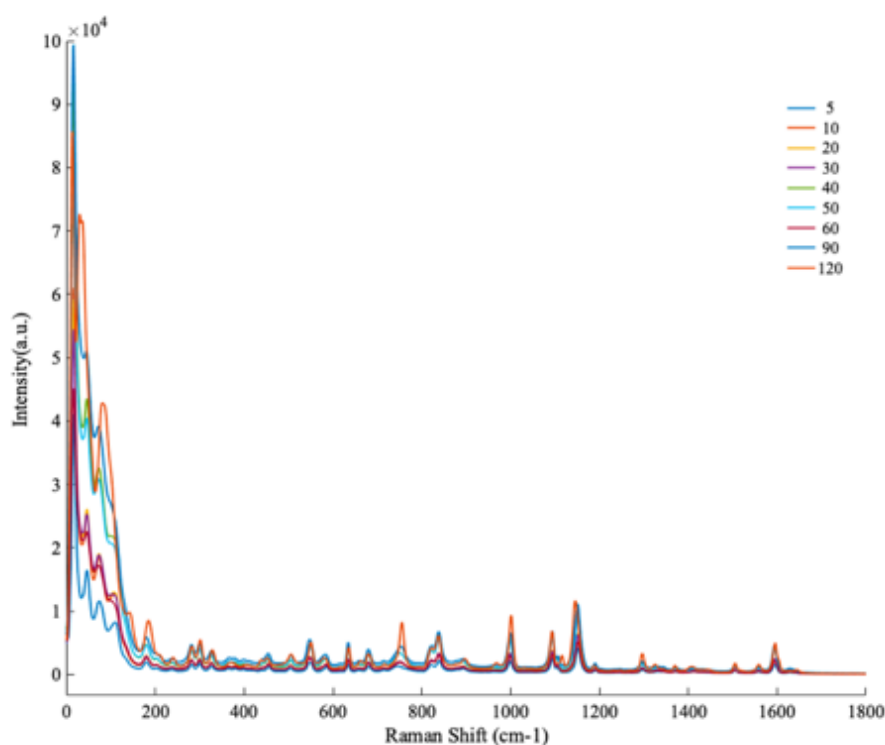


Figure 6.8 Raman spectra obtained using the Ondax probe with the Kaiser RXN1 Raman spectrometer of sulfamerazine milled at room temperature from 5 to 120 minutes.

The 1115 cm^{-1} peak in the MFR region after 120 minutes of room temperature milling indicates the presence of FII but otherwise it is quite hard to make out the spectral differences in the MFR region.

Figure 6.9 shows the LFR region, here we can see that the formation of FII correlates with a change in signal in this region. As the sample is milled, there is a clear change in the intensities of the signal below 200 cm^{-1} , the differences in strengths of the intra- and

interionic forces of the lattice modes will be changing as the molecule is being milled, particle sizes are changing and the degree of crystallisation within this sample will be changing. These intramolecular changes are likely the cause of the change in intensity of the signal.

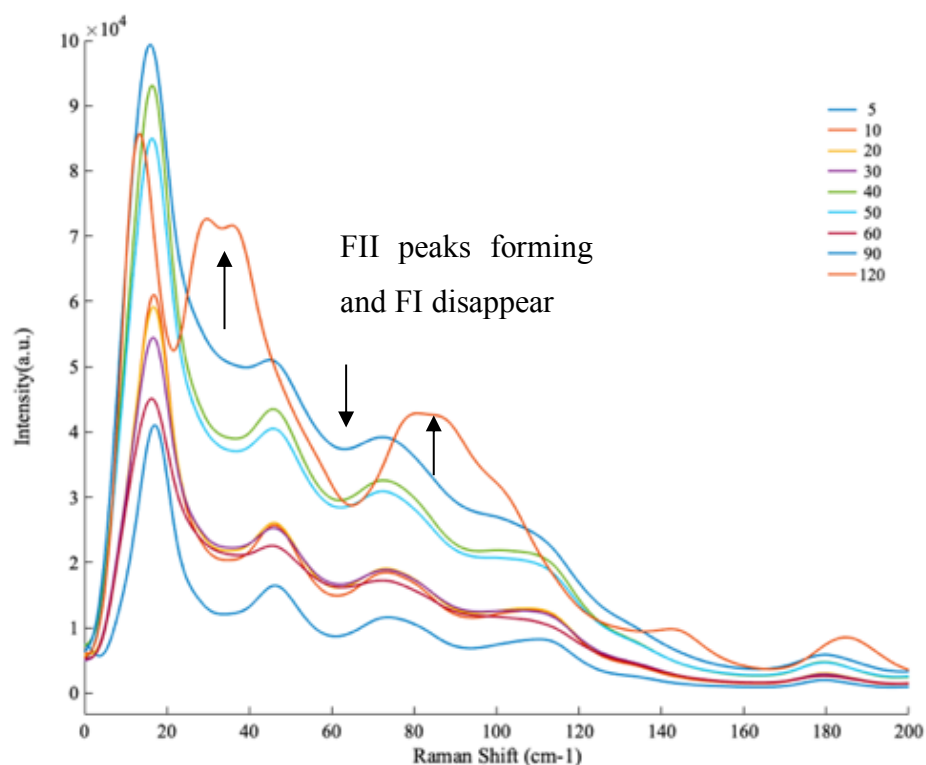


Figure 6.9 THz Raman spectra (0 – 200 cm^{-1}) of samples that were milled at room temperature for 5, 10, 20, 30, 40, 50, 60, 90 and 120 minutes.

As the sample is milled there is a change in the LFR signal, as the sample is milled through 40 and 50 minutes the peak intensities increase and as the sample is milled to 90 minutes the peaks become a lot smoother and lack definition, the smooth broad peak across the LFR region is indicative of the presence of FA. As the sample is milled further there is a polymorphic transition and the presence of FII is very clear by the presence of the distinctive double peak at 29 and 36 cm^{-1} and the presence of peaks at 84, 145 and

186 cm^{-1} : The resultant MFR spectra are shown in Figure 6.10. The main peak of interest in this spectra have been highlighted as it is more difficult to see the differences due to all of the spectral peaks present.

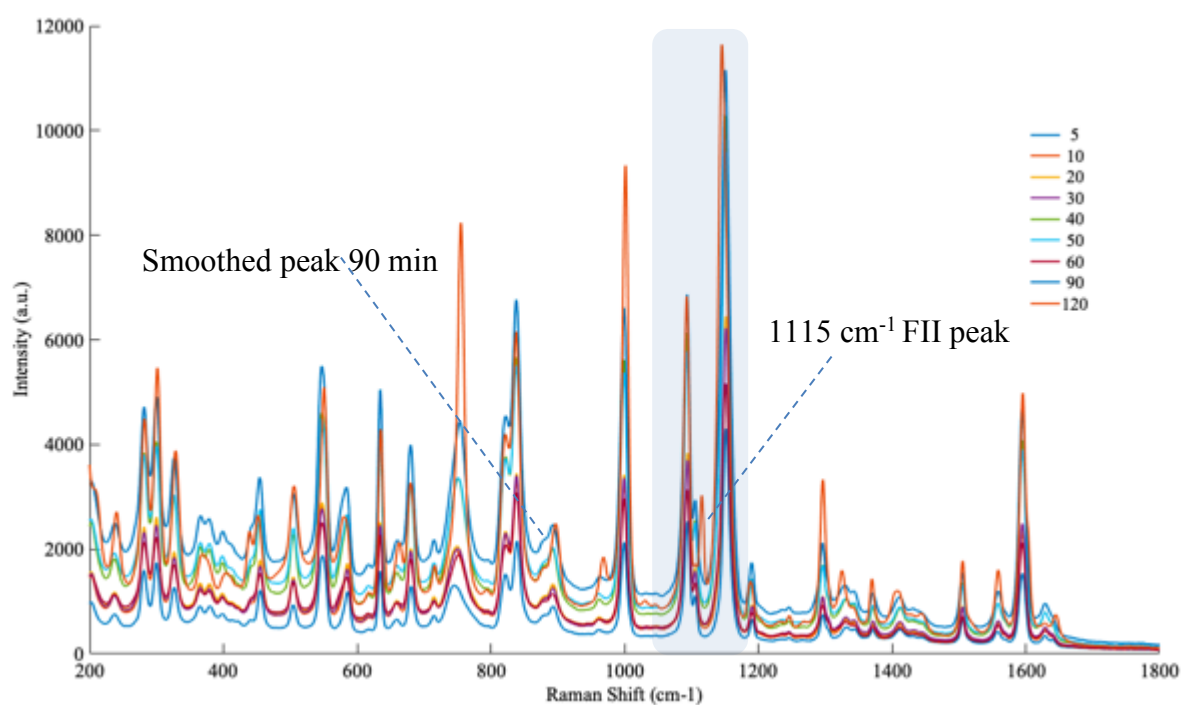


Figure 6.10 Raman spectra (200 – 1800 cm^{-1}) of samples of form I of SMZ that were milled at room temperature for 5, 10, 20, 30, 40, 50, 60, 90 and 120 minutes

As the sample is milled there is broadening of the peaks across the spectral range, this smoothing is most easily observed in the spectra at 90 minutes. It appears that the sample as it is milled moves through a semi amorphous phase before it changes to FII, as observed in the LFR signal. The corresponding FT-IR spectra were collected and can be seen in Figure 6.11, the FT-IR results from FI and FII reported earlier in Figure 6.5 confirm that the sample has changed to FII by 120 min.

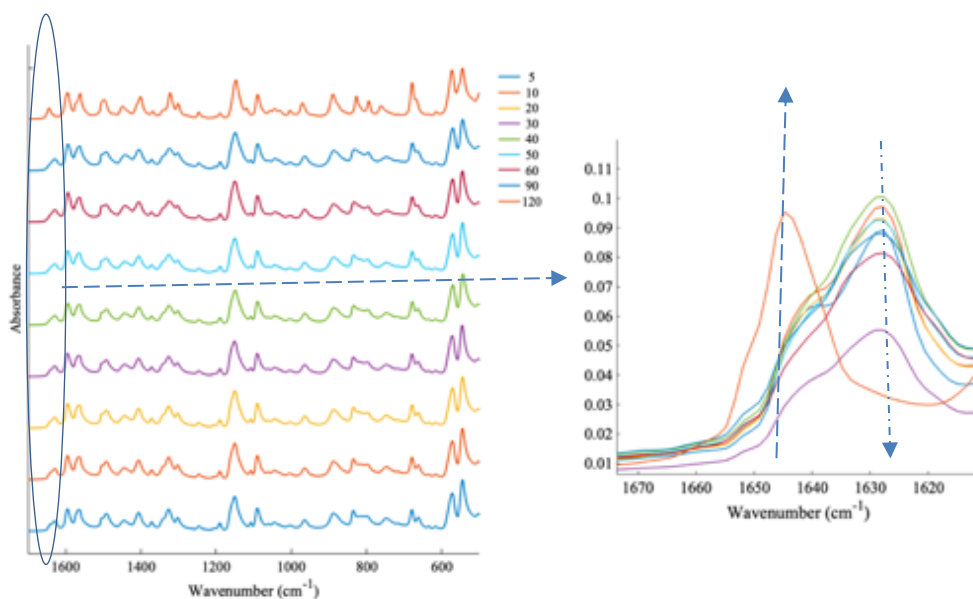


Figure 6.11 FT-IR analysis of room temperature milled samples 500-1650 cm^{-1} and on the right overlaid spectra showing the distinctive peak change for FII at 1646 cm^{-1}

The FTIR data of the peaks between 1660 and 1620 cm^{-1} show that FII peaks were clearly present at 120 minutes of milling. The results of this study showed that SMZ went through a transient amorphous phase. The phase transformation took longer to occur here than in a study reported by Macfhionnghaile et al,³⁷ which produced FII by 50 minutes of milling. This study employed a larger sample vial with the same method for analysis.

The experiment was repeated but the sample was milled through to 99 minutes with no analysis and then through to 339 minutes, these were then analysed to see what effect this had on the transformation to FII. The samples were analysed by FT-IR only as the THz Raman probe was being repaired and so not available at this time. The results of the main FTIR peak have been plotted in Figure 6.12.

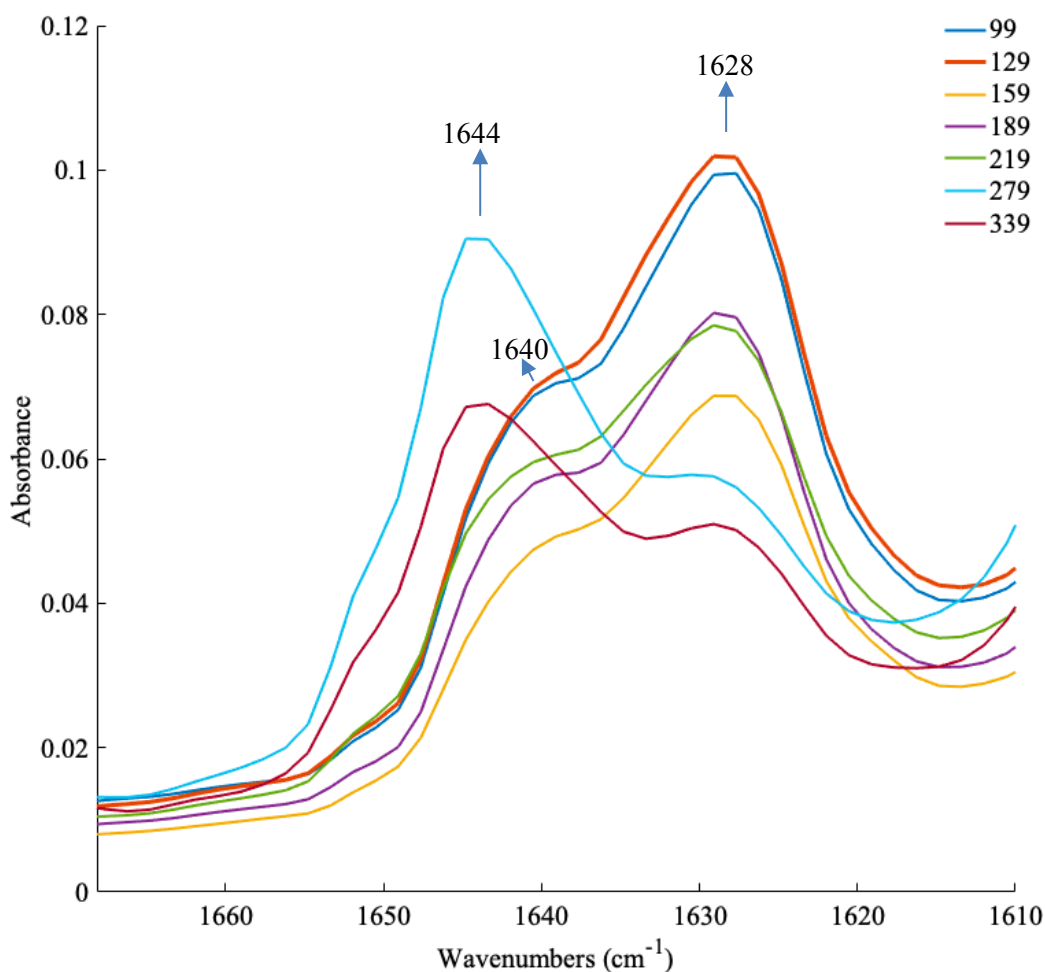


Figure 6.12 FTIR analysis of room temperature milled FI sulfamerazine from 99 to 339 minutes.

Analysis of the FTIR data shows that complete conversion of FI to FII was unsuccessful in this experiment, the peak at 1644 cm^{-1} still contained the FI peak at 1628 cm^{-1} suggesting the presence of FI and FII in the sample milled for both 279 and 339 minutes. Previously FII was present after milling the sample for 120 minutes at room temperature. The small sample vial holder didn't seem to be very effective in producing

FII, once a larger vial had been ordered, the experiment was repeated using the 25 mL holder.

6.3.4 Room temperature milling of Sulfamerazine using a 25mL sample vial

The experiment above was repeated in order to study the effects of sample vial size and repetition between samples. In this experiment, the sample holder was 25 mL, which is much larger than the 5mL sample holder used in the previous experiment, the sample vial also could contain a bigger sample size and had a larger ball bearing for the milling process. In this second experiment, FI was milled at 25 Hz for 5, 10, 20, 30, 40, 45, 50, 55, 60, 65, 70, 90 and 120 minutes. The samples were analysed by THz Raman spectroscopy and the results plotted in Figure 6.13.

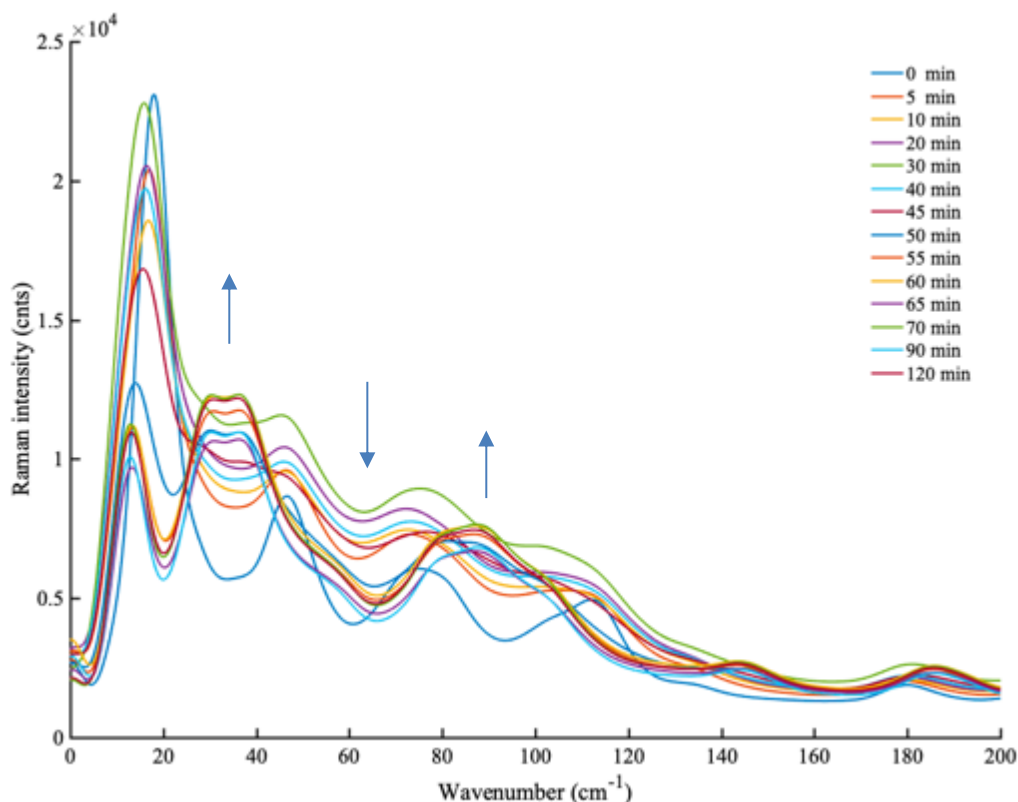


Figure 6.13 THz Raman spectra of sulfamerazine samples milled at room temperature in 25 mL sample vial from 0 to 120 minutes.

The sample milled in the 25 mL sample holder transformed much quicker to FII from FI through milling than that of the results from the 5 mL sample vial shown in Figure 6.7. In the 5 mL sample vial, FII was seen at 120 minutes. In this case, the transition through the semi amorphous material and slight indications of FII are observed at 30 minutes, there is a significant amount of FII then seen in the samples milled after 30 minutes. It is proposed that the difference in stability between FI and FII is small enough that the choice of milling assembly has a big effect on the milling times. Milling of FI again goes through an intermediate, semi amorphous phase before it converts to the more stable FII.

In the 25 mL jar, more of this transient phase and the conversion between FI and FII are observed.

6.3.4.1 Preparation of bulk form II sulfamerazine by solvent mediated phase transformation

LFRS was not available during the experiments so MFR was applied for conformation of the formation of FII of sulfamerazine. Solvent-mediated phase transformations can be considered as two consecutive processes with two major steps; the first is the nucleation of the stable crystals and the second the recrystallisation of the metastable crystals into stable ones in a solution.²³ The Raman results from the in-line MR probe are shown in Figure 6.14. The average height of the peak between 1110 and 1200 cm^{-1} was plotted with the stir rate to see more closely the relationship between stir rate and formation of FII. The results for this are in Figure 6.15. The FBRM results are plotted in Figure 6.16. This experiment was also repeated with an immersive THz Raman probe but complications in the analysis gave poor results so they were omitted from the experiment.

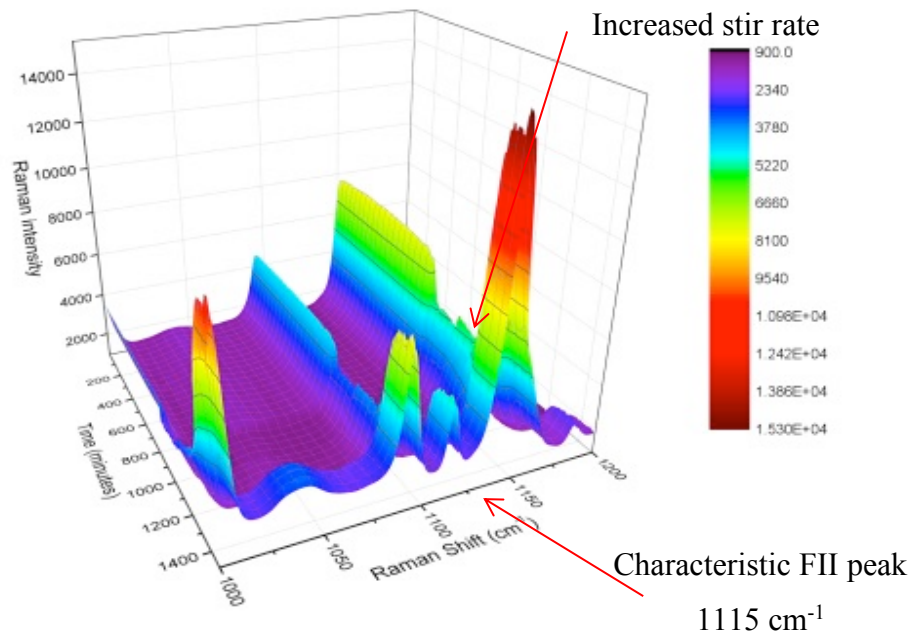


Figure 6.14 3D Plot of Raman spectra obtained between 1000 – 1200 cm⁻¹ showing the characteristic peak 1110 – 1125 cm⁻¹ of SMZ FII appearing with time as stir rate is increased from 400 through to 600 rpm

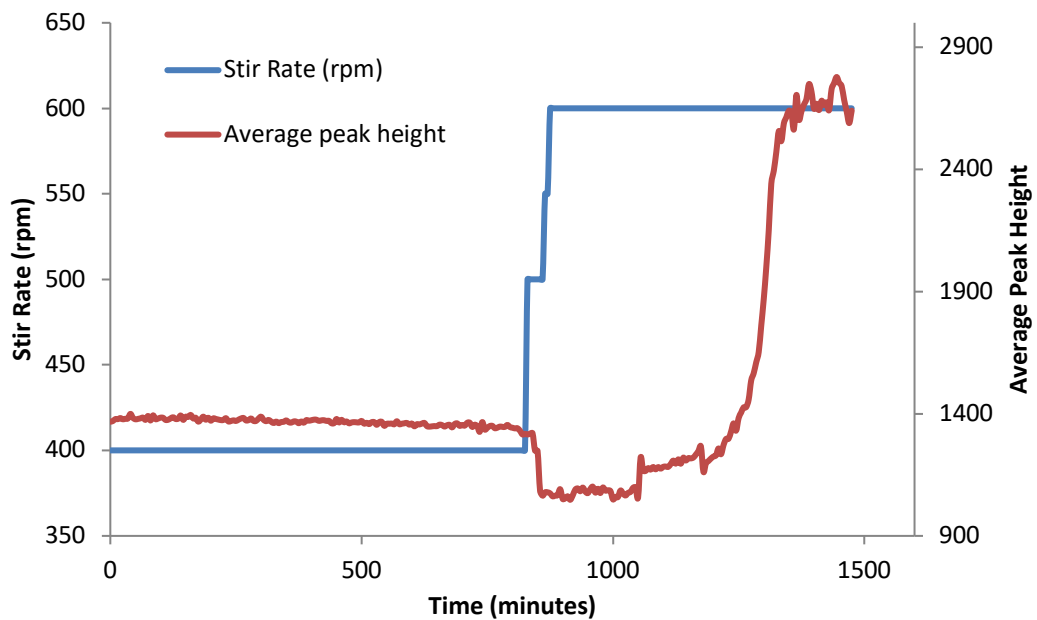


Figure 6.15 Change in average peak height between 1110 and 1125 cm⁻¹ representing the formation of FII SMZ during the SMPT of FI to FII

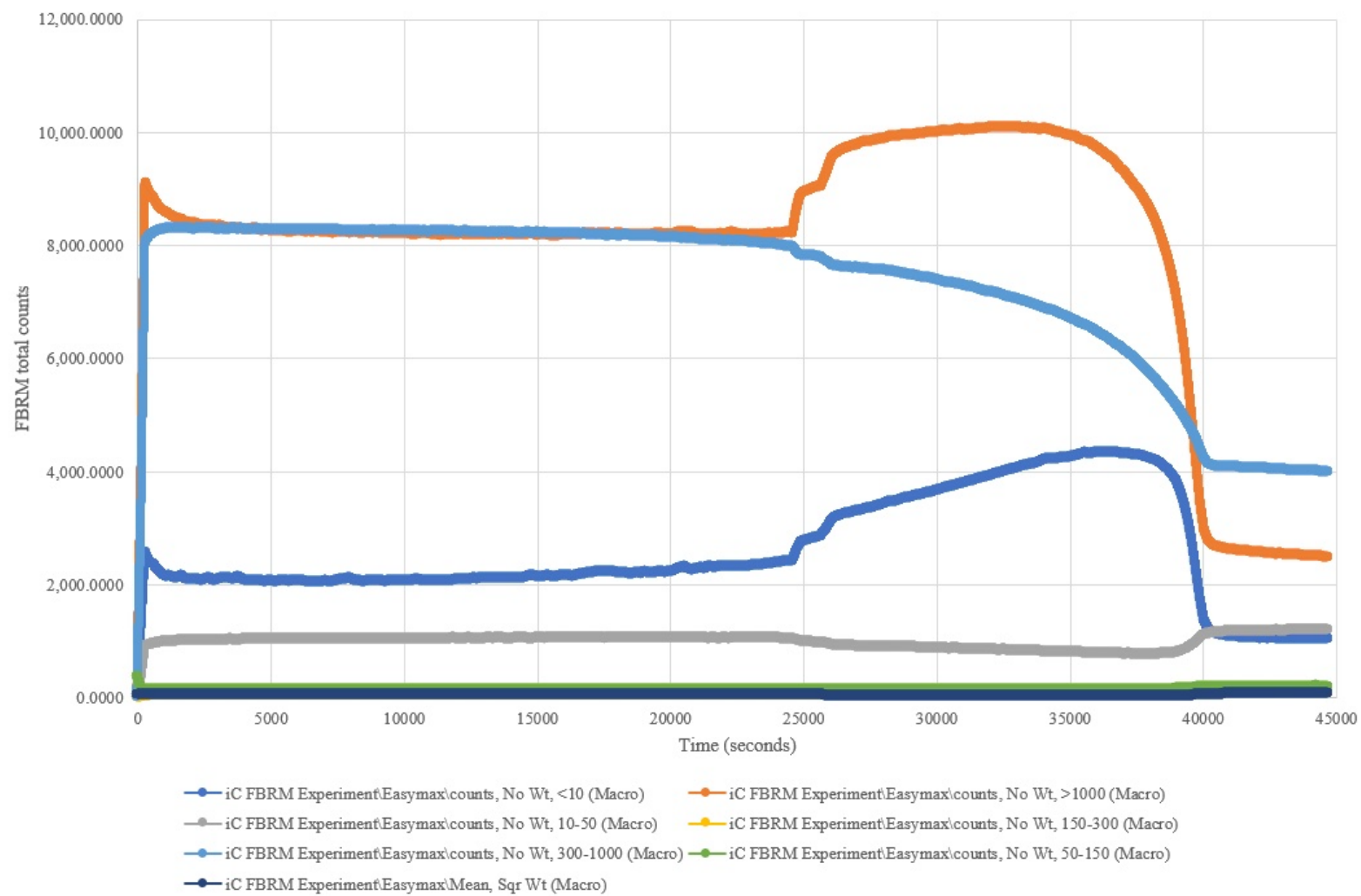


Figure 6.16 FBRM results from the SMPT of FI to FII polymorphic conversion of sulfamerazine

The FBRM results show a spike at the start which is the FI SMZ being added to the sample. Some of this appears to dissolve and there is then a steady signal until 25000 seconds, this is when the agitation is increased. As the agitation increases the sample in solution starts to crystallise out into FII causing a jump in signal of the $<10\ \mu\text{m}$ and a sharp jump in signal of larger particles $> 1000\ \mu\text{m}$. As these increase, there is a decrease in signal from particles at $10 - 50\ \mu\text{m}$ and from particles $10 - 50\ \mu\text{m}$.

6.3.5 FII Sulfamerazine Conformational analysis

6.3.5.1 Differential Scanning Calerometry Analysis

The DSC thermogram results from the experiment are shown in Figure 6.17

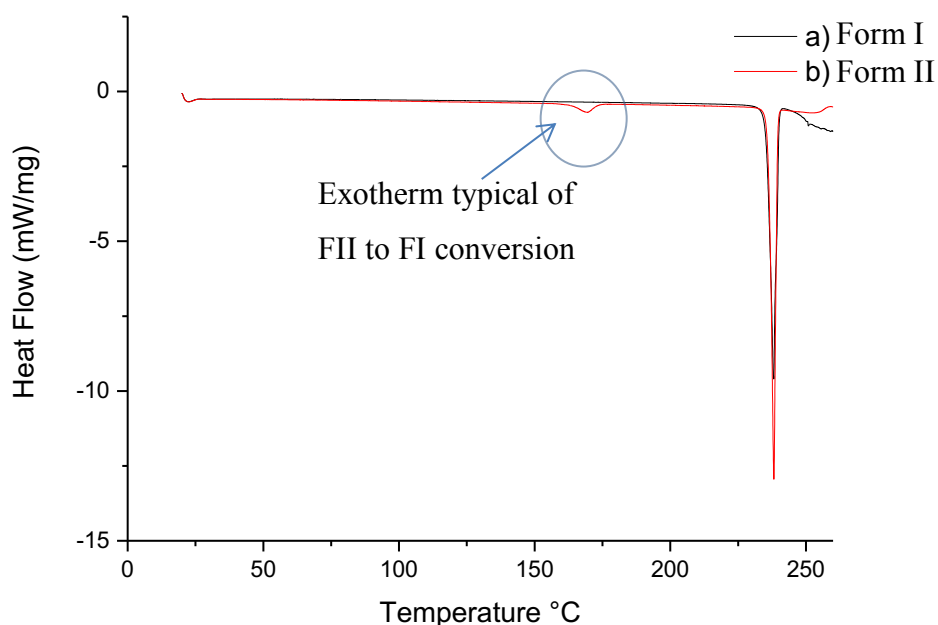


Figure 6.17 DSC analysis of SMZ FI and the sample obtained from SMPT of FI to FII showing a) Form I and experimentally obtained Form II b).

The thermogram results for a) show one exothermic peak between 236 – 237 °C in b) there are two exotherms, one at around 170 °C and the other again 236 – 237 °C. DSC analysis of FI and FII by Roy et al,¹⁷² shows that FI has a single melting exotherm at around 235 °C whereas SMZ FII shows a transition endotherm from the metastable FII to stable SMZ FI at 170 °C a good indicator that FII is present. This is followed by the exotherm at 235 °C from the melting of FI.¹⁷⁶ Another paper has also shown similar results but with the transition temperature at 160 °C. A small peak near 170 °C this is reportedly caused by the enantiotropic transformation of FII to FI.^{63, 185}

6.3.5.2 XRPD analysis

XRPD results comparing the starting material and the material produced by the SMPT are shown in Figure 6.18.

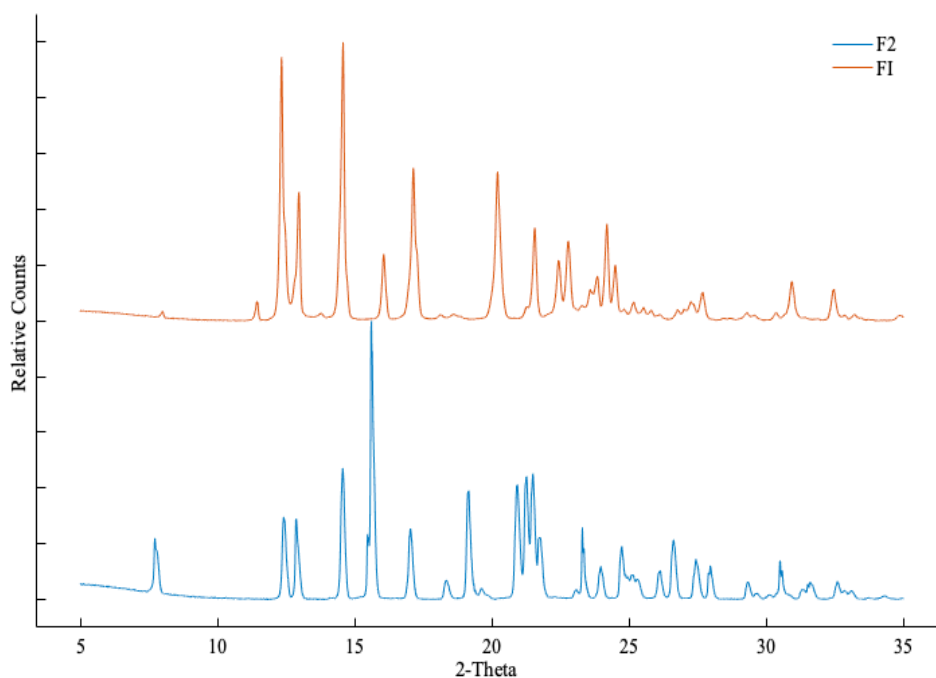


Figure 6.18 Conformational XRPD analysis of FI and FII of sulfamerazine produced by solvent mediated phase transformation

6.3.5.3 Microscopy

Microscopy analysis of SMZ was carried out to examine the morphology of samples. It has been noted that FI crystals are more plate like whereas FII take on a more prismatic shape.¹⁷⁵ Another paper reported that for the bulk material no preferred particle shape was preferred for FI or FII but for single crystal analysis FI tended to be rectangular laths while FII were more rectangular.¹⁷⁹ Another paper reported FI bulk powder to be typically shaped like thin plates whereas FII prepared from SMPT had the appearance of small distorted cubes.⁶³ Microscopy images of FI (Figure 6.19) and FII (Figure 6.20) show crystals of FI and FII.

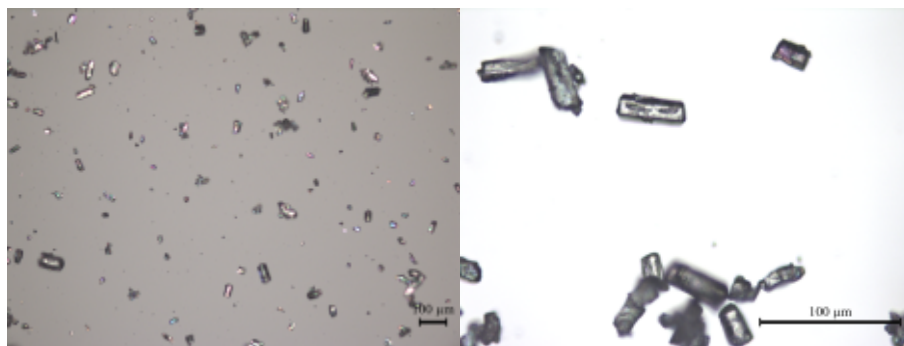


Figure 6.19 Microscopic image of FI SMZ samples taken of the bulk powder showing long hexagonal structures typical of FI crystals

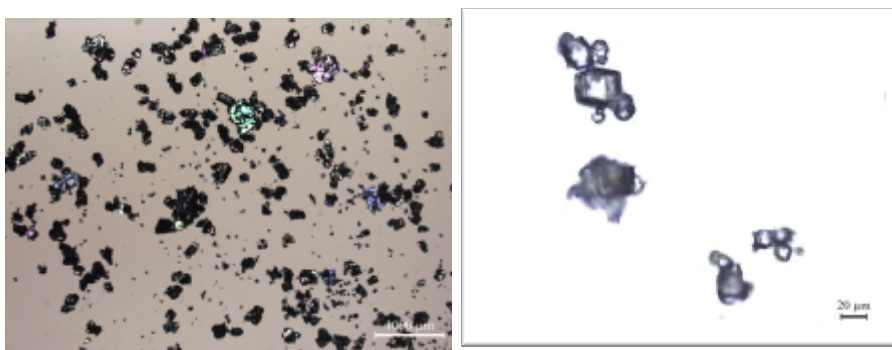


Figure 6.20 Microscopy results of crystals obtained via SMPT of FI showing crystals formed from the packing of distorted hexagonal structures of FII

The FI crystals mostly contained long column like shapes whereas the FII crystals were made up of shorter distorted hexagonal clusters, these shapes were consistent throughout the samples and are similar to those found in the literature.^{186, 187}

6.3.6 Preparation of the amorphous form of sulfamerazine via cryo-milling of FI

The generation of high energy amorphous material is usually undesirable and given the opportunity it spontaneously transforms to a more thermodynamically metastable form. The spontaneity of these molecules makes them hard to work with in the sense that they didn't stay amorphous for long. Samples cryo-milled for 45, 60, 70 and 90 minutes were analysed by XRPD and compared to XRPD samples of known FI and FII. The results are shown in Figure 6.21. Here it can be seen that samples do not show broad signals with no distinctive peaks as would be typical for amorphous material. The time taken for this analysis is almost 50 minutes and it therefore is concluded that samples may have recrystallised during the XRPD analysis.

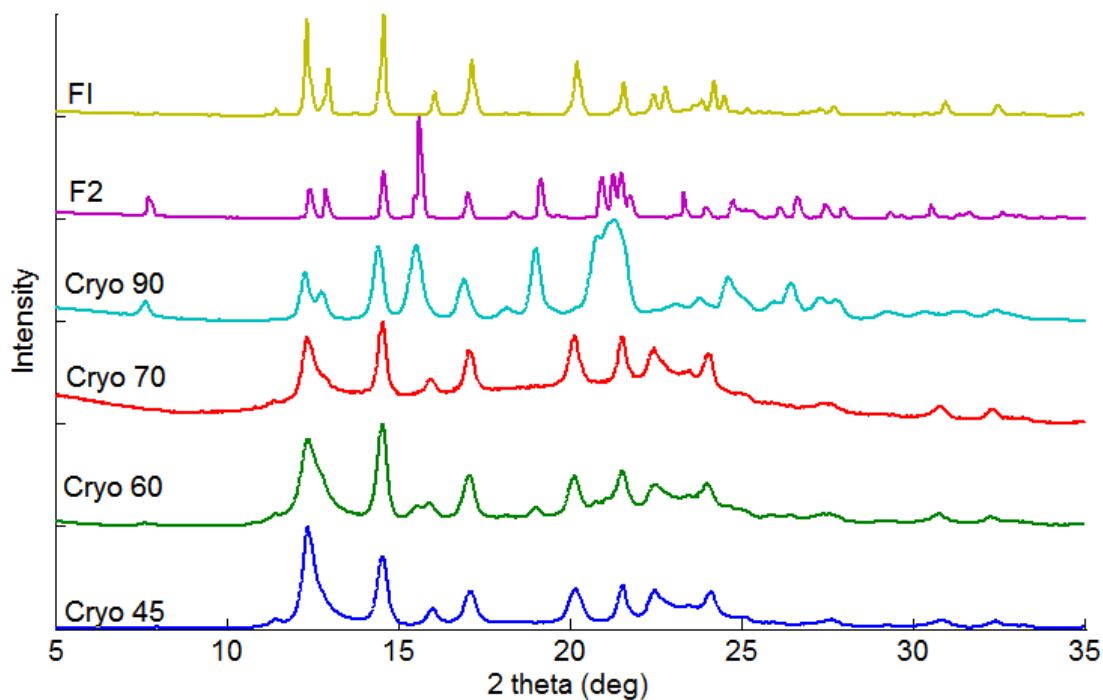


Figure 6.21 XRPD analysis of FI cryo-milled for 45, 60, 70 and 90 minutes plotted with XRPD patterns for FI and FII SMZ

The results also show that the sample cryo-milled for 90 minutes recrystallised into FII, the samples cryo-milled for 70 and 60 minutes have mostly recrystallized into FI but look like they may contain small amounts of FII.

A much faster XRPD analysis was carried out from 10 to 18 degrees in order to try and capture the amorphous material before it converted back to crystalline. Samples milled for 40 and 60 minutes are plotted in Figure 6.22 show the XRPD patterns from these samples. The distinctive amorphous pattern is present for the sample cryo- milled for 60 minutes and the sample cryo-milled for 40 minutes contains crystalline peaks. This indicates that a 40-minute analysis time was not long enough for the FI to convert to FA.

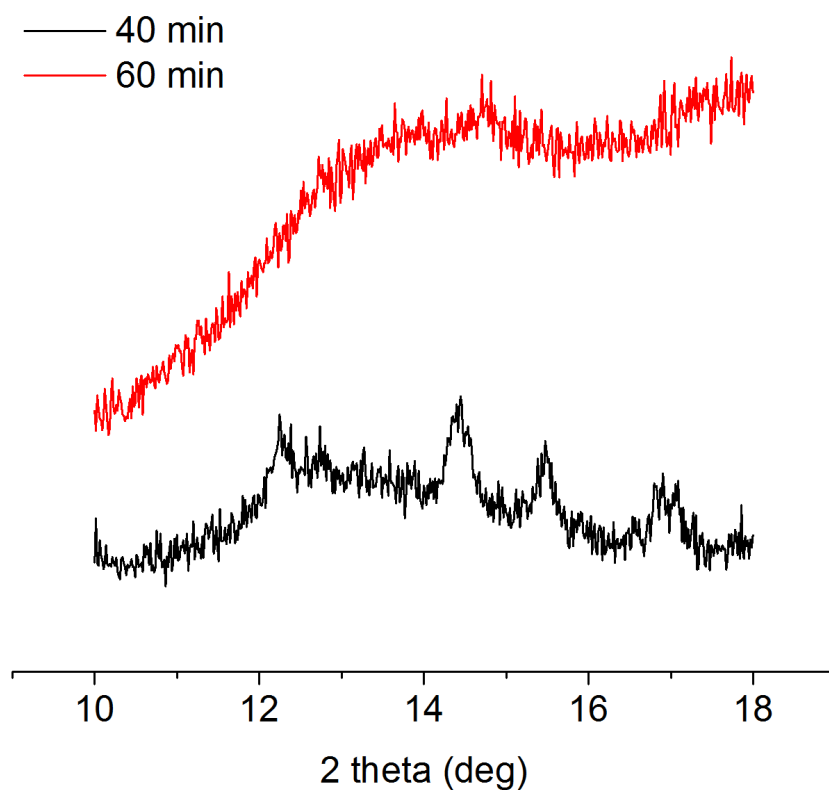


Figure 6.22 Fast scan XRPD analysis of samples of FI of SMZ cryo-milled for 40 and 60 minutes

Samples cryo-milled for 30, 60 and 70 minutes were analysed by LFRS, the results from this analysis are shown in Figure 6.23.

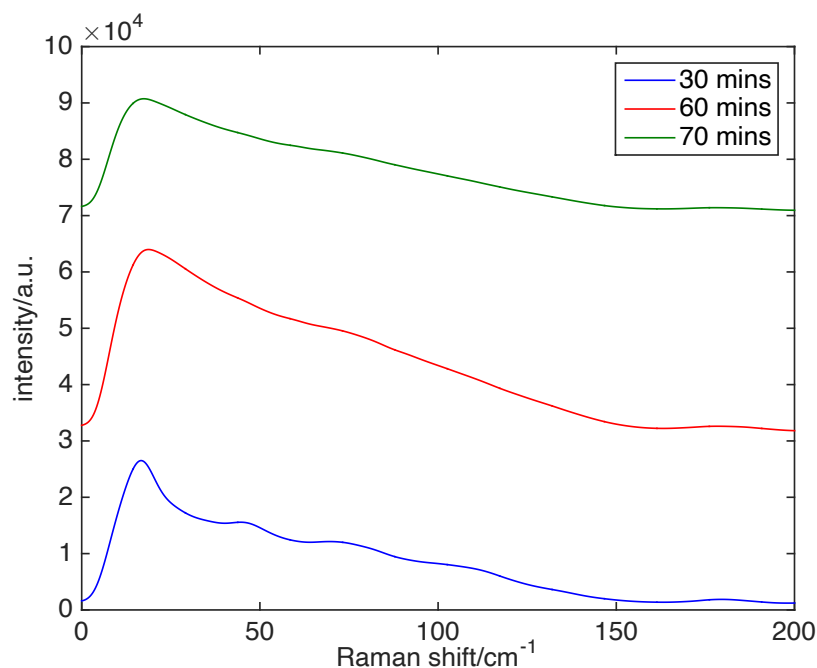


Figure 6.23 LFRS analysis of sulfamerazine samples cryo-milled for 30, 60 and 70 minutes.

The LFRS results show that at 30 minutes of cryo-milling the sample is almost amorphous but still contains some crystalline peaks indicating it is not fully amorphous. By 60 and 70 minutes the sample has the distinctive smooth signal indicative of amorphous material in the LFR region. The samples cryo-milled for 60 and 70 minutes were analysed over time to observe the polymorphic transitions from amorphous to crystalline over time and to try and understand why XRPD analysis was failing to see the amorphous content. The results are shown in Figure 6.24 and Figure 6.25.

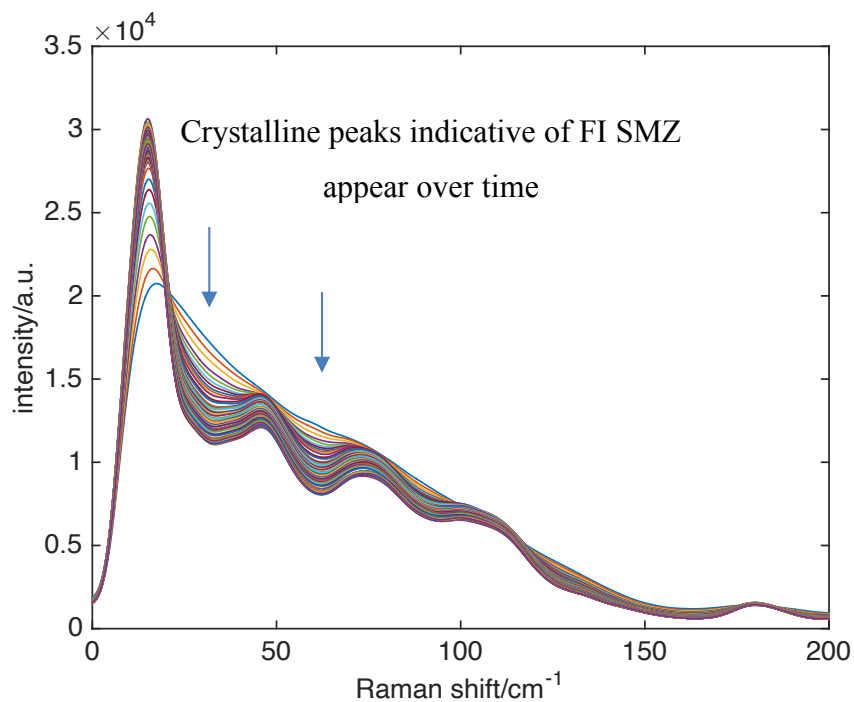


Figure 6.24 Low frequency Raman spectra of polymorphic change with time of sulfamerazine samples cryo-milled for 60 minutes

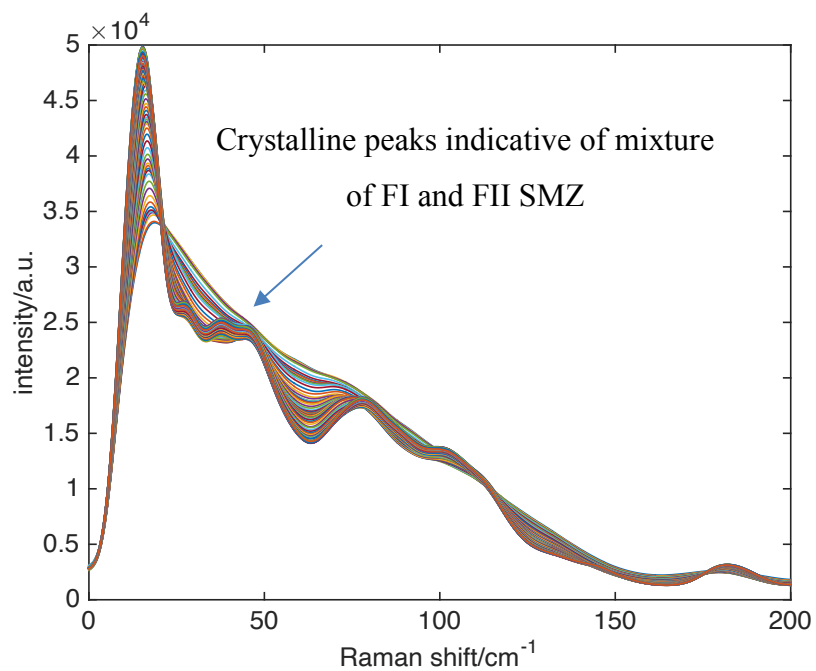


Figure 6.25 Low frequency Raman spectra of polymorphic change with time of sulfamerazine samples cryo-milled for 70 minutes

The sample cryo-milled for 60 minutes moves over time from an amorphous form back down into what appears to be mainly FI of SMZ, however the sample milled for 70 minutes shows peaks distinctive of FII SMZ.

CLS regression was applied to the results in order to and quantify the amounts of FI, FII and FA present in samples. The approach was validated by preparing mixtures of known compositions of FI, FII and FA shown in Figure 6.26 and the calculated CLS Table 6.5.

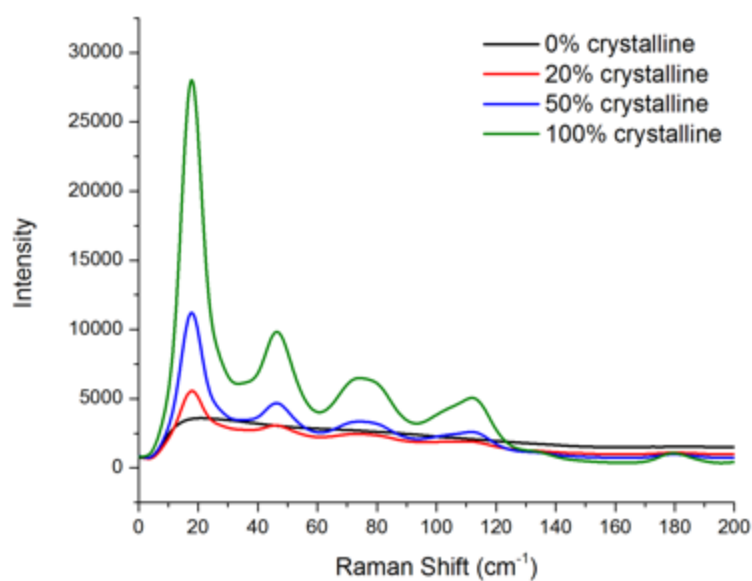


Figure 6.26 LFRS for CLS analysis of samples of known composition of sulfamerazine crystalline forms.

Table 6.5 CLS model

| Sample | F1:Amorphous | CLS Calculated F1: Amorphous |
|-----------------|--------------|---------------------------------|
| 20% Crystalline | 20:80 | 19:81 |
| 50% Crystalline | 50:50 | 49:51 |

The results calculated from the data from Figure 6.24 and Figure 6.25 the calculated results are plotted with time in Figure 6.27 and Figure 6.28.

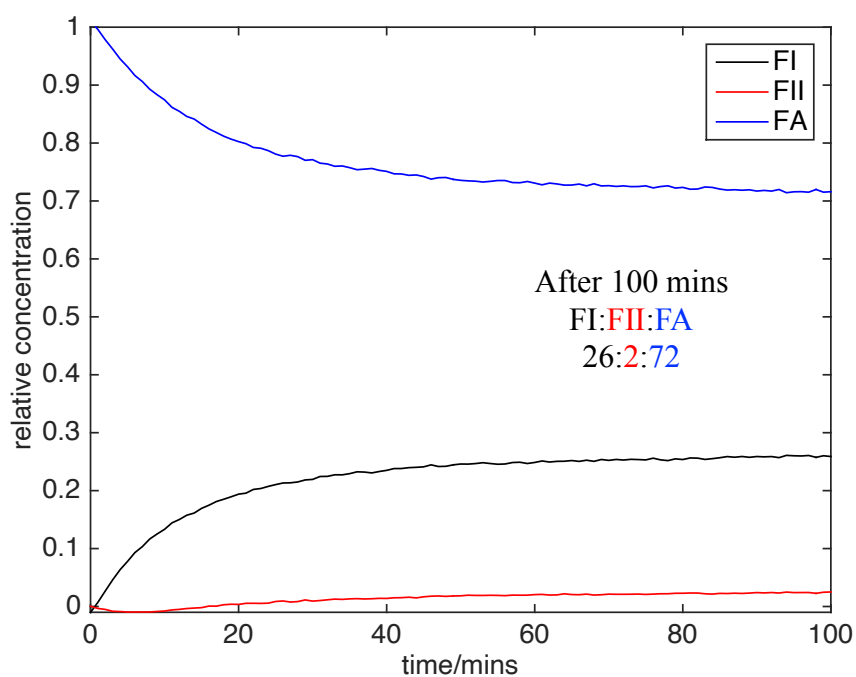


Figure 6.27 CLS regression analysis of 60-minute cryo-milled sample changing with time over 100 minutes

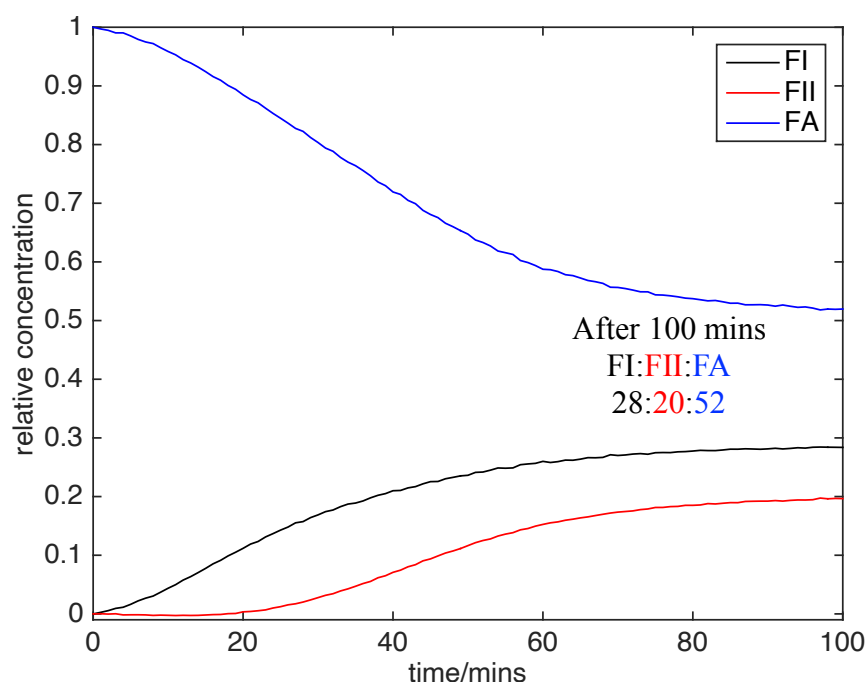


Figure 6.28 CLS regression analysis of 70-minute cryo-milled sample changing with time over 100 minutes

6.4 Conclusions

Room temperature milling of SMZ was successfully monitored with THz Raman Spectroscopy allowing for information on changes in the crystalline lattice to be monitored using low frequency Raman. The results confirmed that Sulfamerazine Form I when milled at room temperature at 25 Hz goes through an intermediate amorphous phase and then converts into form II. The size of the milling compartment and the ball bearing used had an effect on the transition times, the larger ball bearing and sample vial (25 ml) giving much quicker transition times. CLS regression analysis showed change in polymorphic form of FI to FII through an intermediate amorphous phase. Bulk form II Sulfamerazine

was able to be produced using a solvent mediated phase transformation in an overnight experiment taking less than 24 h. This was achieved by the addition of agitation to the process by increasing the stir speed during the reaction. Conformation of FII was achieved by XRPD, DSC and Raman analysis. Cryo-milling of SMZ produced amorphous material after about 60 minutes, XRPD analysis was not able to capture the amorphous material quick enough but THz Raman was able to do so in real time. The ability to analyse amorphous material in real time allowed for the monitoring of the change of amorphous to crystalline material with time, showing that the samples milled for 60 minutes transformed back to mostly FI and those cryo-milled for 70 minutes transformed to mostly FII. This can be used to distinguish between amorphous and crystalline forms of Sulfamerazine significantly faster than off-line techniques such as XRPD.

There are much larger spectral differences between physical forms in THz Raman region compared to FT-IR and Raman. Signals are more intense in the THz Raman region compared to Raman which allows for more sensitive detection of different forms and the transformations between these forms. Both qualitative and quantitative analysis of mixtures of Sulfamerazine were able to be carried out using CLS regression. The addition of low frequency Raman allows for the analysis of both structural and chemical information of Sulfamerazine solid forms.

Chapter Seven

Overall conclusions and future work

7. Overall conclusions and future work

7.1 Conclusions

The aims set at the beginning of this work were:

- To assess the ability of the Eyecon dynamic image analyser as a process analysis technology for granule characterisation both offline and as an on-line application for Twin Screw Granulation analysis.
- To evaluate using a DoE approach the suitability of the Eyecon dynamic image analyser for the application of real time analysis of granules produced by continuous twin screw granulation.
- To assess low frequency Raman spectroscopy as an alternative to XRPD, DSC and Raman Spectroscopy for physiochemical analysis of /crystalline content within amorphous solid dispersions.
- To apply low frequency Raman in-line for real time analysis of a Hot Melt Extrusion process.
- To apply low frequency Raman spectroscopy to an industry relevant Hot Melt Extrusion process.
- To study solid state phase transformations of pharmaceuticals using low frequency Raman spectroscopy in real time.

7.1.1 The assessment of the ability of the Eyecon dynamic image analyser as a process analysis technology for granule characterisation off-line and as an on-line application to Twin Screw Granulation

Samples of different size, shape and surface properties along with some granules of varying sizes were prepared for preliminary off-line tests. The Eyecon Image analyser was then applied on-line for a simple twin-screw granulation process of a placebo formulation, HME parameters were whanged, changing the size of the granules produced. The Eyecon was then applied on-line to test the ability of the Eyecon to pick up on process perturbations. The samples were compared to off-line sieve analysis measurements.

- The RGB lighting was excellent for particle edge detection but limited the analysis, shiny or reflective samples were unable to be analysed due to the reflection of these lights. Off-line analysis was easy, although the movement of the sample stage through the twenty-five-stage pattern was clunky and tedious.
- Off-line analysis of granules fractions showed good correlation with the fraction sizes. The images were clear and the larger granules were easy to disperse. It was however tricky to get a good distribution of the samples on the sample plate without a lot of overlap/overcrowding of particles. The analysis showed good volume and number distributions but no other information on shape or surface properties of the particles/Granules.
- Liquid to solid ratio studies showed an increase in granule size with increased water concentration, this was reflected in the data and images captured from On-line analysis of granules.

- Off-line granule size analysis using the Eyecon showed different response to those taken on-line, this was thought to be due to the granules being dried and poor distribution/overlapping granules. Sieve analysis however showed similar size for all if the experiments.
- The Eyecon image analyser was successfully implemented into a TSG process showing proving to be a viable technique for granule size analysis.

7.1.2 Application of a DoE approach to assess the ability of the Eyecon dynamic image analyser as a process analysis technology for granule size analysis of Twin Screw Granulation Process.

A DoE approach was applied to the TSG process. Three parameters including screw speed, feed rate and water content were varied, the Eyecon was applied on-line to the TSG and the DoE carried out each for five minutes. The granules produced were collected, dried and measured off-line with both sieve and Eyecon analysis. Further experiments were carried out at high flow rates after some issues had been resolved with fouling of the instrument.

- The experiments were successful at low powder feed rates up to 1200 g/h and showed good agreement with sieve analysis in terms of the D50 results. The data obtained from the analysis was able to provide information on size and volume of granules produced and the D values were an easy way to look at the trends in the data.

- At feed rates above 1200 g/h and when the system had been running a while there were issues with fouling at the analytical window of the instrument. Fouling was quickly indicated in the images and spikes in the data response. The addition of the heating element helped to keep the sample chute and analysis window free from moisture and the fouling issues were overcome and the DoE was completed.
- The image analyser after some adaptations was able to analyse TSG at high process conditions up to 6 kg/h and for prolonged periods of time. This is something that has not yet been reported and proved the ability of the Eyecon for inline analysis.
- The Eyecon with its RGB lighting proved to be a useful technique for high flowing material like granule analysis. The software is also able to give a lot of useful information on different size parameters of the particles and the volume weighted D values proved useful for physical characterisation of granules but there definitely could be improvements in this to be able to pick out more morphological properties other than size and volume.

7.1.3 To assess low frequency Raman spectroscopy as an alternative to XRPD, DSC and Raman Spectroscopy for physiochemical analysis of amorphous/crystalline content within amorphous solid dispersions.

ASD's of PCM-AFF were produced by hot a hot melt extrusion process. LFRS, XRPD, Raman Spectroscopy and DSC analysis was applied off-line to investigate physiochemical properties of the ASDs. The ASDs were in the form of Extrudates, studies on the homogeneity and stability over five months was also carried out. PCA analysis of XRPD and LFR results from these studies was carried out.

- The initial investigations with LFR showed clear differences in crystalline peaks that corresponded to the higher concentrations of PCM. Comparison with XRPD and DSC showed good agreement with the detection of crystalline and amorphous material present in the extrudes.
- DSC results showed high sensitivity to crystalline material present in the extrudes and appeared to detect the presence of multiple forms, not detected in XRPD but possibly present in thought to be due to heat transformations induced by the heating process of DSC.
- The stability studies proved to be a success, the changes in crystallisation as the API crystallised out of the polymer with time was successfully detected by LFR and were in good agreement with the XRPD results.
- Homogeneity studied showed that the extrudes were not of uniform distribution, LFR was able to detect variations in solid form along and between the extrudates. Detection of multiple forms with LFR showed sensitivity to this technique although further studies would have to be carried out to confirm this.
- LFR proved to be a very successful technique for analysis of pharmaceutical solid states. The ability to access both chemical and physical information in real time is

advantageous and the THz Raman spectroscopy proved to be an excellent substitute for XRPD analysis of solid state especially for analysis of amorphous content due to its high instability. The application of THz Raman spectroscopy to amorphous dosage forms proved really successful in determining amorphous and polymorphic forms both of-line and in-line during HME.

7.1.4 To apply low frequency Raman in-line for real time analysis of Hot Melt Extrusion process.

LFR was applied in-line to HME process using an in-line Raman spectroscopy probe. The extrusion of PCM-AFF of different drug loadings was carried out. All other parameters were kept fixed. The dispersed extrusions were collected and analysed off-line.

- In-line analysis of HME process using LFRS was really promising, changes in the concentration of API were able to be detected in the HME of PCM-AFF at different drug loadings, the LFR results showed a smooth peak indicative of no crystalline material present indicating that the API was fully dissolved in the polymer carrier and that the material is amorphous during HME.

7.1.5 To apply low frequency Raman spectroscopy to an industry relevant Hot Melt Extrusion process.

An undisclosed company was having issues with a HME system during production whilst extruding stearic acid. The torque measurements were rising suddenly and the system was jamming causing the system to block and the process to have to stop. This would

then result in a full clean of the instrument and a re-run of the system, a time-consuming task and an inconvenience. The parameters were altered while analysis with LFR was carried out in order to try and determine the cause of the problem.

- Off-line analysis studied stearic acid cooling from an amorphous melt at 90 °C to crystalline material. The LFR was able to monitor this change with time easily as it moved through the amorphous crystalline phase.
- THz Raman was applied in-line to the HME of stearic acid. The ability to detect the change in amorphous to crystalline material in the extrusion of stearic acid at varying temperatures and was able to determine the onset of crystallisation in a melt cool crystallisation of stearic acid. The cause of the jamming was due to the stearic acid crystallising at temperature.
- LFR was able to be used as a tool to determine the best temperature for HME of stearic acid. The study showed that at 70 °C the system was able to be run constantly with no jamming hence solving the jamming issue.

7.1.6 To study solid state phase transformations of pharmaceuticals using LFRS in real time.

Solid forms of SMZ were prepared by cryo-milling and milling of FI. The milling and cryo-milling processed were monitored by LFRS, FT-IR method development of a solvent mediated phase transformation of FI to FII in order to prepare mixtures of FI, FII and FA which were studied by CLS regression.

- Room temperature milling of SMZ FI was successfully monitored using both LFRS and FT-IR. Both results showed a transition from FI to FII through an intermediate FA phase. The LFR showed a classic amorphous curve below 200 cm^{-1} and the FT-IR showed more smoothed out peaks when there was amorphous content present.
- When room temperature milling it was found that different size ball Bearings had an effect on the rate of change of solid-state transformation, larger ball bearings resulting in a faster transition. When cryo-milling there were many issues with the stability of the FA which did not co-inside with that of the literature. It was therefore difficult to build stable mixtures of FI, FII and FA.
- FA was able to be formed after 60 minutes though and measurements were able to be made and the transitions monitored in real time with LFRS. It was however found that XRPD could not analyse the FA quick enough to detect the FA that was clearly visible by LFRS. Quantification studies using CLS regression were successful in analysing mixtures of known quantities of FI, FII and FA. It was found that samples cryo-milled for 60 minutes transformed back to FI and those cryo-milled for longer periods transformed back to FII.

7.2 Future Work

- To re-analyse the images collected from the in-line analysis of the granules to detect morphological features such as the circularity, size and elongation of samples, these

filters could really help understand the physical properties of the samples, not only the pharmaceutical industry but for food and material sciences too.

- Analysis of TSG at high feed rates over a prolonged period of time with both chemical and physical analysis in a GMP environment has not yet been reported, it would be good to apply some of the techniques to prevent fouling along with a contained conveyer system for analysis of granules in a continuous process.
- The THz Raman spectrometer has proved to be very successful for solid state analysis and acceptable as an alternative “gold standard” for analysis. The ability to provide information on both chemical and physical properties of samples is invaluable. With regards to the studies in this thesis, the future work I would propose would be to look more in depth at quantitative analysis of samples, for both in-line and off-line analysis. The idea was to build calibration models and achieve these results but unfortunately due to complications and time restraints this was not able to be achieved.
- The high detection limits of THz Raman were also not put to the test, it would be great to see this applied in-line to other process such as blending, milling of API and excipients.
- The application of THz Raman to spray drying and other processes that produce ASDs. While a lot of information can be taken from the spectra, there is still a lot unknown about the THz region, it would be great to couple the analysis of

pharmaceuticals with that of computational methods in order to assign the peaks in the LFR region.

- Further studies of comparing the limits of detection to XRPD and DSC to LFRS. Quantification studies and calibration models along with DoE approach to look at and test the abilities of LFRS for solid state analysis of single pharmaceuticals and mixtures either as a solid dosage form, a blend or as an ASD.

8. References

1. J. Rantanen and J. Khinast, *Journal of Pharmaceutical Sciences*, 2015, **104**, 3612-3638.
2. Q. Su, S. Ganesh, M. Moreno, Y. Bommireddy, M. Gonzalez, G. V. Reklaitis and Z. K. Nagy, *Computers & Chemical Engineering*, 2019, **125**, 216-231.
3. U. Nandi, V. Trivedi, S. A. Ross and D. Douroumis, *Pharmaceutics*, 2021, **13**, 624.
4. www.fda.gov, [www.fda.gov, http://www.fda.gov/downloads/drugs/guidancecomplianceregulatoryinformation/guidances/ucm070305.pdf](http://www.fda.gov/downloads/drugs/guidancecomplianceregulatoryinformation/guidances/ucm070305.pdf), (accessed 9th January 2015).
5. N. Shah, *Comput. Chem. Eng.*, 2004, **28**, 929-941.
6. N. Shan, M. L. Perry, D. R. Weyna and M. J. Zaworotko, *Expert Opinion on Drug Metabolism & Toxicology*, 2014, **10**, 1255-1271.
7. M. Savolainen, K. Kogermann, A. Heinz, J. Aaltonen, L. Peltonen, C. Strachan and J. Yliruusi, *European Journal of Pharmaceutics and Biopharmaceutics*, 2009, **71**, 71-79.
8. S. Vedantam and V. V. Ranade, *Sadhana-Academy Proceedings in Engineering Sciences*, 2013, **38**, 1287-1337.
9. S. Aitipamula, R. Banerjee, A. K. Bansal, K. Biradha, M. L. Cheney, A. R. Choudhury, G. R. Desiraju, A. G. Dikundwar, R. Dubey, N. Duggirala, P. P. Ghogale, S. Ghosh, P. K. Goswami, N. R. Goud, R. K. R. Jetti, P. Karpinski, P. Kaushik, D. Kumar, V. Kumar, B. Moulton, A. Mukherjee, G. Mukherjee, A. S. Myerson, V. Puri, A. Ramanan, T. Rajamannar, C. M. Reddy, N. Rodriguez-Hornedo, R. D. Rogers, T. N. G. Row, P. Sanphui, N. Shan, G. Shete, A. Singh, C. Q. C. Sun, J. A. Swift, R. Thaimattam, T. S. Thakur, R. K. Thaper, S. P. Thomas, S. Tothadi, V. R. Vangala, P. Vishweshwar, D. R. Weyna and M. J. Zaworotko, *Cryst. Growth Des.*, 2012, **12**, 4290-4291.
10. R. Shaikh, R. Singh, G. M. Walker and D. M. Croker, *Trends in Pharmacological Sciences*, 2018, **39**, 1033-1048.
11. S. R. Vippagunta, H. G. Brittain and D. J. W. Grant, *Advanced Drug Delivery Reviews*, 2001, **48**, 3-26.
12. B. Shah, V. K. Kakumanu and A. K. Bansal, *Journal of Pharmaceutical Sciences*, 2006, **95**, 1641-1665.
13. B. Rodríguez-Spong, C. P. Price, A. Jayasankar, A. J. Matzger and N. r. Rodríguez-Hornedo, *Advanced Drug Delivery Reviews*, 2004, **56**, 241-274.
14. K. R. Seddon, *Cryst. Growth Des.*, 2004, **4**, 1087-1087.
15. A. Nangia, *Accounts of Chemical Research*, 2008, **41**, 595-604.
16. E. H. Lee, *Asian Journal of Pharmaceutical Sciences*, 2014, **9**, 163-175.
17. P. H. Karpinski, *Chem. Eng. Technol.*, 2006, **29**, 233-237.
18. D.-K. Bucar, R. W. Lancaster and J. Bernstein, *Angewandte Chemie-International Edition*, 2015, **54**, 6972-6993.
19. P. A. Beckmann, P. R. Rablen, J. Schminck, S. T. Szewczyk and A. L. Rheingold, *Chemphyschem*, 2019, **20**, 2887-2894.

20. L. Zhao, M. P. Hanrahan, P. Chakravarty, A. G. DiPasquale, L. E. Sirois, K. Nagapudi, J. W. Lubach and A. J. Rossini, *Cryst. Growth Des.*, 2018, **18**, 2588-2601.
21. O. N. Kavanagh, D. M. Croker, G. M. Walker and M. J. Zaworotko, *Drug Discovery Today*, 2019, **24**, 796-804.
22. D. Singhal and W. Curatolo, *Advanced Drug Delivery Reviews*, 2004, **56**, 335-347.
23. S. Lee, A. Choi, W.-S. Kim and A. S. Myerson, *Cryst. Growth Des.*, 2011, **11**, 5019-5029.
24. J. F. Krzyzaniak, P. Meenan, C. L. Doherty, K. Pencheva, S. Luthra and A. Cruz-Cabeza, *Computational pharmaceutical solid state chemistry*, 2016, 117.
25. O. Raubenheimer, *Journal of the American Pharmaceutical Association*, 1922, **11**, 34-39.
26. J. Bauer, S. Spanton, R. Henry, J. Quick, W. Dziki, W. Porter and J. Morris, *Pharmaceutical research*, 2001, **18**, 859-866.
27. P. R. ten Wolde and D. Frenkel, *Physical Chemistry Chemical Physics*, 1999, **1**, 2191-2196.
28. A. Bhatia, S. Chopra, K. Nagpal, P. K. Deb, M. Tekade and R. K. Tekade, in *Dosage Form Design Parameters*, ed. R. K. Tekade, Academic Press, 2018, DOI: <https://doi.org/10.1016/B978-0-12-814421-3.00002-6>, pp. 31-65.
29. *Polymorphism in the Pharmaceutical Industry: Solid Form and Drug Development*, 2019, 1-496.
30. E. Hadjittofis, M. A. Isbell, V. Karde, S. Varghese, C. Ghoroi and J. Y. Heng, *Pharmaceutical research*, 2018, **35**, 1-22.
31. E. J. Munson, *Analytical Techniques in Solid-state Characterization*, 2009.
32. S. Datta and D. J. W. Grant, *Nat Rev Drug Discov*, 2004, **3**, 42-57.
33. S. Baghel, H. Cathcart and N. J. O'Reilly, *J Pharm Sci*, 2016, **105**, 2527-2544.
34. B. C. Hancock and M. Parks, *Pharmaceutical Research*, 2000, **17**, 397-404.
35. N. Blagden, M. de Matas, P. T. Gavan and P. York, *Advanced Drug Delivery Reviews*, 2007, **59**, 617-630.
36. Y. Guinet, L. Paccou, F. Danède, J.-F. Willart, P. Derollez and A. Hédoux, *International Journal of Pharmaceutics*, 2016, **509**, 305-313.
37. P. Macfhiionghaile, Y. Hu, K. Gniado, S. Curran, P. McArdle and A. Erxleben, *Journal of Pharmaceutical Sciences*, 2014, **103**, 1766-1778.
38. V. Caron, Y. Hu, L. Tajber, A. Erxleben, O. I. Corrigan, P. McArdle and A. M. Healy, *AAPS PharmSciTech*, 2013, **14**, 464-474.
39. Y. He and C. Ho, *Journal of Pharmaceutical Sciences*, 2015, **104**, 3237-3258.
40. Y. Tian, E. Jacobs, D. S. Jones, C. P. McCoy, H. Wu and G. P. Andrews, *International Journal of Pharmaceutics*, 2020, **586**, 119545.
41. J. S. LaFontaine, S. V. Jermain, L. K. Prasad, C. Brough, D. A. Miller, D. Lubda, J. W. McGinity and R. O. Williams III, *European Journal of Pharmaceutics and Biopharmaceutics*, 2016, **101**, 72-81.
42. S. V. Jermain, D. Miller, A. Spangenberg, X. Lu, C. Moon, Y. Su and R. O. Williams, *Drug Dev. Ind. Pharm.*, 2019, **45**, 724-735.
43. S. V. Jermain, M. B. Lowinger, D. J. Ellenberger, D. A. Miller, Y. Su and R. O. Williams III, *Molecular Pharmaceutics*, 2020, **17**, 2789-2808.

44. A. Rawle, *Malvern Technical Paper*
45. Z. Ma, H. G. Merkus, H. G. van der Veen, M. Wong and B. Scarlett, *Particle & Particle Systems Characterization: Measurement and Description of Particle Properties and Behavior in Powders and Other Disperse Systems*, 2001, **18**, 243-247.
46. E. D. Hirleman, 1983.
47. C. Levoguer, *Metal Powder Report*, 2013, **68**, 15-18.
48. Abismai, x, B. I, J. P. Canselier, A. M. Wilhelm, H. Delmas and C. Gourdon, *Ultrasonics Sonochemistry*, 2000, **7**, 187-192.
49. J. Han, X. Liu, M. Jiang, Z. Wang and M. Xu, *Journal of Hazardous Materials*, 2021, **401**, 123721.
50. T. Närvänen, K. Seppälä, O. Antikainen and J. Yliruusi, *Aaps Pharmscitech*, 2008, **9**, 282-287.
51. M. Fonteyne, S. Soares, J. Vercruyssen, E. Peeters, A. Burggraef, C. Vervaet, J. P. Remon, N. Sandler and T. De Beer, *European Journal of Pharmaceutics and Biopharmaceutics*, 2012, **82**, 429-436.
52. P. Hamilton, D. Littlejohn, A. Nordon, J. Sefcik and P. Slavin, *The Analyst*, 2012, **137**, 118-125.
53. E. J. Hukkanen and R. D. Braatz, *Sensors and Actuators B: Chemical*, 2003, **96**, 451-459.
54. Sympatec,
<http://www.sympatec.com/EN/ImageAnalysis/ImageAnalysis.html>,
<http://www.sympatec.com/EN/ImageAnalysis/ImageAnalysis.html>, (accessed September 2013).
55. P. Hamilton, Pure and Applied Chemistry, University of Strathclyde, 2011.
56. L. Saerens, D. Ghanam, C. Raemdonck, K. Francois, J. Manz, R. Kruger, S. Kruger, C. Vervaet, J. P. Remon and T. De Beer, *European Journal of Pharmaceutics and Biopharmaceutics*, 2014, **87**, 606-615.
57. D. Shandilya and S. Sharma, 2012.
58. E. V. Boldyreva, V. Drebuschak, I. Paukov, Y. A. Kovalevskaya and T. N. Drebuschak, *J. Therm. Anal. Calorim.*, 2004, **77**, 607-623.
59. L. Saerens, L. Dierickx, T. Quinten, P. Adriaenssens, R. Carleer, C. Vervaet, J. P. Remon and T. De Beer, *European Journal of Pharmaceutics and Biopharmaceutics*, 2012, **81**, 230-237.
60. L. Saerens, L. Dierickx, B. Lenain, C. Vervaet, J. P. Remon and T. De Beer, *European Journal of Pharmaceutics and Biopharmaceutics*, 2011, **77**, 158-163.
61. L. Yu, S. M. Reutzel and G. A. Stephenson, *Pharmaceutical Science & Technology Today*, 1998, **1**, 118-127.
62. A. C. Williams, V. B. Cooper, L. Thomas, L. J. Griffith, C. R. Petts and S. W. Booth, *International Journal of Pharmaceutics*, 2004, **275**, 29-39.
63. M. J. Lee, D. Y. Seo, I. C. Wang, N. H. Chun, H. E. Lee, M. Y. Jeong, W. S. Kim and G. J. Choi, *Journal of Pharmaceutical Sciences*, 2012, **101**, 1578-1586.
64. C. J. Strachan, T. Rades, K. C. Gordon and J. Rantanen, *Journal of Pharmacy and Pharmacology*, 2007, **59**, 179-192.

65. M. Fonteyne, J. Vercruyssen, D. C. Diaz, D. Gildemyn, C. Vervaet, J. P. Remon and T. De Beer, *Pharm. Dev. Technol.*, 2013, **18**, 85-97.
66. M. A. Mansouri, E. Ziemons, P.-Y. Sacré, M. Kharbach, I. Barra, Y. Cherrah, P. Hubert and A. Bouklouze, *Journal of Pharmaceutical and Biomedical Analysis*, 2021, **196**, 113922.
67. C. Rustichelli, G. Gamberini, V. Ferioli, M. C. Gamberini, R. Ficarra and S. Tommasini, *Journal of pharmaceutical and biomedical analysis*, 2000, **23**, 41-54.
68. F. G. Vogt, *Future medicinal chemistry*, 2010, **2**, 915-921.
69. R. T. Berendt, D. M. Sperger, E. J. Munson and P. K. Isbester, *TrAC Trends in Analytical Chemistry*, 2006, **25**, 977-984.
70. H. Wu and M. Khan, *Journal of Molecular Structure*, 2012, **1020**, 112-120.
71. G. M. Day, J. A. Zeitler, W. Jones, T. Rades and P. F. Taday, *The Journal of Physical Chemistry B*, 2006, **110**, 447-456.
72. J. B. Baxter and G. W. Guglietta, *Analytical chemistry*, 2011, **83**, 4342-4368.
73. M. R. Patil, S. B. Ganorkar, A. S. Patil and A. A. Shirkhedkar, *Critical Reviews in Analytical Chemistry*, 2020, 1-13.
74. D. Treffer, P. R. Wahl, T. R. Hoermann, D. Markl, S. Schrank, I. Jones, P. Cruise, R.-K. Muerb, G. Koscher, E. Roblegg and J. G. Khinast, *International Journal of Pharmaceutics*, 2014, **466**, 181-189.
75. R. Sayin, L. Martinez-Marcos, J. G. Osorio, P. Cruise, I. Jones, G. W. Halbert, D. A. Lamprou and J. D. Litster, *International Journal of Pharmaceutics*, 2015, **496**, 24-32.
76. A. S. El Hagrasy, P. Cruise, I. Jones and J. D. Litster, *J. Pharm. Innov.*, 2013, **8**, 90-98.
77. W. Meng, A. D. Román-Ospino, S. S. Panikar, C. O'Callaghan, S. J. Gilliam, R. Ramachandran and F. J. Muzzio, *Advanced Powder Technology*, 2019, **30**, 879-894.
78. S. Bandari, D. Nyavanandi, V. R. Kallakunta, K. Y. Janga, S. Sarabu, A. Butreddy and M. A. Repka, *International Journal of Pharmaceutics*, 2020, **580**, 119215.
79. L. Madarász, Z. K. Nagy, I. Hoffer, B. Szabó, I. Csontos, H. Pataki, B. Démuth, B. Szabó, K. Csorba and G. Marosi, *International Journal of Pharmaceutics*, 2018, **547**, 360-367.
80. L. Madarász, Á. Köte, B. Hambalkó, K. Csorba, V. Kovács, L. Lengyel, G. Marosi, A. Farkas, Z. K. Nagy and A. Domokos, *International Journal of Pharmaceutics*, 2022, **612**, 121280.
81. J. Huang, C. Goolcharran, J. Utz, P. Hernandez-Abad, K. Ghosh and A. Nagi, *Journal of pharmaceutical innovation*, 2010, **5**, 58-68.
82. A. Wilms, R. Meier and P. Kleinebudde, *J. Pharm. Innov.*, 2021, **16**, 247-257.
83. A. Wilms, A. Teske, R. Meier, R. Wiedey and P. Kleinebudde, *Journal of Pharmaceutical Innovation*, 2020, 1-11.
84. E. I. Keleb, A. Vermeire, C. Vervaet and J. P. Remon, *International Journal of Pharmaceutics*, 2004, **273**, 183-194.
85. A. F. T. Silva, A. Burggraeve, Q. Denon, P. Van der Meeren, N. Sandler, T. Van Den Kerkhof, M. Hellings, C. Vervaet, J. P. Remon, J. A. Lopes and T.

- De Beer, *European Journal of Pharmaceutics and Biopharmaceutics*, 2013, **85**, 1006-1018.
86. P. Hitzer, T. Bäuerle, T. Drieschner, E. Ostertag, K. Paulsen, H. van Lishaut, G. Lorenz and K. Rebner, *Anal. Bioanal. Chem.*, 2017, **409**, 4321-4333.
 87. E. Räsänen and N. Sandler, *Journal of Pharmacy and Pharmacology*, 2007, **59**, 147-159.
 88. A. Q. Vo, H. He, J. Zhang, S. Martin, R. Chen and M. A. Repka, *Aaps Pharmscitech*, 2018, **19**, 3425-3429.
 89. A. Paudel, D. Rajjada and J. Rantanen, *Advanced drug delivery reviews*, 2015, **89**, 3-20.
 90. M. Karimi-Jafari, R. Soto, A. B. Albadarin, D. Croker and G. Walker, *International Journal of Pharmaceutics*, 2021, **601**, 120555.
 91. L. Saerens, D. Ghanam, C. Raemdonck, K. Francois, J. Manz, R. Krüger, S. Krüger, C. Vervaet, J. P. Remon and T. De Beer, *European Journal of Pharmaceutics and Biopharmaceutics*, 2014, **87**, 606-615.
 92. M. Wilson, M. A. Williams, D. S. Jones and G. P. Andrews, *Therapeutic delivery*, 2012, **3**, 787-797.
 93. L. Saerens, L. Dierickx, B. Lenain, C. Vervaet, J. P. Remon and T. De Beer, *European Journal of Pharmaceutics and Biopharmaceutics*, 2011, **77**, 158-163.
 94. K. Bērziņš, S. J. Fraser-Miller and K. C. Gordon, *International Journal of Pharmaceutics*, 2021, **592**, 120034.
 95. D. Bertoldo Menezes, A. Reyer, A. Yüksel, B. Bertoldo Oliveira and M. Musso, *Spectroscopy Letters*, 2018, **51**, 438-445.
 96. P. J. Larkin, M. Dabros, B. Sarsfield, E. Chan, J. T. Carriere and B. C. Smith, *Applied Spectroscopy*, 2014, **68**, 758-776.
 97. E. Bordos, M. T. Islam, A. J. Florence, G. W. Halbert and J. Robertson, *Molecular Pharmaceutics*, 2019, **16**, 4361-4371.
 98. P. J. Larkin, J. Wasylyk and M. Raglione, *Applied Spectroscopy*, 2015, **69**, 1217-1228.
 99. E. I. Keleb, A. Vermeire, C. Vervaet and J. P. Remon, *International Journal of Pharmaceutics*, 2002, **239**, 69-80.
 100. W. De Soete, J. Dewulf, P. Cappuyns, G. Van der Vorst, B. Heirman, W. Aelterman, K. Schoeters and H. Van Langenhove, *Green Chemistry*, 2013, **15**, 3039-3048.
 101. J. Litster, B. Ennis and L. Lian, *The Science and Engineering of Granulation Processes*, Springer, 2004.
 102. R. M. Dhenge, J. J. Cartwright, M. J. Hounslow and A. D. Salman, *International Journal of Pharmaceutics*, 2012, **438**, 20-32.
 103. W. C. Yang, *Handbook of Fluidization and Fluid-Particle Systems*, Taylor & Francis, 2003.
 104. T. Schaefer and C. Mathiesen, *International Journal of Pharmaceutics*, 1996, **139**, 139-148.
 105. T. Scientific, Thermo Scientific, www.thermoscientific.com, (accessed 20th March 2015, 2015).

106. P. W. D. Treffer, D. Markl, G. Koscher, E. Roblegg, J. Khinast, *Hot melt extrusion as a continuous pharmaceutical manufacturing process*, Springer Publishers, New York, 2013.
107. S. M. Iveson, J. D. Litster, K. Hapgood and B. J. Ennis, *Powder Technol.*, 2001, **117**, 3-39.
108. J. Verduyck, A. Burggraef, M. Fonteyne, P. Cappuyns, U. Delaet, I. Van Assche, T. De Beer, J. P. Remon and C. Vervaet, *International journal of pharmaceutics*, 2015, **479**, 171-180.
109. A. S. El Hagrasy and J. D. Litster, *Aiche J.*, 2013, **59**, 4100-4115.
110. D. Djuric, *Continuous Granulation with a Twin-Screw Extruder*, Cuvillier, 2008.
111. K. T. Lee, Continuous granulation of pharmaceutical powder using a twin screw granulator, (accessed February 2015).
112. Extricom, Screw Elements, (accessed 23rd December 2015, 2015).
113. R. M. Dhenge, R. S. Fyles, J. J. Cartwright, D. G. Doughty, M. J. Hounslow and A. D. Salman, *Chemical Engineering Journal*, 2010, **164**, 322-329.
114. R. M. Dhenge, J. J. Cartwright, D. G. Doughty, M. J. Hounslow and A. D. Salman, *Advanced Powder Technology*, 2011, **22**, 162-166.
115. A. S. El Hagrasy, J. R. Hennenkamp, M. D. Burke, J. J. Cartwright and J. D. Litster, *Powder Technology*, 2013, **238**, 108-115.
116. H. Patil, R. V. Tiwari and M. A. Repka, *AAPS PharmSciTech*, 2016, **17**, 20-42.
117. M. M. Crowley, F. Zhang, M. A. Repka, S. Thumma, S. B. Upadhye, S. K. Battu, J. W. McGinity and C. Martin, *Drug Dev. Ind. Pharm.*, 2007, **33**, 909-926.
118. S. Qi, A. Gryczke, P. Belton and D. Q. M. Craig, *International Journal of Pharmaceutics*, 2008, **354**, 158-167.
119. I. Labs, A guidance to D values in Pharmaceutical Particle Characterisation, (accessed January 2015, 2015).
120. I. Labs, <http://www.innopharmalabs.com/>, <http://www.innopharmalabs.com/>, (accessed 20th March 2015).
121. X. Ma and R. O. Williams III, *Journal of Drug Delivery Science and Technology*, 2019, **50**, 113-124.
122. A. Clearfield, J. H. Reibenspies and N. Bhuvanesh, *Principles and applications of powder diffraction*, John Wiley and Sons, Ltd., 2008.
123. S. D. Thakore, J. Akhtar, R. Jain, A. Paudel and A. K. Bansal, *Molecular Pharmaceutics*, 2021.
124. C. Leyva-Porras, P. Cruz-Alcantar, V. Espinosa-Solís, E. Martínez-Guerra, C. I. Piñón-Balderrama, I. Compean Martínez and M. Z. Saavedra-Leos, *Polymers*, 2019, **12**, 5.
125. A. Smekal, *Die Naturwissenschaften*, 1923, **11**, 873-875.
126. nobelprize.org and S. C. V. Raman, <https://www.nobelprize.org/prizes/physics/1930/raman/biographical/>, (accessed 24th May 2019).
127. Y. Zhang, H. Hong and W. B. Cai, *Curr. Pharm. Biotechnol.*, 2010, **11**, 654-661.

128. H. j. K. Angelo Chianese, *Industrial Crystallization Process Monitoring and Control* 2012.
129. P. M. A. Sherwood and P. M. A. Sherwood, *Vibrational spectroscopy of solids*, CUP Archive, 1972.
130. T. David, *Spectroscopy*, 2019, **34**, 10-21.
131. M. Takahashi, *Crystals*, 2014, **4**, 74-103.
132. W. S. Solutions, Wiley KnowitAll Library <https://sciencesolutions.wiley.com/solutions/technique/raman/knowitall-raman-collection/>, (accessed 25 June 2022, 2022).
133. R. Project, Ruff Database, <https://rruff.info/>, (accessed 22 June 2022, 2022).
134. C. Corp, An Introduction to THZ-Raman Spectroscopy, <https://www.coherent.com/web-resources/white-paper/intro-to-thz-raman-spectroscopy-wp>, (accessed 01 January 2023, 2023).
135. M. Tonouchi, *Nat Photon*, 2007, **1**, 97-105.
136. L. F. World, SPECTROSCOPY: Terahertz Raman: Accessing molecular structure with Raman spectroscopy, <https://www.laserfocusworld.com/test-measurement/spectroscopy/article/16557045/spectroscopy-terahertz-raman-accessing-molecular-structure-with-raman-spectroscopy>, (accessed 23 Feb 2022, 2022).
137. J. Neu and C. A. Schmuttenmaer, *Journal of Applied Physics*, 2018, **124**, 231101.
138. G. D. Reid and K. Wynne, *Encyclopedia of Analytical chemistry*, 2000, **35**.
139. A. Krotkus, *Journal of Physics D: Applied Physics*, 2010, **43**, 273001.
140. K. Ajito, M. Nakamura, T. Tajima and Y. Ueno, in *Encyclopedia of Spectroscopy and Spectrometry (Third Edition)*, eds. J. C. Lindon, G. E. Tranter and D. W. Koppenaal, Academic Press, Oxford, 2017, DOI: <https://doi.org/10.1016/B978-0-12-409547-2.12092-X>, pp. 432-438.
141. N. Munir, M. Nugent, D. Whitaker and M. McAfee, *Pharmaceutics*, 2021, **13**, 1432.
142. S. D. Brown, R. Tauler and B. Walczak, *Comprehensive chemometrics: chemical and biochemical data analysis*, Elsevier, 2020.
143. M. Zeaiter and D. Rutledge, in *Comprehensive Chemometrics*, eds. S. D. Brown, R. Tauler and B. Walczak, Elsevier, Oxford, 2009, DOI: <https://doi.org/10.1016/B978-044452701-1.00074-0>, pp. 121-231.
144. M. N. Triba, L. Le Moyec, R. Amathieu, C. Goossens, N. Bouchemal, P. Nahon, D. N. Rutledge and P. Savarin, *Molecular BioSystems*, 2015, **11**, 13-19.
145. <https://wiki.anton-paar.com/uk-en/particle-size-distribution/#:~:text=D%2Dvalues,can%20be%20undersize%20or%20oversize> (accessed January 2021).
146. K. T. Lee, A. Ingram and N. A. Rowson, *Powder Technology*, 2013, **238**, 91-98.
147. MODDE user guide, <https://www.sartorius.com/download/544636/modde-12-user-guide-en-b-00090-sartorius-data.pdf>, (accessed September 2020).
148. P. Kleinebudde and H. Lindner, *International Journal of Pharmaceutics*, 1993, **94**, 49-58.

149. D. Djuric and P. Kleinebudde, *Pharm. Dev. Technol.*, 2010, **15**, 518-525.
150. T. C. Seem, N. A. Rowson, A. Ingram, Z. Huang, S. Yu, M. de Matas, I. Gabbott and G. K. Reynolds, *Powder Technology*, 2015, **276**, 89-102.
151. R. M. Dhenge, K. Washino, J. J. Cartwright, M. J. Hounslow and A. D. Salman, *Powder Technology*, 2013, **238**, 77-90.
152. M. R. Thompson and J. Sun, *Journal of Pharmaceutical Sciences*, 2010, **99**, 2090-2103.
153. B. Liu, X. Han, Z. Wang, H. Zhang, N. Liu, X. Gao, J. Gao and A. Zheng, *Journal of Drug Delivery Science and Technology*, 2021, **66**, 102855.
154. P. C. Cruz, F. A. Rocha and A. M. Ferreira, *Organic Process Research & Development*, 2019, **23**, 2592-2607.
155. X. Feng, A. Vo, H. Patil, R. V. Tiwari, A. S. Alshetaili, M. B. Pimparade and M. A. Repka, *Journal of Pharmacy and Pharmacology*, 2016, **68**, 692-704.
156. X. Liu, M. Lu, Z. Guo, L. Huang, X. Feng and C. Wu, *Pharmaceutical research*, 2012, **29**, 806-817.
157. S. Huang, K. P. O'Donnell, J. M. Keen, M. A. Rickard, J. W. McGinity and R. O. Williams, *AAPS PharmSciTech*, 2016, **17**, 106-119.
158. S. Qi, P. Avalle, R. Saklatvala and D. Q. Craig, *European Journal of Pharmaceutics and Biopharmaceutics*, 2008, **69**, 364-371.
159. P. Di Martino, A. Guyot-Hermann, P. Conflant, M. Drache and J. Guyot, *International journal of pharmaceutics*, 1996, **128**, 1-8.
160. P. DiMartino, P. Conflant, M. Drache, J. P. Huvenne and A. M. GuyotHermann, *Journal of Thermal Analysis*, 1997, **48**, 447-458.
161. P. Di MARTINO, G. F. Palmieri and S. Martelli, *Chemical and pharmaceutical bulletin*, 2000, **48**, 1105-1108.
162. B. B. Ivanova, *Journal of molecular structure*, 2005, **738**, 233-238.
163. M. A. Perrin, M. A. Neumann, H. Elmaleh and L. Zaske, *Chem. Commun.*, 2009, DOI: 10.1039/b822882e, 3181-3183.
164. I. C. Wang, M. J. Lee, D. Y. Seo, H. E. Lee, Y. Choi, W. S. Kim, C. S. Kim, M. Y. Jeong and G. J. Choi, *AAPS PharmSciTech*, 2011, **12**, 764-770.
165. M. Ibrahim, J. Zhang, M. Repka and R. Chen, *AAPS PharmSciTech*, 2019, **20**, 1-8.
166. Z. Yang, K. Nollenberger, J. Albers, J. Moffat, D. Craig and S. Qi, *European Journal of Pharmaceutics and Biopharmaceutics*, 2014, **88**, 897-908.
167. L. R. Hilden and K. R. Morris, *Journal of Pharmaceutical Sciences*, 2004, **93**, 3-12.
168. S. Al-Dulaimi, A. Aina and J. Burley, *Crystengcomm*, 2010, **12**, 1038-1040.
169. L. F. L. Silva, W. Paschoal, G. S. Pinheiro, J. G. da Silva Filho, P. T. Freire, F. F. de Sousa and S. G. Moreira, *CrystEngComm*, 2019, **21**, 297-309.
170. G. G. Z. Zhang, C. Gu, M. T. Zell, R. T. Burkhardt, E. J. Munson and D. J. W. Grant, *Journal of Pharmaceutical Sciences*, 2002, **91**, 1089-1100.
171. S. A. Park, S. Lee and W. S. Kim, *Cryst. Growth Des.*, 2015, **15**, 3617-3627.
172. A. R. Pallipurath, J. M. Skelton, M. R. Warren, N. Kamali, P. McArdle and A. Erxleben, *Molecular Pharmaceutics*, 2015, **12**, 3735-3748.
173. G. G. Hossain, *Acta Crystallographica Section E: Structure Reports Online*, 2006, **62**, o2166-o2167.

174. M. R. Caira and R. Mohamed, *Acta Crystallographica Section B-Structural Science*, 1992, **48**, 492-498.
175. Y. Li, P. S. Chow and R. B. H. Tan, *International Journal of Pharmaceutics*, 2011, **415**, 110-118.
176. S. Roy, K. S. Alexander, A. T. Riga and K. Chatterjee, *Journal of pharmaceutical sciences*, 2003, **92**, 747-759.
177. M. Kurotani and I. Hirasawa, *Journal of Crystal Growth*, 2008, **310**, 4576-4580.
178. C. Sun and D. J. W. Grant, *Pharmaceutical Research*, **18**, 274-280.
179. X. P. Cao, C. Q. Sun and T. J. Thamann, *Journal of Pharmaceutical Sciences*, 2005, **94**, 1881-1892.
180. M. Tonouchi, *Nature Photonics*, 2007, **1**, 97-105.
181. M. R. Caira and R. Mohamed, *Acta crystallographica. Section B, Structural science*, 1992, **48**, 492-498.
182. M. Kurotani and I. Hirasawa, *Chemical Engineering Research & Design*, 2010, **88**, 1272-1278.
183. C. Liu, F. Cao, S. A. Kulkarni, G. P. F. Wood and E. E. Santiso, *Cryst. Growth Des.*, 2019, **19**, 6925-6934.
184. J. H. Blanco-Márquez, C. P. Ortiz, N. E. Cerquera, F. Martínez, A. Jouyban and D. R. Delgado, *Journal of Molecular Liquids*, 2019, **293**, 111507.
185. K. Ravindra Acharya, K. N. Kuchela and G. Kartha, *Journal of Crystallographic and Spectroscopic Research*, **12**, 369-376.
186. C.-H. Gu, K. Chatterjee, V. Young and D. J. W. Grant, *Journal of Crystal Growth*, 2002, **235**, 471-481.
187. X. Cao, C. Sun and T. J. Thamann, *Journal of pharmaceutical sciences*, 2005, **94**, 1881-1892.

9. Appendix

9.1 Appendix A

9.1.1 Sample Weights from 1 kg/h Doe Experiment

Table 9.1 Sample weights and loss of water on drying

| Run No. | Weight of collected sample (g) | Sample to be dried (g) | Weight dried (g) | of sample | Loss on Drying (g) |
|---------|--------------------------------|------------------------|------------------|-----------|--------------------|
| 1 | 67.3 | 20.1 | 14.8 | | 5.3 |
| 2 | 80.2 | 20.2 | 15.4 | | 4.8 |
| 3 | 122.6 | 20.3 | 15.5 | | 4.8 |
| 4 | 122.4 | 20.2 | 15.6 | | 4.6 |
| 5 | 120.6 | 20.1 | 17.7 | | 2.4 |
| 6 | 64.8 | 20.2 | 17.6 | | 2.6 |
| 6.2 | 120.6 | 20.2 | 17.7 | | 2.5 |
| 7 | 61.0 | 20.0 | 17.7 | | 2.3 |
| 8 | 63.2 | 19.8 | 17.0 | | 2.8 |
| 9 | 93.5 | 19.9 | 16.5 | | 3.4 |
| 10 | 59.0 | 20.0 | 16.6 | | 3.4 |
| 10.2 | 89.7 | 20.3 | 16.3 | | 4 |

9.1.2 Calibration of the Screw Feeder

Loading the feeder:

Tare weight: 0.291 kg

Weight: 0.000 kg

Filled weight 1.265 kg

Maximum output of the hopper recorded as 15.936 kg

The feeder was then set to volumetric feeding.

9.1.2.1 Eyecon™ Equipment Timings

Table 9.2 Eyecon™ Data Capture Timings and Observations during the Experiment

| Run No. | Start Time | Stop Time | Notes |
|---------|------------|-----------|-----------------------------------|
| 1 | 15:15:59 | 15:21:02 | |
| 2 | 15:24:55 | 15:29:58 | |
| 3 | 15:34:06 | 15:39:14 | Crashed not all images processed |
| 4 | 15:44:36 | 15:49:38 | |
| 5 | 15:53:09 | 15:58:13 | |
| 6 | 16:02:29 | 16:05:14 | Crashed not all images processed |
| 6.2 | 16:11:48 | 16:17:01 | Crashed not all images processed |
| 7 | 16:20:50 | 16:25:58 | |
| 8 | 16:28:58 | 16:33:22 | A few pending images but no crash |
| 9 | 16:37:23 | 16:42:26 | |
| 10 | 16:45:34 | 16:48:29 | Refilled granulator. |
| 10.2 | 16:55:07 | 17:00:10 | |

Experiment 6 and 10 were repeated as 6.2 and 10.2, the samples and results from these runs will be reported from now on as samples 6 and 10. As this was the Eyecon™'s first run there were a few glitches in the software which caused it to crash a few times throughout. New software was actually installed after this experiment in which there were no further problems. Enough images were captured for each of the experiments for the analysis to be carried out.

9.1.2.1 Sample Weights for 3 kg/h DoE experiment

Table 9.3 Sample weights and loss of water on drying

| Expt. No. | Weight of collected sample (g) | Sample to be dried (g) | Weight dried (g) | of sample | Loss on Dry-ing (g) |
|-----------|--------------------------------|------------------------|------------------|-----------|---------------------|
| 1 | 67.3 | 20.1 | 14.8 | | 5.3 |
| 2 | 80.2 | 20.2 | 15.4 | | 4.8 |
| 3 | 122.6 | 20.3 | 15.5 | | 4.8 |
| 4 | 122.4 | 20.2 | 15.6 | | 4.6 |
| 5 | 120.6 | 20.1 | 17.7 | | 2.4 |
| 6 | 64.8 | 20.2 | 17.6 | | 2.6 |
| 6.2 | 120.6 | 20.2 | 17.7 | | 2.5 |
| 7 | 61.0 | 20.0 | 17.7 | | 2.3 |
| 8 | 63.2 | 19.8 | 17.0 | | 2.8 |
| 9 | 93.5 | 19.9 | 16.5 | | 3.4 |
| 10 | 59.0 | 20.0 | 16.6 | | 3.4 |
| 10.2 | 89.7 | 20.3 | 16.3 | | 4 |

9.2 Calibration of the Screw Feeder

9.2.1 Twin screw analysis with Raman and Eyecon analysis

The experiment was set up as in Figure 9.1 A hole was drilled in the front of the plastic facing of the TSG granulation port as shown in shows the full set up with the Raman probe and Eyecon in position. Silver foil was used in order to block out any light interference to the Raman detector.

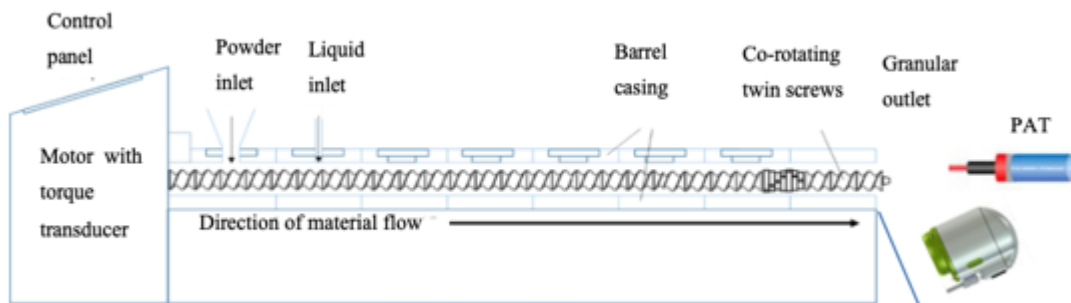
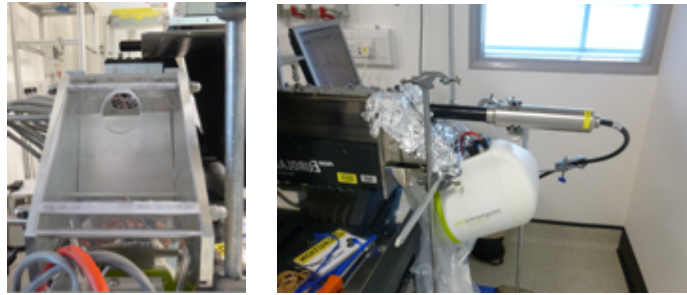


Figure 9.1 Schematic set up showing the position of the Raman and Eyecon PAT, with images above of the actual set up showing an adaptation for the implementation of in-line Raman analysis.

9.2.1.1 Raman analysis

Raman spectra were acquired off-line of croscarmellose, Pharmacoat 603, Avicel and Pharmatose with exposure times of 5s and 1 accumulation. These were taken off-line and were acquired in the Kaiser off-line sampling unit provided with the spectrometer. The purpose of this was to check the feasibility of studying the placebo mixture used in the granulation with Raman Spectroscopy.

The Raman spectrometer was set to take continuous measurements each with a 30s accusation time and 1 accumulation. The cosmic ray filter was turned on to remove any possibilities of interference with the spectra. A total of 230 samples were acquired over two hours. These were then saved as csv files and plotted in MATLAB. Principal

component analysis was carried out on the data. The pre-processing for the PCA was: standard normal variate, 2nd derivative Savitzky-Golay filter and mean centring.

An initial experiment was carried out to look at the feasibility of monitoring the excipients using a Kaiser Raman PhAT probe. Each of the excipients was examined off-line in order to obtain their Raman Spectra. An overlay of each of the spectra are shown in Figure 9.2, which highlights the amount of fluorescence in Na Croscarmellose and Avicel. The spectra are normalised in Figure 9.3.

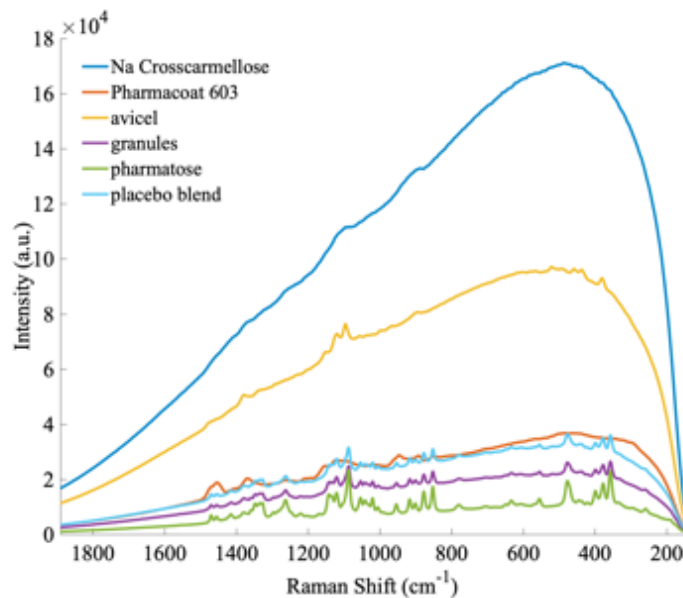


Figure 9.2 Unprocessed spectra of the excipients used for twin screw granulation including a blend of all of them.

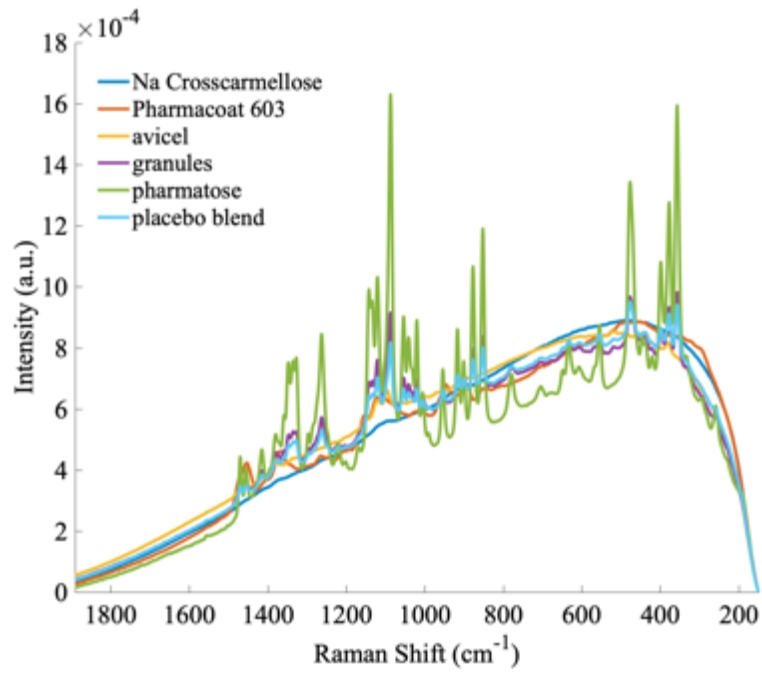


Figure 9.3 Normalised spectra of the excipients used for twin screw granulation including a blend of all of them.

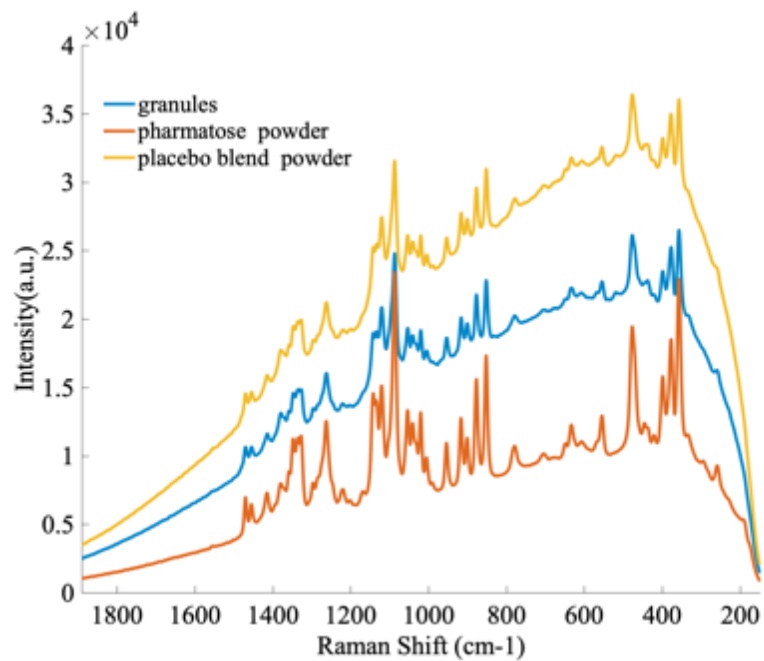


Figure 9.4 Raman spectra of the individual excipients used for the placebo formulations A and B for TSG experiments

The results from on-line analysis of Raman are show in Figure 9.5

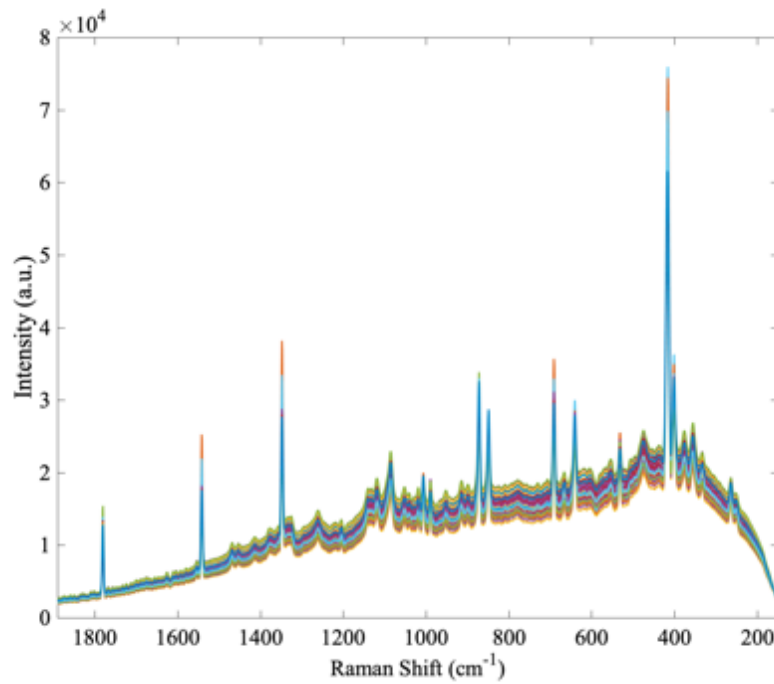


Figure 9.5 Raman results from inline analysis of TSG long run experiment.

There appear to be very sharp peaks in the spectra, that are not present in the excipient spectra, despite all efforts to block out the light these are thought to have come from fluorescent room lights present in the room.

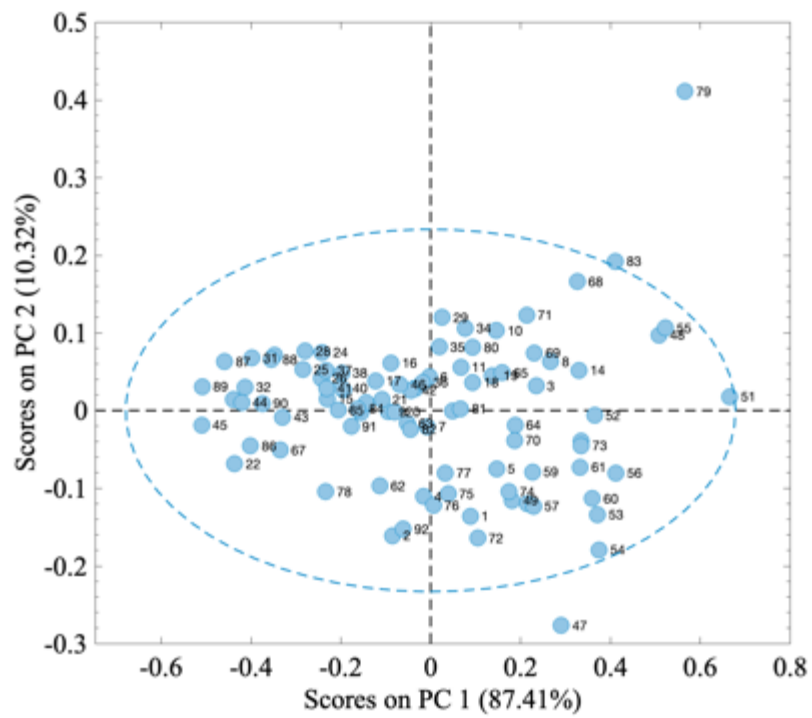


Figure 9.6 Fouling of Raman probe during analysis

9.3 Appendix C

9.3.1 Long run experiments screw A and Screw B

Table 9.4 Screw A

| Time Sample Ac- quired | Sample Num- ber | Tare Weight of crystallis- ing dish | Weight of dish + wet gran- ules | Weight of wet gran- ules | Weight of dish and dry gran- ules | Weight of gran- ules | Water lost |
|---------------------------------|-----------------------|--|---|-----------------------------------|---|-------------------------------|---------------|
| 14:52 | 1 | 136 | 174.8 | 38.8 | 169.06 | 33.06 | 5.74 |
| 15:07 | 2 | 154.1 | 192.4 | 38.3 | 186.69 | 32.59 | 5.71 |
| 15:22 | 3 | 159.6 | 197.5 | 37.9 | 192.29 | 32.69 | 5.21 |
| 15:37 | 4 | 160.4 | 198.6 | 38.2 | 192.98 | 32.58 | 5.62 |
| 15:52 | 5 | 94.41 | 131.76 | 37.35 | 124.19 | 29.78 | 7.57 |
| 16:16 | 6 | 94.48 | 139.05 | 44.57 | 131.16 | 36.68 | 7.89 |

Table 9.5 Screw B

| Time Sample Ac- quired | Sample Num- ber | Tare Weight of crystallis- ing dish | Weight of dish + wet gran- ules | Weight of wet gran- ules | Weight of dish and dry gran- ules | Weight of gran- ules | Water lost |
|---------------------------------|-----------------------|--|---|-----------------------------------|---|-------------------------------|---------------|
| 15:26 | 1 | 94.41 | 131.59 | 37.18 | 125.32 | 30.91 | 6.27 |
| 15:41 | 2 | 135.77 | 175.96 | 40.19 | 169.33 | 33.56 | 6.63 |
| 15:56 | 3 | 192.50 | 230.23 | 37.73 | 223.97 | 31.47 | 6.26 |
| 16:11 | 4 | 94.54 | 132.66 | 38.12 | 126.31 | 31.77 | 6.35 |
| 16:26 | 5 | 135.98 | 181.44 | 45.46 | 172.45 | 36.47 | 8.99 |
| 16:41 | 6 | 192.91 | 240.21 | 47.30 | 231.12 | 38.21 | 9.09 |

9.4 Appendix D

9.4.1 Optimum Focal Length for Non-Invasive THz Raman

Measurement

9.4.1.1 Experimental

The optical focal length is the distance from the optic at which the sample is in focus. The optimum focal length was determined by varying the distance of a reference layer of TiO₂ placed in between two microscope slides. The distance between the sample and the optic was varied between 1 and 16 mm by layering a series of specially cut metal sheets. The sheets had an approximate thickness of 1 mm; a 30 mm diameter circular hole was cut into each to allow the measurement of the TiO₂ plate. The glass plates were also 1 mm thick. The optimum focal length was achieved after a layer of 8 plates had been applied and was calculated, including the layer of glass to be 9 mm away from the optic head.

The system was set up as shown in Figure 9.7. Spectra were collected with an exposure time of 2 seconds and acquisition time of 10 s.

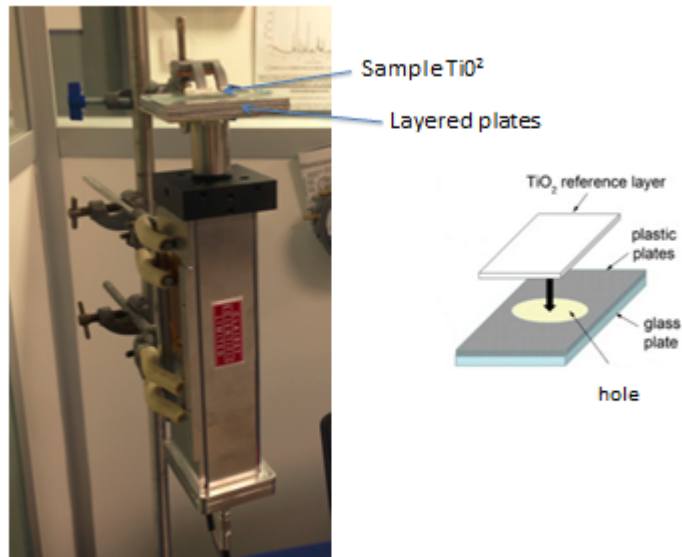


Figure 9.7 THz Raman set up for the optimization of focal length

9.4.2 Results and Discussion

Figure 9.8 shows the raw data of the spectra of TiO_2 produced from the addition of 1 through to 12 plates. The Raman spectra contain peaks at approximately 143, 397, 520 and 640 cm^{-1} . §

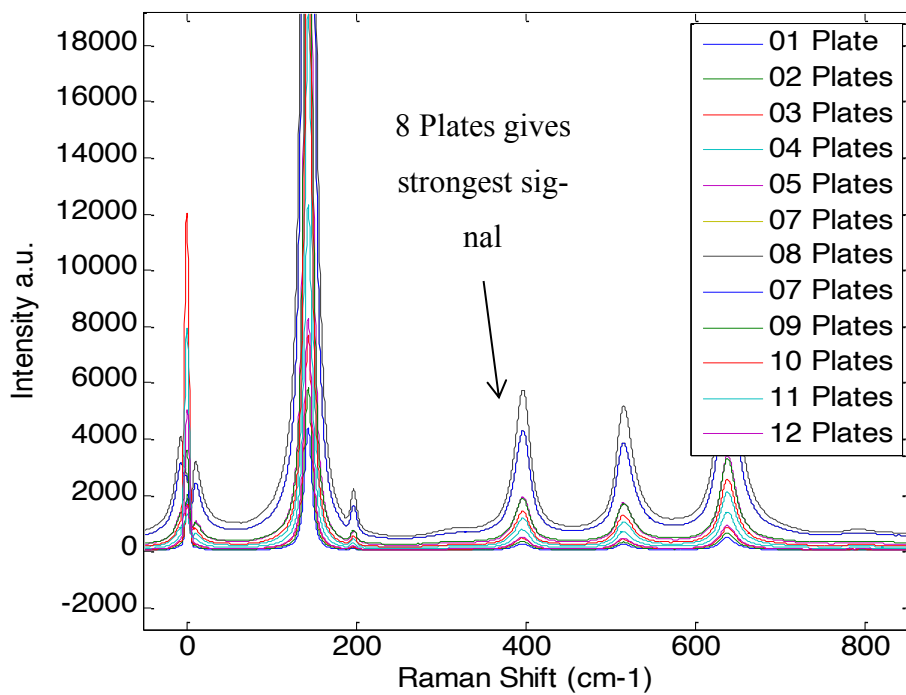


Figure 9.8 Overlay of all the spectra obtained for each addition of the 12 plates

The Savitzky–Golay algorithm was used to calculate the first derivative spectra, this removes the baseline offset, a filter width of 15 and 1st order polynomial was used. Figure 9.9 shows the first derivative spectra of the peaks at roughly 630 cm⁻¹ for TiO₂ where the signal to increase as each of the plates are added, signals of spectra after 8 plates were added showed a decrease in peak height each time an additional plate was added until there was no signal from the TiO₂.

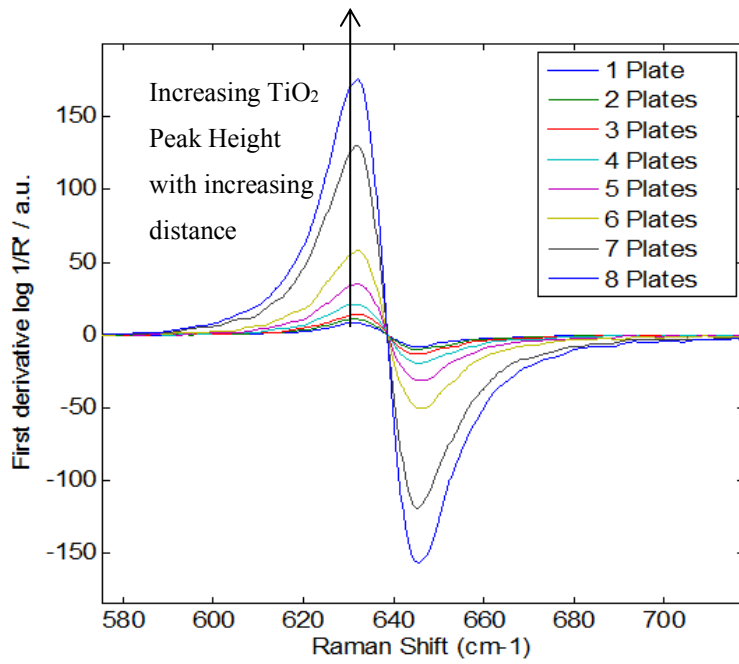


Figure 9.9 First derivative spectra of TiO_2 peak $580\text{-}700\text{ cm}^{-1}$ acquired through the addition of 1-8 plates separating the sample from the optic.

9.4.3 Conclusions

The best signal was obtained when there were 8 metal plates separating the sample from the analytical probe. The optimum sampling distance was calculated to be 9 mm from the optic.